RECIPROCAL CIRCULAR POLARIZATION SELECTIVE SURFACES

By

Jasmin E. Roy

A Thesis

Submitted to the Faculty of Graduate Studies

In Partial Fulfillment of the Requirements

for the Degree of

Doctor of Philosophy

Department of Electrical and Computer Engineering

University of Manitoba

Winnipeg, Manitoba

ISBN 0-612-13488-1

Nom JASMIN ÉMILE ROY

Dissertation Abstracts International et *Masters Abstracts International* sont organisés en catégories de sujets. Veuillez s.v.p. choisir le sujet qui décrit le mieux votre thèse et inscrivez le code numérique approprié dans l'espace réservé ci-dessous.

ENGINEERING, ELECTRONICS AND ELECTRICAL

SUJET

0	5	4	4

CODE DE SUJET

UMI

Catégories par sujets

HUMANITÉS ET SCIENCES SOCIALES

COMMUNICATIONS ET LES ARTS

Architecture 0729
Beaux-arts 0357
Bibliothéconomie 0399
Cinéma 0900
Communication verbale 0459
Communications 0708
Danse 0378
Histoire de l'art 0377
Journalisme 0391
Musique 0413
Sciences de l'information 0723
Théâtre 0465

ÉDUCATION

Généralités 515
Administration 0514
Art 0273
Collèges communautaires 0275
Commerce 0688
Économie domestique 0278
Éducation permanente 0516
Éducation préscolaire 0518
Éducation sanitaire 0680
Enseignement agricole 0517
Enseignement bilingue et multiculturel 0282
Enseignement industriel 0521
Enseignement primaire. 0524
Enseignement professionnel 0747
Enseignement religieux 0527
Enseignement secondaire 0533
Enseignement spécial 0529
Enseignement supérieur 0745
Évaluation 0288
Finances 0277
Formation des enseignants 0530
Histoire de l'éducation 0520
Langues et littérature 0279
Lecture 0535
Mathématiques 0280
Musique 0522
Orientation et consultation 0519
Philosophie de l'éducation 0998
Physique 0523
Programmes d'études et enseignement 0727
Psychologie 0525
Sciences 0714
Sciences sociales 0534
Sociologie de l'éducation 0340
Technologie 0710

LANGUE, LITTÉRATURE ET LINGUISTIQUE

Langues
- Généralités 0679
- Anciennes 0289
- Linguistique 0290
- Modernes 0291

Littérature
- Généralités 0401
- Anciennes 0294
- Comparée 0295
- Médiévale 0297
- Moderne 0298
- Africaine 0316
- Américaine 0591
- Anglaise 0593
- Asiatique 0305
- Canadienne (Anglaise) 0352
- Canadienne (Française) 0355
- Germanique 0311
- Latino-américaine 0312
- Moyen-orientale 0315
- Romane 0313
- Slave et est-européenne 0314

PHILOSOPHIE, RELIGION ET THÉOLOGIE

Philosophie 0422
Religion
- Généralités 0318
- Clergé 0319
- Études bibliques 0321
- Histoire des religions 0320
- Philosophie de la religion 0322

Théologie 0469

SCIENCES SOCIALES

Anthropologie
- Archéologie 0324
- Culturelle 0326
- Physique 0327

Droit 0398
Économie
- Généralités 0501
- Commerce-Affaires 0505
- Économie agricole 0503
- Économie du travail 0510
- Finances 0508
- Histoire 0509
- Théorie 0511

Études américaines 0323
Études canadiennes 0385
Études féministes 0453
Folklore 0358
Géographie 0366
Gérontologie 0351
Gestion des affaires
- Généralités 0310
- Administration 0454
- Banques 0770
- Comptabilité 0272
- Marketing 0338

Histoire
- Histoire générale 0578
- Ancienne 0579
- Médiévale 0581
- Moderne 0582
- Histoire des noirs 0328
- Africaine 0331
- Canadienne 0334
- États-Unis 0337
- Européenne 0335
- Moyen-orientale 0333
- Latino-américaine 0336
- Asie, Australie et Océanie 0332

Histoire des sciences 0585
Loisirs 0814
Planification urbaine et régionale 0999
Science politique
- Généralités 0615
- Administration publique 0617
- Droit et relations internationales 0616

Sociologie
- Généralités 0626
- Aide et bien-âtre social 0630
- Criminologie et établissements pénitentiaires 0627
- Démographie 0938
- Études de l' individu et de la famille 0628
- Études des relations interethniques et des relations raciales 0631
- Structure et développement social 0700
- Théorie et méthodes. 0344
- Travail et relations industrielles 0629

Transports 0709
Travail social 0452

SCIENCES ET INGÉNIERIE

SCIENCES BIOLOGIQUES

Agriculture
- Généralités 0473
- Agronomie. 0285
- Alimentation et technologie alimentaire 0359
- Culture 0479
- Élevage et alimentation 0475
- Exploitation des pâturages 0777
- Pathologie animale 0476
- Pathologie végétale 0480
- Physiologie végétale 0817
- Sylviculture et faune 0478
- Technologie du bois 0746

Biologie
- Généralités 0306
- Anatomie 0287
- Biologie (Statistiques) 0308
- Biologie moléculaire 0307
- Botanique 0309
- Cellule 0379
- Écologie 0329
- Entomologie 0353
- Génétique 0369
- Limnologie 0793
- Microbiologie 0410
- Neurologie 0317
- Océanographie 0416
- Physiologie 0433
- Radiation 0821
- Science vétérinaire 0778
- Zoologie 0472

Biophysique
- Généralités 0786
- Medicale 0760

SCIENCES DE LA TERRE

Biogéochimie 0425
Géochimie 0996
Géodésie 0370
Géographie physique 0368
Géologie 0372
Géophysique 0373
Hydrologie 0388
Minéralogie 0411
Océanographie physique 0415
Paléobotanique 0345
Paléoécologie 0426
Paléontologie 0418
Paléozoologie 0985
Palynologie 0427

SCIENCES DE LA SANTÉ ET DE L'ENVIRONNEMENT

Économie domestique 0386
Sciences de l'environnement 0768
Sciences de la santé
- Généralités 0566
- Administration des hipitaux 0769
- Alimentation et nutrition 0570
- Audiologie 0300
- Chimiothérapie 0992
- Dentisterie 0567
- Développement humain 0758
- Enseignement 0350
- Immunologie 0982
- Loisirs 0575
- Médecine du travail et thérapie 0354
- Médecine et chirurgie 0564
- Obstétrique et gynécologie 0380
- Ophtalmologie 0381
- Orthophonie 0460
- Pathologie 0571
- Pharmacie 0572
- Pharmacologie 0419
- Physiothérapie 0382
- Radiologie 0574
- Santé mentale 0347
- Santé publique 0573
- Soins infirmiers 0569
- Toxicologie 0383

SCIENCES PHYSIQUES

Sciences Pures

Chimie
- Généralités 0485
- Biochimie 487
- Chimie agricole 0749
- Chimie analytique 0486
- Chimie minérale 0488
- Chimie nucléaire 0738
- Chimie organique 0490
- Chimie pharmaceutique 0491
- Physique 0494
- PolymÇres 0495
- Radiation 0754

Mathématiques 0405
Physique
- Généralités 0605
- Acoustique 0986
- Astronomie et astrophysique 0606
- Électronique et électricité 0607
- Fluides et plasma 0759
- Météorologie 0608
- Optique 0752
- Particules (Physique nucléaire) 0798
- Physique atomique 0748
- Physique de l'état solide 0611
- Physique moléculaire 0609
- Physique nucléaire 0610
- Radiation 0756

Statistiques 0463

Sciences Appliqués Et Technologie

Informatique 0984
Ingénierie
- Généralités 0537
- Agricole 0539
- Automobile 0540
- Biomédicale 0541
- Chaleur et thermodynamique 0348
- Conditionnement (Emballage) 0549
- Génie aérospatial 0538
- Génie chimique 0542
- Génie civil 0543
- Génie électronique et électrique 0544
- Génie industriel 0546
- Génie mécanique 0548
- Génie nucléaire 0552
- Ingénierie des systèmes 0790
- Mécanique navale 0547
- Métallurgie 0743
- Science des matériaux 0794
- Technique du pétrole 0765
- Technique minière 0551
- Techniques sanitaires et municipales 0554
- Technologie hydraulique 0545

Mécanique appliquée 0346
Géotechnologie 0428
Matières plastiques (Technologie) 0795
Recherche opérationnelle 0796
Textiles et tissus (Technologie) 0794

PSYCHOLOGIE

Généralités 0621
Personnalité 0625
Psychobiologie 0349
Psychologie clinique 0622
Psychologie du comportement 0384
Psychologie du développement 0620
Psychologie expérimentale 0623
Psychologie industrielle 0624
Psychologie physiologique 0989
Psychologie sociale 0451
Psychométrie 0632

RECIPROCAL CIRCULAR POLARIZATION SELECTIVE SURFACES

BY

JASMIN E. ROY

A Thesis submitted to the Faculty of Graduate Studies of the University of Manitoba in partial fulfillment of the requirements of the degree of

DOCTOR OF PHILOSOPHY

À ma mère,
une femme simple et généreuse
qui aime la vie et ses gens.

Abstract

The objectives of this research are:

- to present the concept of a relatively unknown electromagnetic surface called a Circular Polarization Selective Surface (CPSS),
- to review the prior art in this area,
- to obtain the geometrical constraints placed on the ideal CPSS,
- to propose a new CPSS realization,
- to present numerical simulations of three different CPSS designs.

In the process of conducting this research, a technique based on the Generalized Scattering Matrix (GSM) was developed for identifying the properties compatible with the operation required from a planar layered structure. When this technique was applied to the ideal reciprocal CPSS, it was found that, as far as the dominant mode is concerned, the passive structure must be endowed with the property of $2n$-fold rotational symmetry except in the neighborhood of the normal incidence where the property of reciprocity suffices, but cannot possibly be endowed with the property of longitudinal reflection symmetry. Similarly, it was found that ideal linear polarizers and ideal circular polarizers are possible only at normal incidence, regardless of their specific physical implementations. Numerical simulations with the three known CPSS designs suggested that designs obeying the geometrical constraints of the ideal CPSS tend indeed to perform better.

Table of Contents

List of Tables

List of Figures

Nomenclature

Unless indicated otherwise, the following symbols have this meaning:

a	wire radius
A	the unit of current, Ampere
a_u	voltage travelling wave incident at port numbered $u = \{1, 2, 3, 4\}$
a_u^p	the p mode voltage travelling wave incident at port numbered $u = \{1, 2, 3, 4\}$ with $p = \{E, H, X, Y\}$
a_u^n	voltage travelling wave incident at port numbered $u = \{1, 2, 3, 4\}$ of the scattering matrix numbered $n = \{I, II\}$
ar	axial ratio
ar^r	axial ratio of the reflection beam at the geometrical optics reflection angle
ar^t	axial ratio of the transmission beam at the geometrical optics transmission angle
ar_{Rx}	axial ratio of the receiving antenna
ar_{Tx}	axial ratio of the transmitting antenna
ar_L	axial ratio of a LHCP polarization ellipse
ar_R	axial ratio of a RHCP polarization ellipse
b_u	voltage travelling wave scattered at port numbered $u = \{1, 2, 3, 4\}$
b_u^p	the p mode voltage travelling wave scattered at port numbered $u = \{1, 2, 3, 4\}$ with $p = \{E, H, X, Y\}$
b_u^n	voltage travelling wave scattered at port numbered $u = \{1, 2, 3, 4\}$ of the scattering matrix numbered $n = \{I, II\}$
$Blckg$	indicator of Blockage
$C(E, H)$	the scattering matrix written in terms of the whole electric field of the E and the H modes
C_{uv}^{pq}	scattering coefficient of the C scattering matrix with $\{p, q\} = \{E, H\}$ and $\{u, v\} = \{1, 2, 3, 4\}$

CP	Circularly Polarized or Circular Polarization
CPSS	Circular Polarization Selective Surface
cte	"constant"
d	inter-grid spacing, either generic or for CP polarizers
D	spacing between the CP and LP polarizers for the LHCPSS
e.g.	Latin abbreviation for meaning "for example"
e_a	easy axis of a LP polarizer plate
e_f	fast axis of a retardation plate
e_s	slow axis of a retardation plate
E	electric field
E_z	the z component of the electric field
E^z	the TM^z mode, i.e. $\vec{E}_o = E_o\hat{\theta}$
E mode	the TM^z mode, i.e. the E^z mode
E-type mode	the TM^u mode where u is a transverse direction, i.e. $u = \{x, y\}$
E_o	the whole electric field (phasor)
$\vec{E}_o$	the whole electric field (vector)
E_o^i	the incident whole electric field
E_o^r	the reflected whole electric field
E_o^t	the transmitted whole electric field
E_o^s	the scattered whole electric field with $s = \{r, t\}$
E_t^i	the transverse component of the incident electric field
E_t^r	the transverse component of the reflected electric field
E_t^t	the transverse component of the transmitted electric field
E_t^s	the transverse component of the scattered electric field with $s = \{r, t\}$
$(E_o^i)_u^p$	the p mode whole electric field incident at port u with $p = \{E, H\}$ and $u = \{1, 2, 3, 4\}$
$(E_t^i)_u^p$	the transverse component of the p mode electric field incident at port u with $p = \{E, H\}$ and $u = \{1, 2, 3, 4\}$
$(E_o^s)_u^p$	the p mode whole electric field scattered at port u with $p = \{E, H\}$, $u = \{1, 2, 3, 4\}$ and $s = \{r, t\}$
$(E_t^s)_u^p$	the transverse component of the p mode electric field scattered at port u with $p = \{E, H\}$, $u = \{1, 2, 3, 4\}$ and $s = \{r, t\}$
E_{LHCP}	the LHCP component of the electric field
E_{RHCP}	the RHCP component of the electric field

f	polarization efficiency
f^i	polarization efficiency of the incidence polarization ellipse
f^t	polarization efficiency of the reflection polarization ellipse
f^t	polarization efficiency of the transmission polarization ellipse
G^r	gain of the receiving antenna
G^t	gain of the transmitting antenna
GSM	Generalized Scattering Matrix
H	magnetic field
H_z	the z component of the magnetic field
H^z	the TE^z mode, i.e. $\vec{E}_o = E_o\hat{\phi}$
H mode	the TE^z mode, i.e. the H^z mode
H-type mode	the TE^u mode where u is a transverse direction, i.e. $u = \{x, y\}$
H_o	the whole magnetic field
H_o^i	the incident whole magnetic field
H_o^r	the reflected whole magnetic field
H_o^t	the transmitted whole magnetic field
H_o^s	the scattered whole magnetic field with $s = \{r, t\}$
H_t^i	the transverse component of the incident magnetic field
H_t^r	the transverse component of the reflected magnetic field
H_t^t	the transverse component of the transmitted magnetic field
H_t^s	the transverse component of the scattered magnetic field with $s = \{r, t\}$
I	identity matrix
i.e.	Latin abbreviation for meaning "that is to say"
j	imaginary number equal to $\sqrt{-1}$
$\vec{k}$	generic propagation vector
k	wavenumber equal to the magnitude of $\vec{k}$
k_z	the z component of the propagation vector $\vec{k}$
k_z^1	the z component of the propagation vector $\vec{k}$ in region 1
k_z^2	the z component of the propagation vector $\vec{k}$ in region 2
$\vec{k}^i$	incidence propagation vector
$\vec{k}^r$	reflection propagation vector
$\vec{k}^t$	transmission propagation vector
$\vec{k}^s$	scattered wave propagation vector with $s = \{r, t\}$
$Leakg$	indicator of Leakage

LL	co-polarization scattered LHCP field
LL^p	peak value of LL
LL^r	co-polarization scattered LHCP field of the reflection beam
LL^t	co-polarization scattered LHCP field of the transmission beam
LR	cross-polarization scattered LHCP field
LR^r	cross-polarization scattered LHCP field of the reflection beam
LR^t	cross-polarization scattered LHCP field of the transmission beam
LHCP	Left-Hand Circularly Polarized or Circular Polarization
LHCPSS	Left-Hand CPSS
LP	Linearly Polarized or Linear Polarization
m	the unit of length, meter
MAPLE	registered trademark from Waterloo Maple Software identifying a software package for symbolic computation
NEC-2	Numerical Electromagnetic Code software
p	the magnitude of the polarization ratio $P = pe^{j\delta}$
p_L	the magnitude p for a LHCP polarization ellipse
p_R	the magnitude p for a RHCP polarization ellipse
P	polarization ratio equal to $pe^{j\delta}$
PEC	Perfect Electrical Conductor or Perfect Electrically Conducting
r	observation sphere radius
R	distance between the two apertures of two antennas
RL	cross-polarization scattered RHCP field
RL^r	cross-polarization scattered RHCP field of the reflection beam
RL^t	cross-polarization scattered RHCP field of the transmission beam
RR	co-polarization scattered RHCP field
RR^p	peak value of RR
RR^r	co-polarization scattered RHCP field of the reflection beam
RR^t	co-polarization scattered RHCP field of the transmission beam
R^V	voltage reflection coefficient equal to $(Z_L - Z_o)/(Z_L + Z_0)$
R^I	current reflection coefficient equal to $(Z_o - Z_L)/(Z_o + Z_L)$
R^E	voltage reflection coefficient for the E mode
R^H	voltage reflection coefficient for the H mode
RHCP	Right-Hand Circularly Polarized or Circular Polarization
RHCPSS	Right-Hand CPSS
s	inter-wire spacing within a wire grid

$S(E,H)$	scattering matrix written in terms of the transverse electric field components of the E and the H modes
$S(X,Y)$	scattering matrix written in terms of the Cartesian coordinate x and y components
S_{uv}^{pq}	scattering coefficient of the S scattering matrix with $\{p,q\} = \{E,H\}$ and $\{u,v\} = \{1,2,3,4\}$
T^V	voltage transmission coefficient equal to $2Z_L/(Z_L + Z_o)$
T^I	current transmission coefficient equal to $2Z_o/(Z_o + Z_L)$
T^E	voltage transmission coefficient for the E mode
T^H	voltage transmission coefficient for the H mode
TE^z	Transverse Electric mode with respect to z, i.e. $\vec{E}_o = E_o\hat{\phi}$
TEM^z	Transverse ElectroMagnetic mode with respect to z
TM^z	Transverse Magnetic mode with respect to z, i.e. $\vec{E}_o = E_o\hat{\theta}$
$\hat{u}_{LHCP}$	unit vector for LHCP
$\hat{u}_{RHCP}$	unit vector for RHCP
V	the unit of voltage, Volt
$\hat{x}$	unit vector in the Cartesian coordinate x direction
$\hat{y}$	unit vector in the Cartesian coordinate y direction
$\hat{z}$	unit vector in the Cartesian coordinate z direction
Z_W	modal wave impedance
Z_W^i	modal wave impedance of the incidence region
Z_W^t	modal wave impedance of the transmission region
Z_o	characteristic impedance of a transmission line
Z_o^i	characteristic impedance corresponding to the incidence region
Z_o^t	characteristic impedance corresponding to the transmission region
VSWR	Voltage Standing Wave Ratio
θ	spherical coordinate zenith angle
$\hat{\theta}$	unit vector in the spherical coordinate θ direction
θ^i	spherical coordinate zenith angle for the incident wave
θ^r	spherical coordinate zenith angle for the reflected wave
θ^t	spherical coordinate zenith angle for the transmitted wave
θ^s	spherical coordinate zenith angle for the scattered wave with $s = \{r,t\}$
ϕ	spherical coordinate azimuth angle
$\hat{\phi}$	unit vector in the spherical coordinate ϕ direction
ϕ^i	spherical coordinate azimuth angle for the incident wave

ϕ^r spherical coordinate azimuth angle for the reflected wave

ϕ^t spherical coordinate azimuth angle for the transmitted wave

ϕ^s spherical coordinate azimuth angle for the scattered wave with $s = \{r, t\}$

ϕ_f azimuth angle identifying the direction of the fast axis of a retardation plate

ϕ_g azimuth angle identifying the direction of the wires of a wire grid

ϕ_L azimuth angle identifying the input LP polarization for obtaining LHCP at the output of a CP polarizer

ϕ_R azimuth angle identifying the input LP polarization for obtaining RHCP at the output of a CP polarizer

$\phi_\#$ azimuth angle equal to $\phi + 90^o - \xi$

η intrinsic impedance of a propagation medium

η^i intrinsic impedance of the propagation medium in the incidence region

η^t intrinsic impedance of the propagation medium in the transmission region

ϵ_H is equal to +1 for $p = q$, and to -1 for $p \neq q$ with $\{p, q\} = \{E, H\}$

ϵ_{Rx} polarization sense of the receiving antenna equal to +1 for RHCP and to -1 for LHCP

ϵ_{Tx} polarization sense of the transmitting antenna equal to +1 for RHCP and to -1 for LHCP

ε permittivity value

ε^1 permittivity value of the region 1

ε^2 permittivity value of the region 2

μ_o permeability value equal to $4\pi \times 10^{-7}(H/m)$

δ the phase of the polarization ratio $P = pe^{j\delta}$

δ_{ij} Kronecker delta function equal to 1 if $i = j$, and to 0 if $i \neq j$

λ wavelength

π the irrational number equal to 3.14159265358979...

χ azimuth angle identifying the n-fold rotational symmetry plane

ς angle between $\hat{\phi}$ and $\vec{E}_o$

$\varsigma^i_{\|}$ angle between $\hat{\phi}^i$ and $\vec{E}^i_o$ with $\vec{E}^i_t$ parallel to the direction corresponding to $\phi = \{\phi_g, \phi_R, \phi_L\}$

$\varsigma^i_{\perp}$ angle between $\hat{\phi}^i$ and $\vec{E}^i_o$ with $\vec{E}^i_t$ perpendicular to the direction corresponding to $\phi = \{\phi_g, \phi_R, \phi_L\}$

$\varsigma^s_{\|}$ angle between $\hat{\phi}^s$ and $\vec{E}^s_o$ with $\vec{E}^s_t$ parallel to the direction corresponding to $\phi = \{\phi_g, \phi_R, \phi_L\}$

$\varsigma_{\perp}^{s}$	angle between $\hat{\phi}^{s}$ and $\vec{E}_{o}^{s}$ with $\vec{E}_{t}^{s}$ perpendicular to the direction corresponding to $\phi = \{\phi_g, \phi_R, \phi_L\}$
ξ	angle between $\hat{\phi}$ and $\vec{E}_t$
ξ_E	angle between $\hat{\phi}$ and $\vec{E}_t$
ξ_H	angle between $\hat{\phi}$ and $\vec{H}_t$
$\xi_{\parallel}^{LP}$	angle between $\hat{\phi}$ and $\vec{E}_t$ with $\vec{E}_t$ parallel to the direction corresponding to $\phi = \phi_g$
$\xi_{\parallel}^{LHCP}$	angle between $\hat{\phi}$ and $\vec{E}_t$ with $\vec{E}_t$ parallel to the direction corresponding to $\phi = \phi_L$
$\xi_{\parallel}^{RHCP}$	angle between $\hat{\phi}$ and $\vec{E}_t$ with $\vec{E}_t$ parallel to the direction corresponding to $\phi = \phi_R$
$\xi_{\parallel}$	angle between $\hat{\phi}$ and $\vec{E}_t$ with $\vec{E}_t$ parallel to the direction corresponding to $\phi = \{\phi_g, \phi_R, \phi_L\}$
$\xi_{\perp}$	angle between $\hat{\phi}$ and $\vec{E}_t$ with $\vec{E}_t$ perpendicular to the direction corresponding to $\phi = \{\phi_g, \phi_R, \phi_L\}$
ψ	tilt angle of the polarization ellipse
ψ_R	tilt angle of the polarization ellipse for the receiving antenna
ψ_T	tilt angle of the polarization ellipse for the transmitting antenna
Ψ	differential tilt angle equal to $\psi_R + \psi_T$
ω	radian frequency
$1-D$	one dimensional
$3-D$	three dimensional
$\Longrightarrow$	"consequently"
$\rightarrow$	"tends to" or "goes into"
$\frac{a}{b} \nearrow\!\!\searrow \frac{c}{d}$	the numerator a goes into the denominator d while the denominator b goes into the numerator c
$\angle$	the phase of a complex number
$\forall$	"for all"
@	"with"

Acknowledgments

The author is grateful to his supervisor Dr. L. Shafai for his guidance, his patience and the complete freedom of thoughts that he granted to this author, to Dr. G.A. Morin for suggesting the topic and providing some important reference documents, and to the University of Manitoba for its financial assistance in the form of the Duff Roblin's Fellowship.

Chapter One

Concept and Prior Art

1.1 Introduction

Linear polarization selection has been used for many years in reflector antenna design, owing to the simplicity and the ease of designing grids of straight or curved wires, and twist reflectors. Circular polarization selection, however, has not been used because no simple electromagnetic surface achieving such a selection has been known. It has even been argued that such a selective surface could be realized physically! In 1976, Cornbleet [1, pp. 322-323] conjectured that the Circular Polarization Selective Surface (CPSS) was an impossible polarizer on the basis that the corresponding Jones polarization matrix is singular, and thus cannot be realized by any combination of physical devices, which by virtue of their realizability have necessarily non-singular polarization matrices, since the product of any non-singular matrices cannot yield a singular matrix. Yet, other researchers [4, 5, 7] have put forward various designs for the CPSS.

This research aims at proving on a theoretical basis that the reciprocal CPSS is possible, at identifying the properties and the geometrical constraints inherent to such a surface, and at presenting the performance of three different designs.

1.2 Concept

An ideal Left Hand Circular Polarization Selective Surface (LHCPSS) is a structure that would reflect completely an impinging Left Hand Circularly Polarized (LHCP) electromagnetic wave and yet, would be completely transparent to an impinging Right Hand Circularly Polarized (RHCP) electromagnetic wave. Similarly, an ideal RHCPSS is a structure that would reflect completely an impinging RHCP wave and yet, would be completely transparent to an impinging LHCP wave. Since both LHCPSS and RHCPSS are similar in concept, only the LHCPSS is dealt with hereafter.

Four types of LHCPSS shown in Figures 1.1, 1.2 and 1.3 are possible depending on the handedness of the Circularly Polarized (CP) wave being scattered by the structure. The first and the second type shown respectively on Figure 1.1 and 1.2 have the handedness of the reflected wave being the same as that of the incident CP wave. The third and the fourth types shown respectively at the top and the bottom of Figure 1.3 have the handedness of the reflected wave being opposite to that of the incident CP wave. The reciprocity principle of electromagnetism dictates that the operation of a reciprocal device remain unchanged upon reversing the direction of all propagation vectors. Thus, only the first and the second types correspond to a reciprocal device, a result that Tilston et al. had briefly stated in references [7] and [8, p. 3], by writing:

> If a surface passes one sense of circular polarization while reflecting the other, by reciprocity, the polarization sense of the reflected wave must be the same as that of the incident wave. Otherwise, the (reciprocal) surface will reflect waves of both senses of polarization.

The type shown on Figure 1.1 is designated as symmetrical because the operation of the structure remains the same whether the wave impinges from the left or from

the right of the structure. By analogy, the type shown at the top of Figure 1.3 is designated as symmetrical. The type shown on Figure 1.2 is designated as asymmetrical because the operation of the structure changes depending on whether the wave impinges from the left or from the right of the structure. By analogy, the type shown at the bottom of Figure 1.3 is designated as asymmetrical. Although this research focuses mainly on the reciprocal symmetrical LHCPSS, an example of the reciprocal asymmetrical LHCPSS will be mentioned in Chapter 3. The non-reciprocal types are not dealt with altogether.

The use of the reciprocity principle as well as that of symmetry properties (rotational, transverse or longitudinal) is of paramount importance in assessing whether or not a given structure is a good candidate for a prescribed operation. This research hinges precisely on such a use. The lesson, however, was hard taught as this author's experience exemplifies. Initially, it was thought that since one is dealing with circular polarization, it would only be natural to use a spiral antenna as the element of the unit cell for the reciprocal CPSS. For months, this author tried many configurations of Archimedean spirals [3], varying the number of arms, the rate of expansion, the number and the individual orientation of spirals in a stack configuration, but to no avail! Afterwards, it was realized [2] that since the winding direction of the arms of a spiral becomes reversed as the incidence angle passes from $\theta = 0^o$ to $\theta = 180^o$, an array of spirals that would reflect, say, LHCP upon LHCP illumination from $\theta = 0^o$ would reflect RHCP upon RHCP illumination from $\theta = 180^o$. Such a response, however, would correspond to the asymmetrical rather than the symmetrical type. The analysis presented below shows in fact that the ideal reciprocal symmetrical CPSS must be endowed with the $2n$-fold rotational symmetry except at normal incidence where reciprocity suffices, but must not be endowed with the longitudinal reflection symmetry.

Since one is interested in realizing the CPSS operation with a purely passive

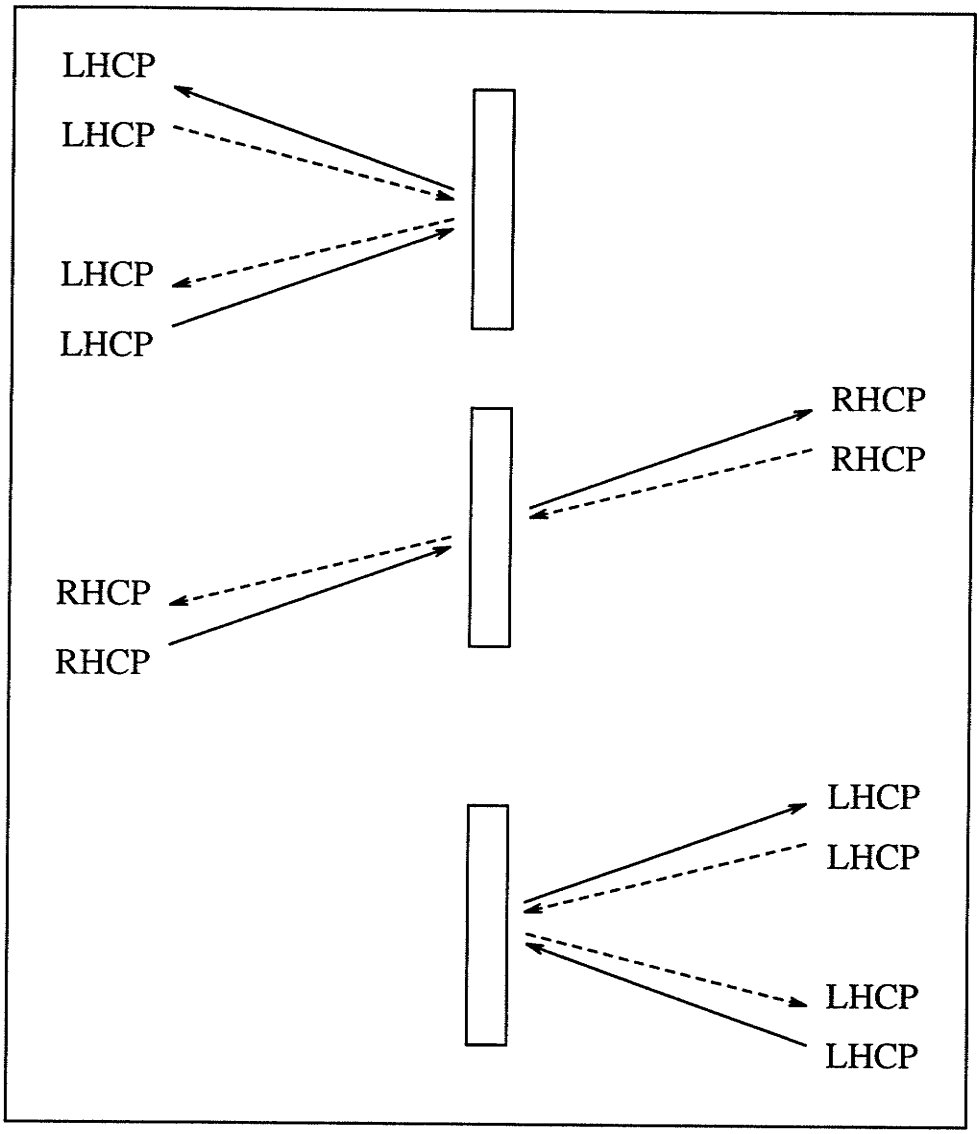

Figure 1.1: The depiction of the operation of the reciprocal symmetrical LHCPSS.

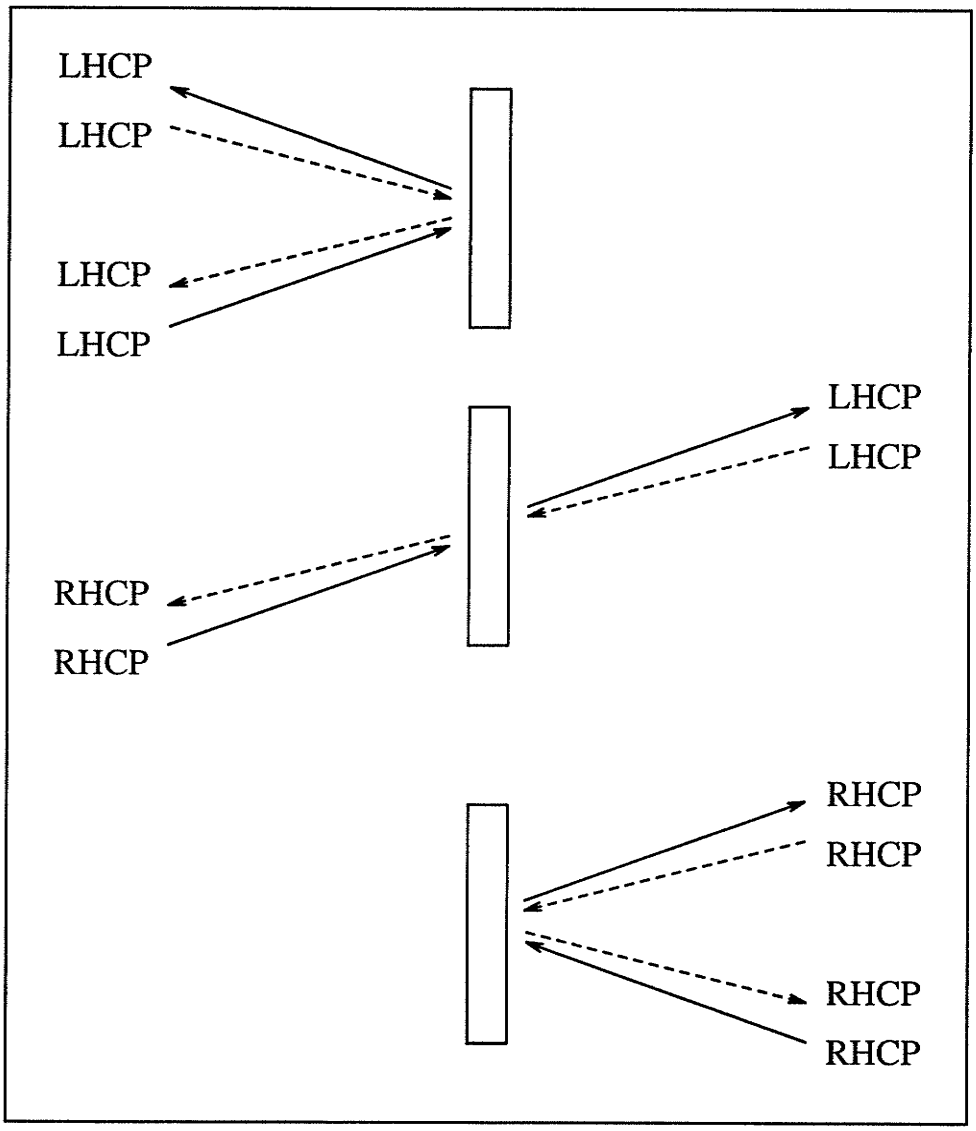

Figure 1.2: The depiction of the operation of the reciprocal asymmetrical LHCPSS.

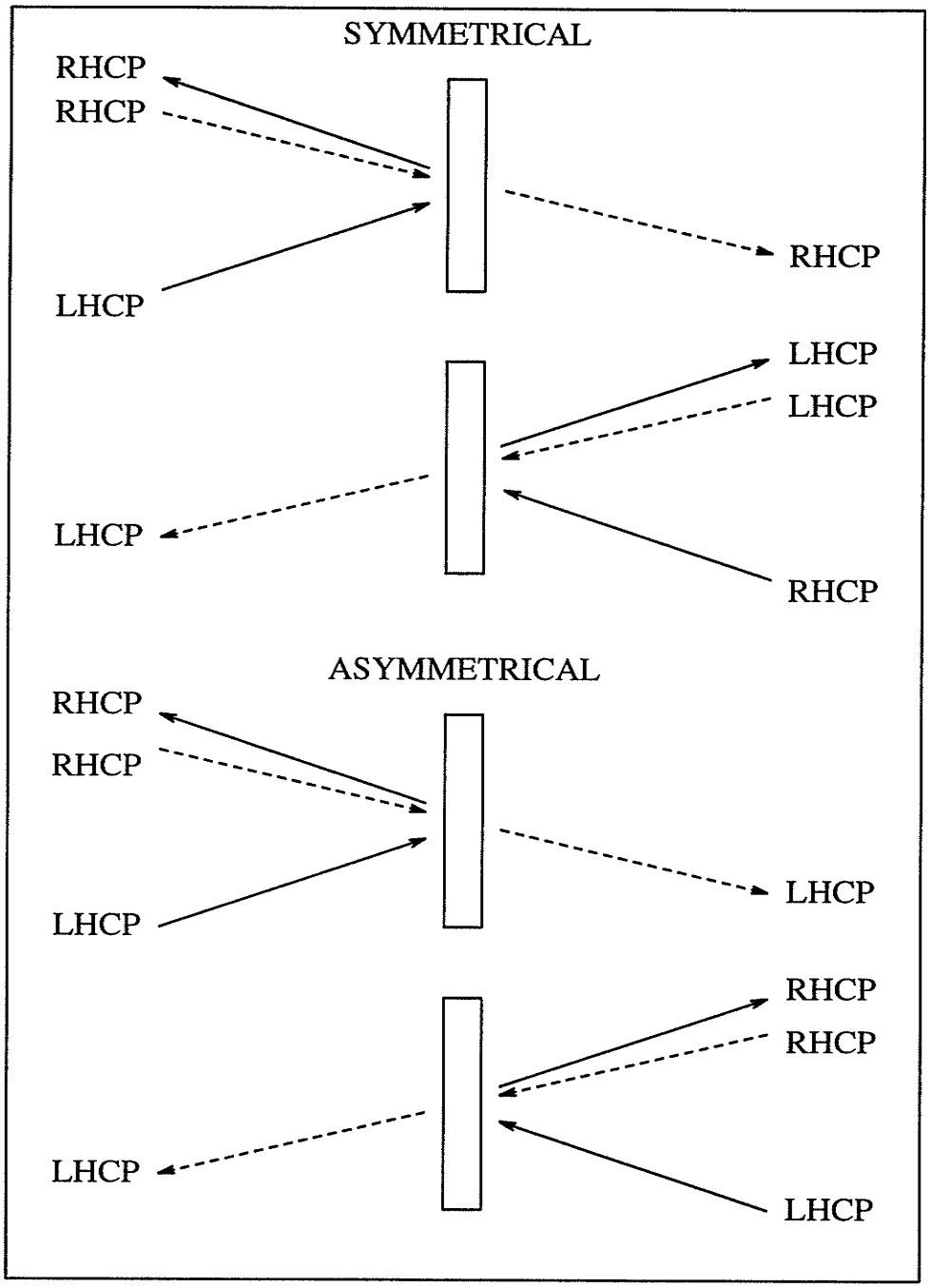

Figure 1.3: Two types of non-reciprocal LHCPSS: symmetrical (top) and asymmetrical (bottom).

structure, the non-reciprocal types are not considered hereafter, thus precluding the use of a gyrotropic medium, e.g. ferrite or plasma. Is is noted in passing that unlike the spiral, the helix has the same handedness whether viewed from one end or the other [47, p. 426]. This observation suggests that the helix, rather than the spiral, antenna would seem to be the natural choice as the element of the unit cell for the reciprocal CPSS. Unfortunately, the use of Pasteur's medium, i.e. an isotropic reciprocal chiral medium, with the property of optical activity [47, p. 425-426] does not produce the desired CP selectivity since a CP wave travelling along the axes of the helices constituting the Pasteur medium is merely phase-delayed or phase-advanced according to the handedness of the helices in relation to the handedness of the CP wave.

1.3 Prior Art

The technical literature on the topic of CPSS is very scarce. This author is aware of three different designs which are presented here in the chronological order. The first design is reported in a French patent filed in 1966 by Pierrot [4] and consists of an array of disjointed wires, each wire being 1λ in overall length and bent into a crank-like shape, with each transverse arm being $3\lambda/4$ long in the x or y direction, and the longitudinal section being $\lambda/4$ long in the z direction. The very same idea was independently rediscovered by Morin [11] more than two decades later. Morin [14] has further modified the design by stringing many crank wires into skewed rectangular helices[1] illuminated sideway, in order to achieve a self-supporting structure.

Pierrot's design for the unit cell of a LHCPSS is shown in Figure 1.4. This design features a great simplicity of manufacturing. The principle of operation is described as follows. For a LHCP illumination at normal incidence, the electric field vector traces a right handed helix about the z axis as the wave propagates in the $+\hat{z}$ direction. Since the two $3\lambda/8$ transverse arms are spaced $\lambda/4$ in the z direction, the currents induced on the transverse arms by the rotating electric field of the incident circularly polarized plane wave add in-phase along the entire length of the wire. The 1λ wire operates then at geometrical resonance and the current distribution is sinusoidal-like with the null at the center of the longitudinal section. The dipoles reradiate a LHCP wave in both $+\hat{z}$ and $-\hat{z}$ directions. The reflected wave is thus LHCP as was the incident wave. In the transmission region, the incident and the scattered waves add out-of-phase to produce ideally a null field behind the structure.

For a RHCP illumination at normal incidence, the electric field vector traces a left handed helix about the z axis as the wave propagates in the $+\hat{z}$ direction and thus, the currents induced on both transverse arms add out-of-phase along the entire length of the wire. The wire is no longer operating at resonance and the resulting

[1]The title of reference [14] is misleading for the structures are not spirals but helices.

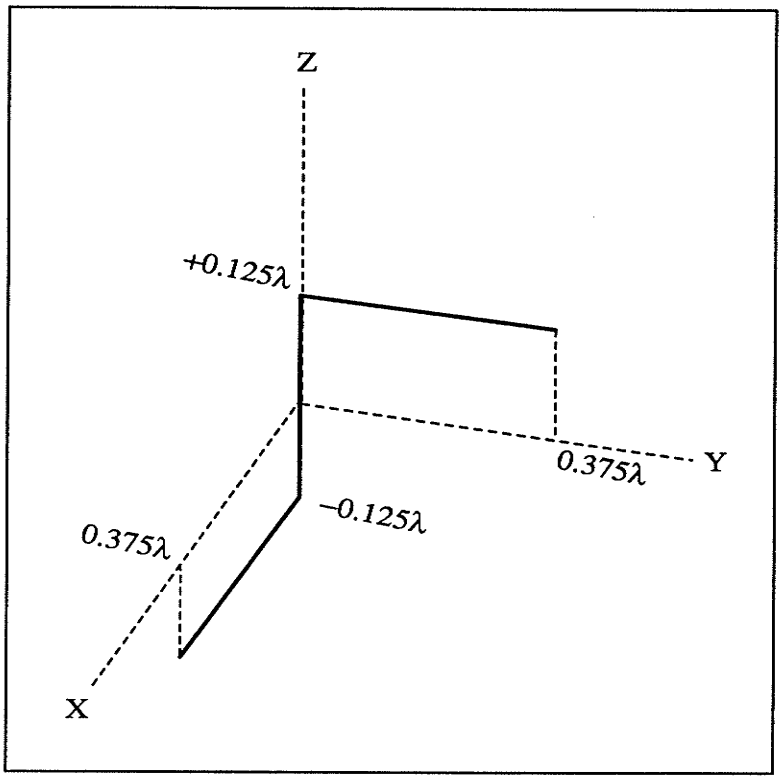

Figure 1.4: Pierrot's LHCPSS.

current is conceptually zero so that the wire appears transparent to the incoming wave.

The second design is reported in two American patents [5, 6] co-authored in 1984 and 1986 by two French researchers, Bossuet and Gautier. It must be pointed out, however, that they are not the original inventors of this design. Let one define the operation of an ideal LHCP polarizer run forward as the conversion of an input linearly polarized (LP) wave incident on the input face of the polarizer with a polarization corresponding to $\phi = \phi_L$, into a LHCP wave exiting from the output face of the polarizer, as in case a) of Figure 3.1. The operation of an ideal LHCP polarizer run backward corresponds to the reciprocal operation, i.e. the LHCP wave is incident onto the output face and the LP wave exits from the input face with the polarization $\phi = \phi_L$, as in case b) of Figure 3.1. The definition is similar for an ideal RHCP polarizer except that ϕ_L and LHCP are replaced by ϕ_R and RHCP, respectively.

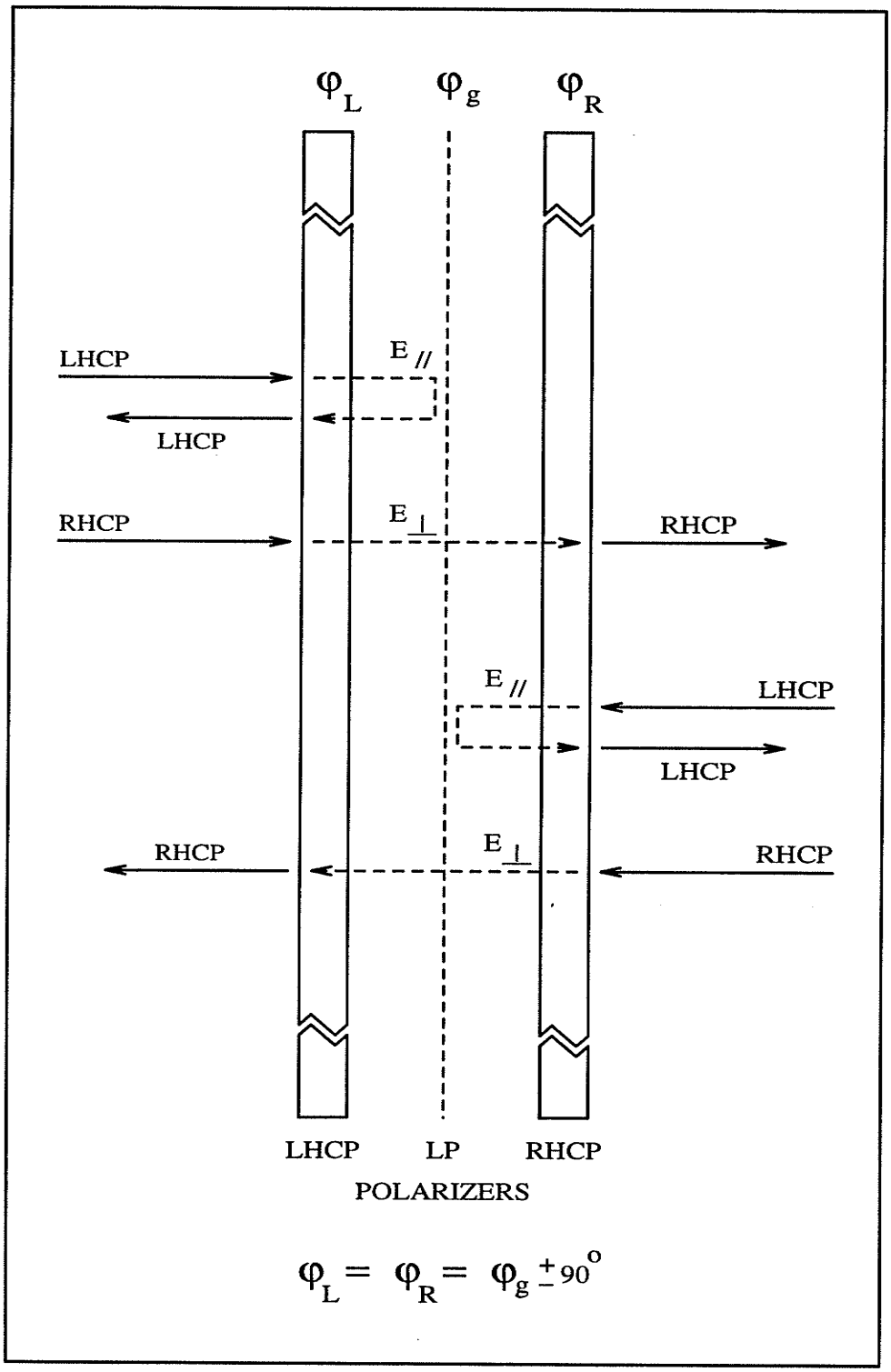

Figure 1.5: The cascade polarizer LHCPSS

The idea, depicted in Figure 1.5, consists in converting with a LHCP polarizer run backward the incident CP wave into a LP wave whose linear polarization is then filtered out with the usual wire grid acting as a LP polarizer. The output of the grid is then converted with a RHCP polarizer run forward into a RHCP wave for the symmetrical LHCPSS type, or converted with a LHCP polarizer run forward into a LHCP wave for the asymmetrical LHCPSS type. Bossuet and Gautier reported that the CP polarizers could consist of two parallel grids of PEC wires with an inter-wire separation close to $\lambda/4$ within each grid. The orientation of the various plates is given by $\phi_L = \phi_g \pm 90^o = \phi_R$ such that the LP grid appears as a perfectly reflecting surface when the input wave is LHCP, and a perfectly transparent surface when the input CP wave is RHCP. In the first case, the wave is reflected back into the input LHCP polarizer and comes out from the front face of the LHCPSS as a LHCP wave. In the second case, the wave goes through the LP polarizer, reaches the RHCP polarizer and comes out of the rear face of the LHCPSS as a RHCP wave. As this design shall be treated in Chapter 3, further comments are postponed until then.

The third design, which appeared in 1988, is by Tilston et al. [8, 7, 9]. It consists of a dipole turnstile so modified as to incorporate a $\lambda/2$ transmission line within the $\lambda/4$ spacing separating the two dipoles of the turnstile. These researchers relied on the use of a dielectric medium of appropriate permittivity value to make the transmission line appear longer than the spacing between the dipoles. Chow [10] has mitigated this design limitation by embedding the excess length of the transmission line into the turnstile dipoles so as to allow the use of a greater range of permittivity values. Shi and Zao [15] have analyzed Tilston's structure by the Spectral Domain Technique and confirmed the circular polarization selectivity of the structure. It is not clear, however, how they accounted for the difference between the electrical length of the transmission line and the spacing between the dipoles.

Tilston's design for the unit cell of a LHCPSS is shown in Figure 1.6. Tilston's

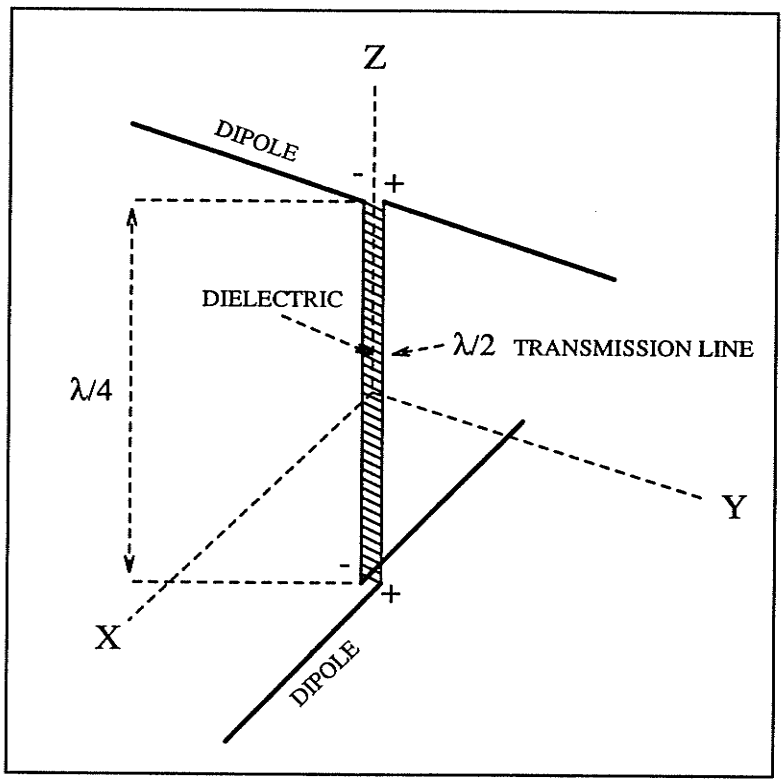

Figure 1.6: Tilston's LHCPSS.

structure should not be construed as being merely two Pierrot's crank wires facing one another with some dielectric between the two longitudinal sections.

The principle of operation is described in reference [7] and is repeated here for convenience:

> An incident circularly polarized wave is reflected from such a surface when the two orthogonal components of the wave arrive at the respective dipoles in phase and is transmitted when the two components are incident upon the respective dipoles out of phase. The quarter wave separation between the dipoles ensures that the two components of the circularly polarized wave reach the respective dipoles in phase or out of phase.
>
> When these components arrive in phase, the two waves of equal amplitude and phase enter opposite ends of the transmission line causing

an open-circuit to appear at its mid-point. This open-circuit when transformed back through the transmission line causes a short-circuit to appear at the feed point of the dipoles. Thus, both dipoles appear as half wave reflectors and the incident wave is reflected back.

On the other hand, if the circularity of polarization of the incident wave is such that its two orthogonal components reach the dipoles 180 degrees out of phase, it causes a short-circuit to appear across the mid-point of the transmission line and hence, both dipoles appear to be open-circuited at their feed points. The incident wave will be transmitted through the surface in this case. Thus, a circular polarization selective surface can be constructed which will either reflect or transmit circularly polarized radiation of any given sense of polarization.

This principle of operation implies that open-circuited dipoles are transparent, as though they were not present. This behavior is possible only from ideal Canonical Minimum Scattering antennas (CMS) [97, 98, 99] [92, pp. 123-133]. In general, this is only an approximation since the boundary conditions presented by the dipoles remain always present [96]. The induced current on each dipole is not zero either, although it is much weaker than that when the dipoles are resonant under short-circuit condition.

Tilston in reference [8] modelled the cell by a network consisting of two independent generators to account for the voltages at the terminals of the two dipoles, two radiation resistances, each one representing the self plus the mutual resistance arising from the coupling between the cells of the array, and a connection network modelled by the ABCD matrix to account for the transmission line and the reactive parts of the dipole impedances. Under the assumption that the connection network be lossless, reciprocal and symmetrical, Tilston obtained the requirements for the structure to be transparent from the requirements that the currents at both ports of the connection network be zero. This lead to the requirements that the spacing between the

dipoles be an odd number of quarter-wavelengths and that the transmission line be an integral number of half-wavelengths.

Tilston then proceeded to analyze the frequency response of the connection network current for the stop-band, i.e. for the case that the two ends of the transmission line were fed in-phase so that the surface reflected, as the frequency response of the series combination of the transmission line open-circuited at its mid-length and the dipole impedance. The frequency response of the dipole impedance was modelled from the results published by Anderson for a single array of parallel dipoles laid as per a rectangular grid. Tilston's analysis suggested that the characteristic impedance of the transmission line had to be only a fraction of the dipole impedance in order for the frequency bandwidth of the array with transmission lines to remain comparable to the frequency bandwidth of the array without transmission lines. Tilston concluded also that the choice of the characteristic impedance value for the transmission line needed to be balanced between obtaining a good rejection for one sense of CP polarization and a good transmission for the other sense of CP polarization. The results from Tilston's frequency response analysis, however, agreed only qualitatively with Tilston's own experimental results. These experiments showed also that, without adjusting the dipole length, the frequency at which the surface reflected best one sense of CP polarization was not necessarily the frequency at which the surface transmitted best the other sense of CP polarization.

In the appendix of the same reference [8], Hurd produced a different and more general analysis of the structure which he modelled as two parallel arrays of dipoles, each dipole being loaded with the series combination of the dipole impedance (self plus mutual impedance) for this dipole and the input impedance presented by the transmission line loaded at its other end by the dipole impedance (self plus mutual impedance) for the other dipole. Since the analysis was no longer restricted to the case of the dipoles of one array being orthogonal to the dipoles of the other array,

Hurd decomposed the incident electric field into two components, one component being perpendicular to the dipoles of one array and the other component being perpendicular to the dipoles of the other array. He then assumed that the scattered wave for each component of the incident wave consisted of the summation of the field re-radiated by the array of dipoles that were not perpendicular to the component of interest, and the field transmitted by the dipoles of the other array, perpendicular to the field component of interest, which were fed via the transmission lines by the voltages developed across the terminals of the dipoles of the former array. Hurd admittedly neglected second order couplings between the two arrays, namely the re-radiation from the dipoles of the first array illuminated by the transmitting dipoles of the second array, as well as the re-radiation from the dipoles of the second array illuminated by the re-radiating dipoles of the first array.

The Hertz vector for the electric field was obtained by summing the contribution from each dipole while taking into account the periodicity of each array by including a progressive phase shift in the expression of the current on each dipole in accordance with Floquet's theorem. By setting to zero the electric field parallel to each dipole, an integral integral equation was obtained. The solution is a current distribution that goes to zero at the end of each dipole.

Different expressions with various degrees of accuracy exist in the technical literature. For the re-radiating dipoles, Hurd took example on Munk [16] and used the symmetrical zero-order distribution of the induced current on an isolated loaded dipole as an approximation of the distribution of the induced current on the loaded dipole in the array. This current distribution consists of two terms, one term accounting for the current distribution that would exist on the unloaded, i.e. short-circuited, dipole acting as a scatterer, and the other term accounting for the current distribution that would exist on the dipole driven by an equivalent voltage source whose numerical value would be equal to the external load value times the actual antenna

current. For the transmitting dipoles, Hurd used the current distribution of the dipole driven by the transmission line, which is of the same form as that for the second term of the current distribution for the re-radiating dipoles. Hence, the total current on each dipole was the sum of two currents, one for each component of the incident field, one component corresponding to the dipoles acting as re-radiating antennas, the other component corresponding to the dipoles acting as transmitting antennas. The far-field was then computed from the Hertz vector potential.

For the canonical case identified previously by Tilston for which the dipoles of one array are orthogonal to the dipoles of the other array, the requirement that the surface be transparent leads to the requirement that the dipole impedance be matched to the input impedance of the transmission line and be equal to:

$$Z_A \approx \frac{60}{\pi} \frac{\lambda^2}{ab}$$

where a and b are the periods in the two transverse directions of the arrays. Since the dipole impedance of an array of parallel dipoles varies significantly with the incidence angle [16] when the array period is greater than a half-wavelength and since the cell size is about at least a half-wavelength in width and in height, the required value for Z_A is met only over a small range of incidence angles. Hence, Hurd's analysis predicts correctly that the performance of the surface varies significantly with the incidence angle. Grazing lobes can also be expected for some large incidence angles since the inter-element spacing of the arrays is greater than a half-wavelength.

For the more general case where the dipoles of one array are not orthogonal to the dipoles of the other array, the requirements lead again to the dipole impedance being matched to the input impedance of the transmission line, and to the transmission line being an integral number of half-wavelengths. As a result, the value of the characteristic impedance for the transmission line is not critical since the input impedance at one end of a half-wavelength transmission line has the same value as the impedance of the load connected to the other end of that transmission line. The expression for

the dipole impedance that provides the CPSS operation, however, turns out to be much more complicated.

The important feature of Hurd's analysis resides in Hurd's conclusion that many CPSS designs consisting of two arrays of resonant dipoles spaced a quarter-wavelength apart and connected with half-wavelength transmission lines, are possible by varying the angle between the transverse orientations of the dipoles of the two arrays. Based on Hurd's observation, this author surmises that a choice of different angle values might be best suited for different incidence angles. The investigation of such a possibility, however, is left aside for future research.

Chapter Two

Geometrical Constraints Placed on the Ideal CPSS

2.1 Introduction

As this mathematical development is based on the use of the GSM, the first section of this chapter is dedicated to introducing the conceptual framework and subtleties of the GSM. In the second section, the GSM is applied to known structures in order to validate its accuracy, and then to the CPSS structure in order to bring out the constraints placed upon its geometry. It is shown that if the structure can be accurately modelled by the GSM incorporating only the dominant mode, the ideal reciprocal CPSS must have the $2n$-fold rotational symmetry except at normal incidence where reciprocity suffices, but cannot have the reflection symmetry about the $z = 0$ plane.

The power of the GSM-based technique developed herein lies in the generality of the method by treating the structure not in terms of its boundary conditions but in terms of the more general principles of reflection symmetry, rotational symmetry, electromagnetic reciprocity and power conservation. The method is partly a synthesis tool in that it allows to identify if a particular operation prescribed for the structure is compatible with the various aforementioned principles since a prescribed operation imposes various relationships between the elements of the GSM.

This analysis does not corroborate Cornbleet's conjecture that a structure with a operation corresponding to that of a CPSS represents an impossible polarizer [1]. Cornbleet's argument is based on the observation that the Jones polarization matrix for a CPSS structure is singular, and thus cannot be realized by any combination of physical devices, which by virtue of their realizability have necessarily non-singular polarization matrices, since the product of any non-singular matrices cannot yield a singular matrix[1] .

It must be noted, however, that whereas Cornbleet's argument encompasses non-reciprocal and reciprocal devices alike, the argument made in this chapter on the basis of the GSM shows only that a reciprocal CPSS is not ruled out as being impossible. One can only be definite in the negative because proof that a operation does not violate any fundamental principles of electromagnetism is not proof that the operation exists physically, as the case for the physical existence of magnetic charges and magnetic currents exemplifies abundantly. In the next chapter, however, it will be proven with the GSM-based technique that the cascade polarizer design represents an ideal CPSS at normal incidence, thereby refuting Cornbleet's conjecture.

[1] $det(AB) = det(A) \times det(B)$.

2.2 Generalized Scattering Matrix

2.2.1 Generalities

The formalism of the scattering wave matrix originally developed for closed waveguides and transmission lines is phrased in terms of time harmonic (power, voltage or current) travelling waves being incident, reflected or transmitted on a transmission line supporting only the TEM propagation mode. Each wave in each region is in fact a composite of all the actual waves travelling simultaneously in the same direction. Figure 2.1 depicts the scattering matrix which reads as follows:

$$\begin{pmatrix} b_1 \\ b_2 \end{pmatrix} = \begin{pmatrix} S_{11} & S_{12} \\ S_{21} & S_{22} \end{pmatrix} \begin{pmatrix} a_1 \\ a_2 \end{pmatrix}$$

The properties of the scattering matrix are [20]:

- the matrix is symmetrical for reciprocal structures, i.e. $S_{ij} = S_{ji}$, providing that the travelling waves in each region have been normalized with respect to the characteristic impedance of the transmission line modelling that region.

- the matrix is unitary for lossless structures, i.e.:

$$\sum_{m=1}^{2} S_{mi} S_{mj}^{*} = \delta_{ij} = \begin{cases} 1 & \text{for } i = j \\ 0 & \text{for } i \neq j \end{cases}$$

  where δ is the Kronecker delta function.

In making the correspondence between the transmission line travelling waves and the electromagnetic field plane waves, one must realize that with, say, $(a_2 = 0, a_1 \neq 0)$, although b_1 represents truly the scattered field in region 1, however, b_2 represents the total field, not just the scattered field, in region 2. The same observation can be made about solving the wave propagating in 1-D, i.e. although two waves are postulated to coexist in region 1, only one wave is postulated to exist in region 2; the final solution is then obtained by matching the two partial solutions at the boundary interface.

In modelling anisotropic surfaces, the polarization of each wave must also be taken into account. This is done by considering the two transverse electric field components, say the x and y components, explicitly in the matrix formulation. The scattering matrix becomes:

$$\begin{pmatrix} b_1^X \\ b_1^Y \\ b_2^X \\ b_2^Y \end{pmatrix} = \begin{pmatrix} S_{11}^{XX} & S_{11}^{XY} & S_{12}^{XX} & S_{12}^{XY} \\ S_{11}^{YX} & S_{11}^{YY} & S_{12}^{YX} & S_{12}^{YY} \\ S_{21}^{XX} & S_{21}^{XY} & S_{22}^{XX} & S_{22}^{XY} \\ S_{21}^{YX} & S_{21}^{YY} & S_{22}^{YX} & S_{22}^{YY} \end{pmatrix} \begin{pmatrix} a_1^X \\ a_1^Y \\ a_2^X \\ a_2^Y \end{pmatrix}$$

The unitary property still applies if the structure is lossless. The matrix symmetry still applies if the structure is reciprocal.

When the scattering wave formalism is extended to the case of open 3-D space, i.e. free space is taken to be a waveguide of infinite transverse dimensions, the incident wave and the reflected wave are no longer travelling always in exactly opposite directions. In fact, at near grazing incidence (say, $\theta^i = 89^o$), the reflected wave travels in nearly the same direction as that of the incident wave. Similarly, the incident wave and the transmitted wave are no longer necessarily travelling in exactly the same direction. Consequently, as depicted in Figure 2.2, eight rather than four waves are now typically required to characterize the operation of the structure. These eight waves form a complete and self-consistent set as each wave finds a counterpart in the opposite direction. When the incidence becomes normal to the surface, waves a_1 and a_3 merge and similarly for the other waves so that the set reduces to just four waves.

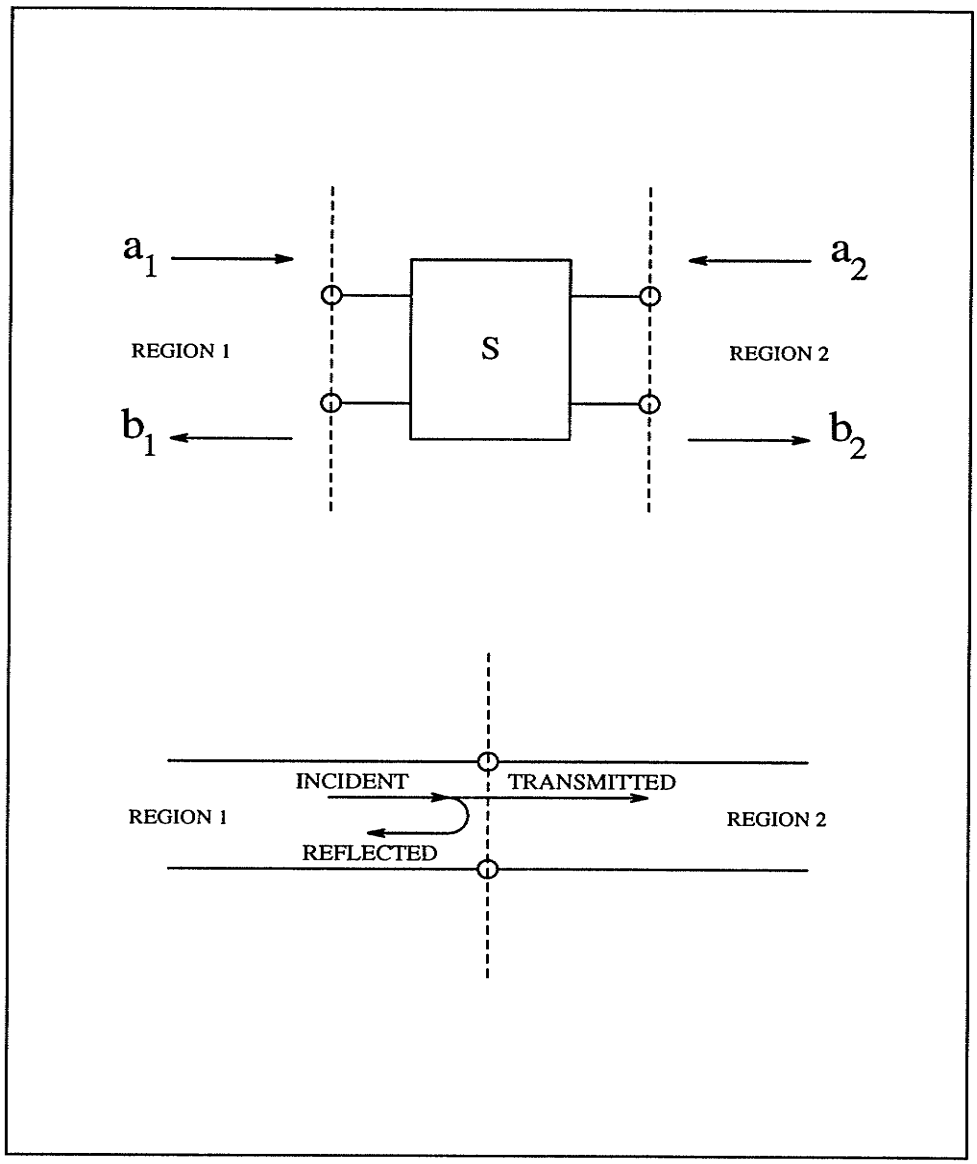

Figure 2.1: Two-port scattering matrix (top) and 1-D wave propagation problem (bottom).

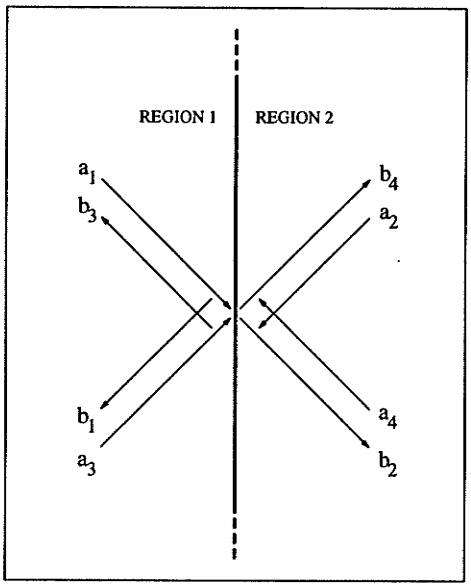

Figure 2.2: Generalization of the travelling wave scattering process for arbitrary incidence angles.

The odd-numbered waves exist in region 1 and form two ports, one port consisting of the incident wave a_1 and the reflected wave b_1, the other port consisting of the incident wave a_3 and the reflected wave b_3. Similarly, the even-numbered waves exist in region 2 and form two ports, one port consisting of the incident wave a_2 and the reflected wave b_2, the other port consisting of the incident wave a_4 and the reflected wave b_4. The relations between these various waves are as follows:

Incident	Reflected	Transmitted
a_1	b_1	b_2
a_2	b_2	b_1
a_3	b_3	b_4
a_4	b_4	b_3

and the corresponding scattering matrix becomes:

$$\begin{pmatrix} b_1 \\ b_2 \\ b_3 \\ b_4 \end{pmatrix} = \begin{pmatrix} S_{11} & S_{12} & 0 & 0 \\ S_{21} & S_{22} & 0 & 0 \\ 0 & 0 & S_{33} & S_{34} \\ 0 & 0 & S_{43} & S_{44} \end{pmatrix} \begin{pmatrix} a_1 \\ a_2 \\ a_3 \\ a_4 \end{pmatrix}$$

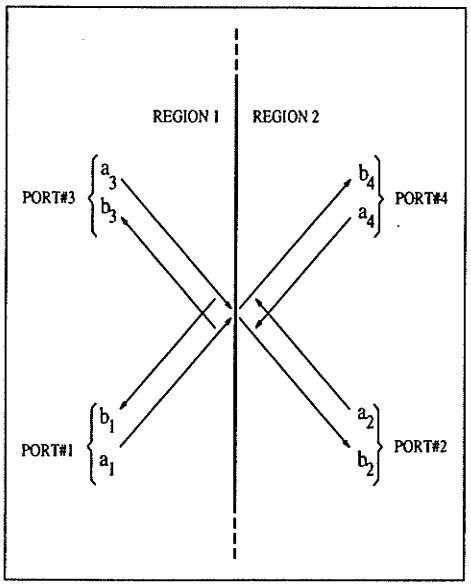

Figure 2.3: Travelling wave scattering process for arbitrary incidence angles with relabelled incident waves.

The matrix coefficients that are equal, providing that the structure is reciprocal and that the travelling waves have been normalized, are now:

$$S_{11} = S_{33}, \qquad S_{22} = S_{44}, \qquad S_{12} = S_{43}, \qquad S_{21} = S_{34}$$

Thus, one observes that the matrix for a reciprocal structure is not symmetrical. However, it is possible to rearrange the terms so as to make the matrix symmetrical. For instance:

$$\begin{pmatrix} b_1 \\ b_2 \\ b_3 \\ b_4 \end{pmatrix} = \begin{pmatrix} 0 & 0 & S_{11} & S_{12} \\ 0 & 0 & S_{21} & S_{22} \\ S_{33} & S_{34} & 0 & 0 \\ S_{43} & S_{44} & 0 & 0 \end{pmatrix} \begin{pmatrix} a_3 \\ a_4 \\ a_1 \\ a_2 \end{pmatrix}$$

In effect, this rearrangement corresponds to taking for port 1 the reflected wave b_1 but the incident wave a_3 instead of the incident wave a_1, and relabelling the incident waves so that port 1 corresponds to the relabelled incident wave a_1 and the original reflected wave b_1, and similarly for the other ports as shown in Figure 2.3. One

obtains:

$$\begin{pmatrix} b_1 \\ b_2 \\ b_3 \\ b_4 \end{pmatrix} = \begin{pmatrix} 0 & 0 & S_{13} & S_{14} \\ 0 & 0 & S_{23} & S_{24} \\ S_{31} & S_{32} & 0 & 0 \\ S_{41} & S_{42} & 0 & 0 \end{pmatrix} \begin{pmatrix} a_1 \\ a_2 \\ a_3 \\ a_4 \end{pmatrix}$$

With this relabelling, the matrix would be possibly symmetrical without rearranging the terms but the matrix would now appear different since a reflection coefficient would have been turned into a transmission coefficient. This author finds it physically more meaningful *not* to relabel the incident waves.

The polarization of each wave can again be taken into account explicitly by taking each scattering coefficient to be a submatrix. The polarization, however, needs now to be described in terms of TE (or H) and TM (or E) modes rather than X and Y components. Thus, the incident EM field must be first decomposed into a TM^u mode and a TE^u mode, and the scattered field must be decomposed into TM^u modes and TE^u modes. In this development, it is convenient to take $u \equiv z$ where z is the coordinate axis perpendicular to the surface of the planar structure. With respect to the notation, it is more convenient to account for the polarization explicitly by means of superscripts pq rather than to assign a different port to each polarization combination. Thus, each port can be understood as consisting of four sub-ports, one sub-port per possible polarization combination of the incident and the reflected waves, i.e. $(a^E, b^E), (a^E, b^H), (a^H, b^E), (a^H, b^H)$. The scattering matrix becomes:

$$\begin{pmatrix} b_1^E \\ b_1^H \\ b_2^E \\ b_2^H \\ b_3^E \\ b_3^H \\ b_4^E \\ b_4^H \end{pmatrix} = \begin{pmatrix} 0 & 0 & 0 & 0 & S_{11}^{EE} & S_{11}^{EH} & S_{12}^{EE} & S_{12}^{EH} \\ 0 & 0 & 0 & 0 & S_{11}^{HE} & S_{11}^{HH} & S_{12}^{HE} & S_{12}^{HH} \\ 0 & 0 & 0 & 0 & S_{21}^{EE} & S_{21}^{EH} & S_{22}^{EE} & S_{22}^{EH} \\ 0 & 0 & 0 & 0 & S_{21}^{HE} & S_{21}^{HH} & S_{22}^{HE} & S_{22}^{HH} \\ S_{33}^{EE} & S_{33}^{EH} & S_{34}^{EE} & S_{34}^{EH} & 0 & 0 & 0 & 0 \\ S_{33}^{HE} & S_{33}^{HH} & S_{34}^{HE} & S_{34}^{HH} & 0 & 0 & 0 & 0 \\ S_{43}^{EE} & S_{43}^{EH} & S_{44}^{EE} & S_{44}^{EH} & 0 & 0 & 0 & 0 \\ S_{43}^{HE} & S_{43}^{HH} & S_{44}^{HE} & S_{44}^{HH} & 0 & 0 & 0 & 0 \end{pmatrix} \begin{pmatrix} a_3^E \\ a_3^H \\ a_4^E \\ a_4^H \\ a_1^E \\ a_1^H \\ a_2^E \\ a_2^H \end{pmatrix}$$

One finds it convenient for the purpose of subsequent generalization to regroup the terms according to:

1. the region to which they belong, as indicated below by a triple line separation
2. the polarization combination, as indicated below by a double line separation
3. the spatial direction, as indicated below by a single line separation.

One obtains:

$$\left(\begin{array}{c} b_1^E \\ \hline b_3^E \\ \hline\hline b_1^H \\ \hline b_3^H \\ \hline\hline\hline b_2^E \\ \hline b_4^E \\ \hline\hline b_2^H \\ \hline b_4^H \end{array}\right) = \left(\begin{array}{c|c||c|c||c|c||c|c} S_{11}^{EE} & 0 & S_{11}^{EH} & 0 & S_{12}^{EE} & 0 & S_{12}^{EH} & 0 \\ \hline 0 & S_{33}^{EE} & 0 & S_{33}^{EH} & 0 & S_{34}^{EE} & 0 & S_{34}^{EH} \\ \hline\hline S_{11}^{HE} & 0 & S_{11}^{HH} & 0 & S_{12}^{HE} & 0 & S_{12}^{HH} & 0 \\ \hline 0 & S_{33}^{HE} & 0 & S_{33}^{HH} & 0 & S_{34}^{HE} & 0 & S_{34}^{HH} \\ \hline\hline\hline S_{21}^{EE} & 0 & S_{21}^{EH} & 0 & S_{22}^{EE} & 0 & S_{22}^{EH} & 0 \\ \hline 0 & S_{43}^{EE} & 0 & S_{43}^{EH} & 0 & S_{44}^{EE} & 0 & S_{44}^{EH} \\ \hline\hline S_{21}^{HE} & 0 & S_{21}^{HH} & 0 & S_{22}^{HE} & 0 & S_{22}^{HH} & 0 \\ \hline 0 & S_{43}^{HE} & 0 & S_{43}^{HH} & 0 & S_{44}^{HE} & 0 & S_{44}^{HH} \end{array}\right) \left(\begin{array}{c} a_1^E \\ \hline a_3^E \\ \hline\hline a_1^H \\ \hline a_3^H \\ \hline\hline\hline a_2^E \\ \hline a_4^E \\ \hline\hline a_2^H \\ \hline a_4^H \end{array}\right)$$

The terms could be rearranged so as to obtain a possibly symmetrical matrix (but it will be seen later that due to some other consideration, $S(E,H)$ is not symmetrical in general, even after rearranging the terms). One would obtain (without relabelling the waves):

$$\left(\begin{array}{c} b_1^E \\ b_3^E \\ b_1^H \\ b_3^H \\ b_2^E \\ b_4^E \\ b_2^H \\ b_4^H \end{array}\right) = \left(\begin{array}{cccccccc} 0 & S_{11}^{EE} & 0 & S_{11}^{EH} & 0 & S_{12}^{EE} & 0 & S_{12}^{EH} \\ S_{33}^{EE} & 0 & S_{33}^{EH} & 0 & S_{34}^{EE} & 0 & S_{34}^{EH} & 0 \\ 0 & S_{11}^{HE} & 0 & S_{11}^{HH} & 0 & S_{12}^{HE} & 0 & S_{12}^{HH} \\ S_{33}^{HE} & 0 & S_{33}^{HH} & 0 & S_{34}^{HE} & 0 & S_{34}^{HH} & 0 \\ 0 & S_{21}^{EE} & 0 & S_{21}^{EH} & 0 & S_{22}^{EE} & 0 & S_{22}^{EH} \\ S_{43}^{EE} & 0 & S_{43}^{EH} & 0 & S_{44}^{EE} & 0 & S_{44}^{EH} & 0 \\ 0 & S_{21}^{HE} & 0 & S_{21}^{HH} & 0 & S_{22}^{HE} & 0 & S_{22}^{HH} \\ S_{43}^{HE} & 0 & S_{43}^{HH} & 0 & S_{44}^{HE} & 0 & S_{44}^{HH} & 0 \end{array}\right) \left(\begin{array}{c} a_3^E \\ a_1^E \\ a_3^H \\ a_1^H \\ a_4^E \\ a_2^E \\ a_4^H \\ a_2^H \end{array}\right)$$

However, one finds it more convenient for future generalization to keep the various incident waves in the same order as that of the reflected waves.

Some structures require even more than eight waves. For instance, a grating scatters the incident wave into a multitude of modes, each mode propagating in a different direction. The most general formulation requires in fact an infinite number of waves, one wave (two if one considers also the polarization) for every possible direction, in agreement with the principle that any spatial waveform can be decomposed into an infinite sum of plane waves propagating in all directions. The scattering matrix representation thus assigns a different port to waves propagating in different directions in each region. The *generalized* scattering matrix formalism [23, 24, 25, 27, 28, 29] extends this representation to evanescent modes as well as to propagating modes, but then, the unitary property of the matrix for a lossless structure no longer applies because evanescent modes do not carry average power on their own [23, p. 514].

The matrix is of infinite size even for a scatterer with only two faces if all observation directions are considered. The number of spatial waves needs also to be infinite when the scattering surface is of finite size owing to the scattered wave spreading into a bundle of plane waves rather than remaining a single plane wave. This angular spreading of the beam results from the spatial windowing phenomenon. The larger the scattering surface, the smaller the angular spread. For that reason, the GSM written in terms of plane waves is not very practical for finite size surfaces.

In concept, this formalism could be generalized to structures with more than two faces or regions. Ultimately, if the number of faces became infinite, any arbitrarily shaped scatterers could be modelled. In practice however, complications would arise from the overlap in the angular coverage corresponding to each face as the two regions would no longer be necessarily mutually exclusive. Hence, a single uniform plane wave could now illuminate simultaneously more than one face with a possibly different incidence angle at each face, and the transmitted wave would no longer necessarily represent the total wave in its corresponding region.

For arbitrarily shaped scatterers, a better approach consists in decomposing the scattered field into spherical rather than planar modes, and assigning a different port to every different spherical mode [92, pp. 123-133] [99]. Modes other than spherical ones might also be appropriate, e.g. the Inagaki modes [100, 101], the characteristic modes [102] and the generalized characteristic modes [103]. The resulting GSM defined in these references, however, is different from the GSM defined herein since their GSM for a transparent structure is the identity matrix whereas here, as it will be seen later, the GSM for the free space slab is *not* the identity matrix. In the remaining part of this chapter, only planar structures with two parallel faces extending to infinity are considered.

To each sub-port corresponds an incident voltage travelling wave and a reflected voltage travelling wave which are made out of the transverse electric field component of the corresponding mode. The equivalence is based on the fact that the longitudinal component, herein the z component, does not carry any complex power in the longitudinal direction, i.e. $\pm\hat{z}$. Now, with a true TEM transmission line, the definition of voltage and current is unique with respect to the choice of the integration path in space, in the Faraday and the Ampere integral equations, respectively. In other words, the Helmholtz equation reduces to the Laplace equation and the electromagnetic field distribution is exactly the same as the superposition of the corresponding electrostatic and magnetostatic field distributions. Consequently, the definitions of the characteristic and the input impedances of the transmission line are also unique. For the transmission line corresponding to a TM^z or TE^z mode however, this uniqueness of the definitions of voltage, current and impedances is destroyed by the presence, in the mode, of the longitudinal field component which now makes the voltage and the current dependent on the choice of the integration path in space. In other words, the Laplace equation does not apply here.

Although no longer unique, the concepts of voltage, current and impedance remain nevertheless useful, providing that in using the transmission line theory and its associated scattering matrix formalism, normalization and denormalization be made with respect to the same definition of characteristic impedance. This definition can be made on a pseudo-voltage/pseudo-current basis, or power/pseudo-voltage basis or power/pseudo-current basis [21]. Alternatively, one can use the concept of wave impedance which is defined as the ratio of the transverse components:

$$Z_W = \frac{E_t}{H_t} = \begin{cases} \frac{k_z}{\omega\varepsilon} = \frac{k_z}{k_o}\eta = \eta\, cos(\theta) & \text{for } TM^z \\ \frac{\omega\mu}{k_z} = \frac{k_o}{k_z}\eta = \frac{\eta}{cos(\theta)} & \text{for } TE^z \end{cases}$$

Taking the wave impedance as the characteristic impedance of the equivalent transmission line has the physical interpretation of taking both the transverse electric and the transverse magnetic fields of the mode of interest, be it TE^z or TM^z, as the electric and magnetic fields of the equivalent TEM^z mode travelling on the equivalent transmission line. The expressions $\frac{k_z}{\omega\varepsilon}$ and $\frac{\omega\mu}{k_z}$ come respectively from performing $\frac{E_x^A}{H_y^A} = -\frac{E_y^A}{H_x^A}$ and $\frac{E_x^F}{H_y^F} = -\frac{E_y^F}{H_x^F}$ where A and F refer to the magnetic and to the electric vector potentials, respectively (see Appendix B). It is no coincidence that the expressions $\frac{\eta}{cos(\theta)}$ and $\eta cos(\theta)$ correspond also to the expressions for the characteristic impedance of the equivalent transmission line modelling a planar dielectric interface [22, pp. 413 & 415], and to the expressions for the ratio $\frac{E_t^i}{H_t^i}$ when a uniform plane wave is incident onto a planar surface at an arbitrary angle with an arbitrary polarization (see Appendix C).

One notes that the scattering matrix has half of its coefficients being zero. Furthermore, when the structure is reciprocal, the use of eight waves incurs even more redundancy since, for example, the relationship between the waves a_1 and b_1 is the same as that between the waves a_3 and b_3. The use of an equivalent transmission line whose TEM^z field consists of the transverse field components of the actual TE^z or

TM^z mode makes it possible to treat the arbitrary incidence as if it were a normal incidence since the arbitrary incidence is taken into account implicitly by means of making the characteristic impedance of the equivalent transmission line Z_o dependent on θ^i and ϕ^i upon taking $Z_o = Z_W$. Thus, the scattering matrix can remain written in terms of just four rather than eight waves so that the scattering matrix formalism of the transmission line theory can be used without modification.

Since the transmission line and the usual scattering matrix representations deal only with the transverse components of the modes, so do the corresponding scattering coefficients which are phrased, here, in terms of solely voltage travelling waves as:

$$\begin{aligned} S_{uv}^{pq} &= \frac{b_u^p}{a_v^q} \qquad \text{for } a_w^l = 0, w \neq v, l = \{p, q\} \\ &= \frac{(E_t^s)_u^p}{(E_t^i)_v^q} \qquad \text{for } (E_t^i)_w^l = 0, w \neq v, l = \{p, q\} \end{aligned}$$

where $\vec{E}_o^l = \vec{E}_t^l + \vec{E}_z^l$ with $l = \{i, r, t\}$. The superscripts i, r, t, s stand for incident, reflected, transmitted and scattered, respectively, with $s = \{r, t\}$. The subscripts o, t, z refer to the whole electric field, the transverse component and the z component of the electric field, respectively. The superscripts q and p refer to the mode of the a and b waves, respectively, and take on either the designation E or H where E refers to the TM^z mode (i.e. E^z mode, i.e. $\vec{E}_o = E_o\hat{\theta}$), and H refers to the TE^z mode (i.e. H^z mode, i.e. $\vec{E}_o = E_o\hat{\phi}$).

$$\text{If } \begin{cases} p = q \Longrightarrow S_{uv}^{pq} \text{ corresponds to a co-polarization coefficient;} \\ p \neq q \Longrightarrow S_{uv}^{pq} \text{ corresponds to a cross-polarization coefficient.} \end{cases}$$

$$\text{If } \begin{cases} u = v \Longrightarrow S_{uv}^{pq} \text{ corresponds to a reflection coefficient;} \\ u \neq v \Longrightarrow S_{uv}^{pq} \text{ corresponds to a transmission coefficient.} \end{cases}$$

In the present formalism, a scattering coefficient is considered to correspond to a transmission coefficient even if both ports belong to the same region.

In order to obtain the voltage scattering coefficients in terms of the whole electric field rather than just the transverse electric field, the angles must also be taken into

account as per Appendices A and B (see also Figure 2.4). Taking also into account Snell's law of reflection, i.e. $\theta^r = \pi - \theta^i$, there obtains for the case $a_1 \neq 0, a_2 = a_3 = a_4 = 0$:

$$\frac{E_o^r}{E_o^i} = \begin{cases} \frac{E_t^r/|cos(\theta^r)|}{E_t^i/|cos(\pi-\theta^i)|} = \frac{E_t^r}{E_t^i} & \text{for } TM^z \\ \frac{E_t^r}{E_t^i} & \text{for } TE^z \end{cases}$$

$$\frac{E_o^t}{E_o^i} = \begin{cases} \frac{E_t^t/|cos(\pi-\theta^t)|}{E_t^i/|cos(\pi-\theta^i)|} = \frac{|cos(\theta^i)|}{|cos(\theta^t)|}\frac{E_t^t}{E_t^i} & \text{for } TM^z \\ \frac{E_t^t}{E_t^i} & \text{for } TE^z \end{cases}$$

The voltage scattering coefficients in terms of the whole electric field becomes:

$$C_{uv}^{pq} = \frac{(E_o^s)_u^p}{(E_o^i)_v^q} \text{ for } (E_o^i)_w^l = 0, w \neq v, l = \{p, q\}$$

In order to ease the notation, the scattering matrix is written hereafter as a generic 2-port scattering matrix with each port being arbitrary. Owing to the earlier choice of keeping the incident waves in the same order as that of the reflected waves (and to some other consideration which will be seen later), the resulting matrix is not symmetrical even when the two generic ports happen to correspond to ports that are in a possible reciprocal relationship (e.g. port 1 and port 3, or port 1 and port 4, but not port 1 and port 2). There obtains:

$$\begin{pmatrix} b_{u1}^E \\ b_{u1}^H \\ b_{u2}^E \\ b_{u2}^H \end{pmatrix} = \begin{pmatrix} S_{u1,v1}^{EE} & S_{u1,v1}^{EH} & S_{u1,v2}^{EE} & S_{u1,v2}^{EH} \\ S_{u1,v1}^{HE} & S_{u1,v1}^{HH} & S_{u1,v2}^{HE} & S_{u1,v2}^{HH} \\ S_{u2,v1}^{EE} & S_{u2,v1}^{EH} & S_{u2,v2}^{EE} & S_{u2,v2}^{EH} \\ S_{u2,v1}^{HE} & S_{u2,v1}^{HH} & S_{u2,v2}^{HE} & S_{u2,v2}^{HH} \end{pmatrix} \begin{pmatrix} a_{v1}^E \\ a_{v1}^H \\ a_{v2}^E \\ a_{v2}^H \end{pmatrix}$$

The above formalism is generalized by allowing u_i and v_j to be described more generally by a scattering angle (θ^s, ϕ^s) and an incidence angle (θ^i, ϕ^i), respectively. Although a given port was defined earlier as being confined to a given region, these

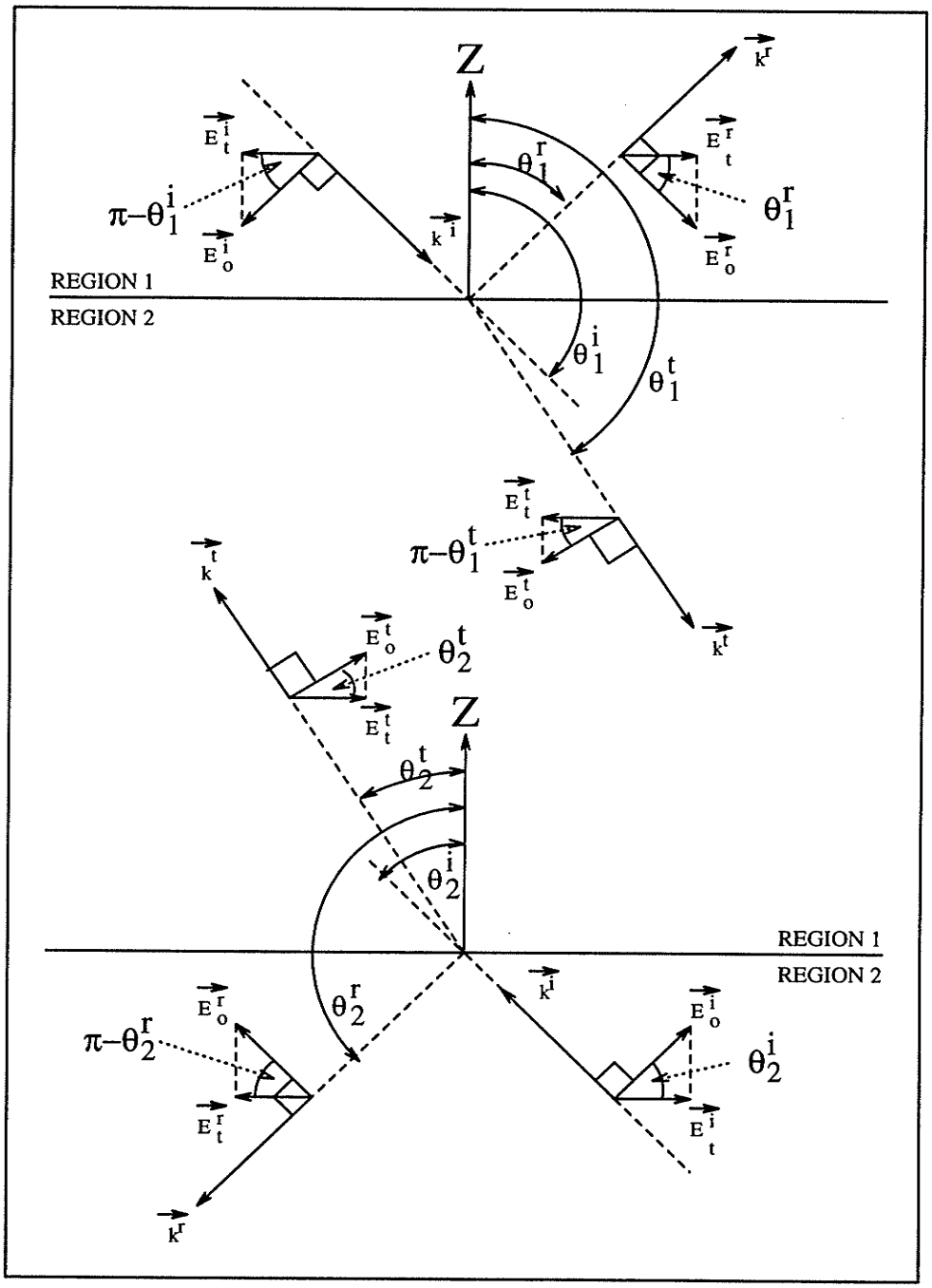

Figure 2.4: Representation of the electric field vector for the TM^z mode for the two cases where the incident wave originates from medium #1 (top) or medium #2 (bottom).

angles are assumed more generally to take arbitrary values. This formalism can also be justified on the basis that the use of the equivalent transmission line allows the use of only four rather than eight waves, as mentioned earlier. The generic voltage scattering coefficient becomes:

$$\begin{aligned} S_{uv}^{pq}(\theta^s,\phi^s|\theta^i,\phi^i) &= \frac{b_u^p(\theta^s,\phi^s)}{a_v^q(\theta^i,\phi^i)} \qquad \text{for } a_w^l = 0, w \neq v, l = \{p,q\} \\ &= \frac{(E_t^s)_u^p(\theta^s,\phi^s)}{(E_t^i)_v^q(\theta^i,\phi^i)} \qquad \text{for } (E_t^i)_w^l = 0, w \neq v, l = \{p,q\} \end{aligned}$$

$$C_{uv}^{pq}(\theta^s,\phi^s|\theta^i,\phi^i) = \frac{(E_o^s)_u^p(\theta^s,\phi^s)}{(E_o^i)_v^q(\theta^i,\phi^i)} \qquad \text{for } (E_o^i)_w^l = 0, w \neq v, l = \{p,q\}$$

$$\text{If } \begin{cases} \theta^s = \pi - \theta^i, \text{ and } \phi^s = \pi + \phi^i & \Longrightarrow \text{ monostatic scattering} \\ \theta^s = \pi - \theta^i, \text{ and } \phi^s = \phi^i & \Longrightarrow \text{ bistatic scattering} \\ \theta^s = \theta^i, \text{ and } \phi^s = \phi^i & \Longrightarrow \text{ forward scattering} \\ \theta^s = \text{any angle, and } \phi^s = \text{any angle} & \Longrightarrow \text{ general scattering} \end{cases}$$

To fix ideas, the two generic ports are taken hereafter as being ports 1 and 2. With the help of Figure 2.4, the matrix $C(E,H)$ can be obtained explicitly as follows:

$$\begin{pmatrix} b_1^E = (E_t^s)_1^E = (E_o^s)_1^E|cos(\Theta_1^s)| \\ b_1^H = (E_t^s)_1^H = (E_o^s)_1^H \\ b_2^E = (E_t^s)_2^E = (E_o^s)_2^E|cos(\Theta_2^s)| \\ b_2^H = (E_t^s)_2^H = (E_o^s)_2^H \end{pmatrix} = \begin{pmatrix} |cos(\Theta_1^s)| & 0 & 0 & 0 \\ 0 & 1 & 0 & 0 \\ 0 & 0 & |cos(\Theta_2^s)| & 0 \\ 0 & 0 & 0 & 1 \end{pmatrix} \begin{pmatrix} (E_o^s)_1^E \\ (E_o^s)_1^H \\ (E_o^s)_2^E \\ (E_o^s)_2^H \end{pmatrix}$$

$$\text{where } \Theta_1^s = \begin{cases} \theta_1^s & \text{if } s = r \\ \pi - \theta_1^s & \text{if } s = t \end{cases} \quad \text{and} \quad \Theta_2^s = \begin{cases} \pi - \theta_2^s & \text{if } s = r \\ \theta_2^s & \text{if } s = t \end{cases}$$

$$\begin{pmatrix} a_1^E = (E_t^i)_1^E = (E_o^i)_1^E|cos(\Theta_1^i)| \\ a_1^H = (E_t^i)_1^H = (E_o^i)_1^H \\ a_2^E = (E_t^i)_2^E = (E_o^i)_2^E|cos(\Theta_2^i)| \\ a_2^H = (E_t^i)_2^H = (E_o^i)_2^H \end{pmatrix} = \begin{pmatrix} |cos(\Theta_1^i)| & 0 & 0 & 0 \\ 0 & 1 & 0 & 0 \\ 0 & 0 & |cos(\Theta_2^i)| & 0 \\ 0 & 0 & 0 & 1 \end{pmatrix} \begin{pmatrix} (E_o^i)_1^E \\ (E_o^i)_1^H \\ (E_o^i)_2^E \\ (E_o^i)_2^H \end{pmatrix}$$

$$\text{where } \Theta_1^i = \pi - \theta_1^i \quad \text{and} \quad \Theta_2^i = \theta_2^i$$

$$\begin{pmatrix} (E_t^s)_1^E \\ (E_t^s)_1^H \\ (E_t^s)_2^E \\ (E_t^s)_2^H \end{pmatrix} = \begin{pmatrix} S_{11}^{EE} & S_{11}^{EH} & S_{12}^{EE} & S_{12}^{EH} \\ S_{11}^{HE} & S_{11}^{HH} & S_{12}^{HE} & S_{12}^{HH} \\ S_{21}^{EE} & S_{21}^{EH} & S_{22}^{EE} & S_{22}^{EH} \\ S_{21}^{HE} & S_{21}^{HH} & S_{22}^{HE} & S_{22}^{HH} \end{pmatrix} \begin{pmatrix} (E_t^i)_1^E \\ (E_t^i)_1^H \\ (E_t^i)_2^E \\ (E_t^i)_2^H \end{pmatrix}$$

$$\begin{pmatrix} (E_o^s)_1^E \\ (E_o^s)_1^H \\ (E_o^s)_2^E \\ (E_o^s)_2^H \end{pmatrix} = \begin{pmatrix} C_{11}^{EE} & C_{11}^{EH} & C_{12}^{EE} & C_{12}^{EH} \\ C_{11}^{HE} & C_{11}^{HH} & C_{12}^{HE} & C_{12}^{HH} \\ C_{21}^{EE} & C_{21}^{EH} & C_{22}^{EE} & C_{22}^{EH} \\ C_{21}^{HE} & C_{21}^{HH} & C_{22}^{HE} & C_{22}^{HH} \end{pmatrix} \begin{pmatrix} (E_o^i)_1^E \\ (E_o^i)_1^H \\ (E_o^i)_2^E \\ (E_o^i)_2^H \end{pmatrix}$$

Performing the required matrix manipulations, one obtains:

$$C(E,H) = \begin{pmatrix} \frac{|cos(\Theta_1^i)|}{|cos(\Theta_1^s)|} S_{11}^{EE} & \frac{1}{|cos(\Theta_1^s)|} S_{11}^{EH} & \frac{|cos(\Theta_2^i)|}{|cos(\Theta_1^s)|} S_{12}^{EE} & \frac{1}{|cos(\Theta_1^s)|} S_{12}^{EH} \\ \frac{|cos(\Theta_1^i)|}{1} S_{11}^{HE} & S_{11}^{HH} & \frac{|cos(\Theta_2^i)|}{1} S_{12}^{HE} & S_{12}^{HH} \\ \frac{|cos(\Theta_1^i)|}{|cos(\Theta_2^s)|} S_{21}^{EE} & \frac{1}{|cos(\Theta_2^s)|} S_{21}^{EH} & \frac{|cos(\Theta_2^i)|}{|cos(\Theta_2^s)|} S_{22}^{EE} & \frac{1}{|cos(\Theta_2^s)|} S_{22}^{EH} \\ \frac{|cos(\Theta_1^i)|}{1} S_{21}^{HE} & S_{21}^{HH} & \frac{|cos(\Theta_2^i)|}{1} S_{22}^{HE} & S_{22}^{HH} \end{pmatrix}$$

Substituting for Θ_j^i and Θ_j^s, one obtains:

$$C(E,H) = \begin{pmatrix} \frac{|cos(\theta_1^i)|}{|cos(\theta_1^s)|} S_{11}^{EE} & \frac{1}{|cos(\theta_1^s)|} S_{11}^{EH} & \frac{|cos(\theta_2^i)|}{|cos(\theta_1^s)|} S_{12}^{EE} & \frac{1}{|cos(\theta_1^s)|} S_{12}^{EH} \\ \frac{|cos(\theta_1^i)|}{1} S_{11}^{HE} & S_{11}^{HH} & \frac{|cos(\theta_2^i)|}{1} S_{12}^{HE} & S_{12}^{HH} \\ \frac{|cos(\theta_1^i)|}{|cos(\theta_2^s)|} S_{21}^{EE} & \frac{1}{|cos(\theta_2^s)|} S_{21}^{EH} & \frac{|cos(\theta_2^i)|}{|cos(\theta_2^s)|} S_{22}^{EE} & \frac{1}{|cos(\theta_2^s)|} S_{22}^{EH} \\ \frac{|cos(\theta_1^i)|}{1} S_{21}^{HE} & S_{21}^{HH} & \frac{|cos(\theta_2^i)|}{1} S_{22}^{HE} & S_{22}^{HH} \end{pmatrix}$$

Applying Snell's law of reflection with the angle θ defined as per Appendix A, i.e. $\theta^r = \pi - \theta^i$, one obtains:

$$C(E,H) = \begin{pmatrix} S_{11}^{EE} & \frac{1}{|cos(\theta_1^i)|} S_{11}^{EH} & \frac{|cos(\theta_2^i)|}{|cos(\theta_1^i)|} S_{12}^{EE} & \frac{1}{|cos(\theta_1^i)|} S_{12}^{EH} \\ \frac{|cos(\theta_1^i)|}{1} S_{11}^{HE} & S_{11}^{HH} & \frac{|cos(\theta_2^i)|}{1} S_{12}^{HE} & S_{12}^{HH} \\ \frac{|cos(\theta_1^i)|}{|cos(\theta_2^i)|} S_{21}^{EE} & \frac{1}{|cos(\theta_2^i)|} S_{21}^{EH} & S_{22}^{EE} & \frac{1}{|cos(\theta_2^i)|} S_{22}^{EH} \\ \frac{|cos(\theta_1^i)|}{1} S_{21}^{HE} & S_{21}^{HH} & \frac{|cos(\theta_2^i)|}{1} S_{22}^{HE} & S_{22}^{HH} \end{pmatrix}$$

$$\Longrightarrow S(E,H) = \begin{pmatrix} C_{11}^{EE} & \frac{|cos(\theta_1^i)|}{1}C_{11}^{EH} & \frac{|cos(\theta_1^t)|}{|cos(\theta_2^i)|}C_{12}^{EE} & \frac{|cos(\theta_1^t)|}{1}C_{12}^{EH} \\ \frac{1}{|cos(\theta_1^i)|}C_{11}^{HE} & C_{11}^{HH} & \frac{1}{|cos(\theta_2^i)|}C_{12}^{HE} & C_{12}^{HH} \\ \frac{|cos(\theta_2^t)|}{|cos(\theta_1^i)|}C_{21}^{EE} & \frac{|cos(\theta_2^t)|}{1}C_{21}^{EH} & C_{22}^{EE} & \frac{|cos(\theta_2^i)|}{1}C_{22}^{EH} \\ \frac{1}{|cos(\theta_1^i)|}C_{21}^{HE} & C_{21}^{HH} & \frac{1}{|cos(\theta_2^i)|}C_{22}^{HE} & C_{22}^{HH} \end{pmatrix}$$

If the two generic ports correspond to reciprocal directions through the structure in free space, one obtains:

$$\begin{cases} \theta_1^i = \pi - \theta_2^i \\ \theta_1^t = \pi - \theta_2^t \\ \theta_1^i = \theta_1^t \\ \theta_2^i = \theta_2^t \end{cases}$$

and thus:

$$S(E,H) = \begin{pmatrix} C_{11}^{EE} & \frac{|cos(\theta_1^i)|}{1}C_{11}^{EH} & C_{12}^{EE} & \frac{|cos(\theta_1^i)|}{1}C_{12}^{EH} \\ \frac{1}{|cos(\theta_1^i)|}C_{11}^{HE} & C_{11}^{HH} & \frac{1}{|cos(\theta_1^i)|}C_{12}^{HE} & C_{12}^{HH} \\ C_{21}^{EE} & \frac{|cos(\theta_1^i)|}{1}C_{21}^{EH} & C_{22}^{EE} & \frac{|cos(\theta_1^i)|}{1}C_{22}^{EH} \\ \frac{1}{|cos(\theta_1^i)|}C_{21}^{HE} & C_{21}^{HH} & \frac{1}{|cos(\theta_1^i)|}C_{22}^{HE} & C_{22}^{HH} \end{pmatrix} \quad (2.1)$$

In the above matrices, it is understood that if the incident wave $(E_o^i)_v^q = 0$ the corresponding angles $\theta_v^i = 0$ and $\theta_v^t = 0$ so that the scattered wave $(E_o^s)_u^p | \, u \neq v$ and the corresponding scattering elements C_{uv}^{pq} be not affected. When the incidence is normal to the surface, $|cos(\theta_1^i)| = 1$ and thus, $C(E,H) \equiv S(E,H)$. Let us recall that, owing to the earlier choice of keeping the incident waves in the same order as that of the reflected waves (and to some other consideration which will be seen later), the scattering matrices $C(E,H)$ and $S(E,H)$ are not symmetrical in general.

2.2.2 Normal Incidence

Rigorously, one cannot speak of the E^z and H^z modes at normal incidence, i.e. for $\theta^i = \{0, \pi\}$, because in such a case, these modes coalesce and $k_o^2 - k_z^2 = 0$ appear in the denominator of the expressions for the field components (see Appendix B). Furthermore, when $\theta = \{0, \pi\}$, the spherical coordinate system has an ambiguity in ϕ. However, the same formalism and concepts apply if one replaces the E^z mode, for which $\vec{E}_o = E_o\hat{\theta}$, and the H^z mode, for which $\vec{E}_o = E_o\hat{\phi}$, by say, the X and the Y components of $\vec{E}$, respectively. The scattering coefficients with the Cartesian coordinates, however, are not all identical to the corresponding scattering coefficients with the spherical coordinates because the spherical coordinate unit vectors $\hat{\theta}$ and $\hat{\phi}$ which are used to describe the polarization of the waves in the arbitrary incidence case, vary with position whereas the Cartesian coordinate unit vectors $\hat{x}$ and $\hat{y}$ which are used to describe the polarization of the waves in the normal incidence case, do not vary with position (see Appendix A). One obtains:

$$\left\{ \begin{array}{lcl} v=1 \implies & \left\{ \begin{array}{l} \left\{ \begin{array}{rcl} \theta^i = \theta^t & \rightarrow & \pi \\ \phi^i = \phi^t & = & \pi \end{array} \right\} \\ \left\{ \begin{array}{rcl} \theta^r & \rightarrow & 0 \\ \phi^r & = & \pi \end{array} \right\} \end{array} \right. & \begin{array}{l} \implies \left\{ \begin{array}{rcl} \hat{\theta}^i = \hat{\theta}^t & \rightarrow & (+\hat{x}) \\ \hat{\phi}^i = \hat{\phi}^t & = & (-\hat{y}) \end{array} \right. \\ \implies \left\{ \begin{array}{rcl} \hat{\theta}^r & \rightarrow & (-\hat{x}) \\ \hat{\phi}^r & = & (-\hat{y}) \end{array} \right. \end{array} \\ v=2 \implies & \left\{ \begin{array}{l} \left\{ \begin{array}{rcl} \theta^i = \theta^t & \rightarrow & 0 \\ \phi^i = \phi^t & = & 0 \end{array} \right\} \\ \left\{ \begin{array}{rcl} \theta^r & \rightarrow & \pi \\ \phi^r & = & 0 \end{array} \right\} \end{array} \right. & \begin{array}{l} \implies \left\{ \begin{array}{rcl} \hat{\theta}^i = \hat{\theta}^t & \rightarrow & (+\hat{x}) \\ \hat{\phi}^i = \hat{\phi}^t & = & (+\hat{y}) \end{array} \right. \\ \implies \left\{ \begin{array}{rcl} \hat{\theta}^r & \rightarrow & (-\hat{x}) \\ \hat{\phi}^r & = & (+\hat{y}) \end{array} \right. \end{array} \end{array} \right\} \tag{2.2}$$

Hence, with δ corresponding to the Kronecker delta, one obtains:

$$\left(\begin{array}{rcl} b_1^E & = & (-\delta_{sr} + \delta_{st}) b_1^X \\ b_1^H & = & (-\delta_{sr} + \delta_{st}) b_1^Y \\ b_2^E & = & (-\delta_{sr} + \delta_{st}) b_2^X \\ b_2^H & = & (+\delta_{sr} - \delta_{st}) b_2^Y \end{array} \right) = \left(\begin{array}{cccc} S_{11}^{EE} & S_{11}^{EH} & S_{12}^{EE} & S_{12}^{EH} \\ S_{11}^{HE} & S_{11}^{HH} & S_{12}^{HE} & S_{12}^{HH} \\ S_{21}^{EE} & S_{21}^{EH} & S_{22}^{EE} & S_{22}^{EH} \\ S_{21}^{HE} & S_{21}^{HH} & S_{22}^{HE} & S_{22}^{HH} \end{array} \right) \left(\begin{array}{rcl} a_1^E & = & +a_1^X \\ a_1^H & = & -a_1^Y \\ a_2^E & = & +a_2^X \\ a_2^H & = & +a_2^Y \end{array} \right)$$

$$\Longrightarrow \begin{pmatrix} b_1^E \\ b_1^H \\ b_2^E \\ b_2^H \end{pmatrix} = \begin{pmatrix} -\delta_{sr}+\delta_{st} & 0 & 0 & 0 \\ 0 & -\delta_{sr}+\delta_{st} & 0 & 0 \\ 0 & 0 & -\delta_{sr}+\delta_{st} & 0 \\ 0 & 0 & 0 & +\delta_{sr}-\delta_{st} \end{pmatrix} \begin{pmatrix} b_1^X \\ b_1^Y \\ b_2^X \\ b_2^Y \end{pmatrix}$$

$$\Longrightarrow \begin{pmatrix} a_1^E \\ a_1^H \\ a_2^E \\ a_2^H \end{pmatrix} = \begin{pmatrix} 1 & 0 & 0 & 0 \\ 0 & -1 & 0 & 0 \\ 0 & 0 & 1 & 0 \\ 0 & 0 & 0 & 1 \end{pmatrix} \begin{pmatrix} a_1^X \\ a_1^Y \\ a_2^X \\ a_2^Y \end{pmatrix}$$

Performing the required matrix manipulations, one obtains:

$$S(X,Y) = \begin{pmatrix} \frac{1}{-\delta_{sr}+\delta_{st}} S_{11}^{EE} & \frac{-1}{-\delta_{sr}+\delta_{st}} S_{11}^{EH} & \frac{1}{-\delta_{sr}+\delta_{st}} S_{12}^{EE} & \frac{1}{-\delta_{sr}+\delta_{st}} S_{12}^{EH} \\ \frac{1}{-\delta_{sr}+\delta_{st}} S_{11}^{EE} & \frac{-1}{-\delta_{sr}+\delta_{st}} S_{11}^{EH} & \frac{1}{-\delta_{sr}+\delta_{st}} S_{12}^{EE} & \frac{1}{-\delta_{sr}+\delta_{st}} S_{12}^{EH} \\ \frac{1}{-\delta_{sr}+\delta_{st}} S_{11}^{EE} & \frac{-1}{-\delta_{sr}+\delta_{st}} S_{11}^{EH} & \frac{1}{-\delta_{sr}+\delta_{st}} S_{12}^{EE} & \frac{1}{-\delta_{sr}+\delta_{st}} S_{12}^{EH} \\ \frac{1}{+\delta_{sr}-\delta_{st}} S_{11}^{EE} & \frac{-1}{+\delta_{sr}-\delta_{st}} S_{11}^{EH} & \frac{1}{+\delta_{sr}-\delta_{st}} S_{12}^{EE} & \frac{1}{+\delta_{sr}-\delta_{st}} S_{12}^{EH} \end{pmatrix}$$

Now expanding the Kronecker delta, one obtains:

$$\left\{ \begin{array}{l} \delta_{sr} = \left\{ \begin{array}{ll} 1 & u = v \\ 0 & u \neq v \end{array} \right. \\ \delta_{st} = \left\{ \begin{array}{ll} 0 & u = v \\ 1 & u \neq v \end{array} \right. \end{array} \right\} \Longrightarrow S(X,Y) = \begin{pmatrix} -S_{11}^{EE} & S_{11}^{EH} & S_{12}^{EE} & S_{12}^{EH} \\ -S_{11}^{HE} & S_{11}^{HH} & S_{12}^{HE} & S_{12}^{HH} \\ S_{21}^{EE} & -S_{21}^{EH} & -S_{22}^{EE} & -S_{22}^{EH} \\ -S_{21}^{HE} & S_{21}^{HH} & S_{22}^{HE} & S_{22}^{HH} \end{pmatrix} \quad (2.3)$$

Now, $S(X,Y)$ is symmetrical if the structure is reciprocal [37]. Therefore, $S(E,H)$ cannot be symmetrical even after normalizing the voltage travelling waves.

Hill and Cornbleet [37] have used the voltage scattering matrix in the Cartesian coordinate system to analyze the performance of linear polarization rotators at normal incidence[2] . Amitay and Saleh [38] have used the same approach to study the performance of linear polarization rotators under arbitrary incidence angles, by first

[2]This author notes in passing that a discrepancy exists in the expression for the scattering coefficient A_{14} between reference [37] and reference [1, p. 303]. This author believes the expression in reference [37] to be the correct one.

projecting the polarization vectors onto the plane of each grid composing the rotator and then proceeding as if the incidence were normal. Ando et al. in references [40, 41] have proceeded conversely by projecting the grid onto the transverse plane of the propagation vectors. Alternatively, Gimeno et al. in reference [42], Chu and Lee[3] in reference [80, 81], and Chen[4] in reference [39] have proceeded differently by decomposing the waves into E-type and H-type modes (i.e. TE and TM modes with respect to a transverse direction rather than to the longitudinal direction). These approaches are most convenient for arbitrary incidence angles only when the structure under analysis is simple like a grid made of straight wires or strips. For instance, if the incident wave is of a pure E-type or H-type mode, the wave scattered from a free-standing lossless metallic grid of infinite transverse dimensions is also of a pure E-type or H-type mode, i.e. there is no coupling between the E-type and the H-type modes [43, p. 220] [44] (see also Appendix B). This absence of type-mode coupling reduces the scattering matrix from a single 4x4 matrix to two independent 2x2 matrices since the cross-polarization coefficients written in terms of the type-modes become all zero.

For general planar structures, however, it is preferable to use the GSM in the spherical coordinate system because the choice of this coordinate system is the natural choice for describing the polarization of the waves in terms of the familiar TE^z and TM^z modes whose generality is well known (see Appendix B). This approach is followed in numerous papers [23, 24, 25, 26, 27, 28, 29, 30].

---

[3]Some confusion seems to run throughout this paper. In analyzing the meander line geometry for oblique incidence, Chu and Lee use the expressions for the E-type and the H-type modes developed by Altschuler and Goldstone in reference [43], even though this E-type mode deals with the H component perpendicular to y and this H-type mode deals with the E component perpendicular to y whereas Chu and Lee mean to analyze the geometry in terms of the E component parallel to x and the E component perpendicular to x. These two decompositions are not identical for arbitrarily oblique incidence.

[4]This author notes in passing that he has some serious reservations as to the accuracy of the modelling shown in Figure 6, p. 366, since if the inductance loading approached a short-circuit as mentioned on p. 365, the two ideal transformers in Figure 4, p. 365, would become nearly short-circuited, thereby invalidating the equivalent networks of Figure 6.

2.2.3 An Example: the Planar Dielectric Interface

To demonstrate the various aspects of the GSM framework, the example of the planar dielectric interface is presented. The Fresnel equations for the dielectric interface are most conveniently obtained from the interpretation that the transverse electric field of the TE^z mode corresponds to a voltage travelling wave whereas the transverse magnetic field of the TM^z mode corresponds to a current travelling wave.

For the TM^z mode, one obtains:

$$R^I = \frac{H_o^r}{H_o^i} = \frac{E_o^r/(-\eta^i)}{E_o^i/(+\eta^i)} = -\frac{E_o^r}{E_o^i} = \frac{Z_W^i - Z_W^t}{Z_W^i + Z_W^t}$$

$$\Longrightarrow \frac{E_o^r}{E_o^i} = -R^I = \frac{Z_W^t - Z_W^i}{Z_W^t + Z_W^i} = \frac{\varepsilon^i k_z^t - \varepsilon^t k_z^i}{\varepsilon^i k_z^t + \varepsilon^t k_z^i} = \frac{\varepsilon^i |k_z^t| - \varepsilon^t |k_z^i|}{\varepsilon^i |k_z^t| + \varepsilon^t |k_z^i|}$$

$$T^I = \frac{H_o^t}{H_o^i} = \frac{E_o^t/(+\eta^t)}{E_o^i/(+\eta^i)} = \left(\frac{\eta^i}{\eta^t}\right)\frac{E_o^t}{E_o^i} = \frac{2Z_W^i}{Z_W^i + Z_W^t}$$

$$\Longrightarrow \frac{E_o^t}{E_o^i} = \left(\frac{\eta^t}{\eta^i}\right) T^I = \left(\frac{\eta^t}{\eta^i}\right)\frac{2Z_W^i}{Z_W^t + Z_W^i} = \frac{\sqrt{\varepsilon^i\varepsilon^t}2k_z^i}{\varepsilon^i k_z^t + \varepsilon^t k_z^i} = \frac{\sqrt{\varepsilon^i\varepsilon^t}2|k_z^i|}{\varepsilon^i |k_z^t| + \varepsilon^t |k_z^i|}$$

where the superindices i and t refer to the incidence and the transmission regions, respectively, the superindex I refers to current travelling wave parameters, $\eta^l = \sqrt{\mu_o/\varepsilon^l}$ is the intrinsic impedance of the region l and $Z_W^l = k_z^l/(\omega\varepsilon^l)$ is the wave impedance of the region l with $l = \{i, t\}$.

For the TE^z mode, one obtains:

$$R^V = \frac{E_o^r}{E_o^i} = \frac{E_t^r}{E_t^i} = \frac{Z_W^t - Z_W^i}{Z_W^t + Z_W^i}$$

$$\Longrightarrow \frac{E_o^r}{E_o^i} = +R^V = \frac{Z_W^t - Z_W^i}{Z_W^t + Z_W^i} = \frac{k_z^i - k_z^t}{k_z^i + k_z^t} = \frac{|k_z^i| - |k_z^t|}{|k_z^i| + |k_z^t|}$$

$$T^V = \frac{E_o^t}{E_o^i} = \frac{E_t^t}{E_t^i} = \frac{2Z_W^t}{Z_W^t + Z_W^i}$$

$$\Longrightarrow \frac{E_o^t}{E_o^i} = T^V = \frac{2Z_W^t}{Z_W^t + Z_W^i} = \frac{2k_z^i}{k_z^i + k_z^t} = \frac{2|k_z^i|}{|k_z^i| + |k_z^t|}$$

where the superindex V refers to voltage travelling wave parameters and $Z_W^l = (\omega\mu_o)/k_z^l$.

By substituting the region number for the superindices i and t, the voltage scattering matrix $C(E,H)$ for the two ports that are in a reciprocal relationship through the interface is obtained as:

$$C(E,H) = \begin{pmatrix} \frac{\varepsilon^1|k_z^2| - \varepsilon^2|k_z^1|}{\varepsilon^1|k_z^2| + \varepsilon^2|k_z^1|} & 0 & \frac{2\sqrt{\varepsilon^2\varepsilon^1}|k_z^2|}{\varepsilon^2|k_z^1| + \varepsilon^1|k_z^2|} & 0 \\ 0 & \frac{|k_z^1| - |k_z^2|}{|k_z^1| + |k_z^2|} & 0 & \frac{2|k_z^2|}{|k_z^1| + |k_z^2|} \\ \frac{2\sqrt{\varepsilon^1\varepsilon^2}|k_z^1|}{\varepsilon^1|k_z^2| + \varepsilon^2|k_z^1|} & 0 & \frac{\varepsilon^2|k_z^1| - \varepsilon^1|k_z^2|}{\varepsilon^2|k_z^1| + \varepsilon^1|k_z^2|} & 0 \\ 0 & \frac{2|k_z^1|}{|k_z^1| + |k_z^2|} & 0 & \frac{|k_z^2| - |k_z^1|}{|k_z^2| + |k_z^1|} \end{pmatrix}$$

Now, following the concepts and formalism developed in this chapter, the corresponding $S(E,H)$ matrix can be derived from an equivalent network of transmission lines where the characteristic impedance of each transmission line corresponds to the wave impedance of the region for the mode of interest. This approach differs slightly in concept from the one above in the basis on which the network equivalence is made. In the approach above, the network equivalence is based on the field component that characterizes the mode, i.e. E_z for the TE^z mode and H_z for the TM^z mode, corresponding to a voltage and to a current travelling wave, respectively; this characteristic field component is entirely transverse. In the approach here, however, the network equivalence is based solely on the transverse part of the electric field, and this transverse part corresponds solely to a voltage travelling wave as evidenced by the ratio of solely electric field variables $(E_t^s)_u^p/(E_t^i)_v^q$.

Using the familiar transmission line formulae with $Z_o = Z_W$, one obtains:

$$R^V = \frac{E_t^r}{E_t^i} = \frac{Z_o^t - Z_o^i}{Z_o^t + Z_o^i} = \begin{cases} \frac{\varepsilon^i k_z^t - \varepsilon^t k_z^i}{\varepsilon^i k_z^t + \varepsilon^t k_z^i} = \frac{\varepsilon^i|k_z^t| - \varepsilon^t|k_z^i|}{\varepsilon^i|k_z^t| + \varepsilon^t|k_z^i|} & \text{for } TM^z \\ \frac{k_z^i - k_z^t}{k_z^i + k_z^t} = \frac{|k_z^i| - |k_z^t|}{|k_z^i| + |k_z^t|} & \text{for } TE^z \end{cases}$$

$$T^V = \frac{E_t^t}{E_t^i} = \frac{2Z_o^t}{Z_o^t + Z_o^i} = \begin{cases} \frac{2\varepsilon^i k_z^t}{\varepsilon^i k_z^t + \varepsilon^t k_z^i} = \frac{2\varepsilon^i |k_z^t|}{\varepsilon^i |k_z^t| + \varepsilon^t |k_z^i|} & \text{for } TM^z \\ \frac{2k_z^i}{k_z^i + k_z^t} = \frac{2|k_z^i|}{|k_z^i| + |k_z^t|} & \text{for } TE^z \end{cases}$$

By substituting the region number for the superindices i and t, one obtains the voltage scattering matrix $S(E,H)$ as:

$$S(E,H) = \begin{pmatrix} \frac{\varepsilon^1|k_z^2| - \varepsilon^2|k_z^1|}{\varepsilon^1|k_z^2| + \varepsilon^2|k_z^1|} & 0 & \frac{2\varepsilon^2|k_z^1|}{\varepsilon^2|k_z^1| + \varepsilon^1|k_z^2|} & 0 \\ 0 & \frac{|k_z^1| - |k_z^2|}{|k_z^1| + |k_z^2|} & 0 & \frac{2|k_z^2|}{|k_z^1| + |k_z^2|} \\ \frac{2\varepsilon^1|k_z^2|}{\varepsilon^1|k_z^2| + \varepsilon^2|k_z^1|} & 0 & \frac{\varepsilon^2|k_z^1| - \varepsilon^1|k_z^2|}{\varepsilon^2|k_z^1| + \varepsilon^1|k_z^2|} & 0 \\ 0 & \frac{2|k_z^1|}{|k_z^1| + |k_z^2|} & 0 & \frac{|k_z^2| - |k_z^1|}{|k_z^2| + |k_z^1|} \end{pmatrix}$$

Now since one has:

$$\frac{|cos(\theta_1^t)|}{|cos(\theta_2^i)|} = \frac{|k_z^1|/k_o^1}{|k_z^2|/k_o^2} = \frac{k_o^2}{k_o^1}\frac{|k_z^1|}{|k_z^2|} = \sqrt{\frac{\varepsilon^2}{\varepsilon^1}}\frac{|k_z^1|}{|k_z^2|}$$

and similarly:

$$\frac{|cos(\theta_2^t)|}{|cos(\theta_1^i)|} = \frac{|k_z^2|/k_o^2}{|k_z^1|/k_o^1} = \frac{k_o^1}{k_o^2}\frac{|k_z^2|}{|k_z^1|} = \sqrt{\frac{\varepsilon^1}{\varepsilon^2}}\frac{|k_z^2|}{|k_z^1|}$$

thus, one has:

$$\begin{aligned} \frac{|cos(\theta_1^t)|}{|cos(\theta_2^i)|} C_{12}^{EE} &= \sqrt{\frac{\varepsilon^2}{\varepsilon^1}}\frac{|k_z^1|}{|k_z^2|}\frac{2\sqrt{\varepsilon^2\varepsilon^1}|k_z^2|}{\varepsilon^2|k_z^1| + \varepsilon^1|k_z^2|} \\ &= \frac{2\varepsilon^2|k_z^1|}{\varepsilon^2|k_z^1| + \varepsilon^1|k_z^2|} \\ &= S_{12}^{EE} \end{aligned}$$

$$\begin{aligned}\frac{|cos(\theta_2^t)|}{|cos(\theta_1^i)|}C_{21}^{EE} &= \sqrt{\frac{\varepsilon^1}{\varepsilon^2}}\frac{\left|k_z^2\right|}{\left|k_z^1\right|}\frac{2\sqrt{\varepsilon^1\varepsilon^2}\left|k_z^1\right|}{\varepsilon^1\left|k_z^2\right|+\varepsilon^2\left|k_z^1\right|} \\ &= \frac{2\varepsilon^1\left|k_z^2\right|}{\varepsilon^1\left|k_z^2\right|+\varepsilon^2\left|k_z^1\right|} \\ &= S_{21}^{EE}\end{aligned}$$

This confirms the relation that was developed between the matrices $C(E,H)$ and $S(E,H)$. For the case of normal incidence, one has:

$$k_z = k_o \Longrightarrow \left\{ \begin{array}{l} \varepsilon^2\left|k_z^1\right| = \omega\sqrt{\mu_o\varepsilon^1}\varepsilon^2 = \sqrt{\varepsilon^2\varepsilon^1}\left|k_z^2\right| \\ \varepsilon^1\left|k_z^2\right| = \omega\sqrt{\mu_o\varepsilon^2}\varepsilon^1 = \sqrt{\varepsilon^1\varepsilon^2}\left|k_z^1\right| \end{array} \right\} \Longrightarrow S(E,H) \equiv C(E,H)$$

as expected since at normal incidence one has:

$$\frac{|cos(\theta_1^t)|}{|cos(\theta_2^i)|} = 1 = \frac{|cos(\theta_2^t)|}{|cos(\theta_1^i)|}$$

The matrix $C(E,H)$ (or $S(E,H)$ in the case of normal incidence) would not be symmetrical even if the order of the incidence waves had been changed and although all cross-polarization scattering coefficients are zero, because the voltage travelling waves have not been normalized and because $S(E,H) \neq S(X,Y)$.

This author notes in passing that from the above expressions, it appears that the expressions given by Hall et al. [23, p. 513] for the transmission coefficients of a planar dielectric interface are in error by the factor $|k_z^2/k_z^1|^{\pm\frac{1}{2}}$.

2.2.4 Composite Scattering Matrix

This section presents the development of the composite scattering matrix resulting from the series combination of two scattering matrices separated by a transmission line of length d. Such a combination is apt to model any two transverse discontinuities separated in the longitudinal direction by a distance d where $0 \leq d \leq \infty$.

This development is important because an entire planar multilayer structure can be modelled by a single scattering matrix by applying successively the composite technique to any two consecutive matrices modelling two consecutive planar interfaces or layers, thereby reducing the number of scattering matrices by one with each successive application of the technique until only one matrix remains. It is from this single overall composite scattering matrix that the characteristics of a general multilayer structure are then investigated by obtaining the constraints placed on the elements of the matrix by a particular operation prescribed for the structure.

This technique extends readily to the generalized scattering matrix by taking each element of the matrix to be a submatrix to represent the co-polarization and the cross-polarization coefficients, with these submatrices being themselves submatrices to represent the different spatial harmonics, either propagating or evanescent. This format, which was adopted earlier by rearranging the terms of the matrices, lends itself readily to generalization to any number of ports, one port per spatial direction in each region. Consequently, this development is carried out with each scattering element being treated as a submatrix. Figure 2.5 depicts the case under study.

One has:

$$\begin{pmatrix} b_1^I \\ b_2^I \end{pmatrix} = \begin{pmatrix} S_{11}^I & S_{12}^I \\ S_{21}^I & S_{22}^I \end{pmatrix} \begin{pmatrix} a_1^I \\ a_2^I \end{pmatrix}$$

$$\begin{pmatrix} b_1^{II} \\ b_2^{II} \end{pmatrix} = \begin{pmatrix} S_{11}^{II} & S_{12}^{II} \\ S_{21}^{II} & S_{22}^{II} \end{pmatrix} \begin{pmatrix} a_1^{II} \\ a_2^{II} \end{pmatrix}$$

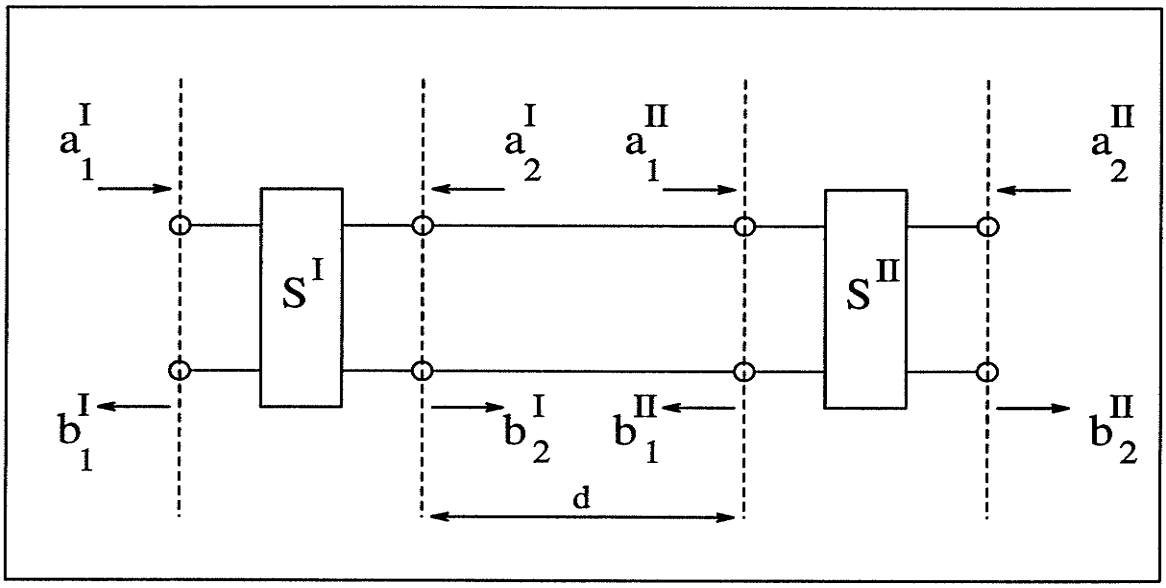

Figure 2.5: The series connection of two scattering matrices separated by a transmission line of length d.

$$\begin{pmatrix} a_1^{II} \\ a_2^{I} \end{pmatrix} = \begin{pmatrix} e^{-jk_z d} & 0 \\ 0 & e^{-jk_z d} \end{pmatrix} \begin{pmatrix} b_2^{I} \\ b_1^{II} \end{pmatrix}$$

$$\begin{pmatrix} b_1^{I} \\ b_2^{II} \end{pmatrix} = \begin{pmatrix} S_{11}^{\Sigma} & S_{12}^{\Sigma} \\ S_{21}^{\Sigma} & S_{22}^{\Sigma} \end{pmatrix} \begin{pmatrix} a_1^{I} \\ a_2^{II} \end{pmatrix}$$

From simple matrix manipulations, the submatrix elements of the composite scattering matrix are obtained as:

$$\begin{aligned} S_{11}^{\Sigma} &= S_{11}^{I} + S_{12}^{I} H_2 S_{11}^{II} P S_{21}^{I} \\ S_{12}^{\Sigma} &= S_{12}^{I} H_2 S_{12}^{II} \\ S_{21}^{\Sigma} &= S_{21}^{II} H_1 S_{21}^{I} \\ S_{22}^{\Sigma} &= S_{22}^{II} + S_{21}^{II} H_1 S_{22}^{I} P S_{12}^{II} \end{aligned}$$

where:

$$\begin{aligned} P &= e^{-jk_z d} I \\ H_1 &= (P^{-1} - S_{22}^{I} P S_{11}^{II})^{-1} \\ H_2 &= (P^{-1} - S_{11}^{II} P S_{22}^{I})^{-1} \end{aligned}$$

with I representing the identity matrix.

All these expressions, except that for S_{21}^{Σ}, agree with those given by Cwik and Mittra [24, 26]. The expression for S_{21}^{Σ} reported in both papers as $S_{\gamma\alpha}^{\Sigma}$ contains, however, the same two typographical errors. $S_{\gamma\alpha}^{\Sigma}$ should read as being equal to $S_{\gamma\beta_2}H_1S_{\beta_1\alpha}$ instead of $S_{\alpha\beta_2}H_1S_{\beta_2\alpha}$.

The composite matrix technique is readily extended to the arbitrary incidence case by augmenting each matrix to include all eight waves. There obtains with $n = \{I, II\}$:

$$\begin{pmatrix} b_1^n \\ b_3^n \\ b_2^n \\ b_4^n \end{pmatrix} = \begin{pmatrix} S_{11}^n & S_{13}^n & S_{12}^n & S_{14}^n \\ S_{31}^n & S_{33}^n & S_{32}^n & S_{34}^n \\ S_{21}^n & S_{23}^n & S_{22}^n & S_{24}^n \\ S_{41}^n & S_{43}^n & S_{42}^n & S_{44}^n \end{pmatrix} \begin{pmatrix} a_1^n \\ a_3^n \\ a_2^n \\ a_4^n \end{pmatrix}$$

$$\begin{pmatrix} a_1^{II} \\ a_3^{II} \\ a_2^{I} \\ a_4^{I} \end{pmatrix} = \begin{pmatrix} e^{-jk_zd} & 0 & 0 & 0 \\ 0 & e^{-jk_zd} & 0 & 0 \\ 0 & 0 & e^{-jk_zd} & 0 \\ 0 & 0 & 0 & e^{-jk_zd} \end{pmatrix} \begin{pmatrix} b_2^{I} \\ b_4^{I} \\ b_1^{II} \\ b_3^{II} \end{pmatrix}$$

The solution is formally the same as before upon regrouping as follows:

$$\beta_1^n = \begin{pmatrix} b_1^n \\ b_3^n \end{pmatrix} \quad \text{and} \quad \beta_2^n = \begin{pmatrix} b_2^n \\ b_4^n \end{pmatrix}$$

$$\alpha_1^n = \begin{pmatrix} a_1^n \\ a_3^n \end{pmatrix} \quad \text{and} \quad \alpha_2^n = \begin{pmatrix} a_2^n \\ a_4^n \end{pmatrix}$$

$$\mathcal{S}_{11}^n = \begin{pmatrix} S_{11}^n & S_{13}^n \\ S_{31}^n & S_{33}^n \end{pmatrix} \quad \text{and} \quad \mathcal{S}_{12}^n = \begin{pmatrix} S_{12}^n & S_{14}^n \\ S_{32}^n & S_{34}^n \end{pmatrix}$$

$$\mathcal{S}_{21}^n = \begin{pmatrix} S_{21}^n & S_{23}^n \\ S_{41}^n & S_{43}^n \end{pmatrix} \quad \text{and} \quad \mathcal{S}_{22}^n = \begin{pmatrix} S_{22}^n & S_{24}^n \\ S_{42}^n & S_{44}^n \end{pmatrix}$$

$$\begin{aligned} \mathcal{H}_1 &= (P^{-1} - \mathcal{S}_{22}^I P \mathcal{S}_{11}^{II})^{-1} \\ \mathcal{H}_2 &= (P^{-1} - \mathcal{S}_{11}^{II} P \mathcal{S}_{22}^I)^{-1} \end{aligned}$$

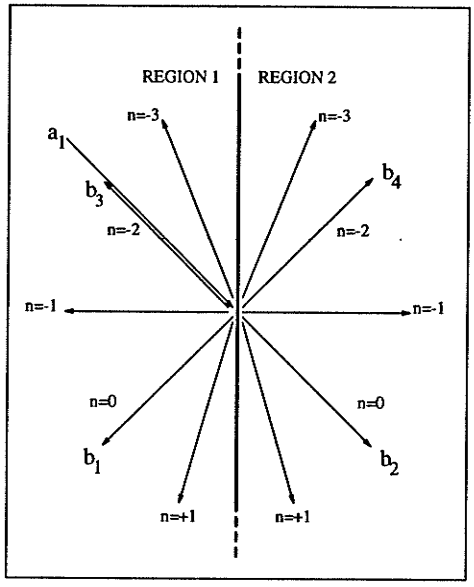

Figure 2.6: The case of treating the principal waves as if they corresponded to spatial harmonics.

and performing the obvious change of symbols, i.e. $\mathcal{S}$ in place of S, and $\mathcal{H}$ in place of H.

Alternatively, the solution remains identically the same if the eight waves are treated as if they were spatial harmonics, since the incorporation of a higher order mode augments also each matrix in the same way. In other words, the mathematical computation would remain numerically the same if the eight waves were treated as being various spatial harmonics. Figure 2.6 depicts the arbitrary case where the principal waves b_1 and b_2 would correspond to the spatial harmonics of order $n = 0$, and the principal waves b_3 and b_4 would correspond to the spatial harmonics of order $n = -2$. Thirdly, this formalism can also be justified on the basis that the use of the equivalent transmission line allows the use of only four rather than eight waves, as mentioned earlier.

The above technique is, in principle, exact if the number of spatial harmonics is allowed to be infinite. In practice, however, one must necessarily truncate the matrix to a finite size, thereby introducing an approximation in the modelling of the system. Hence, to avoid dealing with a large number of evanescent modes, many

researchers [25, 27, 28] recommend not to model a planar surface mounted on a dielectric slab as a series connection of the free standing structure and the dielectric slab. The number of spatial waves is also infinite when the scattering surface is of finite size owing to the angular spreading of the beam incurred by the spatial windowing effect, as mentioned earlier. For this reason, the GSM written in terms of plane waves is not very practical for finite size surfaces.

Most authors proceed differently in obtaining the scattering matrix of a system. In a first step, they transform the scattering matrix of each subsystem into a corresponding transmission matrix. Then they multiply the transmission matrices of all the subsystems to obtain the composite transmission matrix of the whole system. Finally they transform this composite transmission matrix back into a scattering matrix. Mittra et al. [26, p. 1608] report, however, that the transmission matrix approach is sometimes numerically unstable.

2.2.5 Principles and Notation

For notational convenience, it is assumed hereafter that:

$$C_{uv}^{pq} = C_{ij}^{bd} \Longleftrightarrow C_{uv}^{pq}(\theta^s, \phi^s|\theta^i, \phi^i) = C_{ij}^{bd}(\theta^s, \phi^s|\theta^i, \phi^i)$$

where the angle dependence is the same for both scattering coefficients, as indicated by the context descriptor $(\theta^s, \phi^s|\theta^i, \phi^i)$.

Various principles [30, 31, 32, 33, 34, 35, 36] are expressed in this section. Figure 2.7 depicts the reciprocity principle. Since the physical interpretation of enforcing the reciprocity principle consists in reversing all propagation vectors while maintaining their respective polarization, one finds with this symbolism and notational convention (see Appendix A and $u, v = \{1, 2\}$ where 1 and 2 represents the labels of two generic ports, each port corresponding to any direction irrespectively of the region) that the process of reversing all propagation vectors results in:

$$\begin{cases} (E_o^r)_v^p(\theta^r, \phi^r) & \rightarrow & \epsilon_V^r (E_o^i)_v^p(\pi - \theta^r, \pi + \phi^r) \\ (E_o^t)_u^p(\theta^t, \phi^t) & \rightarrow & \epsilon_V^t (E_o^i)_u^p(\pi - \theta^t, \pi + \phi^t) \\ (E_o^i)_v^q(\theta^i, \phi^i) & \rightarrow & \begin{cases} \epsilon_V^i (E_o^r)_v^q(\pi - \theta^i, \pi + \phi^i) & \text{for } s = r \\ \epsilon_V^i (E_o^t)_v^q(\pi - \theta^i, \pi + \phi^i) & \text{for } s = t \end{cases} \end{cases}$$

for $(E_o^i)_w^l = 0, w \neq \{u, v\}, l = \{E, H\}$ and where:

$$\epsilon_V^l = \left\{ \begin{array}{ll} +1 & \text{if the wave is } E^z\text{-polarized} \\ -1 & \text{if the wave is } H^z\text{-polarized} \end{array} \right\} \text{ with } l = \{i, r, t\}$$

owing to the inversion in $\hat{\phi}$ incurred with the 180° rotation in ϕ upon reversing the direction of the propagation vectors (see Figure 2.8 for an example). Hence, for the reflected wave, one obtains:

$$\begin{aligned} C_{vv}^{pq}(\theta^r, \phi^r|\theta^i, \phi^i) &= \frac{(E_o^r)_v^p(\theta^r, \phi^r)}{(E_o^i)_v^q(\theta^i, \phi^i)} \diagup\!\!\!\diagdown \frac{\epsilon_V^i (E_o^r)_v^q(\pi - \theta^i, \pi + \phi^i)}{\epsilon_V^r (E_o^i)_v^p(\pi - \theta^r, \pi + \phi^r)} \\ &= \epsilon_H C_{vv}^{qp}(\pi - \theta^i, \pi + \phi^i|\pi - \theta^r, \pi + \phi^r) \end{aligned}$$

for $(E_o^i)_w^l = 0, w \neq v, l = \{E, H\}$, and where:

$$\epsilon_H = \left\{ \begin{array}{ll} +1 & \text{if } p = q \\ -1 & \text{if } p \neq q \end{array} \right.$$

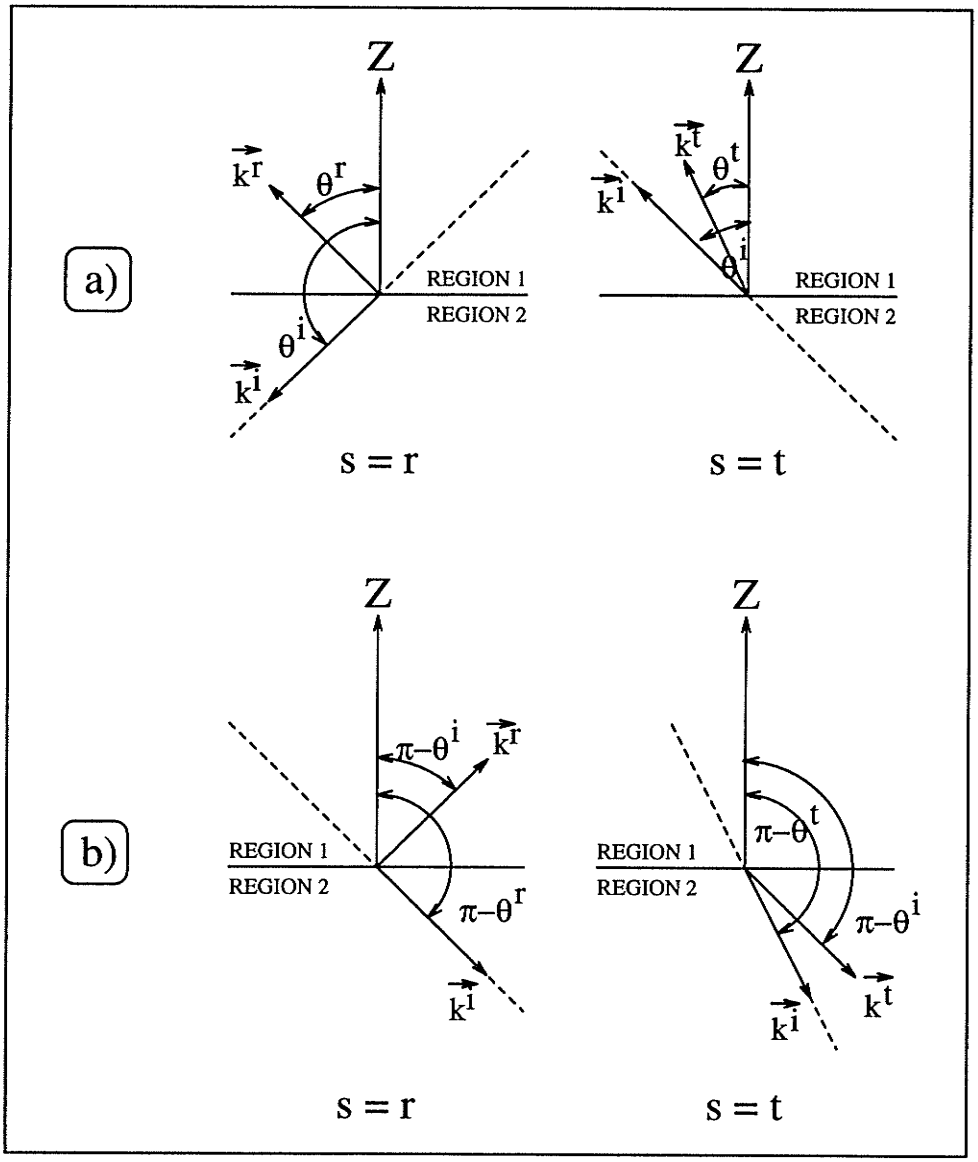

Figure 2.7: The depiction of the situation corresponding a) to $C_{uv}^{pq}(\theta^s, \phi^s|\theta^i, \phi^i)$ and b) to $C_{vu}^{qp}(\pi-\theta^i, \pi+\phi^i|\pi-\theta^s, \pi+\phi^s)$, for both cases of $s = r$ and $s = t$.

Similarly for the transmitted wave, one obtains:

$$C_{uv}^{pq}(\theta^t,\phi^t|\theta^i,\phi^i) = \frac{(E_o^t)_u^p(\theta^t,\phi^t)}{(E_o^i)_v^q(\theta^i,\phi^i)} \times \frac{\epsilon_V^i(E_o^t)_v^q(\pi-\theta^i,\pi+\phi^i)}{\epsilon_V^t(E_o^i)_u^p(\pi-\theta^t,\pi+\phi^t)}$$
$$= \epsilon_H C_{vu}^{qp}(\pi-\theta^i,\pi+\phi^i|\pi-\theta^t,\pi+\phi^t)$$

for $(E_o^i)_w^l = 0, w \neq u, l = \{E,H\}$. Therefore, the reciprocity principle of electromagnetism can be expressed as:

$$C_{uv}^{pq}(\theta^s,\phi^s|\theta^i,\phi^i) = \epsilon_H C_{vu}^{qp}(\pi-\theta^i,\pi+\phi^i|\pi-\theta^s,\pi+\phi^s)$$

Thus generally, every voltage scattering coefficient C_{uv}^{pq} involving one and only one H-polarized wave, i.e. $p \neq q$, has a "-" sign in the formulation of the reciprocity principle because of the inversion in $\hat{\phi}$ incurred with the 180^o rotation in ϕ upon reversing the direction of the propagation vectors (see Figure 2.8 for an example). When both waves are H-polarized however, the ratio of the two waves remains unaffected because both waves incur a change of sign. This complication arises with the reciprocity principle because in the process of reversing all propagation vectors, the electric field components must remain the same in magnitude and in phase irrespectively of the variation of the spherical coordinate unit vectors with the position.

The factor ϵ_H is also required for the principle of reflection symmetry, either transverse or longitudinal. For the transverse reflection symmetry about a plane $y = tan(\chi)x$, the complication consists in that although the real image of each wave has, say, $\hat{E}_\phi^+ = +\hat{\phi}^+$, however, the corresponding virtual image has then $\hat{E}_\phi^- = -\hat{\phi}^-$ (see Figure 2.9). Similarly, for the longitudinal reflection symmetry about the plane $z = 0$, although the real image of each wave has, say, $\hat{E}_\theta^+ = +\hat{\theta}^+$, however, the corresponding virtual image has then $\hat{E}_\theta^- = -\hat{\theta}^-$ (see Figure 2.10).

In summary, the various principles, for both cases $p = q$ and $p \neq q$, are:

- Reciprocity principle of electromagnetism:

$$C_{uv}^{pq}(\theta^s,\phi^s|\theta^i,\phi^i) = \epsilon_H C_{vu}^{qp}(\pi-\theta^i,\pi+\phi^i|\pi-\theta^s,\pi+\phi^s)$$

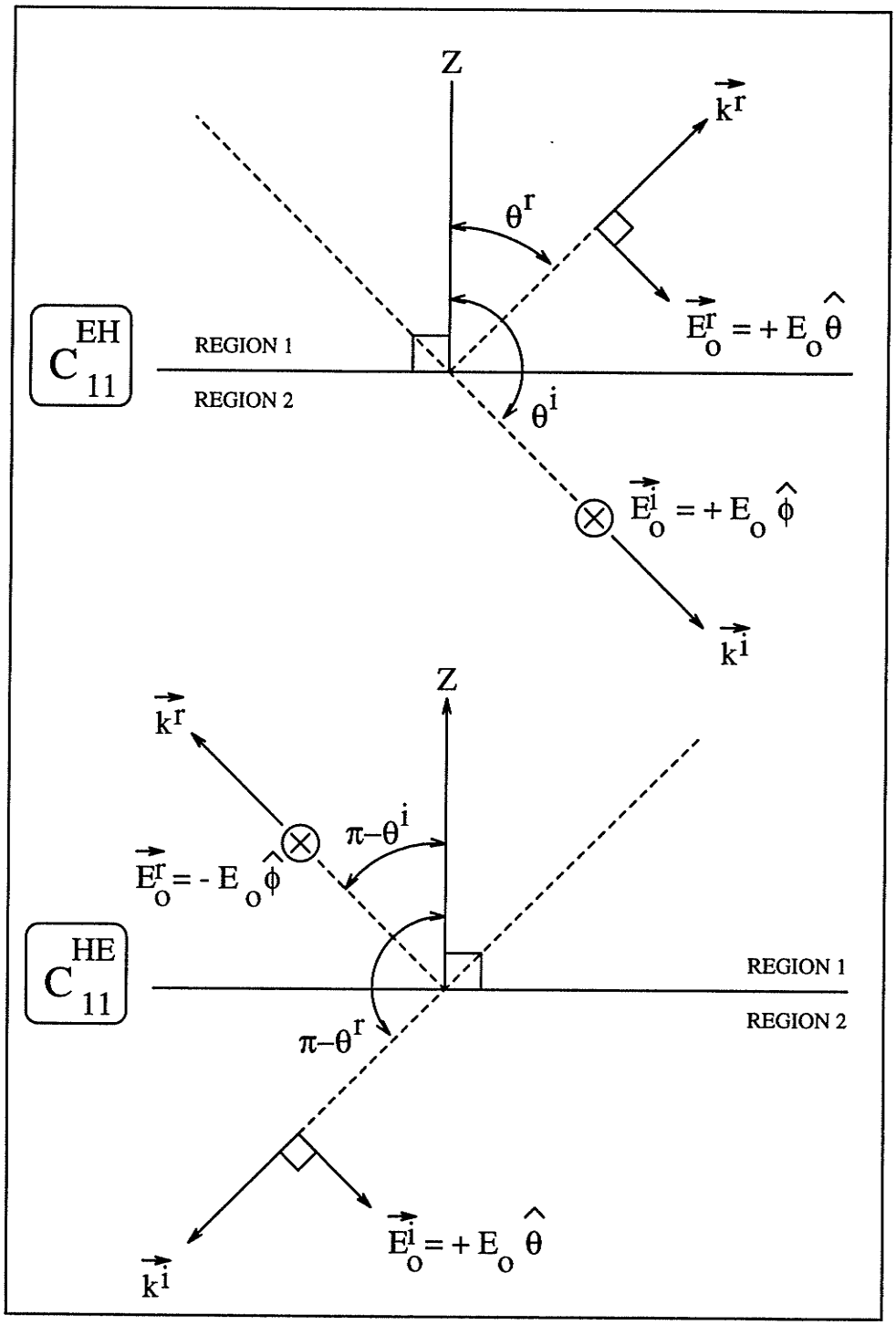

Figure 2.8: The formulation of the reciprocity principle incurs a "-" sign whenever one and only one of the two waves whose ratio forms the voltage scattering coefficient is a H-polarized wave.

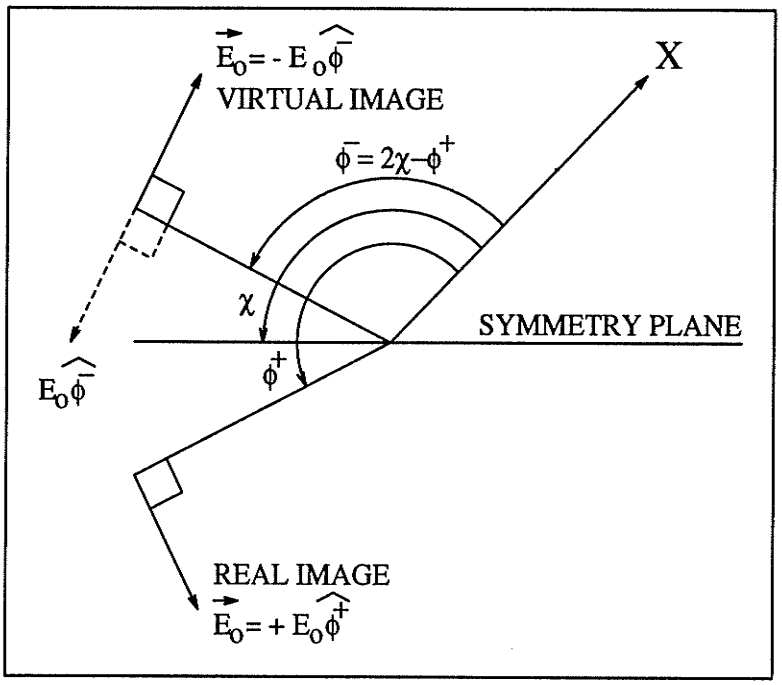

Figure 2.9: Two waves in a transverse reflection symmetry relationship.

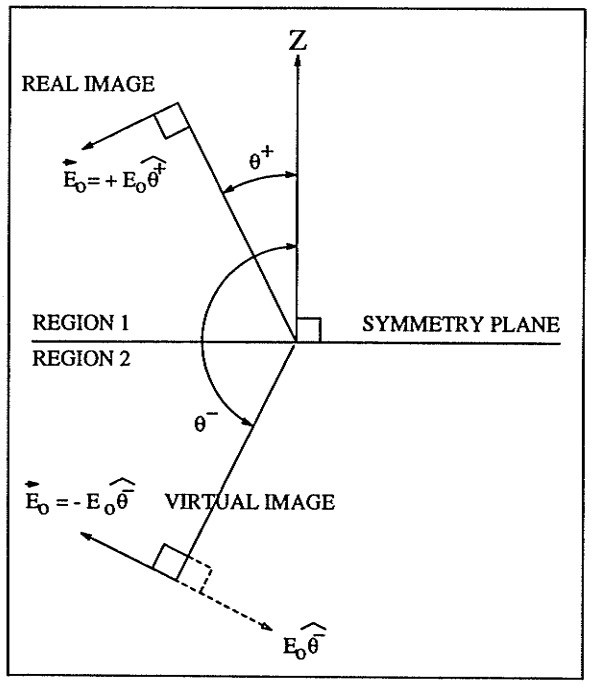

Figure 2.10: Two waves in a longitudinal reflection symmetry relationship.

This expression with $u = v$ and $p \neq q$ corresponds to that given by Whites and Mittra in reference [30, eqn. 13].

- Longitudinal reflection symmetry about the $z = 0$ plane, with u and v pertaining to different regions:

$$u \neq v \begin{cases} \text{transmission:} & C_{uv}^{pq}(\theta^t, \phi^t | \theta^i, \phi^i) = \epsilon_H C_{vu}^{pq}(\pi - \theta^t, \phi^t | \pi - \theta^i, \phi^i) \\ \text{reflection:} & C_{uu}^{pq}(\theta^r, \phi^r | \theta^i, \phi^i) = \epsilon_H C_{vv}^{pq}(\pi - \theta^r, \phi^r | \pi - \theta^i, \phi^i) \end{cases}$$

- Transverse reflection symmetry about a plane $y = tan(\chi)x$:

$$\begin{cases} C_{uv}^{pq}(\theta^s, \phi^s | \theta^i, \phi^i) = \epsilon_H C_{uv}^{pq}(\theta^s, 2\chi - \phi^s | \theta^i, 2\chi - \phi^i) \\ C_{uv}^{pq}(\theta^s, \phi^s = \chi + m\pi | \theta^i, \phi^i = \chi + m\pi) = 0 \text{ for } p \neq q \text{ and } m = 0, \pm 1, \pm 2, \ldots. \end{cases}$$

The first expression corresponds to that given by Whites and Mittra in reference [30, eqn. 27 & 28]. The second expression is a specific case of the first one and corresponds to the expression given by Whites and Mittra in reference [30, eqn. 30].

- n-fold rotational symmetry:

$$C_{uv}^{pq}(\theta^s, \phi^s | \theta^i, \phi^i) = C_{uv}^{pq}(\theta^s, \phi^s + (2\pi/n) | \theta^i, \phi^i + (2\pi/n))$$

- Both reciprocity and longitudinal reflection symmetry, for transmission and $u \neq v$:

$$\begin{aligned} C_{uv}^{pq}(\theta^t, \phi^t | \theta^i, \phi^i) &= \epsilon_H C_{vu}^{qp}(\pi - \theta^i, \pi + \phi^i | \pi - \theta^t, \pi + \phi^t) \\ &= (\epsilon_H)^2 C_{uv}^{qp}(\pi - (\pi - \theta^i), (\pi + \phi^i) | \pi - (\pi - \theta^t), (\pi + \phi^t)) \\ &= C_{uv}^{qp}(\theta^i, \pi + \phi^i | \theta^t, \pi + \phi^t) \end{aligned}$$

Both reciprocity and longitudinal reflection symmetry, for reflection and $u \neq v$:

$$\begin{aligned} C_{uu}^{pq}(\theta^r, \phi^r | \theta^i, \phi^i) &= \epsilon_H C_{uu}^{qp}(\pi - \theta^i, \pi + \phi^i | \pi - \theta^r, \pi + \phi^r) \\ &= (\epsilon_H)^2 C_{vv}^{qp}(\pi - (\pi - \theta^i), (\pi + \phi^i) | \pi - (\pi - \theta^r), (\pi + \phi^r)) \\ &= C_{vv}^{qp}(\theta^i, \pi + \phi^i | \theta^r, \pi + \phi^r) \end{aligned}$$

Adding $2n$-fold rotational symmetry to the combination produces:

$$u \neq v \begin{cases} \text{transmission:} & C_{uv}^{pq}(\theta^t, \phi^t | \theta^i, \phi^i) = C_{uv}^{qp}(\theta^i, \phi^i | \theta^t, \phi^t) \\ \text{reflection:} & C_{uu}^{pq}(\theta^r, \phi^r | \theta^i, \phi^i) = C_{vv}^{qp}(\theta^i, \phi^i | \theta^r, \phi^r) \end{cases}$$

Adding Snell's law of refraction, with $\theta^t = \theta^i$, to the combination produces, for transmission and $u \neq v$:

$$C_{uv}^{pq}(\theta^t, \phi^t|\theta^i, \phi^i) = C_{uv}^{qp}(\theta^t, \phi^t|\theta^i, \phi^i) \Longrightarrow C_{uv}^{pq} = C_{uv}^{qp}$$

- Both reciprocity and Snell's law of reflection, i.e. $\theta^r = \pi - \theta^i$ and $\phi^r = \phi^i$:

$$\begin{aligned} C_{vv}^{pq}(\theta^r, \phi^r|\theta^i, \phi^i) &= \epsilon_H C_{vv}^{qp}(\pi - \theta^i, \pi + \phi^i|\pi - \theta^r, \pi + \phi^r) \\ &= \epsilon_H C_{vv}^{qp}(\theta^r, \pi + \phi^r|\theta^i, \pi + \phi^i) \end{aligned}$$

Note: When $p = q$, hence when $\epsilon_H = +1$, one might be tempted to think that this last equality is a statement of the 2-fold rotational symmetry with $u = v$. However, if one were to think that way, one would reach the conclusion that when $p = q$ the combination of reciprocity and Snell's law of reflection implies the 2-fold rotational symmetry. By running the mathematical development backward, one would also reach the startling conclusion that when $p = q$ the combination of the 2-fold rotational symmetry and Snell's law of reflection implies reciprocity, i.e. the startling conclusion that a passive structure would not be reciprocal unless it has the 2-fold rotational symmetry. Such a conclusion, however, would be erroneous because the statement of the 2-fold rotational symmetry must also deal with the case for $p \neq q$, not just with the case for $p = q$ as with the last development.

Adding the $2n$-fold rotational symmetry to the combination produces:

$$C_{vv}^{pq}(\theta^r, \phi^r|\theta^i, \phi^i) = \epsilon_H C_{vv}^{qp}(\theta^r, \phi^r|\theta^i, \phi^i) \Longrightarrow C_{vv}^{pq} = \epsilon_H C_{vv}^{qp}$$

This expression with $p \neq q$ corresponds to the result given by Whites and Mittra in reference [30, eqn. 15]. The result for $p = q$ is just an identity.

However, it must be pointed out that, for the case of normal incidence, one has $S_{vv}^{pq} = -S_{vv}^{qp}$ even if the reciprocal structure is not endowed with the property of $2n$-fold rotational symmetry. This situation owes to the fact that reciprocity

implies that $S(X,Y)$ be symmetrical, and to the relationships between $S(X,Y)$ and $S(E,H)$ given in equation (2.3). For instance, one has:

$$\left.\begin{array}{l} S(X,Y) \text{ is symmetrical} \Longrightarrow S_{11}^{XY} = S_{11}^{YX} \\ \text{equation (2.3)} \Longrightarrow \left\{\begin{array}{l} S_{11}^{XY} = +S_{11}^{EH} \\ S_{11}^{YX} = -S_{11}^{HE} \end{array}\right. \end{array}\right\} \Longrightarrow S_{11}^{EH} = -S_{11}^{HE}$$

Now, it does not seem reasonable that for a reciprocal structure without the $2n$-fold rotational symmetry, the transition between the relationship $C_{vv}^{pq} = -C_{vv}^{qp}$ at precisely normal incidence, and the relationship $C_{vv}^{pq} \neq -C_{vv}^{qp}$ for just a small departure from normal incidence would be abrupt. However, a smooth transition would imply that all reciprocal structures, regardless of whether or not they are endowed with the property of $2n$-fold rotational symmetry, would obey the relationship $C_{vv}^{pq} \approx -C_{vv}^{qp}$ within a certain tolerance over a limited range of incidence angles centered about the normal incidence. As it will be shown later in the validation section, this situation is indeed the case and it brings about an important consequence in the synthesis process treated at the end of this section.

- The combination of reciprocity, Snell's law of refraction with $\theta^t = \theta^i$, and $2n$-fold rotational symmetry produces, for transmission and $u \neq v$:

$$\begin{aligned} C_{uv}^{pq}(\theta^t, \phi^t | \theta^i, \phi^i) &= \epsilon_H C_{vu}^{qp}(\pi - \theta^i, \pi + \phi^i | \pi - \theta^t, \pi + \phi^t) \\ &= \epsilon_H C_{vu}^{qp}(\pi - \theta^t, \pi + \phi^t | \pi - \theta^i, \pi + \phi^i) \\ &= \epsilon_H C_{vu}^{qp}(\pi - \theta^t, \phi^t | \pi - \theta^i, \phi^i) \end{aligned}$$

Note: At this point, one might be tempted to think that when $p = q$ this last equality is a statement of the longitudinal reflection symmetry. However, if one were to think that way, one would reach the conclusion that when $p = q$ the combination of reciprocity, Snell's law of refraction with $\theta^t = \theta^i$, and 2-fold rotational symmetry implies the longitudinal reflection symmetry. By running the mathematical development backward, one would also reach the startling

conclusion that when $p = q$ the combination of longitudinal reflection symmetry, 2-fold rotational symmetry and Snell's law of refraction with $\theta^t = \theta^i$, implies reciprocity, i.e. the startling conclusion that a passive structure would not be reciprocal unless it has the 2-fold rotational symmetry and the longitudinal reflection symmetry. Such a conclusion, however, would be erroneous because the statement of longitudinal reflection symmetry must also deal with the statement about reflection, i.e. $u = v$, not just with the statement about transmission, i.e. $u \neq v$, as with the last development.

Adding longitudinal reflection symmetry to the combination produces:

$$u \neq v \left\{ \begin{array}{rcl} C_{uv}^{pq}(\theta^t, \phi^t | \theta^i, \phi^i) & = & (\epsilon_H)^2 C_{uv}^{qp}(\theta^t, \phi^t | \theta^i, \phi^i) \\ & = & C_{uv}^{qp}(\theta^t, \phi^t | \theta^i, \phi^i) \end{array} \right\} \Longrightarrow C_{uv}^{pq} = C_{uv}^{qp}$$

This result was obtained previously by invoking the same principles but in a different order. This result agrees also with that given by Whites and Mittra in reference [30, eqn. 18]. It must be pointed out, however, that their development relies on the structure being infinitely thin which condition is quite restrictive whereas the development here relies, instead, on using the combination of longitudinal reflection symmetry and Snell's law of refraction with $\theta^t = \theta^i$.

For analysis purposes, these relations are very useful as it will be seen later. For synthesis purposes, it would be equally useful to determine if the converse of these relations hold, i.e. if these relations are one-to-one. However, to prove that the converse holds, it is not sufficient to run the mathematical developments backward. For instance, running backward the mathematical development for the statement $C_{vv}^{pq} = \epsilon_H C_{vv}^{qp}$ says nothing about the case for C_{uv}^{pq} with $u \neq v$, which case must be dealt with for assessing whether reciprocity and $2n$-fold rotational symmetry hold individually. Hence mathematically, one can be definite only in the negative, i.e. only if $C_{vv}^{pq} \neq \epsilon_H C_{vv}^{qp}$ can one be sure that not all principles invoked in the development are completely satisfied, whereas if $C_{vv}^{pq} = \epsilon_H C_{vv}^{qp}$, one cannot be sure that all principles

invoked in the development are completely satisfied.

Generally speaking, it does not seem feasible that a translucent surface could display a $2n$-fold rotational symmetric response upon reflection but not so upon transmission, since the reflection and the transmission responses of a translucent structure depend both on the constitutive parameters throughout the entire structure. For instance, at a dielectric interface, one has:

$$\left.\begin{array}{lcll} C_{uv}^{pq} & = & 0 & \text{for } p \neq q \\ 1 + C_{vv}^{HH} & = & C_{uv}^{HH} & \text{for } u \neq v \\ 1 + C_{vv}^{EE} & = & \frac{|cos(\theta_u^i)|}{|cos(\theta_v^i)|} C_{uv}^{EE} & \text{for } u \neq v \end{array}\right\} \quad \text{for} \quad \left\{\begin{array}{lcl} \{p,q\} & = & \{E,H\} \\ \{u,v\} & = & \{1,2,3,4\} \end{array}\right.$$

Thus, if C_{vv}^{pp} displays a $2n$-fold rotational symmetry, so does C_{uv}^{pp} and vice versa. The situation is similar for a dielectric slab since the GSM for the whole slab is the composite matrix of the GSM for each dielectric interface and the matrix for the transmission line modelling the homogeneous dielectric medium.

Therefore, since running backward the mathematical development for the statement $C_{vv}^{pq} = \epsilon_H C_{vv}^{qp}$ implies that the statement:

$$C_{uv}^{pq}(\theta^s, \phi^s | \theta^i, \phi^i) = C_{uv}^{pq}(\theta^s, \phi^s + \pi | \theta^i, \phi^i + \pi)$$

holds true for $u = v$ and since, if this last statement holds true for $u = v$, then, in practice, it holds true for $u \neq v$ as well, this author believes that, *in practice*, the statement $C_{vv}^{pq} = \epsilon_H C_{vv}^{qp}$ is indeed sufficient for a passive structure obeying Snell's law of reflection to be endowed with the property of 2-fold rotational symmetry. However, one must be quick to point out one exception to the above conjecture: the reciprocal structure at normal incidence. Indeed, it was found earlier that the relationship $C_{vv}^{pq} = -C_{vv}^{qp}$ with $p \neq q$ is *exactly* satisfied by all reciprocal structures at normal incidence regardless of whether or not they are endowed with the property of $2n$-fold rotational symmetry. Furthermore, in practice, this relationship is also *approximatively* satisfied within a certain tolerance in a limited neighborhood of the normal incidence. Consequently, in practice, the above conjecture holds true only

outside this neighborhood.

A similar conjecture does not hold true for the statement $C_{uv}^{pq} = C_{uv}^{qp}$ with $u \neq v$ since this author knows of at least one structure for which this relationship is satisfied in spite of the fact that the structure is not endowed with the property of longitudinal reflection symmetry. This structure is a grating whose strips are rotated out of the plane of the grating, and can be found in the paper by Whites and Mittra in reference [30, p. 725].

Therefore, one obtains these useful relationships:

$$\left\{ \begin{array}{r} \text{Snell's law of reflection} \\ \text{reciprocity} \\ \text{2-fold rotational symmetry} \end{array} \right\} \iff C_{vv}^{pq} = \epsilon_H C_{vv}^{qp}$$

with this relationship showing a double arrow (except in a limited neighborhood of the normal incidence), and:

$$\left\{ \begin{array}{r} \text{Snell's law of refraction with } \theta^t = \theta^i \\ \text{reciprocity} \\ \text{2-fold rotational symmetry} \\ \text{reflection symmetry about the } z = 0 \text{ plane} \end{array} \right\} \implies C_{uv}^{pq} = C_{uv}^{qp} \quad \text{for } u \neq v$$

with this relationship showing a single rather than a double arrow.

Validation of the Symmetry Relationships

The above relationships were confirmed by running NEC-2 simulations of various structures endowed with various geometrical properties. Four structures, shown in Figures 2.11 to 2.14, were investigated and the results are presented in Table 2.2. These results show that:

- $C_{uv}^{pq}(\theta^s, \phi^s|\theta^i, \phi^i) = -C_{vu}^{qp}(\pi - \theta^i, \pi + \phi^i|\pi - \theta^s, \pi + \phi^s)$ with $p \neq q$ and $u \neq v$, for all structures owing to reciprocity.

- $C_{vv}^{pq} = -C_{vv}^{qp}$ with $p \neq q$ for structures #2 and #4.

- $C_{uv}^{pq} = +C_{uv}^{qp}$ with $p \neq q$ and $u \neq v$ for structure #4.

Table 2.1 shows the result of performing $|C_{11}^{EH} + C_{11}^{HE}|$ for structures #1 and #2 as a function of θ^i. It is clear that both structures obey the relationship $C_{vv}^{pq} \approx -C_{vv}^{qp}$ with $p \neq q$ in the neighborhood of normal incidence but only structure #2 obeys this relationship for all θ^i values.

The segmentation of these structures was as follows: 13 segments for each transverse arm and 14 segments for the longitudinal section. The frequency was 1.0 GHz and the wire radius was 0.002 $m \approx 0.007\lambda$. It must be pointed out that these results are not presented with the convention used in NEC-2 but with that used in Appendix A, i.e. the incidence propagation vector is represented as pointing outwardly from the origin of the coordinate system. The incidence angle was arbitrarily chosen as $(\theta^i = 150^o, \phi^i = 250^o)$, and its reciprocal $(\theta^i = 30^o, \phi^i = 70^o)$. The parameter η, as defined in NEC-2, pertains to the polarization angle as the angle between the vector $\vec{E}$ and the unit vector $+\hat{\theta}^i$. This angle is counted positive in the direction winding from $+\hat{\theta}^i$ to $+\hat{\phi}^i$. The transmission coefficients shown in Table 2.2 are not

Table 2.1: The result of performing $|C_{11}^{EH} + C_{11}^{HE}|$ for structures #1 and #2 with $\phi^i = 250°$.

θ^i	#1	#2
180.0	2.37E-05	1.36E-04
179.9	5.26E-05	1.36E-04
179.8	1.18E-04	1.36E-04
179.7	1.84E-04	1.36E-04
179.6	2.52E-04	1.36E-04
179.5	3.17E-04	1.36E-04
179.0	6.51E-04	1.36E-04
178.0	1.32E-03	1.29E-04
177.0	1.98E-03	1.29E-04
176.0	2.65E-03	1.35E-04
175.0	3.30E-03	1.28E-04
170.0	6.47E-03	1.24E-04
165.0	9.34E-03	1.17E-04
160.0	1.18E-02	1.09E-04
155.0	1.37E-02	9.91E-05
150.0	1.51E-02	8.47E-05
145.0	1.60E-02	7.11E-05
140.0	1.62E-02	5.87E-05
135.0	1.61E-02	4.75E-05
130.0	1.56E-02	3.75E-05
120.0	1.44E-02	2.65E-05
110.0	1.43E-02	2.30E-05
100.0	1.63E-02	2.88E-05
90.0	1.99E-02	4.06E-05

really transmission coefficients since these results do not include the vectorial addition of the incident field phasor. However, this addition is not relevant to the present purpose of assessing whether or not $C_{uv}^{pq} = C_{uv}^{qp}$.

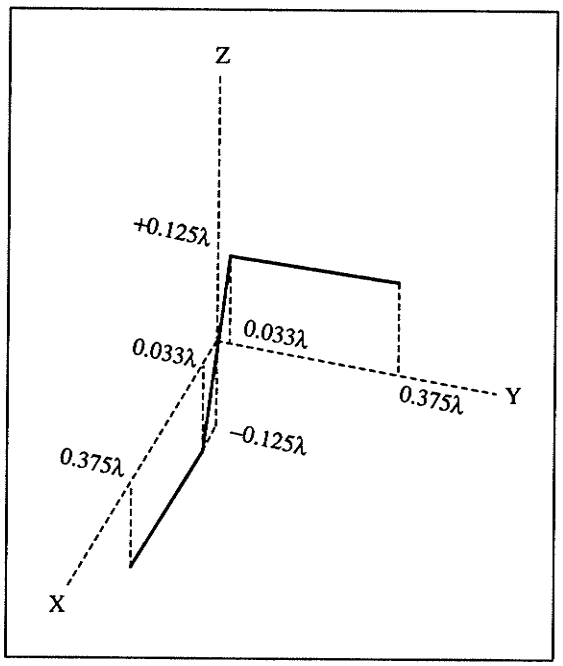

Figure 2.11: Structure #1, with no 2-fold rotational symmetry nor longitudinal reflection symmetry.

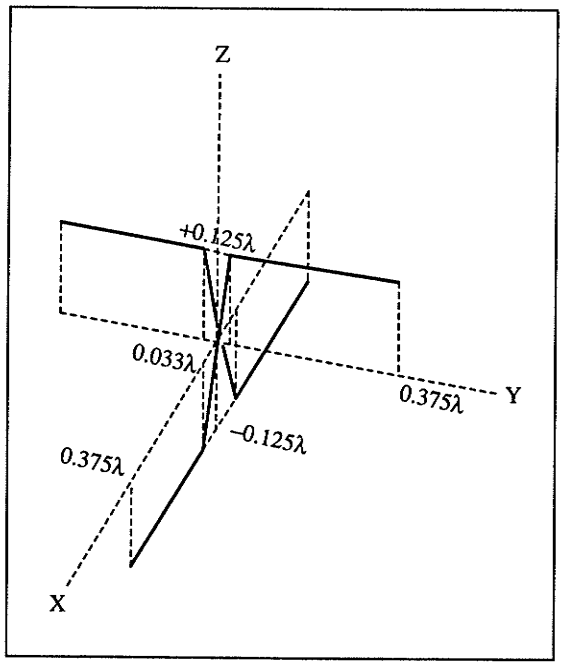

Figure 2.12: Structure #2, with 2-fold rotational symmetry but no longitudinal reflection symmetry.

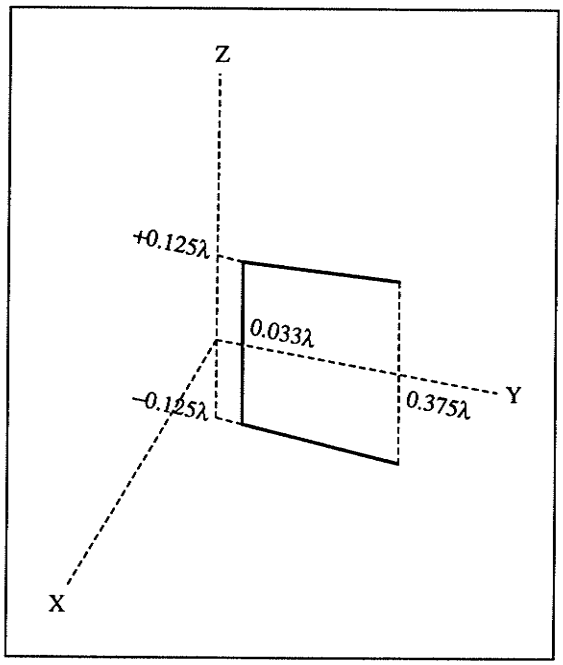

Figure 2.13: Structure #3, with no 2-fold rotational symmetry but with longitudinal reflection symmetry.

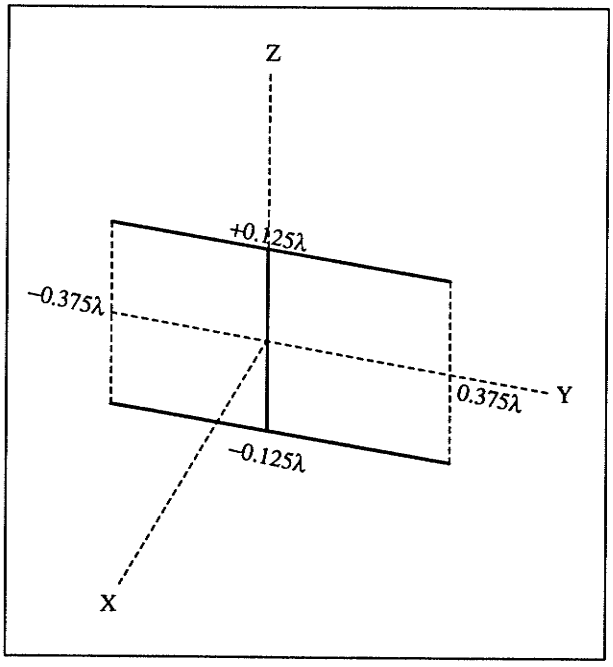

Figure 2.14: Structure #4, with both 2-fold rotational symmetry and longitudinal reflection symmetry.

Table 2.2: Scattered E far-field results obtained from NEC-2 simulations for various structures endowed with various symmetry properties.

#	Incidence			Scattered		E_θ			E_ϕ		
	θ^i	ϕ^i	η	θ^s	ϕ^s	C_{uv}^{pq}	(V/m)	$(^o)$	C_{uv}^{pq}	(V/m)	$(^o)$
1	150	250	0	30	250	C_{11}^{EE}	0.027953	+170.45	C_{11}^{HE}	0.014849	-84.50
»	»	»	»	150	250	C_{21}^{EE}	0.018599	-53.86	C_{21}^{HE}	0.023407	+53.71
»	»	»	-90	30	250	C_{11}^{EH}	0.029953	+93.30	C_{11}^{HH}	0.033007	-170.93
»	»	»	»	150	250	C_{21}^{EH}	0.028787	-138.84	C_{21}^{HH}	0.033700	-56.58
»	30	70	0	30	70	C_{12}^{EE}	0.018478	-53.82	C_{12}^{HE}	0.028812	+40.92
»	»	»	»	150	70	C_{22}^{EE}	0.018857	+94.43	C_{22}^{HE}	0.021411	+145.98
»	»	»	-90	30	70	C_{12}^{EH}	0.023523	-126.52	C_{12}^{HH}	0.033677	-56.64
»	»	»	»	150	70	C_{22}^{EH}	0.039378	+2.53	C_{22}^{HH}	0.022872	+73.28
2	150	250	0	30	250	C_{11}^{EE}	0.033956	+124.79	C_{11}^{HE}	0.024238	-153.27
»	»	»	»	150	250	C_{21}^{EE}	0.032502	-112.74	C_{21}^{HE}	0.025895	-9.25
»	»	»	-90	30	250	C_{11}^{EH}	0.024241	+26.53	C_{11}^{HH}	0.052583	+143.76
»	»	»	»	150	250	C_{21}^{EH}	0.029367	-166.21	C_{21}^{HH}	0.047306	-121.46
»	30	70	0	30	70	C_{12}^{EE}	0.032526	-112.67	C_{12}^{HE}	0.029331	+13.69
»	»	»	»	150	70	C_{22}^{EE}	0.021828	+32.62	C_{22}^{HE}	0.038224	+124.23
»	»	»	-90	30	70	C_{12}^{EH}	0.025884	+170.85	C_{12}^{HH}	0.047260	-121.52
»	»	»	»	150	70	C_{22}^{EH}	0.038351	-55.81	C_{22}^{HH}	0.027096	-16.54
3	150	250	0	30	250	C_{11}^{EE}	0.031494	+139.77	C_{11}^{HE}	0.011507	+137.37
»	»	»	»	150	250	C_{21}^{EE}	0.026428	-65.37	C_{21}^{HE}	0.013257	+114.20
»	»	»	-90	30	250	C_{11}^{EH}	0.014072	-45.86	C_{11}^{HH}	0.0052986	-47.28
»	»	»	»	150	250	C_{21}^{EH}	0.010212	+127.12	C_{21}^{HH}	0.0051594	-56.90
»	30	70	0	30	70	C_{12}^{EE}	0.026227	-65.38	C_{12}^{HE}	0.010152	-53.00
»	»	»	»	150	70	C_{22}^{EE}	0.031642	+139.34	C_{22}^{HE}	0.014120	-46.14
»	»	»	-90	30	70	C_{12}^{EH}	0.013216	-65.85	C_{12}^{HH}	0.0051522	-57.09
»	»	»	»	150	70	C_{22}^{EH}	0.011538	+136.91	C_{22}^{HH}	0.0053048	-47.58
4	150	250	0	30	250	C_{11}^{EE}	0.023882	+130.61	C_{11}^{HE}	0.0094100	+122.53
»	»	»	»	150	250	C_{21}^{EE}	0.036317	-132.89	C_{21}^{HE}	0.013875	+53.23
»	»	»	-90	30	250	C_{11}^{EH}	0.0094048	-57.27	C_{11}^{HH}	0.0038481	-62.77
»	»	»	»	150	250	C_{21}^{EH}	0.013934	+52.85	C_{21}^{HH}	0.0054747	-121.27
»	30	70	0	30	70	C_{12}^{EE}	0.036317	-132.89	C_{12}^{HE}	0.013875	-126.77
»	»	»	»	150	70	C_{22}^{EE}	0.023882	+130.61	C_{22}^{HE}	0.0094099	-57.47
»	»	»	-90	30	70	C_{12}^{EH}	0.013934	-127.15	C_{12}^{HH}	0.0054747	-121.27
»	»	»	»	150	70	C_{22}^{EH}	0.0094047	+122.74	C_{22}^{HH}	0.0038480	-62.77

NOTE: # pertains to the identification number of the structure

2.3 GSM-based Technique

In Appendix E, structures with known operations are analyzed in order to demonstrate and to validate the GSM-based technique. These structures are the solid Perfect Electrically Conducting (PEC) planar reflector, the free space slab, the artificially soft or hard surfaces[5] , the ideal LP, LHCP and RHCP polarizers. In this section, the GSM-based technique is used to obtain the GSM for the ideal CPSS and the non-ideal CPSS.

For all these structures, it is assumed that only the dominant mode prevails in the far field, thereby making the scattering matrix unitary. It is assumed also that these structures are free standing, hence, the wave impedance of a given mode is the same in both regions surrounding the structure. Only one wave is incident onto the structure at the time. All structures have their operations phrased in terms of incident CP waves, even though some structures could admittedly have their operation phrased more readily in terms of incident linearly polarized waves. This is done so as to demonstrate the validity of the approach in preparation for treating the CPSS problem. Since a sign error can spell the difference between whether or not the structure under study is endowed with one or many of the various properties developed earlier, the mathematical development is shown as explicitly as reasonable.

The generic 2-port voltage scattering matrix notation is used instead of the full 4-port voltage scattering matrix notation. The terminology u-ness $\neq$ v-ness is used to mean that the u-wave and the v-wave belong to different regions while being simultaneously in a possibly reciprocal relationship, i.e. if u is odd-numbered then v

[5]These artificially soft and hard surfaces are meaningful surfaces to use for validation because they display half the operation of the desired CPSS, i.e. they reflect an incident CP wave into a CP wave with the same handedness as that of the incident CP wave. It is not however a CPSS because it displays this behavior whether the incident CP wave is RHCP or LHCP. This behavior befits also the planar array of dipole turnstiles with $\lambda/4$ front-to-back thickness, illuminated by a plane wave at normal incidence.

is even-numbered and vice versa, such that one has:

$$(u = 2, v = 1), (u = 1, v = 2), (u = 4, v = 3), (u = 3, v = 4)$$

Only the case for $v = 1$ is treated explicitly. The solution for the remaining cases are obtained by a simple change of variables.

2.3.1 Ideal CPSS

The operation consisting in reflecting an incident LHCP plane wave into a LHCP plane wave while being perfectly transparent to an incident RHCP plane wave is phrased as:

$$\begin{cases} \text{If } (E_o^i)_v^H = +j(E_o^i)_v^E \text{ for } (E_o^i)_u^l = 0, u \neq v, l = \{E,H\} \\ \text{then} \begin{cases} (E_o^s)_v^H = +j(E_o^s)_v^E & v = \{1,2,3,4\} \\ (E_o^s)_u^H = (E_o^s)_u^E = 0 & u\text{-ness} \neq v\text{-ness} \end{cases} \\ \text{If } (E_o^i)_v^H = -j(E_o^i)_v^E \text{ for } (E_o^i)_u^l = 0, u \neq v, l = \{E,H\} \\ \text{then} \begin{cases} (E_o^s)_v^H = (E_o^s)_v^E = 0 & v = \{1,2,3,4\} \\ (E_o^s)_u^H = -j(E_o^s)_u^E & u\text{-ness} \neq v\text{-ness} \end{cases} \end{cases}$$

Say, $v = 1$. One obtains:

$$\begin{cases} (E_o^s)_1^E &= C_{11}^{EE}(E_o^i)_1^E + C_{11}^{EH}(E_o^i)_1^H \\ (E_o^s)_1^H &= C_{11}^{HE}(E_o^i)_1^E + C_{11}^{HH}(E_o^i)_1^H \end{cases}$$

$$(E_o^i)_1^H = +j(E_o^i)_1^E \Longrightarrow \begin{cases} (E_o^s)_1^E = \left(C_{11}^{EE} + jC_{11}^{EH}\right)(E_o^i)_1^E \\ (E_o^s)_1^H = \left(C_{11}^{HE} + jC_{11}^{HH}\right)(E_o^i)_1^E \end{cases}$$

$$\begin{aligned} (E_o^s)_1^H = +j(E_o^s)_1^E &\Longrightarrow \left(C_{11}^{HE} + jC_{11}^{HH}\right) = +j\left(C_{11}^{EE} + jC_{11}^{EH}\right) \\ &\Longrightarrow \left(C_{11}^{HE} + C_{11}^{EH}\right) = +j\left(C_{11}^{EE} - C_{11}^{HH}\right) \end{aligned}$$

$$\begin{cases} (E_o^s)_2^E &= C_{21}^{EE}(E_o^i)_1^E + C_{21}^{EH}(E_o^i)_1^H \\ (E_o^s)_2^H &= C_{21}^{HE}(E_o^i)_1^E + C_{21}^{HH}(E_o^i)_1^H \end{cases}$$

$$(E_o^i)_1^H = +j(E_o^i)_1^E \Longrightarrow \begin{cases} (E_o^s)_2^E = \left(C_{21}^{EE} + jC_{21}^{EH}\right)(E_o^i)_1^E \\ (E_o^s)_2^H = \left(C_{21}^{HE} + jC_{21}^{HH}\right)(E_o^i)_1^E \end{cases}$$

$$\begin{cases} (E_o^s)_2^E = 0 \Longrightarrow C_{21}^{EE} = -jC_{21}^{EH} \\ (E_o^s)_2^H = 0 \Longrightarrow C_{21}^{HE} = -jC_{21}^{HH} \end{cases}$$

Similarly, one has:

$$\begin{cases} (E_o^s)_2^E &= C_{21}^{EE}(E_o^i)_1^E + C_{21}^{EH}(E_o^i)_1^H \\ (E_o^s)_2^H &= C_{21}^{HE}(E_o^i)_1^E + C_{21}^{HH}(E_o^i)_1^H \end{cases}$$

$$(E_o^i)_1^H = -j(E_o^i)_1^E \Longrightarrow \begin{cases} (E_o^s)_2^E = \left(C_{21}^{EE} - jC_{21}^{EH}\right)(E_o^i)_1^E \\ (E_o^s)_2^H = \left(C_{21}^{HE} - jC_{21}^{HH}\right)(E_o^i)_1^E \end{cases}$$

$$\begin{aligned} (E_o^s)_2^H = -j(E_o^s)_2^E &\Longrightarrow \left(C_{21}^{HE} - jC_{21}^{HH}\right) = -j\left(C_{21}^{EE} - jC_{21}^{EH}\right) \\ &\Longrightarrow \left(C_{21}^{HE} + C_{21}^{EH}\right) = -j\left(C_{21}^{EE} - C_{21}^{HH}\right) \end{aligned}$$

$$\begin{cases} (E_o^s)_1^E &= C_{11}^{EE}(E_o^i)_1^E + C_{11}^{EH}(E_o^i)_1^H \\ (E_o^s)_1^H &= C_{11}^{HE}(E_o^i)_1^E + C_{11}^{HH}(E_o^i)_1^H \end{cases}$$

$$(E_o^i)_1^H = -j(E_o^i)_1^E \Longrightarrow \begin{cases} (E_o^s)_1^E = \left(C_{11}^{EE} - jC_{11}^{EH}\right)(E_o^i)_1^E \\ (E_o^s)_1^H = \left(C_{11}^{HE} - jC_{11}^{HH}\right)(E_o^i)_1^E \end{cases}$$

$$\begin{cases} (E_o^s)_1^E = 0 \implies C_{11}^{EE} = +jC_{11}^{EH} \\ (E_o^s)_1^H = 0 \implies C_{11}^{HE} = +jC_{11}^{HH} \end{cases}$$

Therefore, one obtains:

$$\left.\begin{cases} C_{21}^{EE} &= -jC_{21}^{EH} \\ C_{21}^{HE} &= -jC_{21}^{HH} \\ C_{21}^{HE} + C_{21}^{EH} &= -j\left(C_{21}^{EE} - C_{21}^{HH}\right) \end{cases}\right\} \Longrightarrow C_{21}^{EE} = C_{21}^{HH}$$

$$\left.\begin{cases} C_{11}^{EE} &= +jC_{11}^{EH} \\ C_{11}^{HE} &= +jC_{11}^{HH} \\ C_{11}^{HE} + C_{11}^{EH} &= +j\left(C_{11}^{EE} - C_{11}^{HH}\right) \end{cases}\right\} \Longrightarrow C_{11}^{EE} = C_{11}^{HH}$$

Now, from the unitary property of the matrix, one has:

$$C_{11}^{EE}(C_{11}^{EH})^* + C_{11}^{HE}(C_{11}^{HH})^* + C_{21}^{EE}(C_{21}^{EH})^* + C_{21}^{HE}(C_{21}^{HH})^* = 0$$

Substituting in this expression the various equivalences obtained above, one finds:

$$\left|C_{11}^{EE}\right| = \left|C_{21}^{EE}\right|$$

Also from the unitary property of the matrix, one has:

$$\left|C_{11}^{EE}\right|^2 + \left|C_{11}^{HE}\right|^2 + \left|C_{21}^{EE}\right|^2 + \left|C_{21}^{HE}\right|^2 = 1$$

Again, substituting in this expression the various equivalences obtained above, one finds:

$$\left|C_{11}^{EE}\right| = \frac{1}{2} \Longrightarrow \left|C_{11}^{EH}\right| = \left|C_{11}^{HE}\right| = \left|C_{11}^{HH}\right| = \left|C_{21}^{EE}\right| = \left|C_{21}^{EH}\right| = \left|C_{21}^{HE}\right| = \left|C_{21}^{HH}\right| = \frac{1}{2}$$

One notes that the phases of the scattering coefficients are yet undetermined. This means that a purely reactive surface is admissible.

From the combination of reciprocity, 2-fold rotational symmetry and Snell's law of reflection, with $u = v = 1, p = E, q = H$, one obtains:

$$C_{11}^{EH} = -C_{11}^{HE}$$

This last equation is consistent with the equations:

$$\left\{ \begin{array}{rcl} C_{11}^{EE} & = & +jC_{11}^{EH} \\ C_{11}^{HE} & = & +jC_{11}^{HH} \\ C_{11}^{EE} & = & +C_{11}^{HH} \end{array} \right\} \Longrightarrow C_{11}^{EH} = -C_{11}^{HE}$$

Hence, an ideal CPSS must have the $2n$-fold rotational symmetry.

One also knows:

$$C_{21}^{EE}(\theta^s, \phi^s | \theta^i, \phi^i) = -jC_{21}^{EH}(\theta^s, \phi^s | \theta^i, \phi^i)$$

From the combination of reciprocity and longitudinal reflection symmetry, with $u = 2, v = 1, p = E, q = H$, one has:

$$C_{21}^{EH}(\theta^s, \phi^s | \theta^i, \phi^i) = C_{21}^{HE}(\theta^i, \pi + \phi^i | \theta^s, \pi + \phi^s)$$

From above, one also knows:

$$C_{21}^{HE}(\theta^i, \pi + \phi^i | \theta^s, \pi + \phi^s) = -jC_{21}^{HH}(\theta^i, \pi + \phi^i | \theta^s, \pi + \phi^s)$$

From the combination of reciprocity and longitudinal reflection symmetry, with $u = 2, v = 1, p = q = H$, one has:

$$C_{21}^{HH}(\theta^i, \pi + \phi^i | \theta^s, \pi + \phi^s) = C_{21}^{HH}(\theta^s, 2\pi + \phi^s | \theta^i, 2\pi + \phi^i)$$

From the 2π periodicity of the angle ϕ, one obtains:

$$C_{21}^{HH}(\theta^s, 2\pi + \phi^s|\theta^i, 2\pi + \phi^i) = C_{21}^{HH}(\theta^s, \phi^s|\theta^i, \phi^i)$$

Consequently, pulling everything together, one obtains:

$$C_{21}^{EE}(\theta^s, \phi^s|\theta^i, \phi^i) = -C_{21}^{HH}(\theta^s, \phi^s|\theta^i, \phi^i)$$

Therefore:

$$C_{21}^{EE} = -C_{21}^{HH}$$

This last equation is inconsistent with the previously derived equation $C_{21}^{EE} = C_{21}^{HH}$. This means that an ideal reciprocal CPSS cannot have the longitudinal reflection symmetry. As a further check, it is known that from the combination of reciprocity, 2-fold rotational symmetry, Snell's law of refraction with $\theta^t = \theta^i$ and longitudinal reflection symmetry, with $u = 2, v = 1, p = E, q = H$, one must have:

$$C_{21}^{EH} = C_{21}^{HE}$$

This last equation is inconsistent with the previously derived equations:

$$\left\{ \begin{array}{rcl} C_{21}^{EE} & = & -jC_{21}^{EH} \\ C_{21}^{HE} & = & -jC_{21}^{HH} \\ C_{21}^{EE} & = & +C_{21}^{HH} \end{array} \right\} \Longrightarrow C_{21}^{EH} = -C_{21}^{HE}$$

This means that an ideal reciprocal CPSS cannot have both the 2-fold rotational symmetry and the longitudinal reflection symmetry. Since it was determined just above that the structure has the 2-fold rotational symmetry, then the structure cannot have the longitudinal reflection symmetry. These characteristics befit perfectly the cascade polarizer CPSS and the Tilston CPSS but not the Pierrot CPSS which is not 2-fold rotationally symmetrical.

On the basis of this important finding, one might be led to believe that the Pierrot CPSS cannot possibly achieve the performance of an ideal CPSS even for the case of normal incidence! However, in Chapter 2, it was found that all reciprocal structures,

regardless of whether or not they are endowed with the property of $2n$-fold rotational symmetry, obey the relationship $C_{vv}^{pq} \approx -C_{vv}^{qp}$ within a certain tolerance over a range of incidence angles centered about the normal incidence. Therefore, many practical CPSS designs that do not have the $2n$-fold rotational symmetry might still be possible for some range of incidence angles in a limited neighborhood of the normal incidence.

The same analysis can be repeated for the other cases of v. Finally, one obtains the voltage scattering matrix for the LHCPSS as:

$$C(E,H) = \frac{1}{2}\begin{pmatrix} A^1 & -jA^1 & A^2 & jA^2 \\ jA^1 & A^1 & -jA^2 & A^2 \\ A^2 & jA^2 & A^1 & -jA^1 \\ -jA^2 & A^2 & jA^1 & A^1 \end{pmatrix}$$

where $A^l = e^{j\alpha_l}$ and α_l is real valued.

The voltage scattering matrix for the RHCPSS is obtained from the voltage scattering matrix for the LHCPSS by replacing all occurrences of j by $-j$ except in the exponents of the arbitrary phase terms A^1 and A^2. The voltage scattering matrix for the RHCPSS becomes:

$$C(E,H) = \frac{1}{2}\begin{pmatrix} A^1 & jA^1 & A^2 & -jA^2 \\ -jA^1 & A^1 & jA^2 & A^2 \\ A^2 & -jA^2 & A^1 & jA^1 \\ jA^2 & A^2 & -jA^1 & A^1 \end{pmatrix}$$

where $A^l = e^{j\alpha_l}$ and α_l is real valued.

Interestingly, it is observed that, if $\alpha_1 = \alpha_2$, the voltage scattering matrices for the LHCPSS and the RHCPSS become circulant matrices!

2.3.2 Non-Ideal CPSS

The operation consisting in reflecting an incident LHCP plane wave into an elliptically polarized plane wave with polarization ratio $P = p\ e^{j\delta}$, axial ratio ar and tilt angle ψ (see Appendix C) while being imperfectly transparent to an incident RHCP plane wave is phrased as:

$$\left\{\begin{array}{l} \text{If } (E_o^i)_v^H = +j(E_o^i)_v^E \text{ for } (E_o^i)_u^l = 0, u \neq v, l = \{E,H\} \\ \quad \text{then} \left\{\begin{array}{ll} (E_o^s)_v^H = p_L\ e^{j\delta_L}(E_o^s)_v^E & v = \{1,2,3,4\} \\ \dfrac{\left|(E_o^s)_u^H\right|}{\left|(E_o^i)_v^H\right|} \leq T^H & \\ \dfrac{\left|(E_o^s)_u^E\right|}{\left|(E_o^i)_v^E\right|} \leq T^E & u\text{-ness} \neq v\text{-ness} \end{array}\right. \\ \text{If } (E_o^i)_v^H = -j(E_o^i)_v^E \text{ for } (E_o^i)_u^l = 0, u \neq v, l = \{E,H\} \\ \quad \text{then} \left\{\begin{array}{ll} \dfrac{\left|(E_o^s)_v^H\right|}{\left|(E_o^i)_v^H\right|} \leq R^H & \\ \dfrac{\left|(E_o^s)_v^E\right|}{\left|(E_o^i)_v^E\right|} \leq R^E & v = \{1,2,3,4\} \\ (E_o^s)_u^H = p_R\ e^{j\delta_R}(E_o^s)_u^E & u\text{-ness} \neq v\text{-ness} \end{array}\right. \end{array}\right.$$

To fix ideas, the ideal LHCPSS has $p_L = p_R = 1$, $\delta_L = \pi/2 = -\delta_R$ so that $P_L = +j$ and $P_R = -j$, thus $ar = 1$ and ψ becomes irrelevant, and $T^E = T^H = R^E = R^H = 0$.

Say, $v = 1$. One obtains:

$$\left\{\begin{array}{rcl} (E_o^s)_1^E & = & C_{11}^{EE}(E_o^i)_1^E + C_{11}^{EH}(E_o^i)_1^H \\ (E_o^s)_1^H & = & C_{11}^{HE}(E_o^i)_1^E + C_{11}^{HH}(E_o^i)_1^H \end{array}\right.$$

$$(E_o^i)_1^H = +j(E_o^i)_1^E \Longrightarrow \left\{\begin{array}{l} (E_o^s)_1^E = \left(C_{11}^{EE} + jC_{11}^{EH}\right)(E_o^i)_1^E \\ (E_o^s)_1^H = \left(C_{11}^{HE} + jC_{11}^{HH}\right)(E_o^i)_1^E \end{array}\right.$$

$$(E_o^s)_1^H = p_L\ e^{j\delta_L}(E_o^s)_1^E \implies \left(C_{11}^{HE} + jC_{11}^{HH}\right) = p_L\ e^{j\delta_L}\left(C_{11}^{EE} + jC_{11}^{EH}\right)$$

$$p_L\ e^{j\delta_L} = \alpha_L + j\beta_L \implies \left(C_{11}^{HE} - \alpha_L C_{11}^{EE} + \beta_L C_{11}^{EH}\right) = -j\left(C_{11}^{HH} - \beta_L C_{11}^{EE} - \alpha_L C_{11}^{EH}\right)$$

$$\begin{cases} (E_o^s)_2^E &= C_{21}^{EE}(E_o^i)_1^E + C_{21}^{EH}(E_o^i)_1^H \\ (E_o^s)_2^H &= C_{21}^{HE}(E_o^i)_1^E + C_{21}^{HH}(E_o^i)_1^H \end{cases}$$

$$(E_o^i)_1^H = +j(E_o^i)_1^E \Longrightarrow \begin{cases} (E_o^s)_2^E = \left(C_{21}^{EE} + jC_{21}^{EH}\right)(E_o^i)_1^E \\ (E_o^s)_2^H = \left(C_{21}^{HE} + jC_{21}^{HH}\right)(E_o^i)_1^E \end{cases}$$

$$\begin{cases} \left|(E_o^s)_2^E\right| \le T^E \left|(E_o^i)_1^E\right| &\Longrightarrow \left|C_{21}^{EE} + jC_{21}^{EH}\right| \le T^E \\ &\Longrightarrow \left(C_{21}^{EE} + jC_{21}^{EH}\right)\left(C_{21}^{EE} + jC_{21}^{EH}\right)^* \le (T^E)^2 \\ &\Longrightarrow \left|C_{21}^{EE}\right|^2 + \left|C_{21}^{EH}\right|^2 + 2\ Imag\left[C_{21}^{EE}(C_{21}^{EH})^*\right] \le (T^E)^2 \\ \left|(E_o^s)_2^H\right| \le T^H \left|(E_o^i)_1^H\right| &\Longrightarrow \left|(E_o^s)_2^H\right| \le T^H \left|(E_o^i)_1^E\right| \\ &\Longrightarrow \left|C_{21}^{HE} + jC_{21}^{HH}\right| \le T^H \\ &\Longrightarrow \left(C_{21}^{HE} + jC_{21}^{HH}\right)\left(C_{21}^{HE} + jC_{21}^{HH}\right)^* \le (T^H)^2 \\ &\Longrightarrow \left|C_{21}^{HE}\right|^2 + \left|C_{21}^{HH}\right|^2 + 2\ Imag\left[C_{21}^{HE}(C_{21}^{HH})^*\right] \le (T^H)^2 \end{cases}$$

Similarly, one has:

$$\begin{cases} (E_o^s)_2^E &= C_{21}^{EE}(E_o^i)_1^E + C_{21}^{EH}(E_o^i)_1^H \\ (E_o^s)_2^H &= C_{21}^{HE}(E_o^i)_1^E + C_{21}^{HH}(E_o^i)_1^H \end{cases}$$

$$(E_o^i)_1^H = -j(E_o^i)_1^E \Longrightarrow \begin{cases} (E_o^s)_2^E = \left(C_{21}^{EE} - jC_{21}^{EH}\right)(E_o^i)_1^E \\ (E_o^s)_2^H = \left(C_{21}^{HE} - jC_{21}^{HH}\right)(E_o^i)_1^E \end{cases}$$

$$\begin{aligned} (E_o^s)_2^H = p_R\ e^{j\delta_R}(E_o^s)_2^E &\Longrightarrow \left(C_{21}^{HE} - jC_{21}^{HH}\right) = p_R\ e^{j\delta_R}\left(C_{21}^{EE} - jC_{21}^{EH}\right) \\ p_R\ e^{j\delta_R} = \alpha_R + j\beta_R &\Longrightarrow \left(C_{21}^{HE} - \alpha_R C_{21}^{EE} - \beta_R C_{21}^{EH}\right) = \begin{matrix} +j\left(C_{21}^{HH} + \beta_R C_{21}^{EE}\right. \\ \left. -\alpha_R C_{21}^{EH}\right) \end{matrix} \end{aligned}$$

$$\begin{cases} (E_o^s)_1^E &= C_{11}^{EE}(E_o^i)_1^E + C_{11}^{EH}(E_o^i)_1^H \\ (E_o^s)_1^H &= C_{11}^{HE}(E_o^i)_1^E + C_{11}^{HH}(E_o^i)_1^H \end{cases}$$

$$(E_o^i)_1^H = -j(E_o^i)_1^E \Longrightarrow \begin{cases} (E_o^s)_1^E = \left(C_{11}^{EE} - jC_{11}^{EH}\right)(E_o^i)_1^E \\ (E_o^s)_1^H = \left(C_{11}^{HE} - jC_{11}^{HH}\right)(E_o^i)_1^E \end{cases}$$

$$\begin{cases} \left|(E_o^s)_1^E\right| \le R^E \left|(E_o^i)_1^E\right| & \Longrightarrow \left|C_{11}^{EE} - jC_{11}^{EH}\right| \le R^E \\ & \Longrightarrow \left(C_{11}^{EE} - jC_{11}^{EH}\right)\left(C_{11}^{EE} - jC_{11}^{EH}\right)^* \le (R^E)^2 \\ & \Longrightarrow \left|C_{11}^{EE}\right|^2 + \left|C_{11}^{EH}\right|^2 - 2\ Imag\left[C_{11}^{EE}(C_{11}^{EH})^*\right] \le (R^E)^2 \\ \left|(E_o^s)_1^H\right| \le R^H \left|(E_o^i)_1^H\right| & \Longrightarrow \left|(E_o^s)_1^H\right| \le R^H \left|(E_o^i)_1^E\right| \\ & \Longrightarrow \left|C_{11}^{HE} - jC_{11}^{HH}\right| \le R^H \\ & \Longrightarrow \left(C_{11}^{HE} - jC_{11}^{HH}\right)\left(C_{11}^{HE} - jC_{11}^{HH}\right)^* \le (R^H)^2 \\ & \Longrightarrow \left|C_{11}^{HE}\right|^2 + \left|C_{11}^{HH}\right|^2 - 2\ Imag\left[C_{11}^{HE}(C_{11}^{HH})^*\right] \le (R^H)^2 \end{cases}$$

In summary, one has:

$$\left(C_{11}^{HE} - \alpha_L C_{11}^{EE} + \beta_L C_{11}^{EH}\right) = -j\left(C_{11}^{HH} - \beta_L C_{11}^{EE} - \alpha_L C_{11}^{EH}\right) \tag{2.4}$$

$$\left(C_{21}^{HE} - \alpha_R C_{21}^{EE} - \beta_R C_{21}^{EH}\right) = +j\left(C_{21}^{HH} + \beta_R C_{21}^{EE} - \alpha_R C_{21}^{EH}\right) \tag{2.5}$$

$$\left|C_{11}^{EE}\right|^2 + \left|C_{11}^{EH}\right|^2 - 2\ Imag\left[C_{11}^{EE}(C_{11}^{EH})^*\right] \le (R^E)^2 \tag{2.6}$$

$$\left|C_{11}^{HE}\right|^2 + \left|C_{11}^{HH}\right|^2 - 2\ Imag\left[C_{11}^{HE}(C_{11}^{HH})^*\right] \le (R^H)^2 \tag{2.7}$$

$$\left|C_{21}^{EE}\right|^2 + \left|C_{21}^{EH}\right|^2 + 2\ Imag\left[C_{21}^{EE}(C_{21}^{EH})^*\right] \le (T^E)^2 \tag{2.8}$$

$$\left|C_{21}^{HE}\right|^2 + \left|C_{21}^{HH}\right|^2 + 2\ Imag\left[C_{21}^{HE}(C_{21}^{HH})^*\right] \le (T^H)^2 \tag{2.9}$$

Now, from the unitary property of the matrix, one has:

$$\begin{cases} C_{11}^{EE}(C_{11}^{EH})^* + C_{11}^{HE}(C_{11}^{HH})^* + C_{21}^{EE}(C_{21}^{EH})^* + C_{21}^{HE}(C_{21}^{HH})^* = 0 \\ \left|C_{11}^{EE}\right|^2 + \left|C_{11}^{HE}\right|^2 + \left|C_{21}^{EE}\right|^2 + \left|C_{21}^{HE}\right|^2 = 1 \\ \left|C_{11}^{EH}\right|^2 + \left|C_{11}^{HH}\right|^2 + \left|C_{21}^{EH}\right|^2 + \left|C_{21}^{HH}\right|^2 = 1 \end{cases}$$

Performing (2.6) + (2.7) + (2.8) + (2.9) and using the unitary property, one obtains:

$$Imag\left[C_{11}^{EE}(C_{11}^{EH})^* + C_{11}^{HE}(C_{11}^{HH})^*\right] \ge 0.5 - W^2 \tag{2.10}$$

$$Imag\left[C_{21}^{EE}(C_{21}^{EH})^* + C_{21}^{HE}(C_{21}^{HH})^*\right] \le W^2 - 0.5 \tag{2.11}$$

where:

$$W^2 = \frac{(R^E)^2 + (R^H)^2 + (T^E)^2 + (T^H)^2}{4}$$

One notes that the relations between the various scattering coefficients for the non-ideal CPSS are no longer as definite as those for the ideal CPSS. The non-ideal performance may be the result of the structure lacking the required symmetry properties or the result of the incidence angle being off-normal. This latter scenario is of special interest, i.e. the structure has the ideal performance at normal incidence but becomes non-ideal at off-normal incidence, as with the cascade polarizer CPSS.

Hence, assuming that the structure has the following two relations required from the ideal LHCPSS, one has:

$$\begin{cases} C_{11}^{EH} &= -C_{11}^{HE} \\ C_{21}^{EH} &= -C_{21}^{HE} \end{cases}$$

Substituting these relations into equations (2.4) and (2.5), one obtains:

$$C_{11}^{HH} = (\beta_L - j\alpha_L)\, C_{11}^{EE} + (\alpha_L + j(\beta_L - 1))\, C_{11}^{EH} \tag{2.12}$$

$$C_{21}^{HH} = (-\beta_R + j\alpha_R)\, C_{21}^{EE} + (\alpha_R + j(\beta_R + 1))\, C_{21}^{EH} \tag{2.13}$$

One observes that:

$$\begin{cases} P_L = +j \implies \{\alpha_L = 0, \beta_L = +1\} \implies C_{11}^{HH} = C_{11}^{EE} \\ P_R = -j \implies \{\alpha_R = 0, \beta_R = -1\} \implies C_{21}^{HH} = C_{21}^{EE} \end{cases}$$

as for the ideal LHCPSS. Substituting equations (2.12) and (2.13) into equations (2.10) and (2.11), respectively, one obtains:

$$\begin{cases} Imag\left[C_{11}^{EE}(C_{11}^{EH})^* - (\beta_L + j\alpha_L)\left(C_{11}^{EE}(C_{11}^{EH})^*\right)^*\right] + (\beta_L - 1)\left|C_{11}^{EH}\right|^2 &\geq 0.5 - W^2 \\ Imag\left[C_{21}^{EE}(C_{21}^{EH})^* + (\beta_R + j\alpha_R)\left(C_{21}^{EE}(C_{21}^{EH})^*\right)^*\right] + (\beta_R + 1)\left|C_{21}^{EH}\right|^2 &\leq W^2 - 0.5 \end{cases}$$

Now, rewriting:

$$\begin{cases} C_{11}^{EE}(C_{11}^{EH})^* &= a_1 + jb_1 \\ C_{21}^{EE}(C_{21}^{EH})^* &= a_2 + jb_2 \end{cases}$$

and substituting into the above equations, one obtains:

$$(1 + \beta_L)b_1 - \alpha_L a_1 + (\beta_L - 1)\left|C_{11}^{EH}\right|^2 \geq 0.5 - W^2 \tag{2.14}$$

$$(1 - \beta_R)b_2 + \alpha_R a_2 + (\beta_R + 1)\left|C_{21}^{EH}\right|^2 \leq W^2 - 0.5 \tag{2.15}$$

One observes that:

$$\begin{cases} P_L = +j & \Longrightarrow \quad \{\alpha_L = 0, \beta_L = +1\} & \Longrightarrow \quad b_1 \geq 0.5\,(0.5 - W^2) \\ P_R = -j & \Longrightarrow \quad \{\alpha_R = 0, \beta_R = -1\} & \Longrightarrow \quad b_2 \leq 0.5\,(W^2 - 0.5) \end{cases}$$

In the last two equations, the equality applies only to the case $W^2 = 0$, i.e. for the ideal LHCPSS, since from the previous section about the ideal LHCPSS and from above one has:

$$\left.\begin{cases} \left|C_{11}^{EH}\right| = \left|C_{21}^{EH}\right| = 0.5 \\ C_{11}^{EE} = +jC_{11}^{EH} \\ C_{21}^{EE} = -jC_{21}^{EH} \\ C_{11}^{EE}(C_{11}^{EH})^* = a_1 + jb_1 \\ C_{21}^{EE}(C_{21}^{EH})^* = a_2 + jb_2 \end{cases}\right\} \Longrightarrow \begin{cases} b_1 = +\left|C_{11}^{EH}\right|^2 = +0.25 \quad \text{and} \quad a_1 = 0 \\ b_2 = -\left|C_{21}^{EH}\right|^2 = -0.25 \quad \text{and} \quad a_2 = 0 \end{cases}$$

Hence, in general, one notes that whereas only two parameters of the scattering coefficients were left undetermined in the case of the ideal LHCPSS, i.e. the phases for C_{11}^{EE} and C_{21}^{EE}, four parameters are left undetermined here, i.e. a_1, b_1, a_2, b_2, and two constraints are to be satisfied, i.e. equations (2.14) and (2.15). Thus, owing to the fact that the constraints can be satisfied by a large number of possibilities, it is no longer useful to sketch the voltage scattering matrix for the non-ideal LHCPSS.

On the other hand, it may proved useful to quantify the performance of the non-ideal CPSS by means of simple figures. The concept of polarization efficiency seems most suited to this task. The polarization efficiency, $0 \leq f \leq 0$, indicates the loss in the power transfer between two antennas, the transmitting antenna (Tx) and the receiving antenna (Rx), owing to the polarization mismatch between the two antennas. One obtains:

$$\frac{P^r}{P^t} = \left(\frac{\lambda}{4\pi R}\right)^2 G^r\, G^t\, f$$

where P^r is the power captured by the Rx antenna, P^t is the power radiated by the Tx antenna, G is the antenna gain[6] of each respective antenna, R is the distance separating the apertures of the two antennas, λ is the wavelength in the propagation

[6]For convenience, it is assumed that each antenna is lossless and perfectly impedance matched.

medium. Appendix D presents various expressions for f according to various scenarios for the two antennas.

In this application, one can compute f by testing each plane wave (incident, transmitted or reflected) against a same test polarization ellipse, as if that plane wave were generated by a fictitious Tx antenna and the test polarization ellipse were that for a fictitious Rx antenna. By making the test polarization ellipse to be identical to the polarization ellipse of the incident plane wave, one can assess the performance of the non-ideal LHCPSS by computing the polarization efficiency of the reflected wave as:

$$f^r = f|\,\text{Rx}= i,\ \text{Tx}= r$$

when the incident plane wave is LHCP, and by computing the polarization efficiency of the transmitted wave as:

$$f^t = f|\,\text{Rx}= i,\ \text{Tx}= t$$

when the incident plane wave is RHCP.

For the LHCPSS, one obtains (see Appendices C and D):

$$ar^r = ar_L = \sqrt{\frac{(1+p_L^2)+\sqrt{1+p_L^4+2p_L^2 cos(2\delta_L)}}{(1+p_L^2)-\sqrt{1+p_L^4+2p_L^2 cos(2\delta_L)}}}$$

$$ar^t = ar_R = \sqrt{\frac{(1+p_R^2)+\sqrt{1+p_R^4+2p_R^2 cos(2\delta_R)}}{(1+p_R^2)-\sqrt{1+p_R^4+2p_R^2 cos(2\delta_R)}}}$$

$$\left\{\begin{array}{l} ar^i = 1 \Longrightarrow f = \frac{(1+\epsilon_{\text{Tx}}\ \epsilon_{\text{Rx}}\ ar_{\text{Rx}})^2}{2\ (1+ar_{\text{Rx}}^2)} \\ \epsilon_{\text{Rx}}^r = -1, \quad \epsilon_{\text{Tx}}^r = -1 \\ \epsilon_{\text{Rx}}^t = +1, \quad \epsilon_{\text{Tx}}^t = +1 \end{array}\right\} \Longrightarrow \left\{\begin{array}{lcl} f^i & = & 1 \\ f^r & = & \frac{(1+ar_L)^2}{2\ (1+ar_L^2)} \\ f^t & = & \frac{(1+ar_R)^2}{2\ (1+ar_R^2)} \end{array}\right\}$$

Figures 2.15 and 2.16 show, respectively, the inverse of the axial ratio $1/ar$ and the polarization efficiency f as functions of p and δ. It is seen that whereas the peak

for the function $1/ar$ is sharp, that for the function f is rounded, thus indicating that the requirement on the axial ratio is not as severe as one might have been led to believe from the plot of Figure 2.15. The maximum occurs for $p = 1$ and $\delta = 90^o$. The minimum is $f = 0.5$ owing to the fact that one of the two polarization ellipses, i.e. the incident one, is perfectly circular.

The concept of polarization efficiency remains valid even if the incident plane wave is not a pure CP wave. This suggests the development of structures even more general than a CPSS in that even the incident plane wave could be elliptically polarized. The polarization efficiency would then also take into account the tilt of the polarization ellipses. The range of applications for such structures, however, appears rather limited.

Hence, the three independent parameters, W^2, f^r and f^t, provides a first order performance characterization in terms of power solely. A more detailed characterization requires the additional knowledge of the independent parameters p_R, δ_R, p_L and δ_L, from which to obtain ar_R, ψ_R, ar_L and ψ_L. In contrast, a complete characterization consists in identifying all the scattering elements of the GSM, hence, requires also the knowledge of a_1, b_1, a_2 and b_2, as well as the inequalities (2.14) and (2.15).

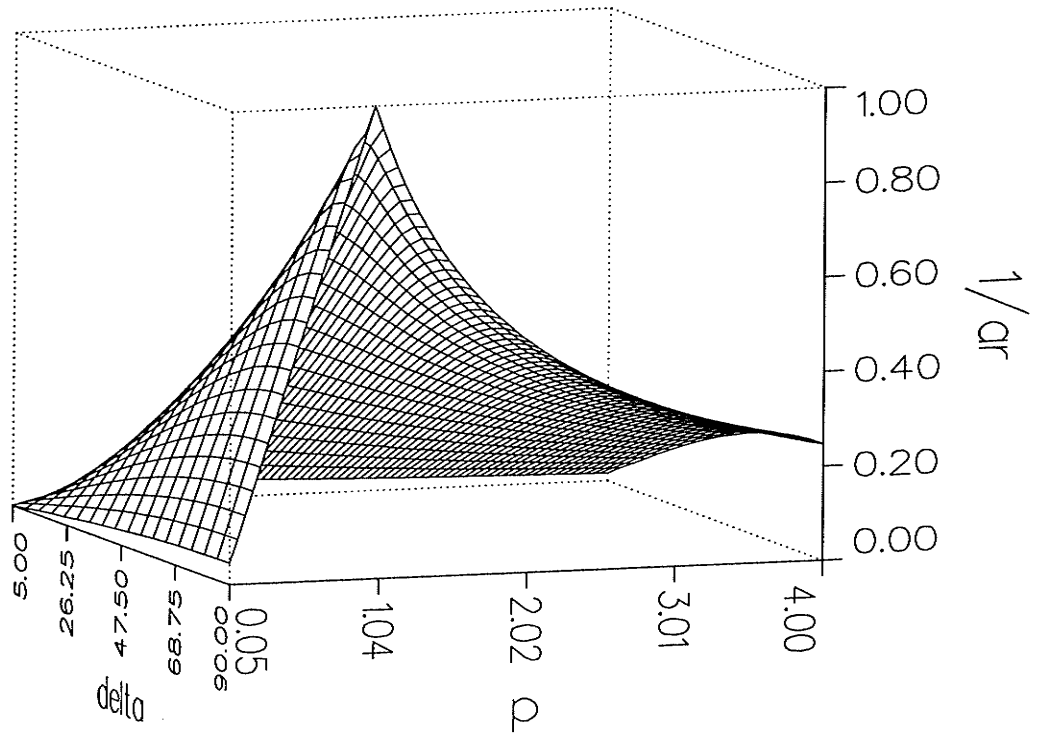

Figure 2.15: The inverse of the axial ratio, i.e. $1/ar$, as a function of p and δ.

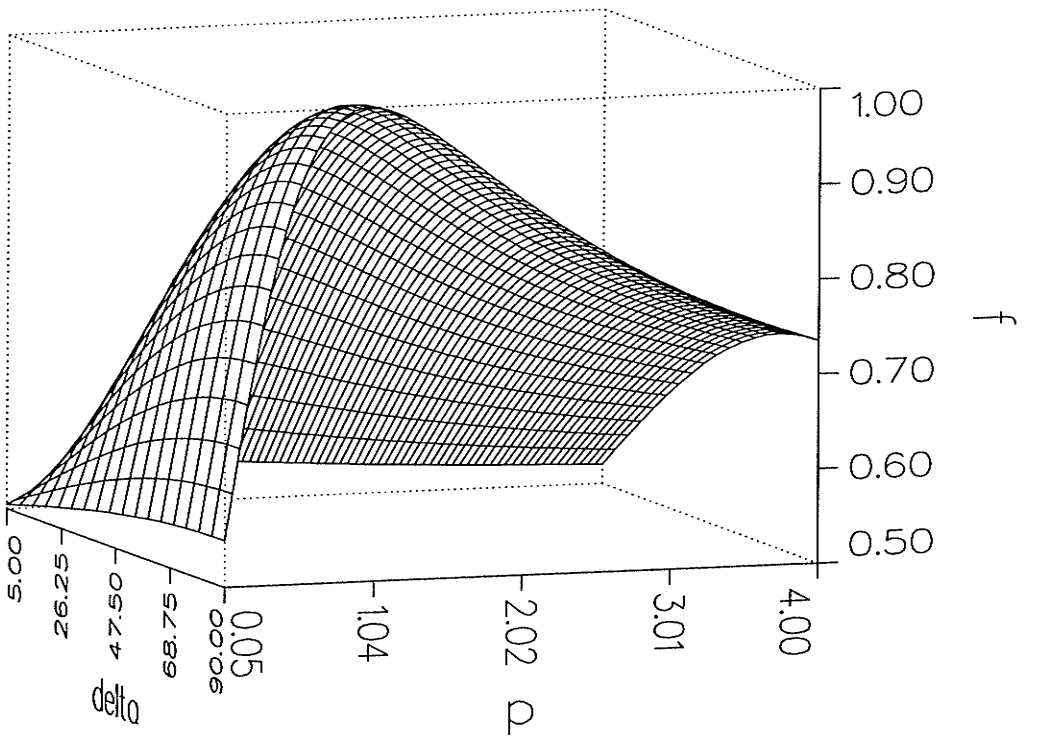

Figure 2.16: The polarization efficiency f as a function of p and δ.

Chapter Three

A New CPSS Realization

3.1 Concept

This chapter presents the cascade polarizer design idea that this author rediscovered independently via a different implementation of the circular polarizers. This author's design was inspired from a problem in reference [47, problem 8.34, p. 449], which reads as follows:

> Polarization "projection operator". If a piece of linear polaroid with easy axis along $\hat{x}$ is placed in a beam of light containing a mixture of all sorts of polarization, the polaroid absorbs all light that does not have linear polarization along $\hat{x}$. It has an "output" at the rear of the polarizer consisting of light linearly polarized along $\hat{x}$. We shall call this piece of polaroid a "projection operator". It "projects out" the $\hat{x}$ polarization without loss (neglecting small reflections) and delivers it at its output end. Note that this "x projection operator" can be run either forward or backward; i.e., either face of the polaroid may be used as the input end. Now consider a piece of circular polarizer consisting of a piece of linear polarizer (input end) glued to a quarter-wave plate with optic axis at 45 degrees to the easy axis of the polaroid. This polarizer puts out (for example) right-handed light. But it absorbs half of any right-handed light incident.

> If it is run backward, it passes incident right-handed light and absorbs left-handed light. But when it thus passes right-handed light incident on the quarter-wave-plate face, it delivers it out the polaroid face as linearly polarized light. Therefore it is *not* what we are calling a polarization projection operator. Here is the problem: Invent circular polarization projection operators, one for left-handed and one for right-handed light. The right-handed projection operator should transmit incident right-handed light with no loss (neglecting small reflections) and should deliver it as right-handed light . It should absorb left-handed light. Question: Is your circular polarization projection operator reversible? Can you use either face for the input end?

The new CPSS realization is precisely this invention, once it is realized that at microwave frequencies, a grid of fine conducting wires acting as the linear polarizer reflects rather than absorbs the electromagnetic wave incident upon it. By the reciprocity theorem, the signal reflected off the grid at normal incidence traces back the wave propagation path of the incident wave and comes out of the input face with the same polarization as the incident wave, hence the CPSS effect.

To be clear, let us work out the details of the operation of a CPSS reflecting an incident LHCP wave, starting with the operation of a quarter-wave plate. Figure 3.1 shows the various cases.

An incident linearly polarized wave with its polarization aligned at -45^o as shown in case a) has equal linearly polarized components along both $-\hat{e}_f$ and $\hat{e}_s$, where the subindices f and s refer to the fast and the slow axes, respectively. In figure 3.1, the slab is viewed from the same side for all cases, i.e. e_s points out of the page and e_f points upward, regardless of the direction of propagation. In the language of anisotropic media, the optic axis is either the slow or the fast axis, which is here parallel to the faces of the uniaxial slab. Since the component along $-\hat{e}_f$ travels at

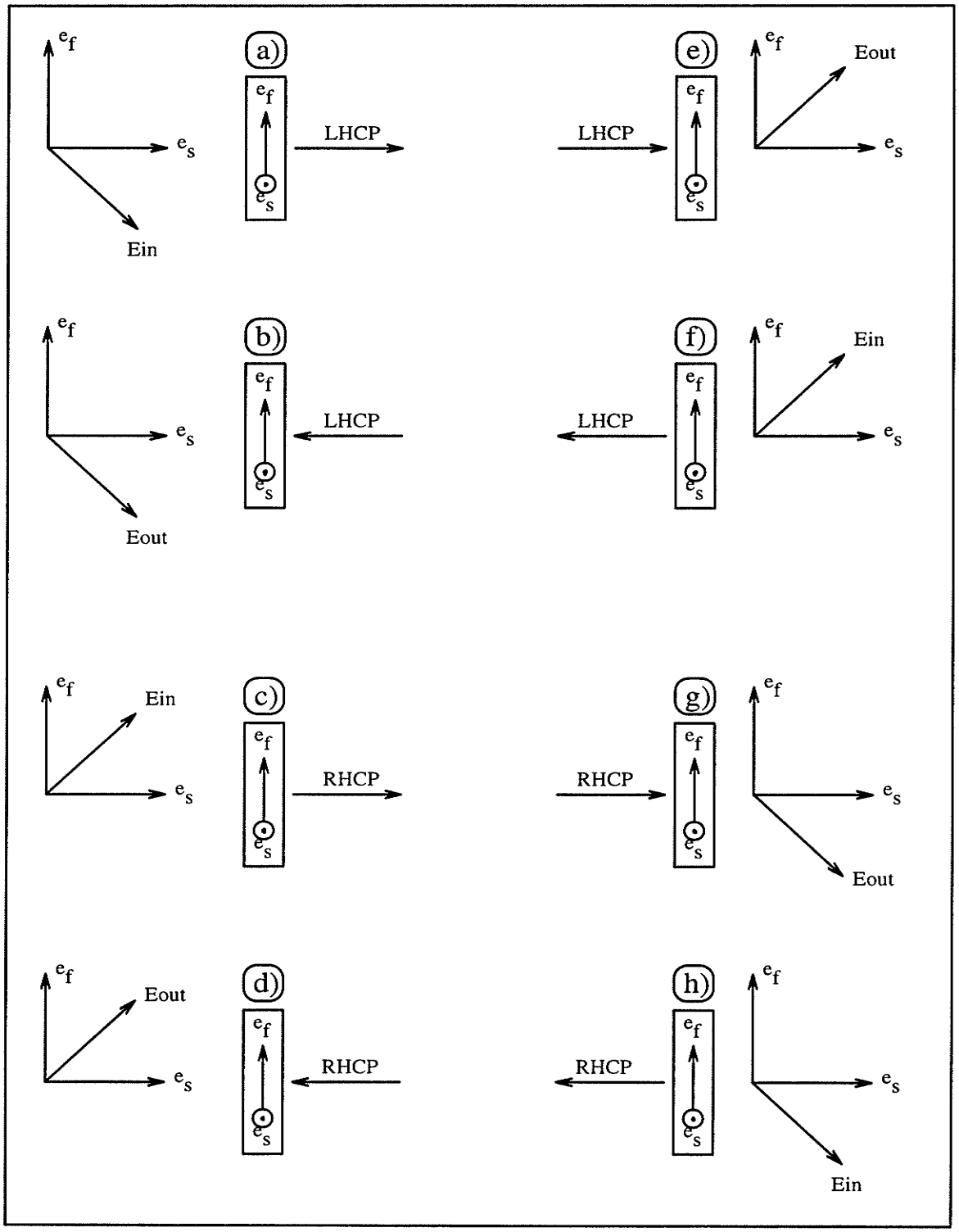

Figure 3.1: The various cases for the operation of a quarter-wave plate.

a group velocity larger than the component along $\hat{e}_s$, a phase difference builds up between the phases of the two components as the wave propagates through the slab. The quarter-wave plate is a slab whose thickness results in a 90^o phase difference. The cases a) and f) result in a LHCP wave at the output face. By the same mechanism, the cases c) and h) result in a RHCP wave at the output face.

One observes from comparing case a) and case h) that the CP wave produced from a same LP wave depends on the direction of propagation of the wave. Similarly, one observes from comparing case e) and case b) that the direction of the LP wave produced from a same CP wave depends also on the direction of propagation of the wave. Such an operation, however, should not be construed as an indication that the structure lacks longitudinal reflection symmetry. In fact, the quarter-wave plate has longitudinal reflection symmetry since it can be regarded as the concatenation of two identical eighth-wave plates oriented identically. The same argument holds also for any thickness of the plate, not just for the quarter-wave plate. Moreover, the uniaxial slab with its optic axis parallel to the interface has also transverse reflection symmetry with respect to the fast and the slow axes.

Although the result from running the waves in the reverse direction could be obtained directly from the reciprocity theorem, it is instructive to detail the reverse operation of obtaining a linearly polarized wave at the output face from a circularly polarized wave incident at the input face. In this case, the incident CP wave decomposes into two linearly polarized waves that are in time and in space quadratures. Again, the linearly polarized component along $\hat{e}_f$ travels faster than that along $\hat{e}_s$, resulting in a phase difference built up as the wave propagates through the slab. However, since the two linearly polarized components were already in time quadrature at the input face, the overall phase difference at the output face of the quarter-wave plate is either 180^o or 0^o, resulting in a linearly polarized output as shown in cases e), b), g) and d).

All the same results are obtained if the incident electric field E_{in} points in the direction opposite to that shown in Figure 3.1, or equivalently, if both axes, e_f and e_s, are reversed simultaneously. In fact, this simple model for the operation of the uniaxial medium does not take into account the absolute phase of each component, only the relative phase between them. Consequently, if a PEC reflector is used to reflect the output wave back into the slab, the 180° phase reversal introduced by the reflector is of no consequence.

By series combination of two quarter-wave plates to form a half-wave plate, one sees that the output wave is cross-polarized with respect to the input wave, i.e. the two waves are orthogonally polarized if linearly polarized [e.g. case a) followed by case e)], or of opposite handedness if circularly polarized [e.g. case e) followed by case c)]. Hence the half-wave plate is a perfect cross-polarizer for both LP and CP waves. Moreover, one sees from comparing the result of case e) followed by case c) with the result of case b) followed by case h) that the polarization handedness reversal is achieved regardless of the direction of propagation, according only to the total distance travelled in the slab. In contrast, one sees that the result of case a) followed by case e) consists of a 90°, say, CCW rotation with respect to the direction of propagation, whereas the result of case h) followed by case d) consists of a 90°, thus, CW rotation with respect to the direction of propagation. The reason that a circularly polarized wave has its polarization handedness reversed independently of the direction of propagation while the polarization rotation of its two linearly polarized components depends on the direction of propagation stems from the fact that $2 \times 90°$ CW rotation is the same as $2 \times 90°$ CCW rotation, i.e. 180°, which results in a polarization handedness reversal. This is a strange result in that one would be forced to say that the half-wave plate has longitudinal reflection symmetry in terms of the CP waves but not so in terms of the LP waves. But reflection symmetry is a purely geometrically dependent principle, independently of the nature of the waves!

The solution to this dilemma lies in that the model used herein does not account for the absolute phase of the waves, hence it is insensitive to the 180^o phase difference between the 90^o CCW and the 90^o CW rotations. In fact, as mentioned earlier, a uniaxial slab whose optic axis is parallel to the interface has both the transverse and the longitudinal reflection symmetries, regardless of its thickness.

By series connection of four quarter-wave plates to form a full-wave plate, one sees that the output wave is identical to the input wave, e.g. case a) followed by case e) followed by case c) followed by case g).

To obtain a CPSS, one simply uses a combination of quarter-wave plates, all plates having the fast axis oriented in the same direction, and a linear polarization filter, e.g. a metallic wire or strip grid, as shown in Figure 3.2. The operation of the structure is most easily described in terms of the various cases shown in Figure 3.1. Assuming that a LHCP wave is incident from the left onto quarter-wave plate #1, we are in presence of case e). The output of the plate is a LP wave polarized in the direction of the wires of the LP filter that follows the plate. The LP wave is thus reflected off the grid and back into quarter-wave plate #1 as in case f), the 180^o phase reversal introduced by the grid being of no consequence. The wave coming out of the input face of quarter-wave plate #1 is thus LHCP, as was the original incident wave. Assuming now that a RHCP wave is incident from the left onto quarter-wave plate #1, we are in presence of case g). The output of the plate is a LP wave polarized perpendicularly to the direction of the wires of the LP filter that follows the plate. The LP wave is thus transmitted, ideally without loss, through the grid and impinges onto quarter-wave plate #2 as in case a). The output of this second plate is LHCP and so one uses quarter-wave plates #3 and #4 to form a half-wave plate that reverses the handedness of the polarization, i.e case e) followed by case c). In fact, since the grid is transparent for this case, the operation of the four quarter-wave plates becomes simply that of a full-wave plate, i.e. no modification is made to the original CP wave.

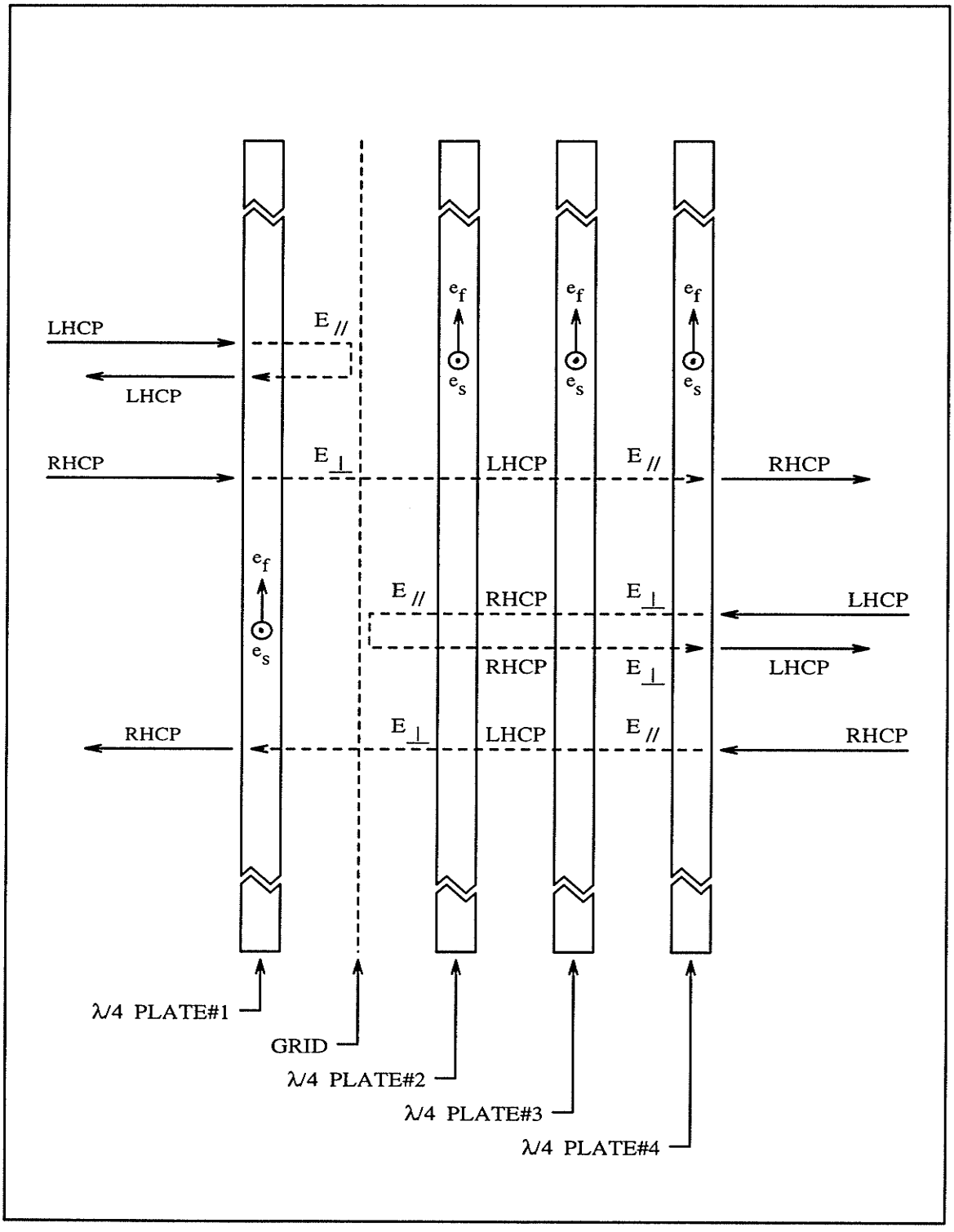

Figure 3.2: A new CPSS realization.

Assuming that a LHCP wave is now incident from the right onto quarter-wave plate #4, we are in presence of case b) followed by case h) followed by case d). The output of quarter-wave plate #2 is a LP wave polarized in the direction of the wires of the grid. Hence, the LP wave is reflected off the grid and back into quarter-wave plate #2, i.e. we have case c) followed by case g) followed by case a). The final output is LHCP, as was the originally incident wave. Assuming that a RHCP wave is now incident from the right onto quarter-wave plate #4, we are in presence of case d) followed by case f) followed by case b). The output of quarter-wave plate #2 is a LP wave polarized perpendicularly to the direction of the wires of the grid. Hence, the LP wave is transmitted, ideally without loss, through the grid and impinges onto quarter-wave plate #1 as in case h). The final output is a RHCP wave. Hence the LHCPSS has been fully realized.

One notes that the RHCPSS is obtained simply by rotating the grid by $\pm 90^o$ in its own plane. One notes also that quarter-wave plate #1 acts as a LHCP polarizer run backward whereas the series combination of quarter-wave plates #2, #3 and #4 acts as a RHCP polarizer run forward, in clear agreement with the cascade polarizer CPSS. One notes also that either one of the following operations reverses the handedness of the CP polarizer:

1. interchanging the two axes e_f and e_s;

2. rotating the plate by $\pm 90^o$ in its own plane;

3. reversing the direction of normal incidence as in case h) compared to case a) of Figure 3.1.

Thus, a quarter-wave plate LHCP polarizer is the same as a quarter-wave plate RHCP polarizer rotated by $\pm 90^o$ in the plane of the plate. Therefore, the quarter-wave plates #2, #3 and #4 can be replaced by a single quarter-wave plate that has been rotated by $\pm 90^o$ in the plane of the plate.

Morin [14] in a preliminary document to the patent office mentions in a sentence that a symmetrical CPSS can be achieved with a single quarter-wave plate in place or the three quarter-wave plates. This author concurs with Morin only if this quarter-wave plate has its two axes interchanged or rotated by $\pm 90^{\circ}$, as explained just above.

One notes in passing that although the design consisting of a single plate without its two axes interchanged would form an asymmetrical rather than a symmetrical CPSS, it might find, nevertheless, interesting applications of its own. Bossuet and Gautier make reference in their patents [5, 6] to such an asymmetrical CPSS, i.e. they show the two CP polarizers having the same handedness on both sides of the LP polarizer. Moreover, they reported that such an idea already belonged to the prior art but they did not give a specific reference for it. Morin [14] indicated without giving a specific reference that such a design originated from the field of Optics. In any case, it is conceptually simple to add a half-wave plate or equivalently to rotate the output CP polarizer by $\pm 90^{\circ}$ in its own plane for changing the handedness of the output CP wave in order to pass from the asymmetrical CPSS to the symmetrical CPSS or vice-versa.

Two major shortcomings of this new realization are its narrow bandwidth and its non-zero reflection coefficient. The first shortcoming owes to the fact that each uniaxial slab only acts as a quarter-wave plate at the single frequency for which the physical thickness of the plate produces the 90° phase difference. A literature survey [49 to 73] was undertaken to see if some particular implementation of the uniaxial medium could alleviate this shortcoming, e.g. perhaps shaping the profile of the grooves in the dielectric slab. This survey[1] , however, was without success!

Since the phase difference between the two components of the electric field is incurred by the total length travelled in the uniaxial medium, this author surmised

[1]This author notes in passing that Figure 23-32 of reference [86, p. 23-26] is erroneous by omission for the figure does not mention the presence of the conducting walls separating each dielectric layers. This omission was revealed by comparison with the original paper [56] from which the plot in Figure 23-32 was taken.

that one would need to cause the effective permittivity along each one of the two axes of the anisotropic medium to vary with frequency in such a way as to counter the variation of the electric length with frequency. Since the electrical length increases as the frequency increases for a fixed physical length, the difference in the effective permittivity between the two axes would need to decrease as the frequency increases. It is usually very difficult to make a constitutive parameter depend on frequency in a prescribed manner. An alternative mean to achieve the same effect would be to vary the effective propagation path length, either by varying the propagation path itself or by varying the contribution from various individual fixed propagation paths such that the sum of the contributions remain unaffected with frequency. In the wake of this latter idea, it was thought that the principle of the multi-step transformer could be used, i.e. a series of discontinuities, each discontinuity corresponding to a particular reflection coefficient and spaced from its two adjacent discontinuities by a quarter wavelength, would produce a filter characteristic with a low reflection value over a prescribed bandwidth by vectorial superposition of the multiple reflections arising from each discontinuity. This principle needs to be applied here to each one of the two components E_f and E_s such that the vectorial sum of the multiple reflections for each one of the two components produces the required 90° phase difference over some useful bandwidth. This approach is not very appealing as each quarter-wave plate would need to be implemented with multiple slabs.

The second shortcoming owes to the fact that the intrinsic impedance of each slab is different from that of the surrounding free space, thus resulting in an impedance mismatch at each interface of every slab. Since the thickness of each slab does not in general correspond to $\lambda/2$, the multiple reflections do not necessarily cancel out on axis, unless, again, each quarter-wave plate is implemented with multiple slabs that are of such a thickness and separated by such a distance as to cause the multiple reflections to sum to zero while also providing the necessary phase difference. In fact,

a similar approach is used for multi-layer meander-line polarizers!

The grid itself does not pose a serious design difficulty as it can be made easily to cover a wide bandwidth. The critical operation is that of the circular polarizer achieved by the quarter-wave plates. Hence, the design would be greatly improved by choosing another structure to play the role of the circular polarizers. A structure that implements this function over a broad bandwidth with little impedance mismatch is the multi-layer meander-line polarizer [74 to 86]. Bossuet and Gautier [5, 6], on the other hand, have reported the use of two parallel wire grids whose inter-wire separation within each grid was close to $\lambda/4$. However, they did not specify the inter-grid separation.

3.2 Composite GSM

First, the voltage scattering matrices for the ideal LP polarizer and the ideal CP polarizers are obtained. Then, the voltage scattering matrix for the LHCPSS is obtained as the composite of the voltage scattering matrix of a LHCP polarizer, the voltage scattering matrix of the LP polarizer and the voltage scattering matrix of the RHCP polarizer. Finally, the composite matrix is compared with the voltage scattering matrix for the ideal LHCPSS obtained in Chapter 2.

Since it was found in the previous sections that the ideal LP and CP polarizers are possible only at normal incidence, one uses the 2-port voltage scattering matrix in Cartesian coordinates which was obtained from the voltage scattering matrix in spherical coordinates by reversing the sign of some voltage scattering coefficients as per equation (2.3). One obtains for the ideal LP polarizer:

$$S^{LP}(X,Y) = \frac{1}{2}\begin{pmatrix} -(1-P)e^{j\alpha} & -Qe^{j\alpha} & (1+P)e^{j\beta} & -Qe^{j\beta} \\ -Qe^{j\alpha} & -(1+P)e^{j\alpha} & -Qe^{j\beta} & (1-P)e^{j\beta} \\ (1+P)e^{j\beta} & -Qe^{j\beta} & -(1-P)e^{j\alpha} & -Qe^{j\alpha} \\ -Qe^{j\beta} & (1-P)e^{j\beta} & -Qe^{j\alpha} & -(1+P)e^{j\alpha} \end{pmatrix}$$

$$\text{where: } \left\{ \begin{array}{l} P = cos(2\xi_{\|}^{LP}) \\ Q = sin(2\xi_{\|}^{LP}) \end{array} \right\} \text{ with } \xi_{\|}^{LP} = \phi^i + 90^o - \phi_g$$

One observes that the voltage scattering matrix is now symmetrical, as expected at normal incidence in the Cartesian coordinates. One observes also that all elements of the antidiagonal are all one and the same, in agreement with reference [37, the matrix of equation (1) being symmetrical]. For the ideal LHCP polarizer with the arbitrary phase coefficient e^{ja}, the case of $\xi_{\|}^{LHCP} = \phi^i + 90^o - \phi_L = -45^o$ leads to:

$$S^{LHCP}(X,Y) = e^{ja}\begin{pmatrix} 0 & 0 & +1 & 0 \\ 0 & 0 & 0 & +j \\ +1 & 0 & 0 & 0 \\ 0 & +j & 0 & 0 \end{pmatrix}$$

For the ideal RHCP polarizer with the arbitrary phase coefficient e^{ja}, the case of $\xi_{\|}^{RHCP} = \phi^i + 90^o - \phi_R = -45^o$ leads to:

$$S^{RHCP}(X,Y) = e^{ja} \begin{pmatrix} 0 & 0 & +1 & 0 \\ 0 & 0 & 0 & -j \\ +1 & 0 & 0 & 0 \\ 0 & -j & 0 & 0 \end{pmatrix}$$

To obtain a LHCPSS, one uses the facts that all plates are subjected to the same ϕ^i and that $\phi_L = \phi_g \pm 90^o = \phi_R$ (see Figure 4.34). Thus, one obtains:

$$\left\{ \begin{array}{l} \phi_L = \phi^i + 90^o - \xi_{\|}^{LHCP} \\ \phi_g = \phi^i + 90^o - \xi_{\|}^{LP} \\ \phi_R = \phi^i + 90^o - \xi_{\|}^{RHCP} \\ \phi_L = \phi_g \pm 90^o = \phi_R \\ \xi_{\|}^{LHCP} = \xi_{\|}^{RHCP} = -45^o \end{array} \right\} \Longrightarrow \xi_{\|}^{LP} = \{+45^o, -135^o\}$$

Using the commercial symbolic mathematical software MAPLE developed at the University of Waterloo (see Appendix F), the composite voltage scattering matrix is computed as:

$$S(X,Y) = \frac{1}{2} \begin{pmatrix} -A^1 & -jA^1 & A^2 & jA^2 \\ -jA^1 & A^1 & -jA^2 & A^2 \\ A^2 & -jA^2 & -A^1 & jA^1 \\ jA^2 & A^2 & jA^1 & A^1 \end{pmatrix}$$

where $A^l = e^{j\alpha_l}$ with: $\left\{ \begin{array}{rcl} \alpha_1 & = & \alpha + 2a - 2k_z D \\ \alpha_2 & = & \beta + 2a - 2k_z D \end{array} \right.$

and D is the spacing between each plate. This matrix is precisely the 2-port voltage scattering matrix for the LHCPSS, converted from $S(E,H)$ to $S(X,Y)$ as per equation (2.3). Again, the matrix is symmetrical.

To obtain a RHCPSS, one uses $\phi_L = \phi_g = \phi_R$ and thus $\xi_{\|}^{LP} = \{-45^o, +135^o\}$. It was confirmed that taking $\xi^{LP} = -45^o$ resulted indeed in the matrix for the RHCPSS.

The above development proves that, on the basis of the GSM analysis incorporating only the dominant mode, the ideal cascade polarizer CPSS is an ideal CPSS

at normal incidence. Thus, to the extent that LP and CP polarizers can be realized physically, the CPSS can also be realized physically. It must be remarked that, according to Cornbleet's conjecture, even the ideal LP polarizer is an impossible polarizer since its corresponding Jones polarization matrix is singular. This observation is rather surprising since a grid of fine metallic wires is known to be a very good physical realization of the ideal LP polarizer! Similarly, CP polarizers can be physically realized with a very good performance, at least over a small frequency bandwidth. This situation suggests that Cornbleet's conjecture is not practically relevant since the fact that the ideal operation of a device might be impossible to achieve physically does not imply that a good approximation of this ideal operation might not be realized and used satisfactorily in practice.

That the cascade polarizer design produce a CPSS is also clearly seen from Jones polarization matrices. A Jones polarization matrix represents the transformation between the input and the output Jones polarization vectors. A Jones polarization vector consists of the E_x and E_y components for a wave propagating in the $+\hat{z}$ direction [48, p. 681]. Thus the Jones polarization matrix corresponds, in fact, to the submatrix $S_{12}(X,Y)$ of the GSM matrix $S(X,Y)$.

$$\begin{pmatrix} E_x^{out} \\ E_y^{out} \end{pmatrix} = S_{12}(X,Y) \begin{pmatrix} E_x^{in} \\ E_y^{in} \end{pmatrix}$$

Cornbleet [1, p. 300, 312-313] gives the following Jones polarization matrices:

- LP polarizer with $\phi_g = 0^o$

$$\begin{pmatrix} 0 & 0 \\ 0 & 1 \end{pmatrix}$$

- LP polarizer with $\phi_g = 90^o$

$$\begin{pmatrix} 1 & 0 \\ 0 & 0 \end{pmatrix}$$

- LP polarizer with $\phi_g = \pm 45^o$

$$\frac{1}{2}\begin{pmatrix} 1 & \mp 1 \\ \mp 1 & 1 \end{pmatrix}$$

- LP polarizer with arbitrary ϕ_g

$$\begin{pmatrix} sin^2(\phi_g) & sin(\phi_g)cos(\phi_g) \\ sin(\phi_g)cos(\phi_g) & cos^2(\phi_g) \end{pmatrix}$$

From simple trigonometric identities and the substitution of the value $\phi^i = 0^o$ from equation (2.2) into the expression $\xi_{\|}^{LP} = \phi^i + 90^o - \phi_g$, one observes that this matrix corresponds indeed to the $S_{12}(X,Y)$ sub-matrix of the LP polarizer. This result agrees also with that given by Hill and Cornbleet in reference [37, equation(2) with $T_{\|} = 0$ and $T_{\perp} = 1$].

- CP polarizer with the fast axis at $\phi = 0^o$

$$\frac{1}{\sqrt{2}} \begin{pmatrix} 1+j & 0 \\ 0 & 1-j \end{pmatrix} = e^{j\frac{\pi}{4}} \begin{pmatrix} +1 & 0 \\ 0 & -j \end{pmatrix}$$

This result corresponds indeed to the $S_{12}(X,Y)$ sub-matrix of the RHCP polarizer with the arbitrary phase term taken as $e^{j\frac{\pi}{4}}$.

- CP polarizer with the fast axis at $\phi = 90^o$

$$\frac{1}{\sqrt{2}} \begin{pmatrix} 1-j & 0 \\ 0 & 1+j \end{pmatrix} = e^{-j\frac{\pi}{4}} \begin{pmatrix} +1 & 0 \\ 0 & +j \end{pmatrix}$$

This result corresponds indeed to the $S_{12}(X,Y)$ sub-matrix of the LHCP polarizer with the arbitrary phase term taken as $e^{-j\frac{\pi}{4}}$.

- CP polarizer with the fast axis at $\phi = \pm 45^o$

$$\frac{1}{\sqrt{2}} \begin{pmatrix} 1 & \pm j \\ \pm j & 1 \end{pmatrix}$$

- LHCPSS

$$\frac{1}{2} \begin{pmatrix} 1 & -j \\ +j & 1 \end{pmatrix}$$

- RHCPSS

$$\frac{1}{2} \begin{pmatrix} 1 & +j \\ -j & 1 \end{pmatrix}$$

In the above, the fast axis has the same meaning as that for the uniaxial slab treated earlier. The composite Jones polarization matrix is the product of the Jones polarization matrices for the constituting devices in the order reverse to that in which the devices are encountered as the wave propagates in the $+\hat{z}$ direction. Hence, from the above matrices and the cascade polarizer design for a LHCPSS (see Figure 4.34) there obtains:

$$\underbrace{\frac{1}{\sqrt{2}}\begin{pmatrix} 1 & +j \\ +j & 1 \end{pmatrix}}_{CP@+45^{o}}\underbrace{\begin{pmatrix} 0 & 0 \\ 0 & 1 \end{pmatrix}}_{LP@0^{o}}\underbrace{\frac{1}{\sqrt{2}}\begin{pmatrix} 1 & -j \\ -j & 1 \end{pmatrix}}_{CP@-45^{o}} = \underbrace{\frac{1}{2}\begin{pmatrix} 1 & +j \\ -j & 1 \end{pmatrix}}_{Jones'\,RHCPSS}$$

or equivalently:

$$\underbrace{\frac{1}{\sqrt{2}}\begin{pmatrix} 1-j & 0 \\ 0 & 1+j \end{pmatrix}}_{CP@+90^{o}}\underbrace{\frac{1}{2}\begin{pmatrix} +1 & -1 \\ -1 & +1 \end{pmatrix}}_{LP@+45^{o}}\underbrace{\frac{1}{\sqrt{2}}\begin{pmatrix} 1+j & 0 \\ 0 & 1-j \end{pmatrix}}_{CP@0^{o}} = \underbrace{\frac{1}{2}\begin{pmatrix} 1 & +j \\ -j & 1 \end{pmatrix}}_{Jones'\,RHCPSS}$$

It is important to point out that Jones' definition of the handedness of a circularly polarized wave is opposite to the definition used herein, i.e. Jones' definition is based on observing, as time goes on, the sense of rotation of the electric field vector at a point in space while looking at the wave in the direction *opposite* to the direction of propagation of the wave [47, pp. 398-401], [1, pp. 293-296], [48, p. 681]. Thus, Jones' RHCPSS corresponds to the LHCPSS as defined herein. Similarly, from the above matrices and the cascade polarizer design for a RHCPSS there obtains:

$$\underbrace{\frac{1}{\sqrt{2}}\begin{pmatrix} 1 & +j \\ +j & 1 \end{pmatrix}}_{CP@+45^{o}}\underbrace{\begin{pmatrix} 1 & 0 \\ 0 & 0 \end{pmatrix}}_{LP@+90^{o}}\underbrace{\frac{1}{\sqrt{2}}\begin{pmatrix} 1 & -j \\ -j & 1 \end{pmatrix}}_{CP@-45^{o}\text{ or }+135^{o}} = \underbrace{\frac{1}{2}\begin{pmatrix} 1 & -j \\ +j & 1 \end{pmatrix}}_{Jones'\,LHCPSS}$$

or equivalently:

$$\underbrace{\frac{1}{\sqrt{2}}\begin{pmatrix} 1-j & 0 \\ 0 & 1+j \end{pmatrix}}_{CP@+90^{o}\text{ or }-90^{o}}\underbrace{\frac{1}{2}\begin{pmatrix} +1 & +1 \\ +1 & +1 \end{pmatrix}}_{LP@-45^{o}}\underbrace{\frac{1}{\sqrt{2}}\begin{pmatrix} 1+j & 0 \\ 0 & 1-j \end{pmatrix}}_{CP@0^{o}} = \underbrace{\frac{1}{2}\begin{pmatrix} 1 & -j \\ +j & 1 \end{pmatrix}}_{Jones'\,LHCPSS}$$

It must be remarked that although the simple development based on Jones polarization matrices is sufficient to prove that the cascade polarizer design is indeed

a CPSS, the advantage of employing the GSM-based technique over employing the Jones polarization matrix technique, i.e. employing all four submatrices of the GSM matrix C(E,H) rather than just the submatrix $S_{12}(X,Y)$, is that, in addition to proving that the cascade polarizer design is a CPSS, the GSM-based technique also identifies some geometrical constraints of the structure.

Chapter Four

NEC-2 Simulations

It was seen earlier that both the Pierrot and the Tilston designs represented imperfect CPSS designs because of some idealization of their principle of operation; namely, the crank wire of the Pierrot design and the open-circuited turnstile dipoles of the Tilston design were assumed to be perfectly transparent to an incoming RHCP wave. It was seen earlier as well that the cascade polarizer design could not be ideal at off-normal incidence. Hence, it is of practical interest to investigate the actual performance of these designs.

Furthermore, the GSM-based analysis revealed that the ideal CPSS at off-normal incidence must have the $2n$-fold rotational symmetry, yet the Pierrot design does not satisfy this requirement. Hence, it would be interesting to investigate the practical importance of the $2n$-fold rotational symmetry requirement. Of course, one acknowledges that merely satisfying the geometrical constraints of the CPSS does not suffice to make the structure behave like a CPSS. Thus, there is no guarantee that the Tilston design would outperform the Pierrot design on the sole basis that the Tilston design does have the 2-fold rotational symmetry whereas the Pierrot design does not. Yet, it would be interesting to find out whether the Pierrot design might outperform the Tilston design in spite of its lack of 2-fold rotational symmetry. In the same line of thinking, it would be interesting to investigate the performance degradation incurred

by the Tilston design as the geometry departs increasingly away from the 2-fold rotational symmetry, as incurred, for instance, by gradually positioning the turnstile dipoles more asymmetrically with respect to the longitudinal axis.

Thus, this chapter presents the numerical analysis performed for the three CPSS designs with the commercial software NEC-2 [17] whose analytical formulation is based on the Method of Moments.

4.1 Generalities

The plots of the electric field were obtained by post-processing the near-field results obtained with NEC-2 so as to present the information directly in terms of the LHCP and RHCP components rather than in the NEC-2 format. It must be pointed out that both the far-field and the near-field results given by NEC-2 pertain to the scattered field alone, i.e. the incident field is not vectorially added in as part of the results. In contrast, in Chapter 2, the transmission coefficient of the scattering matrix characterized the total wave in the transmission region and, thus, the term "scattered" was used there as a generic term to mean either "reflected" or "transmitted", with the understanding that the transmitted wave included the incident wave when the direction of observation corresponded to the direction of incidence.

In terms of RHCP and LHCP uniform plane waves travelling in the $+\hat{r}$ direction, a general elliptical polarization is written with the basis vectors $\hat{u}_{RHCP}$ and $\hat{u}_{LHCP}$ as follows:

$$\left\{ \begin{array}{rcl} \hat{u}_{RHCP} & = & \frac{1}{\sqrt{2}}(\hat{\theta} - j\hat{\phi}) \\ \hat{u}_{LHCP} & = & \frac{1}{\sqrt{2}}(\hat{\theta} + j\hat{\phi}) \end{array} \right\} \Longrightarrow \left\{ \begin{array}{rcl} \hat{\theta} & = & \frac{1}{\sqrt{2}}(\hat{u}_{RHCP} + \hat{u}_{LHCP}) \\ \hat{\phi} & = & \frac{j}{\sqrt{2}}(\hat{u}_{RHCP} - \hat{u}_{LHCP}) \end{array} \right\}$$

There obtains:

$$\begin{aligned} \vec{E} &= E_\theta \hat{\theta} + E_\phi \hat{\phi} \\ &= \left(\frac{\hat{u}_{RHCP}+\hat{u}_{LHCP}}{\sqrt{2}}\right) E_\theta + j \left(\frac{\hat{u}_{RHCP}-\hat{u}_{LHCP}}{\sqrt{2}}\right) E_\phi \\ &= \left(\frac{E_\theta + jE_\phi}{\sqrt{2}}\right) \hat{u}_{RHCP} + \left(\frac{E_\theta - jE_\phi}{\sqrt{2}}\right) \hat{u}_{LHCP} \\ &= E_{RHCP}\ \hat{u}_{RHCP} + E_{LHCP}\ \hat{u}_{LHCP} \end{aligned}$$

where $E, E_\theta, E_\phi, E_{RHCP}, E_{LHCP}$ are phasors. For instance, a LHCP wave in the direction $+\hat{r}$ has $E_\phi = +jE_\theta$. Substituting this result into the above expressions for E_{RHCP} and E_{LHCP}, there obtains:

$$E_\phi = +jE_\theta \Longrightarrow \left\{ \begin{array}{rcl} E_{LHCP} & = & \left(\frac{E_\theta - jE_\phi}{\sqrt{2}}\right) = \sqrt{2}E_\theta \\ E_{RHCP} & = & \left(\frac{E_\theta + jE_\phi}{\sqrt{2}}\right) = 0 \end{array} \right.$$

and thus, indeed, the wave is purely LHCP polarized. It is noted in passing that the symmetry properties and the composite matrix technique that were developed earlier for the polarization decomposition in terms of E-wave (i.e. E^z mode, i.e. $\vec{E}_o = E_o\hat{\theta}$) and H-wave (i.e. H^z mode, i.e. $\vec{E}_o = E_o\hat{\phi}$) can be extended to the polarization decomposition in terms of LHCP and RHCP waves from the knowledge of the above relationships linking these two polarization decompositions.

CP co-polarization and cross-polarization of the scattered wave are defined here with respect to the CP polarization sense being the same as or opposite to the CP polarization sense of the incident wave, respectively. Thus, LL and RR represent the CP co-polarized scattered waves whereas RL and LR represent the CP cross-polarized scattered waves. Each parameter is a phasor, i.e. with both a magnitude and a phase. The first letter identifies the polarization sense of the scattered CP component whereas the second letter identifies the polarization sense of the incident CP wave.

For an ideal CPSS, both CP cross-polarization plots, LR and RL, should be zero at all points of the plots. Since the field results given by NEC-2 for the transmission region pertained to the scattered field rather than the total field, the RHCP co-polarization plot RR for Pierrot's and Tilston's LHCPSS designs should also be zero since the structure must not scatter the incident RHCP wave. In contrast, the RR plot for the cascade polarizer design should not be zero in the transmission region since upon RHCP incidence the structure did not proceed by an absence of scattering but by a transformation of the incident polarization. Finally, the LHCP co-polarization plot, LL, should consist of a scattered plane wave at the specular angle of reflection, and a scattered plane wave at the incidence angle, with a magnitude equal and a phase opposite to the magnitude and the phase of the incident wave, respectively, so that the transmitted wave consisting of the vectorial summation of the incident and the scattered waves produced a zero field value behind the array.

With a finite array illuminated by a single uniform plane wave, however, the reflected and the transmitted waves no longer form single plane waves propagating in single directions but instead, they form bundles of plane waves propagating over a continuous range of directions centered mostly about the reflection and the transmission directions for the corresponding infinite array, respectively. This angular spreading of the beams results from the spatial windowing phenomenon. Furthermore, the transmitted wave resulting from the superposition of the scattered and the incident waves has a zero field value only within a shadow region of limited extent behind the array. Far enough behind the array, diffraction around the edges of the array causes the total field to be non-zero. In terms of the scattering phenomenon, this result can be explained by the fact that the incident wave is a plane wave that propagates according to the function $e^{-j\vec{k}\cdot\vec{r}}$ whereas the scattered wave is a spherical wave centered on the scatterer and propagating according to the function $\frac{e^{-jkr}}{r}$ in the far-field region of the scatterer. Thus, far enough from the scatterer, i.e. for large enough values of r, the magnitude of the scattered wave is so small as to be negligible in comparison with the magnitude of the incident plane wave and thus, the vectorial summation of the scattered spherical wave and the incident plane wave produces the same result as the incident plane wave by itself, i.e. no shadow results in that region.

In order to ensure that the GSM for the finite array be representative of the GSM for the infinite array, and since the transmission coefficients are defined in terms of the total wave, not merely the scattered wave, one would have to ensure that the results from which the transmission coefficients of the GSM are computed be obtained with the observation point lying in the shadow region. Since, however, only the dominant mode is of interest here, and since the NEC-2 results pertain to the scattered rather than the total fields, the GSM coefficients can be computed either from the far-field results with the factor $\frac{e^{-jkr}}{r}$ omitted as an option provided by NEC-2, or from the near-field results with the observation point lying in the far-field region.

For the direction of observation corresponding to the direction of incidence, the co-polarized transmission coefficient is computed by adding the incident wave phasor to the scattered wave phasor. The incident wave phasor has a magnitude of 1 V/m for a linear polarization or $\sqrt{2}$ V/m for a circular polarization, and a phase of 0^o at the origin of the coordinate system. For all other cases, the GSM coefficients are obtained from the scattered wave alone, i.e. without adding the incident wave. The excitation is either linearly polarized in the $\hat{x}$ or $\hat{y}$ direction at normal incidence, and in the E (i.e. TM^z) or H (i.e. TE^z) direction for arbitrary incidence, or circularly polarized.

For the sake of easing the transfer of the results from NEC-2 to the tables in this chapter, the incidence propagation vector is taken as pointing inwardly toward the origin of the coordinate system, as defined in NEC-2, for all results except those pertaining to the GSM since the GSM was developed in Chapter 2 with the convention of taking all propagation vectors as pointing outwardly from the origin of the coordinate system.

All structures are free standing, i.e. as though without dielectric support. To take accurately into account the presence of the dielectric would require a wave solution based on the dyadic Green function. NEC-2 does not have this capability. The presence of the dielectric tends to increase the cross-polarization levels and the VSWR value owing to the mismatch of the intrinsic impedances, but these effects are only of a second order. More seriously, the presence of the dielectric modifies the effective length of the transverse conductors lying on the dielectric interfaces, and the effective length of the longitudinal section embedded in the dielectric substrate. Moreover, when the panel is manufactured by photolithography techniques, the transverse conductors become strips rather than circular wires and thus, a current distribution singularity arises at the edges of the strips for the current component that is parallel to the edges. This current singularity is another difficulty with which one must contend. Therefore, the results reported here could apply only to the case of

the dielectric support being a low loss microwave dielectric foam of a low permittivity value.

Unless mentioned otherwise, a wire radius of 0.002 m, i.e. $\approx 0.007\lambda$, was used throughout and the observation point lied on a 4.2 m, i.e. 14λ, radius sphere centered on the scatterer. This value for the observation sphere radius was chosen as part of a tentative design (see [13]) for a Cassegrain antenna whose subreflector was to be made of a CPSS. As it will be shown below, it turns out, however, that this value is too small for an array of 37 cells, a better value being 30.0 m. The choice of the 1 GHz operating frequency was made on the basis of convenience.

Various indicators were developed to characterize the plots of the scattered E field since all plots cannot possibly be included in this document. These indicators are:

- the reflection and the transmission beam[1] values $|LL^r|$, $|RR^r|$, $|RL^r|$, $|LR^r|$, $|LL^t|$, $|RR^t|$, $|RL^t|$ and $|LR^t|$, where for instance $|LL^r|$ pertains to the $|LL|$ value at the geometrical optics reflection angle, and $|LL^t|$ pertains to the $|LL|$ value at the geometrical optics transmission angle. For the LHCPSS, the $|LR^r|$ and $|RR^r|$ account for unwanted blockage causing the VSWR to depart from the ideal value of 1:1 whereas $|LL^t|$ and $|RL^t|$ account for unwanted leakage through and around the structure. This blockage and leakage are here defined as:

$$Blckg = \left(|LR^r|^2 + |RR^r|^2\right)\left(\frac{r}{A}\right)^2$$

$$Leakg = \left(\left|RL^t\right|^2 + \left|Q^L\left(\sqrt{2}A\frac{e^{-jkr}}{r}\right) + LL^t\right|^2\right)\left(\frac{r}{A}\right)^2$$

where A is the effective surface area[2] of the octagonal array in m^2 and r is

[1]Beam values refer here to the scattered field values at the geometrical optics angles for the reflection or the transmission beams. When the array is small, diffraction around the edges of the array causes these beams to be slightly shifted away from their geometrical optics directions [18], but this shift remains well within the 5° increment used herein to observe the scattering level over an observation sphere centered on the scatterer.

[2]The effective surface area A was not corrected by the factor $cos(\theta^i)$ to account for the change in the aspect profile of the scattering structure when the incidence is off-normal.

the observation sphere radius in m. Since the scattered field level tends, in the far-field region of the array, to increase proportionally with the size of the array and to decrease proportionally with the observation distance, the incorporation of the factor $\left(\frac{r}{A}\right)^2$ into the above definitions is an attempt to make the values of the indicators *Blckg* and *Leakg* independent of the array size or the observation sphere radius when the observation point lies in the far-field range of the array. The incident plane wave has a magnitude of $\sqrt{2}\ V/m$ as a result of each linear component of the incident CP wave having a magnitude of $1\ V/m$.

In order to quantify the amount of energy leaking *through* the surface without taking into account the energy leaking *around* the surface, thus in order to characterize the scatterer as if it were an infinite surface, the incident plane wave is made to behave as though it too were a spherical wave with the same dependence on r and A as does $|LL^t|$, thus with a magnitude of $\sqrt{2}A\ V/m$ and a phase value of 0^o at the origin of the coordinate system. The complex factor Q^L is a calibration parameter obtained from computing the scattered electric far-field of an octagonal solid PEC plate illuminated with a LHCP wave at the incidence angle of interest. Denoting by LL_o^t the LL^t value corresponding to this reflector plate of area A_o for an observation sphere radius r_o, the factor Q^L is computed as the factor that makes $Leakg = 0$ when the scatterer is this reflector plate since there should be no leakage *through* a solid plate. Since $RL^t \approx 0$, one has:

$$Q^L = \left(\sqrt{2}A_o \frac{e^{-jkr_o}}{r_o}\right) + LL_o^t = 0 \Longrightarrow Q^L = -\frac{r_o LL_o^t}{\sqrt{2}A_o} e^{+jkr_o}$$

and the expression for *Leakg* becomes:

$$Leakg = \left(\left|RL^t\right|^2 + \left|LL^t - \left(\frac{A}{A_o}\frac{r_o}{r}e^{-jk(r-r_o)}\right) LL_o^t\right|^2\right)\left(\frac{r}{A}\right)^2$$

This expression becomes more approximative as the incidence becomes increasingly off-normal because the term RL^t, as seen from the NEC-2 results, increases

also with the incidence angle and thus, the value of $Leakg$ becomes increasingly non-zero even for the reflector plate. The reflector plate is shown in Figure 4.1 and consists of a wire-grid [3] model based on the "same-surface-area" rule of thumb [107, 108]. For linear polarization, this rule consists in selecting the wire radius parallel to that polarization as $a = \frac{L}{2\pi}$ where L is the length of one side of the unit cell of the mesh. Since the polarization here is circular, the mesh is made square.

To help one grasp the meaning of these indicators, Table 4.1 presents the expected results for various types of surface. In the far-field region, the minimum $Blckg$ and $Leakg$ values ever possible are $0\left(\frac{V}{m\lambda}\right)^2$. For the baseline scatterer consisting of a structure of size and shape corresponding to an octagonal array of 37 cells with 0.15 m inter-element spacing, illuminated at normal incidence and observed over a 30.0 m sphere radius, the maximum $Blckg$ value is $\approx 2.165\left(\frac{V}{m\lambda}\right)^2$ as obtained for the solid PEC reflector plate, and the maximum $Leakg$ value is equal to $|LL_o^t|^2\left(\frac{r_o}{A_o}\right)^2 = 15.897\left(\frac{V}{m\lambda}\right)^2$, as obtained when $LL^t = RL^t = 0$.

Two different segmentations were used to check on the convergence of the scattered field results for the reflector plate. The first segmentation consisted of 5 wires per each 0.15 m side of the unit cell, thus $L = 0.030$ m and $a = 0.00477$ $m \approx 0.016\lambda$ for a total of 1920 segments. The second segmentation consisted of 6 wires per each 0.15 m side of the unit cell, thus $L = 0.025$ m and

[3] Although NEC-2 has the capability of solving either the Electric Field Integral Equation (EFIE) or the Magnetic Field Integral Equation (MFIE), the wire-grid model corresponding to solving the EFIE was chosen over the patch model corresponding to solving the MFIE because the solution of the MFIE is fraught with numerical instability problems as the thickness of the scatterer goes down to zero [106]. Furthermore, the thin wire kernel rather than the extended kernel of NEC-2 was used here even though the wire radius was not quite smaller than or equal to 0.01λ. This choice owes to the fact that NEC-2 does not use the extended kernel for segments ending at the junction of multiple wires, and that here, every segment ends at a junction of two wires.

Table 4.1: Expected results from the indicators for various types of surface.

Surface type	$\|LL^r\|$	$Blckg$	$Leakg$
Solid PEC reflector plate	0	cte_2	0
Free space slab	0	0	cte_3
Ideal artificially soft or hard surface	cte_1	cte_2	0
Ideal LHCPSS	cte_1	0	0
Ideal RHCPSS	0	cte_2	cte_3
cte_1, cte_2 and cte_3 are some non-zero constants			

Table 4.2: Scattered E field results for two different segmentations of the octagonal wire-grid PEC plate. The observation sphere radius is 30.0 m.

#	θ^i (^{o})	ϕ^i (^{o})	LL_o^t	
			mag. (V/m)	phase (^{o})
5	0.0	0.0	0.13620	+64.75000
6	"	"	0.13530	+64.73000
5	45.0	45.0	0.09664	-117.4537
6	"	"	0.09613	-117.4058
5	30.0	70.0	0.11832	-116.5545
6	"	"	0.11756	-116.5475
# pertains to the number of wires per each 0.15 m side of the unit cell				

$a = 0.00398\ m \approx 0.013\lambda$ for a total of 2748 segments. The results shown in Table 4.2 indicate that convergence is achieved within $\approx 0.7\%$ for the magnitude and $\approx 0.05^o$ for the phase. Thus, the results for the segmentation of 5 wires per each side of the unit cell were used in computing the value for $Leakg$.

Table 4.3 shows the results in assessing the behavior of the indicators $Blckg$ and $Leakg$ for two different sizes of an octagonal array made of the Pierrot LHCPSS cells for various observation sphere radii. Ideally, the values of these indicators should remain constant in spite of the variation in the observation distance and the array size, since the same cell type, inter-element spacing, octagonal geometry and incidence angle were used for all cases in the table.

It is seen that the indicator $Blckg$ is quite constant except for the case of 156

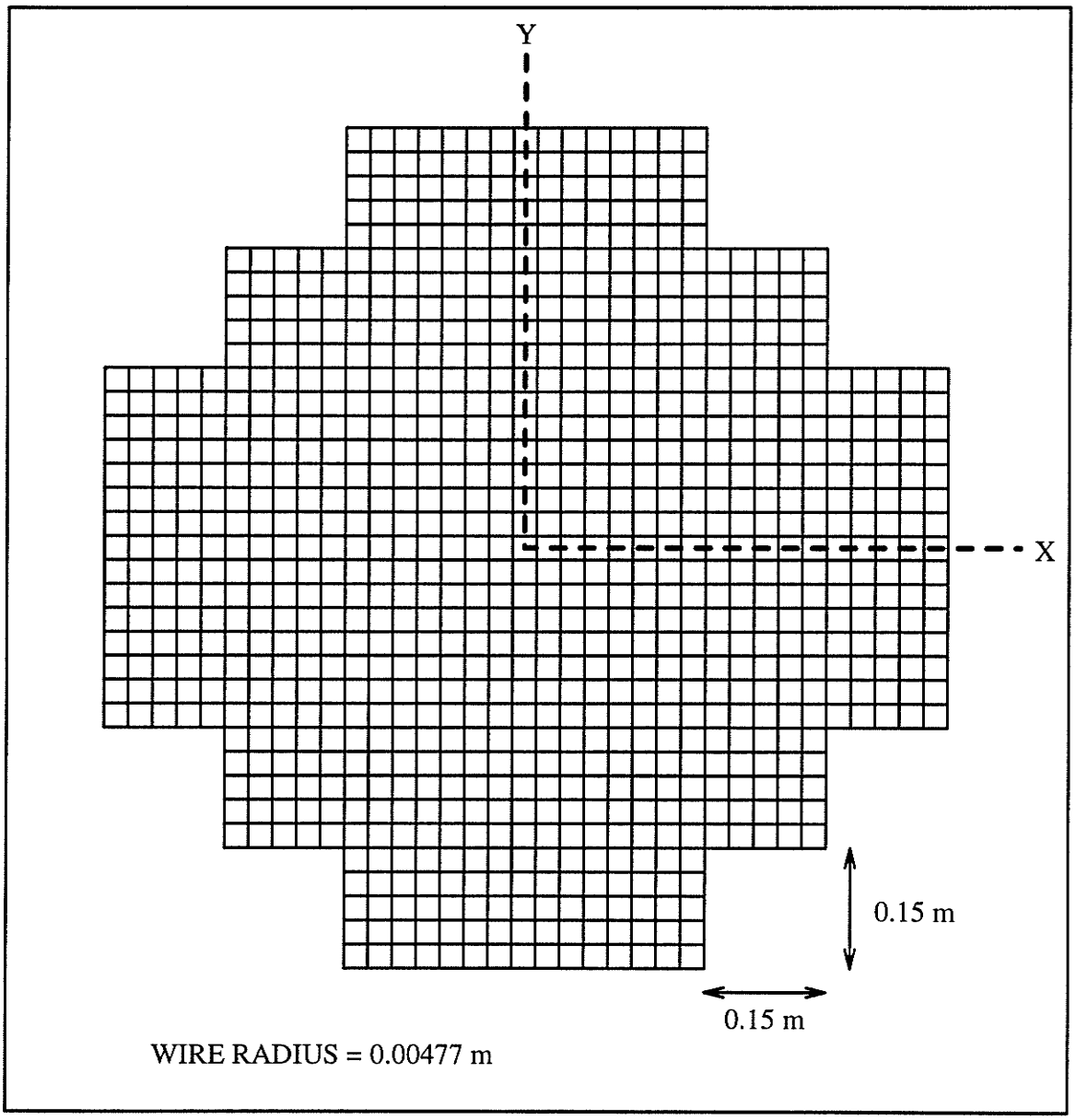

Figure 4.1: Octagonal solid PEC plate modelled with a wire mesh as per the "same-surface-area" rule of thumb. This figure shows the case of a segmentation consisting of 5 wires per each 0.15 m side of the unit cell.

Table 4.3: Assessment of the indicators *Blckg* and *Leakg* for two different sizes of an octagonal array made of the Pierrot LHCPSS cells for various observation sphere radii. The inter-element spacing is 0.15 m and the incidence is normal.

# cells	r (m)	$Blckg \times 10^3$ $\left(\frac{V}{m\lambda}\right)^2$	$Leakg$ $\left(\frac{V}{m\lambda}\right)^2$
37	4.2	20.8518	0.0663914
"	8.4	21.4362	0.187631
"	30.0	21.5619	0.371557
"	42.0	21.5620	0.405025
"	84.0	21.5558	0.473680
156	4.2	11.8085	1.35099
"	30.0	22.4574	0.202090
"	42.0	22.5518	0.266398
"	84.0	22.6110	0.411657
"	136.0	22.6133	0.504890

cells with 4.2 m observation sphere radius, but in this case, the observation point does not lie at all in the far-field region of the array and so, the indicator is not expected to be constant since the assumption of the far-field behavior $\frac{e^{-jkr}}{r}$ is severely violated. It is also meaningful that the case of the 37 cell array with 4.2 m observation sphere radius has the second lowest *Blckg* value and a singularly low *Leakg* value since the observation point does not lie clearly in the far-field region of the array, although the far-field behavior is not as severely violated in this case as in the earlier case of the array with 156 cells and 4.2 m observation sphere radius (see Table 4.7).

The indicator *Leakg* is not quite as constant as was the indicator *Blckg* although it does single out the case of the array with 156 cells and 4.2 m observation sphere radius. Since the reference scattered field value LL_o^t was taken with the reflector plate having a surface area corresponding to that of the 37 cell array with 0.15 m inter-element spacing, and with the observation sphere radius being 30.0 m, it would appear that the compensation scheme used in computing

the *Leakg* values is not very effective when the case under study departs too much from the reference case. In fact, the compensation scheme seems to over-compensate with respect to both A and r. As most simulations, however, will pertain to the case of the 37 cell array with the 30.0 m observation sphere radius, the *Leakg* values are expected to be meaningful.

- the axial ratio for the beam values, defined here as the ratio of the major axis over the minor axis of the polarization ellipse, are obtained as:

$$ar = \begin{cases} ar^r = \dfrac{||RL^r|+|LL^r||}{||RL^r|-|LL^r||} & \text{for LHCP incidence} \\ ar^t = \dfrac{\left|\left|Q^R\left(\sqrt{2}A\frac{e^{-jkr}}{r}\right)+RR^t\right|+\left|LR^t\right|\right|}{\left|\left|Q^R\left(\sqrt{2}A\frac{e^{-jkr}}{r}\right)+RR^t\right|-|LR^t|\right|} & \text{for RHCP incidence} \end{cases}$$

where the term $\sqrt{2}A\frac{e^{-jkr}}{r}$ in the expression for ar^t accounts again for the incident wave made to look like a spherical wave with the same dependence on A and r as that for the phasors $|RR^t|$ and $|LR^t|$ in the far-field region of the scatterer. The complex factor Q^R is also a calibration parameter obtained from computing the scattered electric far-field of an octagonal LP polarizer plate illuminated with a RHCP wave at the incidence angle of interest. Denoting respectively by RR_o^t and LR_o^t the RR^t and LR^t values corresponding to this LP polarizer plate of area A_o for an observation sphere radius r_o, the factor Q^R is computed as the factor that makes:

$$\left|\left|Q^R\left(\sqrt{2}A_o\frac{e^{-jkr_o}}{r_o}\right)+RR_o^t\right|-\left|LR_o^t\right|\right| = 0$$

when the scatterer is this LP polarizer plate since $ar^t = \infty$ for the transmitted LP wave. Choosing the phase of Q^R such that:

$$\left|Q^R\left(\sqrt{2}A_o\frac{e^{-jkr_o}}{r_o}\right)+RR_o^t\right| = \left|Q^R\right|\frac{\sqrt{2}A_o}{r_o}+\left|RR_o^t\right|$$

i.e. choosing:

$$q = kr_o + \rho_o$$

where q and ρ_o are the phase angles for Q^R and RR_o^t, respectively, there obtains:

$$\left|Q^R\right| = \frac{r_o}{\sqrt{2}A_o}\left(\left|LR_o^t\right| - \left|RR_o^t\right|\right)$$

Hence, one has:

$$ar^t = \frac{||W + RR^t| + |LR^t||}{||W + RR^t| - |LR^t||}$$

where:

$$W = \frac{A}{A_o}\frac{r_o}{r}\left(\left|LR_o^t\right| - \left|RR_o^t\right|\right)e^{j(\rho_o - k(r - r_o))}$$

Ideally, $ar = 1.0$, thus indicating perfectly circular polarization.

The octagonal LP polarizer plate of surface area corresponding to the octagonal array of 37 cells with 0.15 m inter-element spacing is shown in Figure 4.2. Two different segmentations were used to check on the convergence of the scattered field results for this octagonal LP polarizer plate. The first segmentation consisted of 5 wires per one 0.15 m side of the unit cell, with $L = 0.030$ m and $a = 0.00477$ $m \approx 0.016\lambda$ for a total of 960 segments. The second segmentation consisted of 6 wires per one 0.15 m side of the unit cell, with $L = 0.025$ m and $a = 0.00398$ $m \approx 0.013\lambda$ for a total of 1374 segments. In fact, the LP polarizer plate was obtained simply from the wire-grid model of the reflector plate by eliminating the vertical wires. The results shown in Table 4.4 indicate that convergence is achieved within $\approx 0.5\%$ for the magnitude and $\approx 0.03^o$ for the phase. Thus, the results for the segmentation of 5 wires per one side of the unit cell were used in computing the value for ar^t.

One sees from Table 4.4 that $|LR_o^t| = |RR_o^t|$ since clearly the scattered wave must necessarily be linearly polarized. Thus, $W = 0$ and ar^t shown in Table 4.5 reduces to just:

$$ar^t = \frac{||RR^t| + |LR^t||}{||RR^t| - |LR^t||}$$

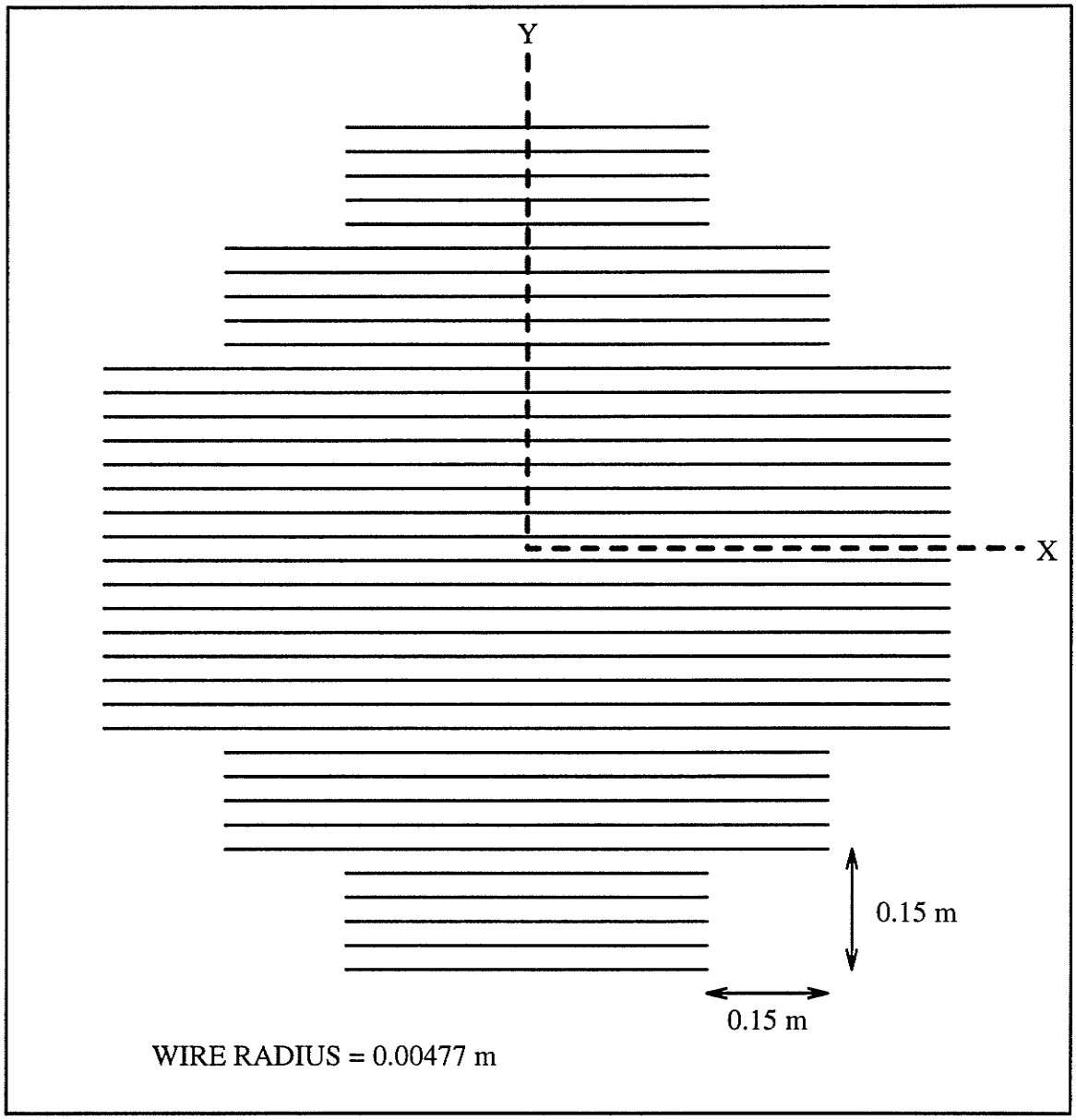

Figure 4.2: Octagonal LP polarizer plate made of circular wires as per the "same-surface-area" rule of thumb. This figure shows the case of a segmentation consisting of 5 wires per one 0.15 m side of the unit cell.

as though the incident wave phasor was not vectorially added to the scattered wave phasor. This situation owes the choice of making the incident wave appear to be a spherical wave so as to put both the incident and the scattered waves on a same footing in an attempt to quantify the process of the wave leaking through but not around the surface.

From Table 4.5, it is seen that the two cases with the 4.2 m observation sphere radius as well as the case of the array of 37 cells with the 8.4 m observation sphere radius stand out for both ar^r and ar^t. These cases correspond again to cases where the observation point does not lie clearly in the far-field region of the scatterer.

- the peak values for the $|LL|$, $|RR|$, $|RL|$ and $|LR|$ plots. Any scattered field value greater than $\sqrt{2}$ is already an indication that the observation point does not lie clearly in the far-field region of the array.

Table 4.4: Scattered E field results for two different segmentations of the octagonal LP polarizer plate. The observation sphere radius is 30.0 m.

#	θ^i ($^\circ$)	ϕ^i ($^\circ$)	RR_o^t		LR_o^t	
			mag. (V/m)	phase ($^\circ$)	mag. (V/m)	phase ($^\circ$)
5	0.0	0.0	0.07481	+63.45000	0.07481	+63.45000
6	"	"	0.07453	+63.45000	0.07453	+63.45000
5	45.0	45.0	0.05039	-120.3628	0.05036	+130.1695
6	"	"	0.05029	-120.3712	0.05026	+130.1579
5	30.0	70.0	0.05782	-118.9196	0.05781	+96.07105
6	"	"	0.05758	-118.9495	0.05757	+96.04097
# pertains to the number of wires per one 0.15 m side of the unit cell						

Table 4.5: Assessment of the indicators ar^r and ar^t for two different sizes of an octagonal array made of the Pierrot LHCPSS cells for various observation sphere radii. The inter-element spacing is 0.15 m and the incidence is normal.

# cells	r (m)	ar^r	ar^t
37	4.2	1.0184	1.0248
"	8.4	1.0093	1.0172
"	30.0	1.0028	1.0119
"	42.0	1.0022	1.0112
"	84.0	1.0014	1.0105
156	4.2	1.0233	1.0219
"	30.0	1.0026	1.0113
"	42.0	1.0014	1.0065
"	84.0	1.0013	1.0103
"	136.0	1.0014	1.0098

4.2 The Pierrot design

This section presents a numerical analysis of the Pierrot LHCPSS unit cell (see Figure 4.3) and of an octagonal array made of identical cells (see Figures 4.4, 4.5 and 4.6). Figure 4.6 pertains to the gangbuster arrangement which takes its name from reference [109]. The particular gangbuster array of Figure 4.6 has 148 cranks produced by introducing along the diagonal direction an additional 3 cranks between every two cranks of the octagonal array of Figure 4.4. Such an arrangement is possible when the transverse arm in the foreground plane of the unit cell is orthogonal to the transverse arm in the background plane of the same unit cell since, in principle, these two transverse arms do not obstruct one another at normal incidence. This situation permits to overlap the cells so as to produce a much denser array. For the gangbuster with 148 cranks, the inter-element spacing between nearest structures was 0.0375 m and so, the wire radius had to be reduced from the nominal 0.002 m down to 0.001 m in order to keep adjacent structures from touching one another.

The parameters under investigation in this section were the incidence angle, the frequency bandwidth, the cell size, the cell thickness, the number of cells and the observation sphere radius. A total of 40 segments was used for the crank wire, 14 segments for the longitudinal section and 13 segments for each transverse section.

Figures 4.7 and 4.8 show the induced current (magnitude and phase) when the incident polarization is LHCP and RHCP, respectively, and the plane wave is incident at $\theta^i = 0^o$ and $\phi^i = 0^o$ onto the single crank. Figures 4.9 and 4.10 show, respectively, the $|LL|$ and $|RL|$ plots for a LHCP plane wave incident at $\theta^i = 0^o$ and $\phi^i = 0^o$ onto the same single crank. Is is observed that the scattered wave is purely LHCP only for $\theta = \{0^o, 180^o\}$. Figures 4.11 and 4.12 show, respectively, the $|LR|$ and $|RR|$ plots for a RHCP plane wave incident at the same angle onto the same single crank. It is observed readily that the scattered field level is much reduced but not quite zero.

For off-normal incidence angles, the current distribution becomes imbalanced as

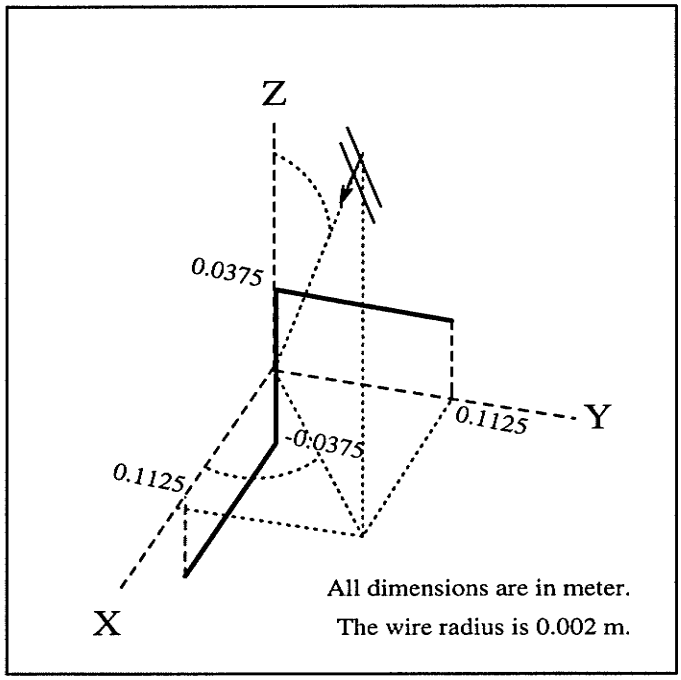

Figure 4.3: Configuration and orientation of the Pierrot LHCPSS cell for operation at 1 GHz.

the peak current is larger on the transverse arm that interacts first with the incident plane wave (the y transverse section corresponds to the length $L \leq 0.375\lambda$ along the wire in Figures 4.13 and 4.14). The rotational asymmetry of the cell was clearly revealed by the fact that the smallest imbalance occurred for the diagonal directions ($\phi = 45^o, 225^o$) and the largest imbalance, for the anti-diagonal directions ($\phi = 135^o, 315^o$). Figures 4.13 and 4.14 show the induced current (magnitude and phase) when the incident polarization is LHCP and RHCP, respectively, and the plane wave is incident at $\theta^i = 45^o$ and $\phi^i = 45^o$ onto the single crank. Figures 4.15, 4.16, 4.17 and 4.18 show, respectively, the $|LL|$, $|RL|$, $|LR|$ and $|RR|$ plots for a plane wave incident at $\theta^i = 45^o$ and $\phi^i = 45^o$ onto the same single crank. It was observed that the $|LL|$ and $|RL|$ plots remained practically the same in shape when the frequency was varied over a 15% range or when the incidence angle was varied within the range $\theta^i < 60^o$. The $|LR|$ and $|RR|$ plots were more sensitive to changes with respect to frequency and incidence angle but their peak values remained still much smaller than

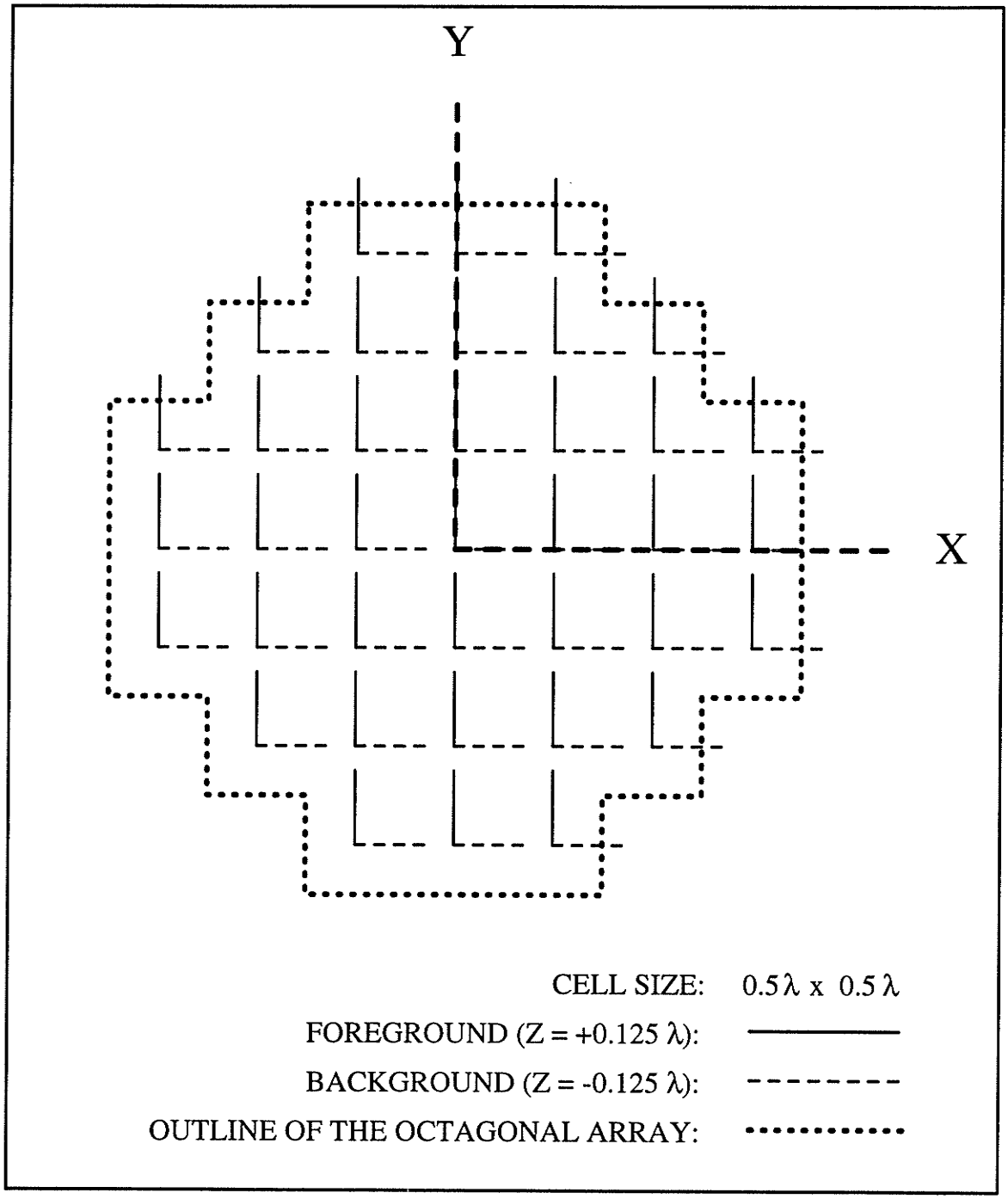

Figure 4.4: Configuration and orientation of the octagonal array made of 37 identical Pierrot LHCPSS cells for operation at 1 GHz.

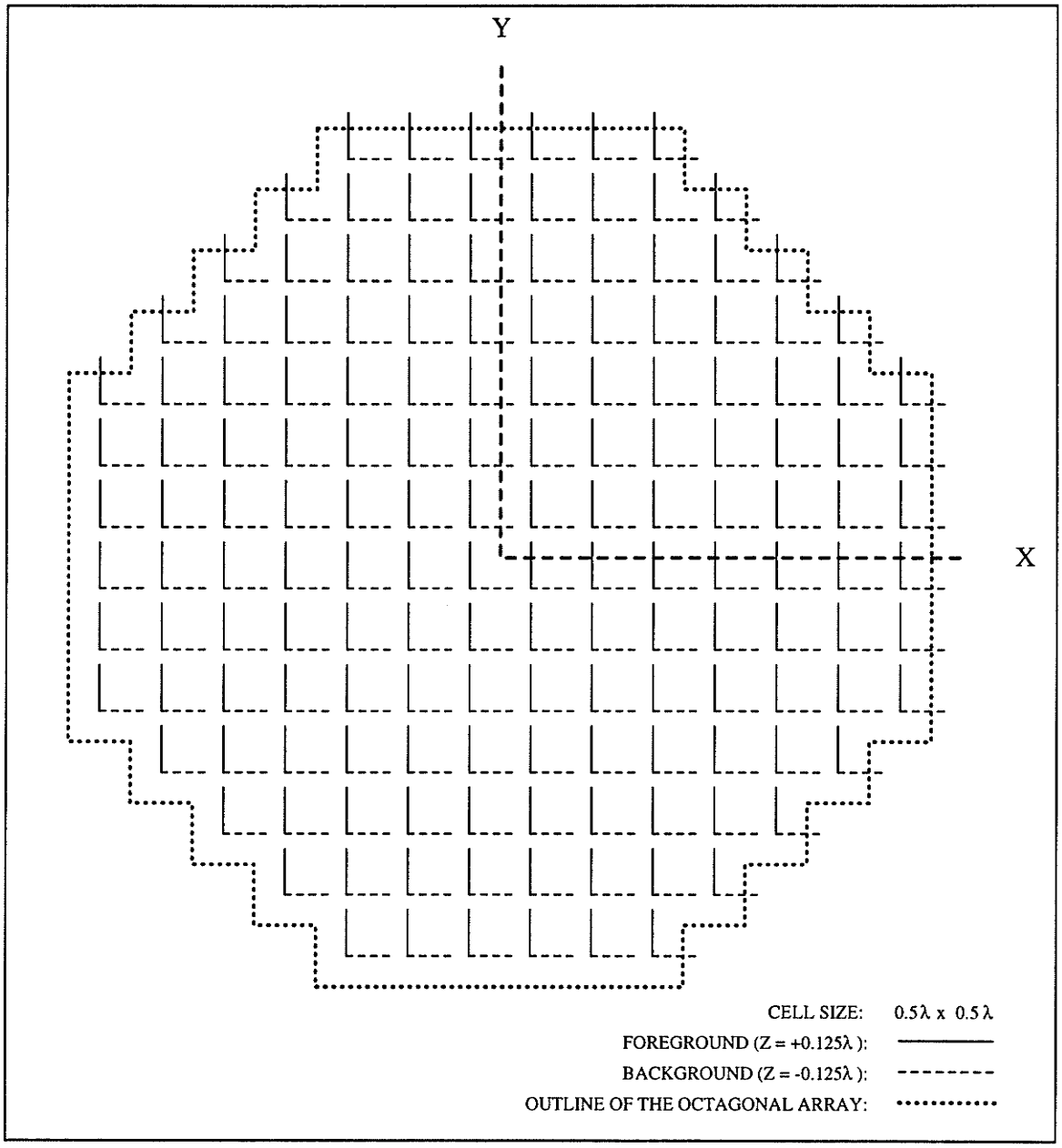

Figure 4.5: Configuration and orientation of the octagonal array made of 156 identical Pierrot LHCPSS cells for operation at 1 GHz.

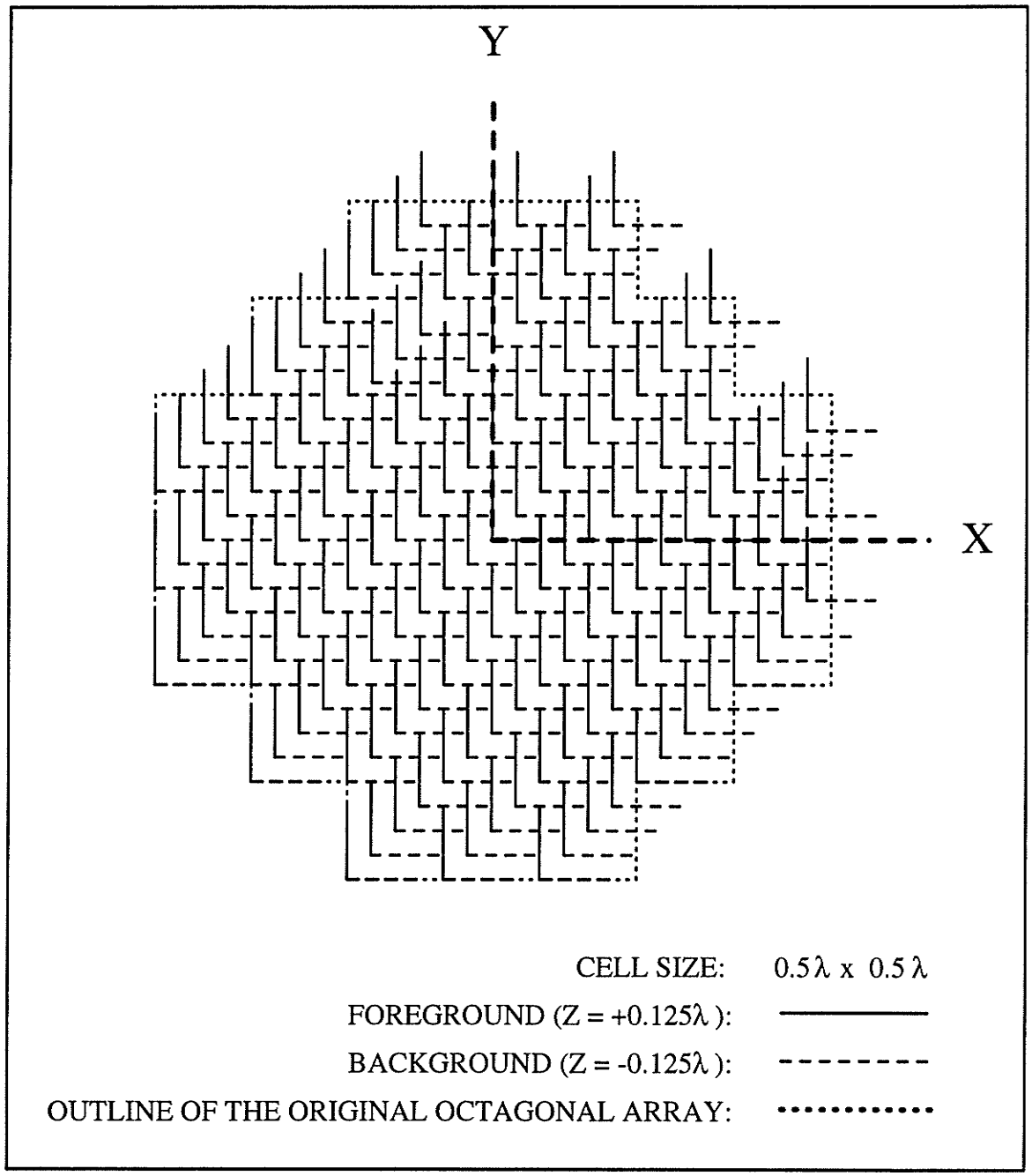

Figure 4.6: Configuration and orientation of the octagonal gangbuster array made of 148 identical Pierrot LHCPSS cells for operation at 1 GHz.

those of their counterparts for LHCP incidence.

The above simulations (Figure 4.19 to Figure 4.26) were repeated for an octagonal array of 37 identical cells laid as per a square grid with 0.15 m, i.e. $\lambda/2$, inter-element spacing. The formation of two pencil beams is clearly seen. It is observed also that the CPSS effect is much stronger for the array since the ratio $|LL/RR|$ was ≈ 11.9 for the octagonal array illuminated at normal incidence instead of just ≈ 0.7 for the single crank. It is noted, however, that this ratio is not equal to 37, the number of cells.

Only 3 segments per longitudinal or transverse section for each wire were used in the octagonal array so as to have the cells of all arrays segmented identically while keeping the total number of segments for the largest array below 1500 so as not to incur too long a CPU run time. For comparison, the shape and the peak magnitude of the plots of the scattered electric field for the single crank remained nearly the same for such a coarser segmentation of the wire as for the earlier segmentation with 40 segments (0.02791 instead of 0.02812 for Figure 4.9 and 0.01920 instead of 0.01936 for Figure 4.10). Hence, it is believed that the scattered electric field obtained for the octagonal array of 37 cells is still meaningful despite the coarser segmentation of each wire.

For corner incidence ($\theta^i = 45^o$ and $\phi^i = 45^o$), the maxima of the beams were slightly off the reflection and the transmission angles predicted by geometrical optics (e.g. $\theta^r \approx 43^o$ instead of 45^o), owing to the finite area of the scattering surface [18].

The reflection beam values were 0.12080 V/m and 0.08948 V/m for the normal and the corner incidences, respectively. For comparison, the corresponding values of LHCP reflected from a solid reflector of identical shape and surface area, analyzed with NEC-2 by wire-grid modelling (see Figure 4.1), were 0.13620 V/m and 0.09664 V/m, respectively (see Figures 4.27, 4.28, 4.29 and 4.30). Thus, the CPSS appears less opaque than the solid PEC reflector.

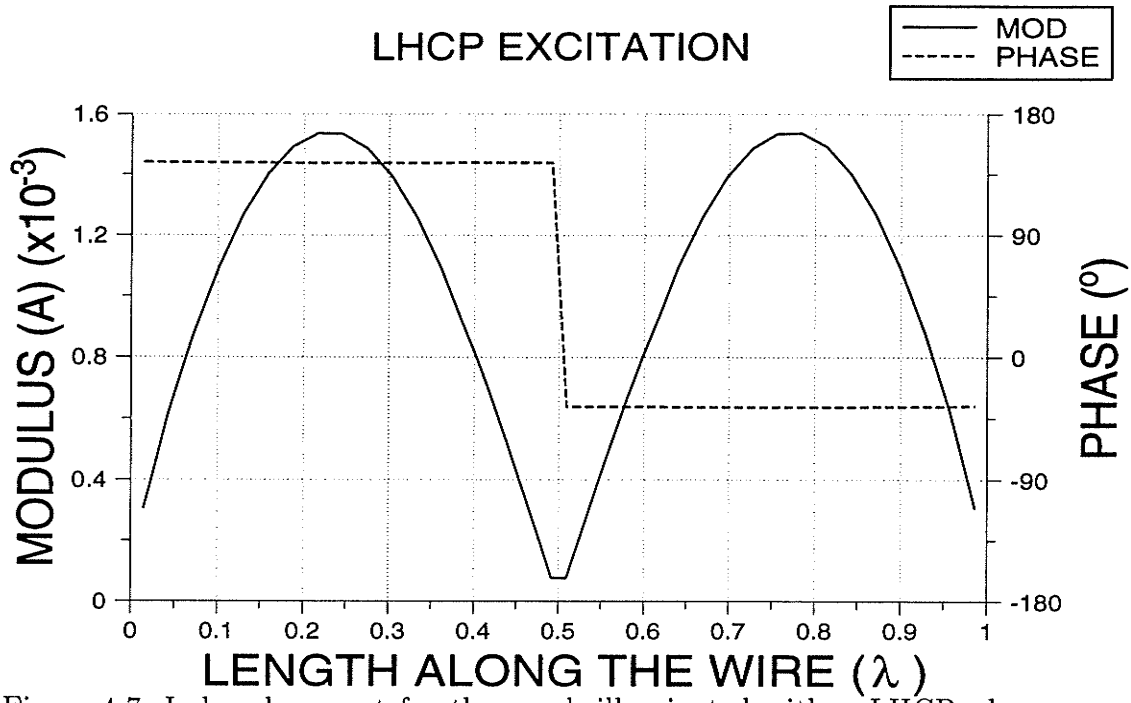

Figure 4.7: Induced current for the crank illuminated with a LHCP plane wave incident at $\theta^i = 0^o$ and $\phi^i = 0^o$.

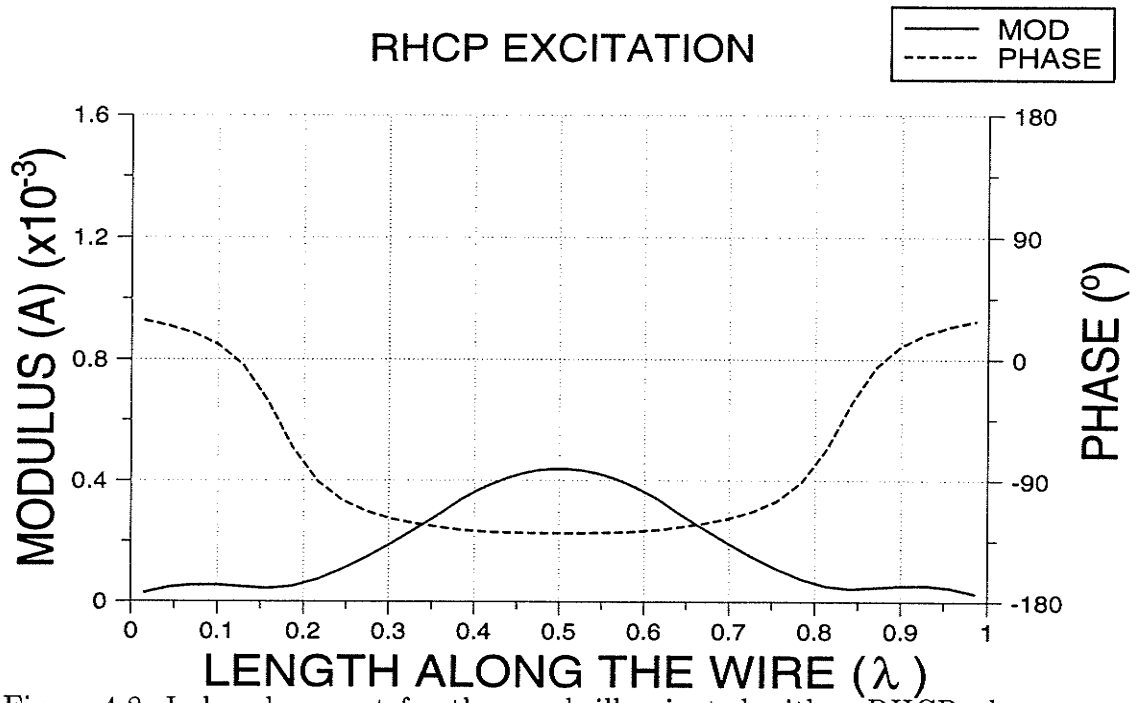

Figure 4.8: Induced current for the crank illuminated with a RHCP plane wave incident at $\theta^i = 0^o$ and $\phi^i = 0^o$.

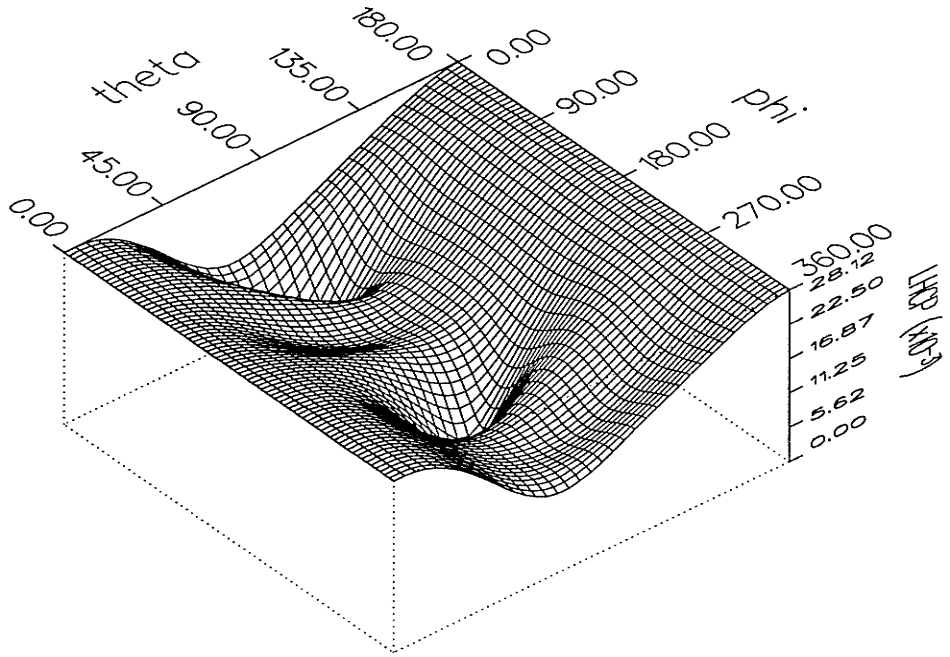

Figure 4.9: $|LL|$ for the crank, with $\theta^i = 0^o$, $\phi^i = 0^o$ and $r = 4.2\ m$.

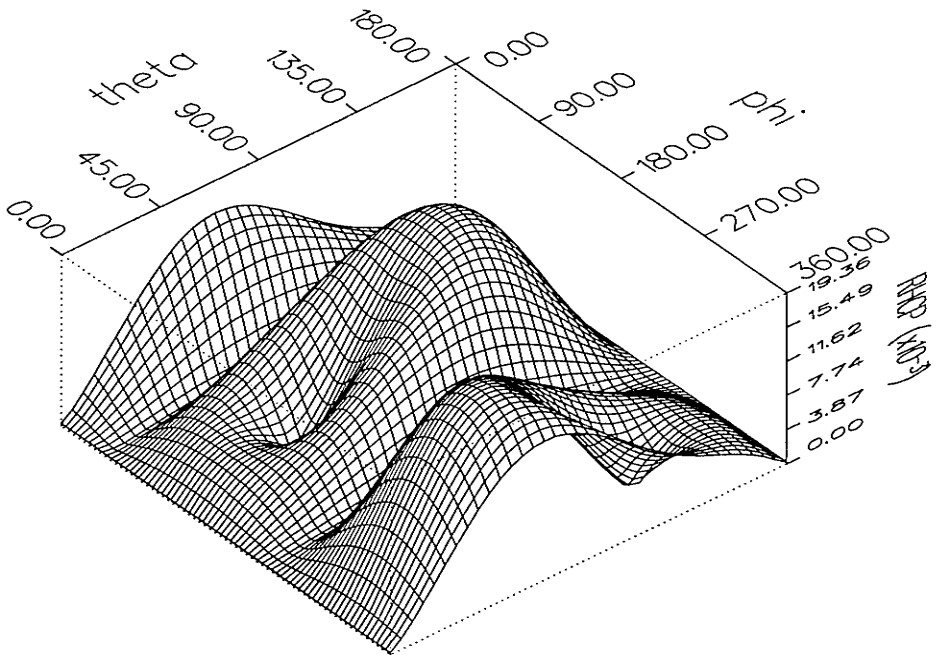

Figure 4.10: $|RL|$ for the crank, with $\theta^i = 0^o$, $\phi^i = 0^o$ and $r = 4.2\ m$.

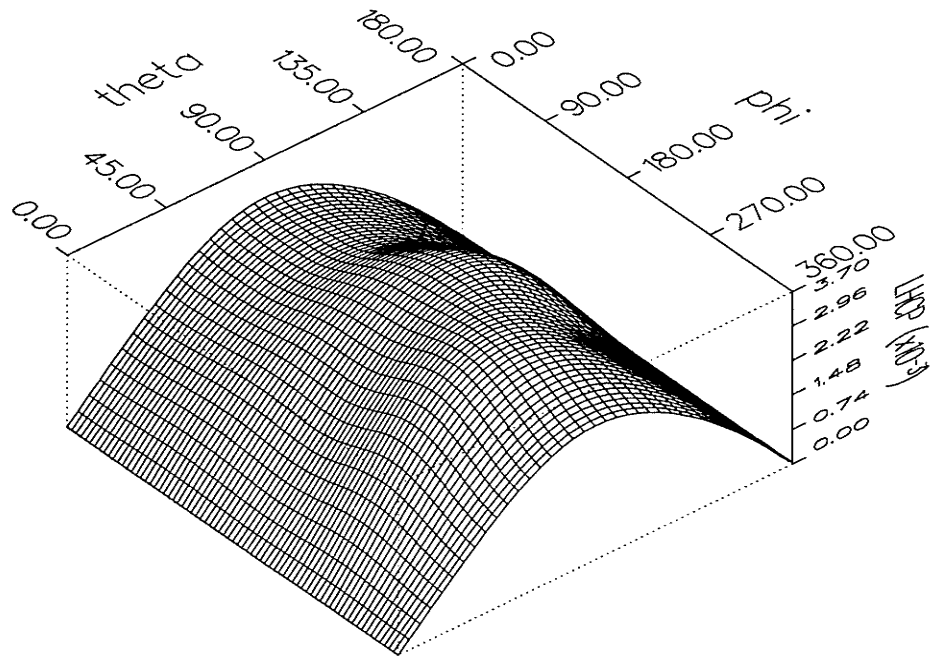

Figure 4.11: $|LR|$ for the crank, with $\theta^i = 0^o$, $\phi^i = 0^o$ and $r = 4.2\ m$.

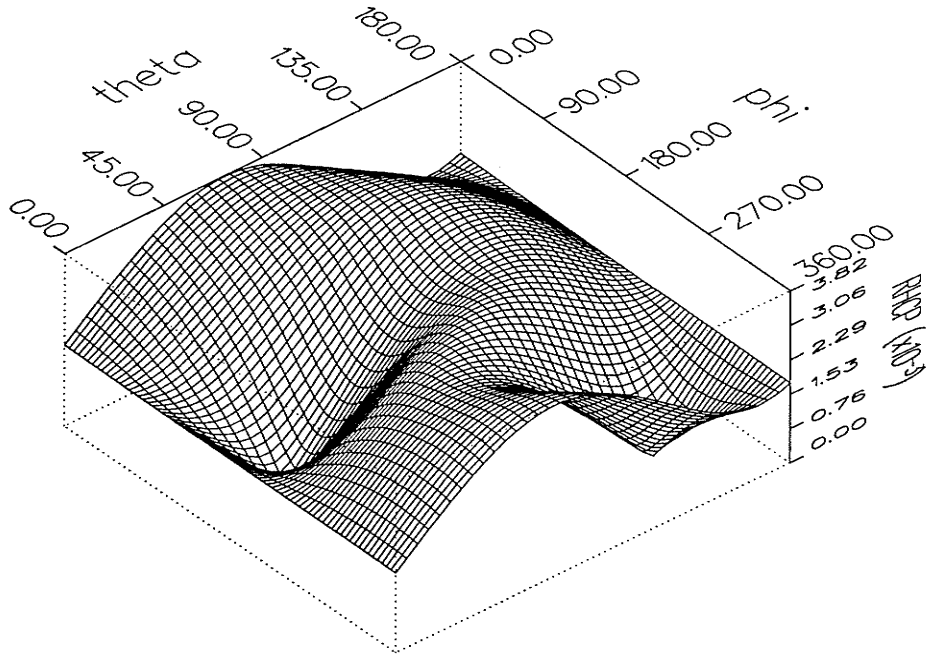

Figure 4.12: $|RR|$ for the crank, with $\theta^i = 0^o$, $\phi^i = 0^o$ and $r = 4.2\ m$.

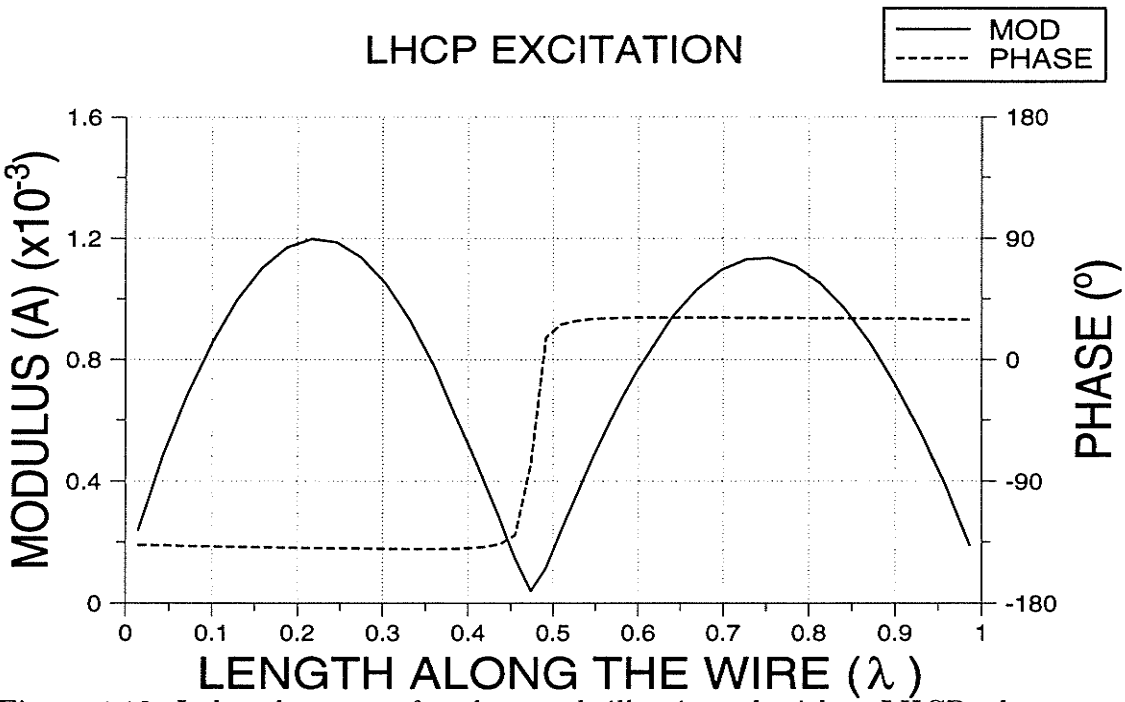

Figure 4.13: Induced current for the crank illuminated with a LHCP plane wave incident at $\theta^i = 45^o$ and $\phi^i = 45^o$.

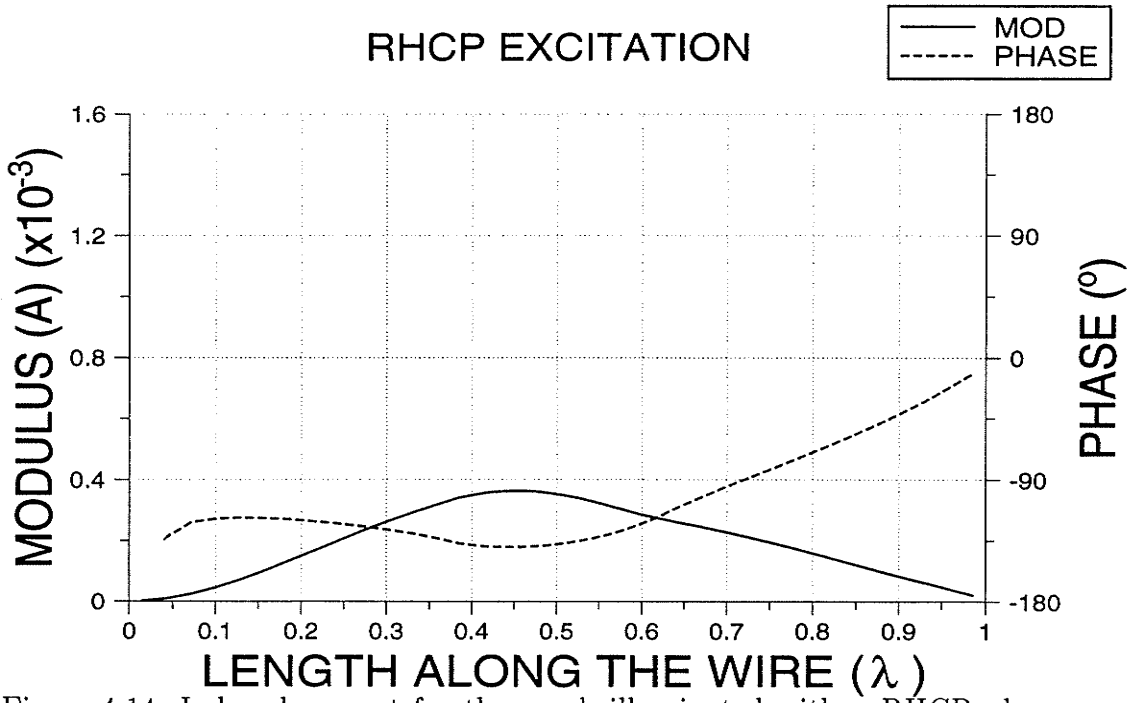

Figure 4.14: Induced current for the crank illuminated with a RHCP plane wave incident at $\theta^i = 45^o$ and $\phi^i = 45^o$.

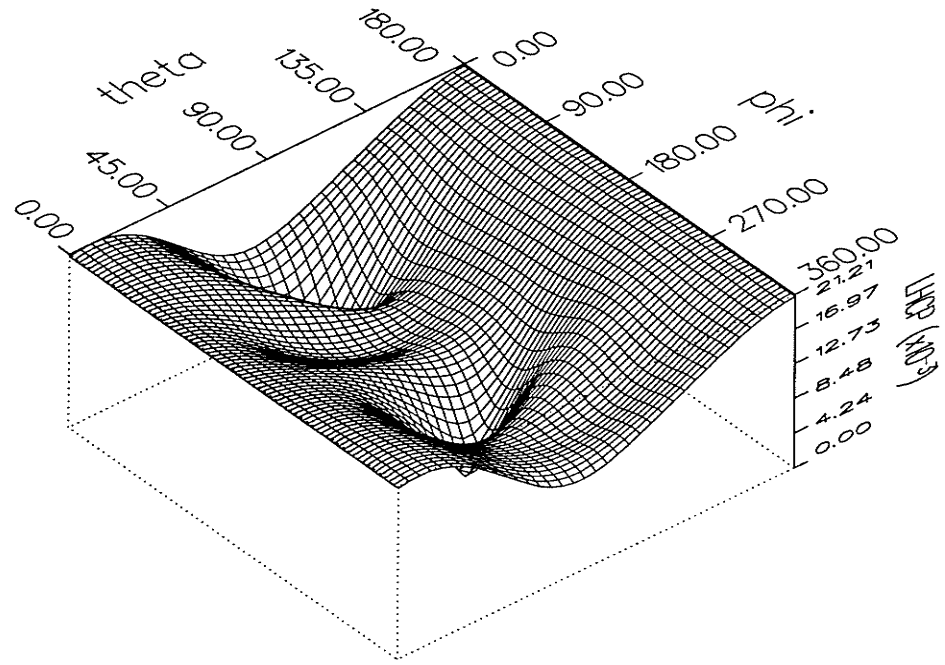

Figure 4.15: $|LL|$ for the crank, with $\theta^i = 45°$, $\phi^i = 45°$ and $r = 4.2\ m$.

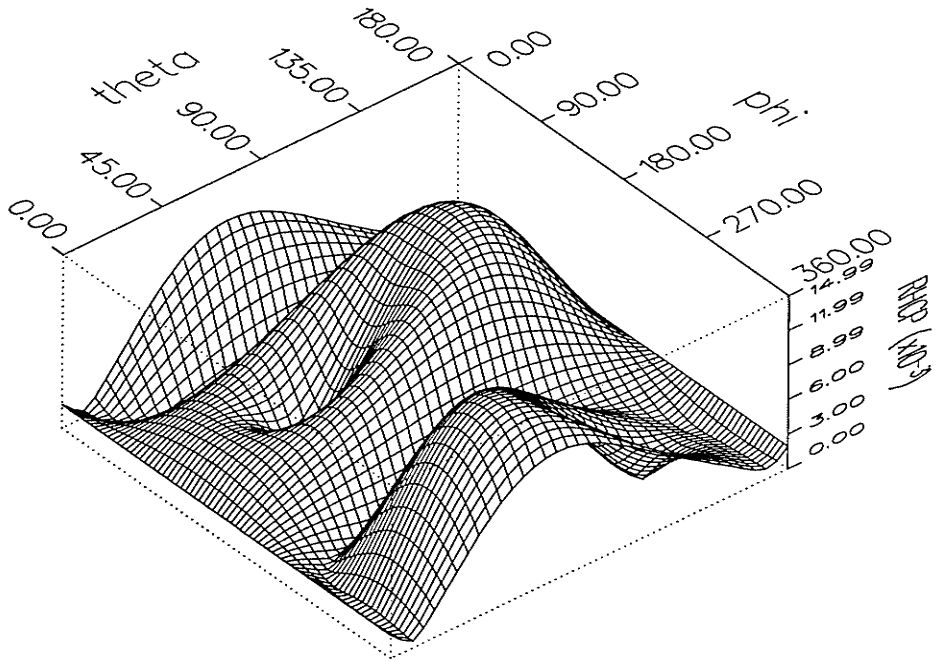

Figure 4.16: $|RL|$ for the crank, with $\theta^i = 45°$, $\phi^i = 45°$ and $r = 4.2\ m$.

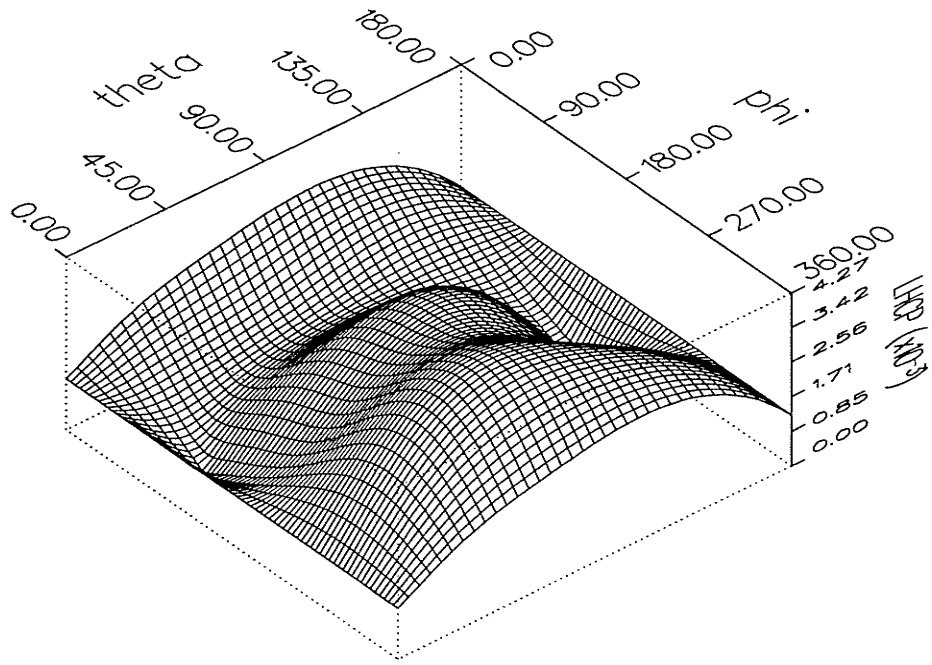

Figure 4.17: $|LR|$ for the crank, with $\theta^i = 45^o$, $\phi^i = 45^o$ and $r = 4.2\ m$.

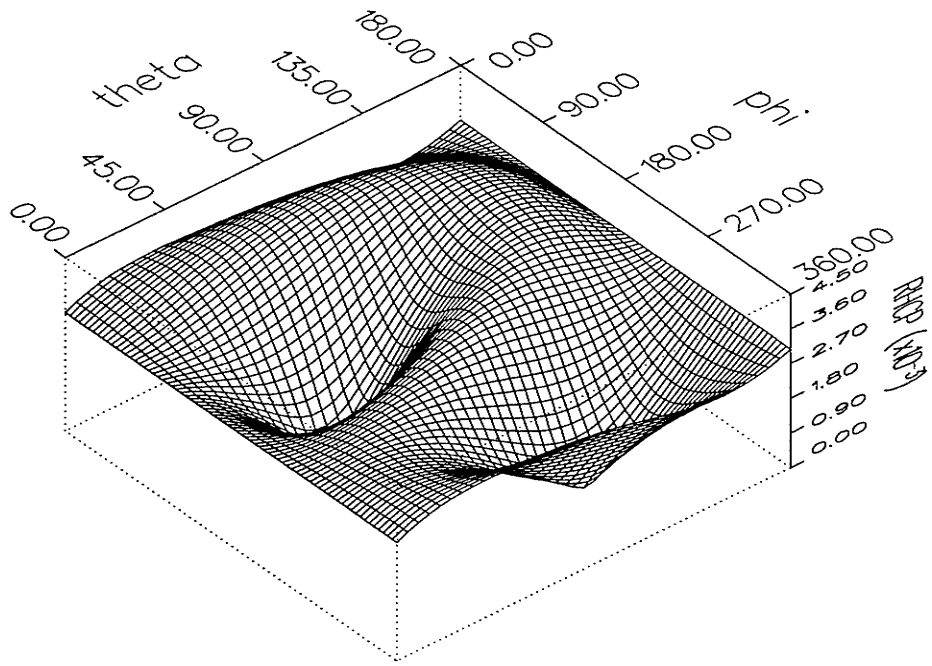

Figure 4.18: $|RR|$ for the crank, with $\theta^i = 45^o$, $\phi^i = 45^o$ and $r = 4.2\ m$.

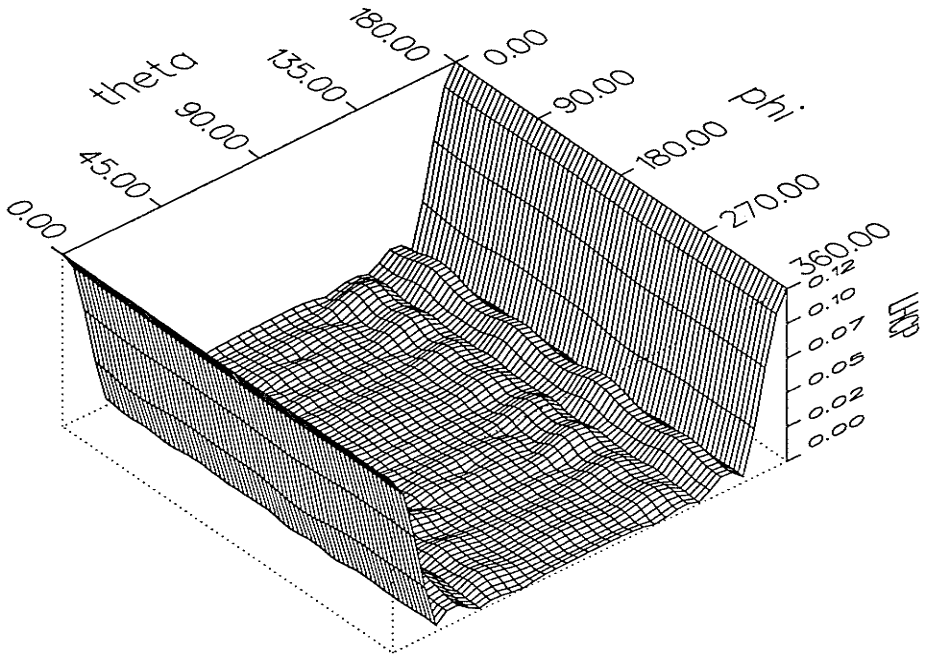

Figure 4.19: $|LL|$ for a 37 Pierrot cell octagonal array, with $\theta^i = 0^o$, $\phi^i = 0^o$ and $r = 30.0\ m$.

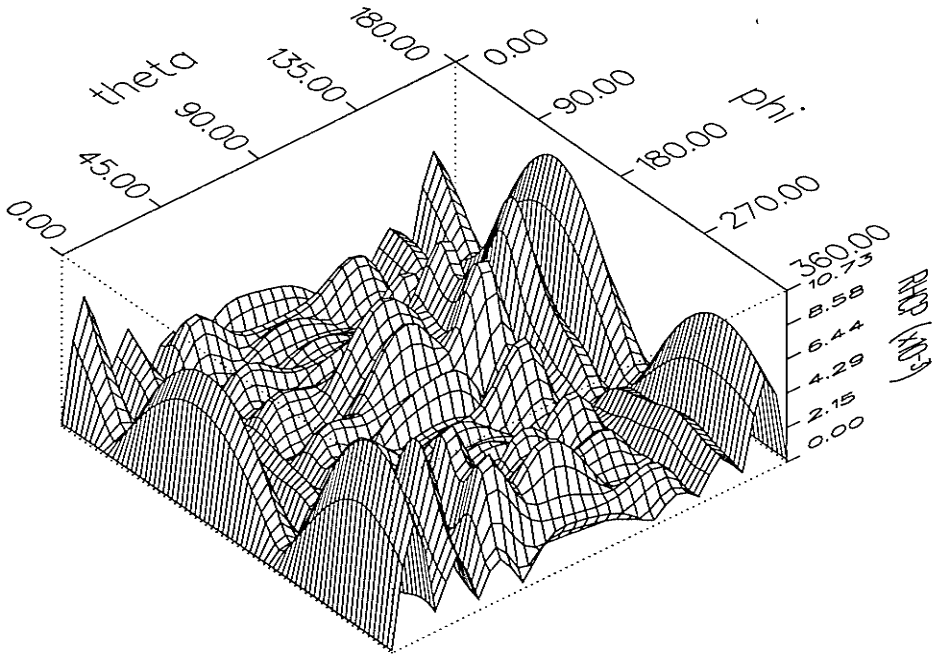

Figure 4.20: $|RL|$ for a 37 Pierrot cell octagonal array, with $\theta^i = 0^o$, $\phi^i = 0^o$ and $r = 30.0\ m$.

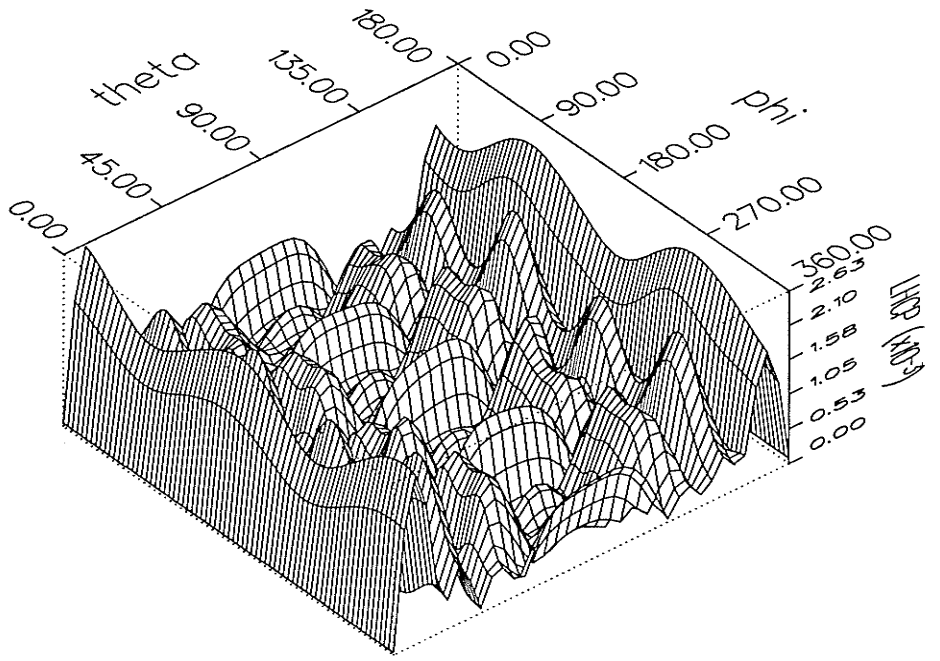

Figure 4.21: $|LR|$ for a 37 Pierrot cell octagonal array, with $\theta^i = 0^o$, $\phi^i = 0^o$ and $r = 30.0\ m$.

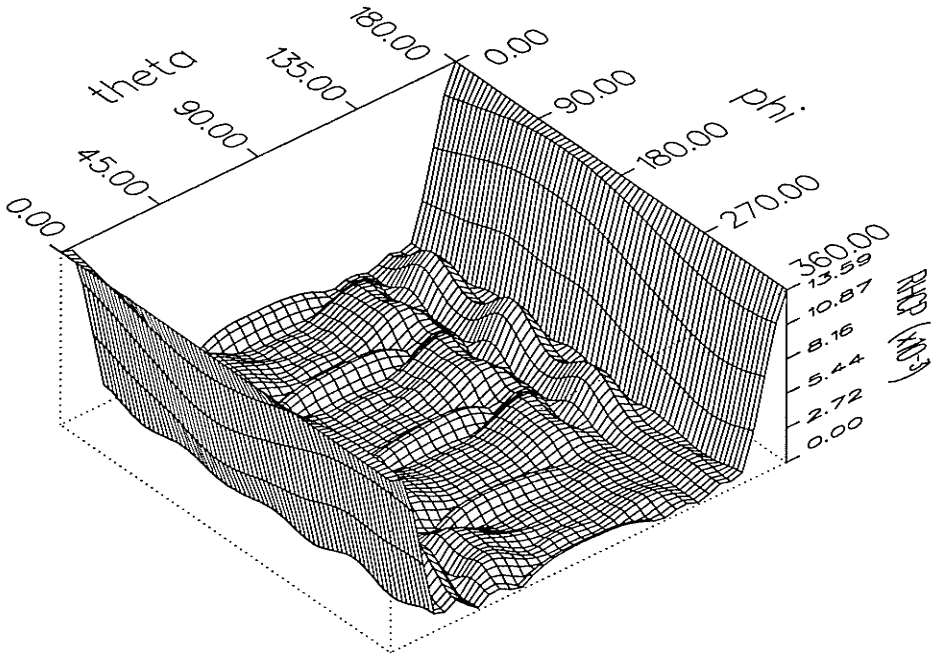

Figure 4.22: $|RR|$ for a 37 Pierrot cell octagonal array, with $\theta^i = 0^o$, $\phi^i = 0^o$ and $r = 30.0\ m$.

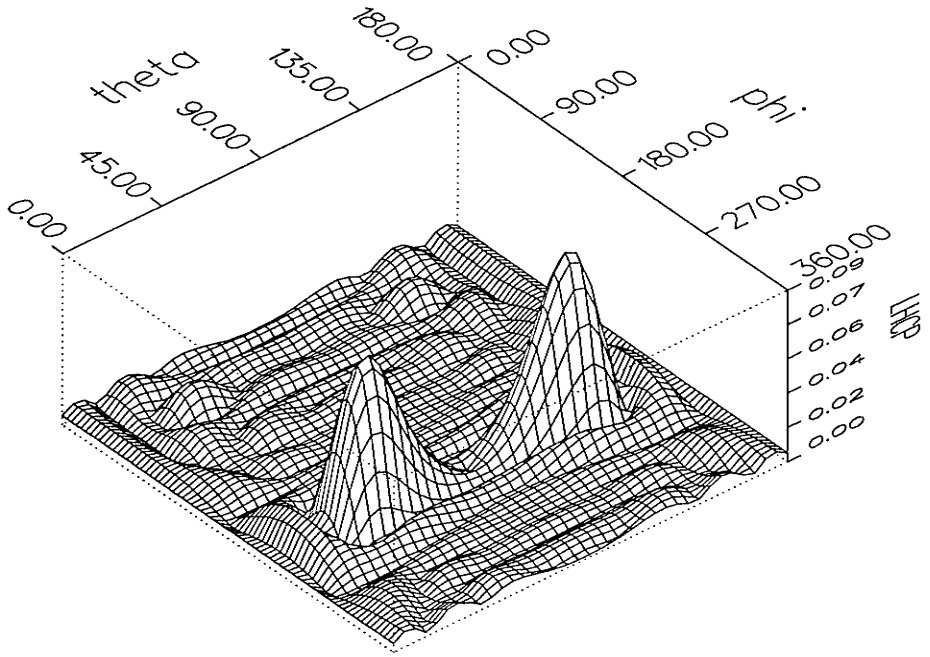

Figure 4.23: $|LL|$ for a 37 Pierrot cell octagonal array, with $\theta^i = 45^o$, $\phi^i = 45^o$ and $r = 30.0\ m$.

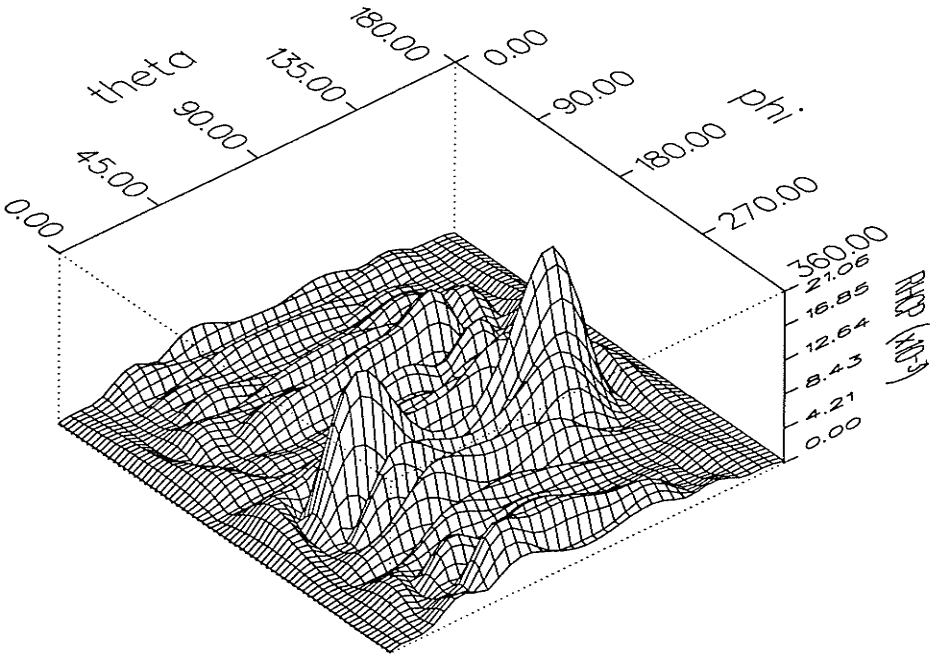

Figure 4.24: $|RL|$ for a 37 Pierrot cell octagonal array, with $\theta^i = 45^o$, $\phi^i = 45^o$ and $r = 30.0\ m$.

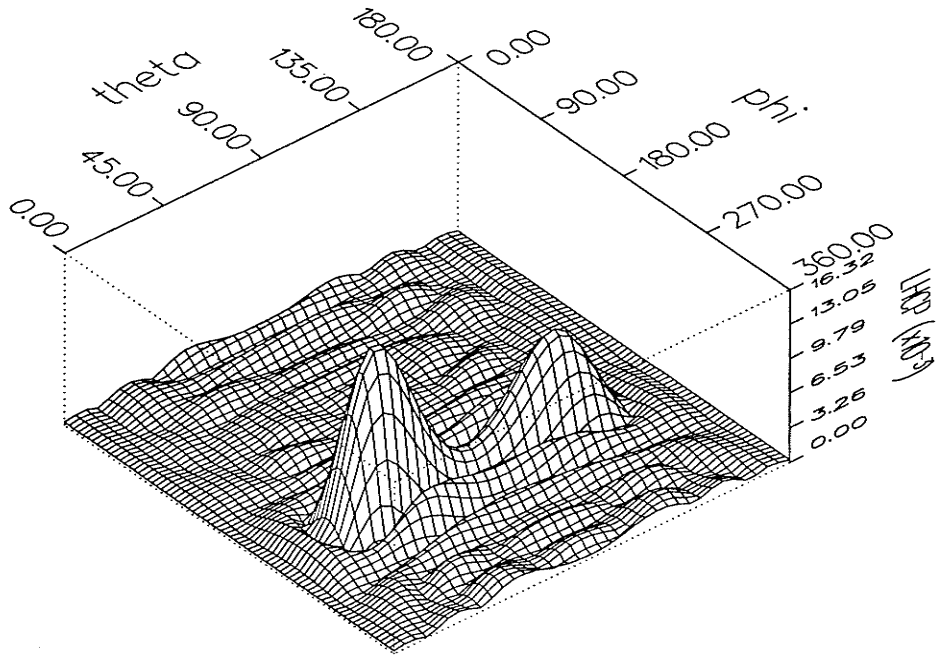

Figure 4.25: $|LR|$ for a 37 Pierrot cell octagonal array, with $\theta^i = 45^o$, $\phi^i = 45^o$ and $r = 30.0\ m$.

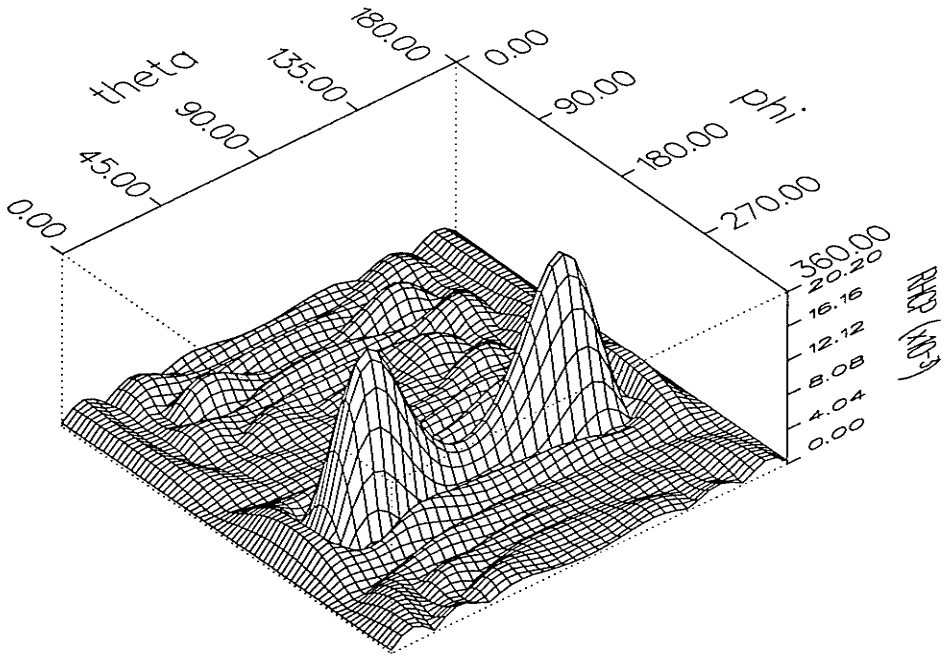

Figure 4.26: $|RR|$ for a 37 Pierrot cell octagonal array, with $\theta^i = 45^o$, $\phi^i = 45^o$ and $r = 30.0\ m$.

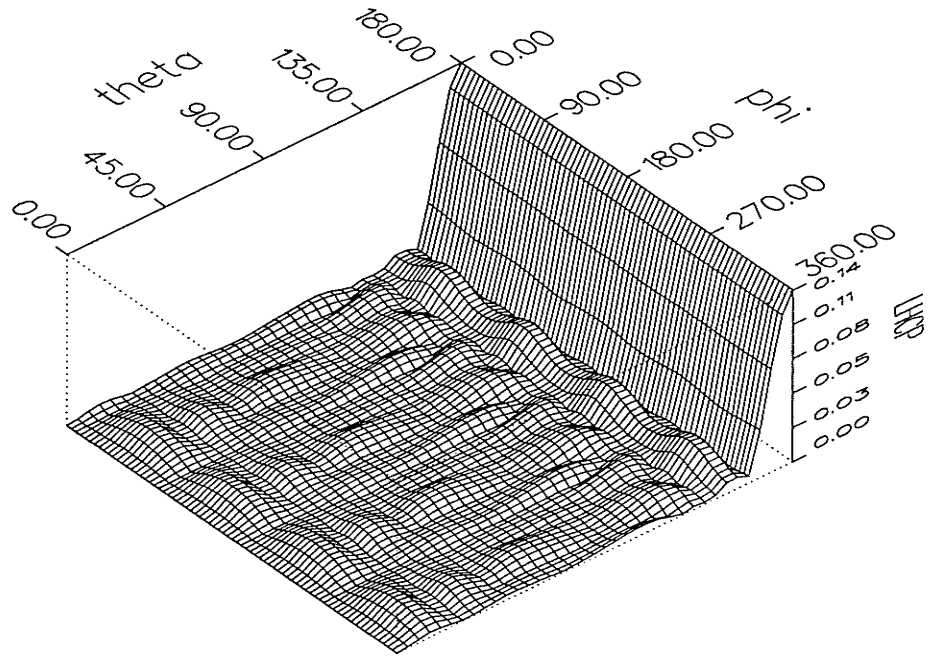

Figure 4.27: $|LL|$ for the octagonal wire-grid reflector, with $\theta^i = 0°$, $\phi^i = 0°$ and $r = 30.0\ m$.

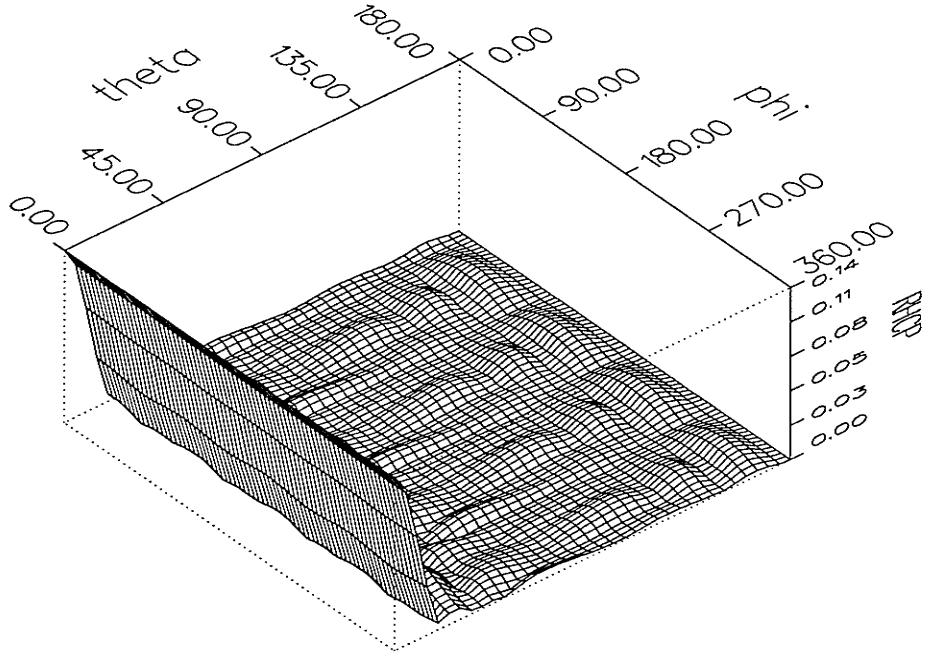

Figure 4.28: $|RL|$ for the octagonal wire-grid reflector, with $\theta^i = 0°$, $\phi^i = 0°$ and $r = 30.0\ m$.

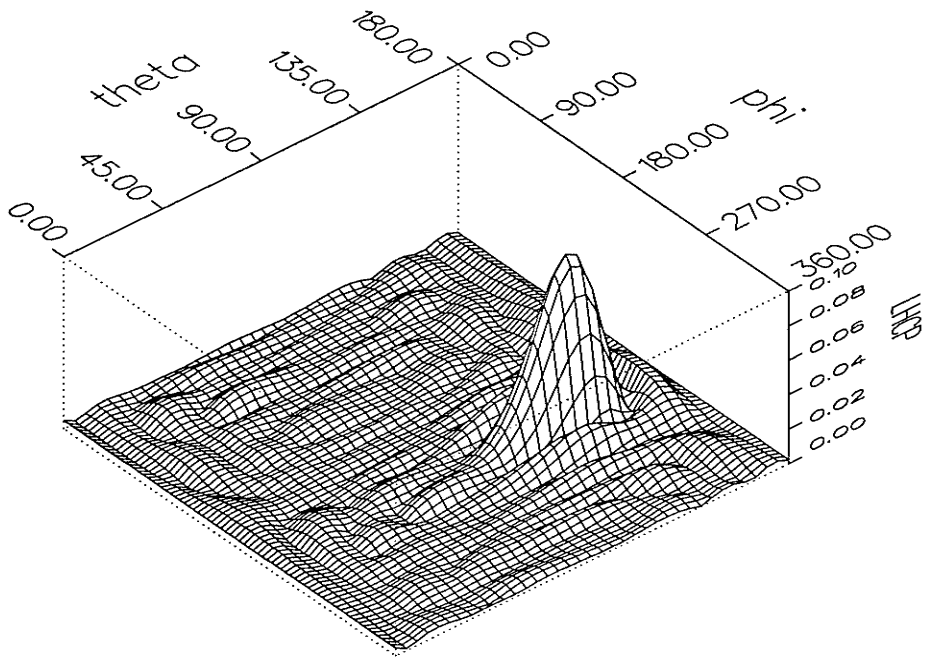

Figure 4.29: $|LL|$ for the octagonal wire-grid reflector, with $\theta^i = 45^o$, $\phi^i = 45^o$ and $r = 30.0\ m$.

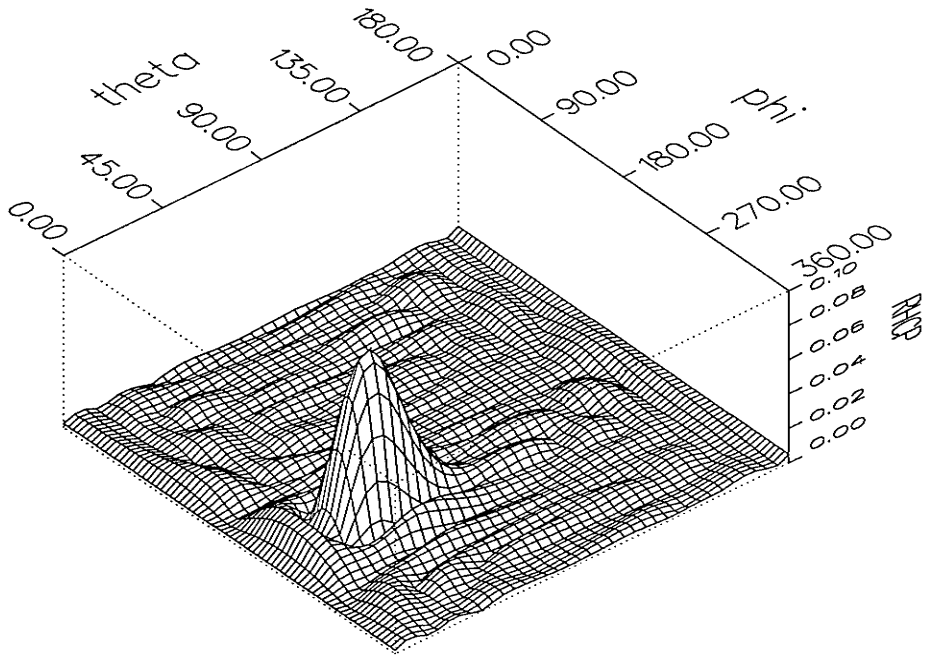

Figure 4.30: $|RL|$ for the octagonal wire-grid reflector, with $\theta^i = 45^o$, $\phi^i = 45^o$ and $r = 30.0\ m$.

Table 4.7 shows the corresponding effective surface area of the arrays. The effective surface area is computed here as the number of cells times the surface area of each cell, thus approximating the contour of the octagonal geometry with step edges. Tables 4.8 to 4.18 show the scattered field levels of the octagonal array with two different numbers of cells, two different incidence angles and three different observation sphere radii.

It was observed that the $|LL|$ and $|RR|$ plots at normal incidence, 0.25 m inter-element spacing and 4.2 m observation sphere radius displayed an anomaly in that the scattering level at $\theta^s = 0^o$ was no longer the peak value of the plot (0.96654 vs 1.79772 for $|LL|$, and 0.02374 vs 0.04282 for $|RR|$). This situation owes to the fact that the array with 0.25 m inter-element spacing is so large (1.75 m radius) that the observation point on the observation sphere with 4.2 m radius can no longer be considered to lie in the far-field region of the array. This situation is even more critical when the observation point lies at large θ values in which case some cells at the edge of the array lie relatively close to the observation point.

The far-field region is usually taken to lie beyond the distance $2D^2/\lambda$ in the direction normal to the array, where D is the diameter of the array. Table 4.7 shows the $2D^2/\lambda$ values for the various cases at hand. The observation sphere radius of 84.0 m ensures that the observation point lies in the far field region of all cells, even for the largest array used herein. The $|LL|$ values in the Tables 4.12, 4.13, 4.15 and 4.16 for the 156 cell array are now consistently from about 4 to about 5 times larger than the corresponding $|LL|$ values for the 37 cell array. This increase is about commensurate with the increase in surface area of the array, i.e. $\frac{156}{37} \approx 4.2$. It was also confirmed that the scattering values at $\theta^s = 0^o$ for the $|LL|$ and $|RR|$ plots of all arrays illuminated at normal incidence were again the peak values of the plots. For the cases that the observations point lied in the far-field regions for both the 30.0 m and the 84.0 m observation sphere radii, the $|LL|$ level is decreased by a factor ≈ 20

in accordance with the $1/r$ behavior of the field in the far-field region. Furthermore, all peak values in Tables 4.11 and 4.14 are below $\sqrt{2}$.

In order to ensure that the observation point lies clearly in the far-field region for the case of the array as large as 156 cells with 0.15 m inter-element spacing while also maintaining the field levels large enough to display a few significant digits for the case of the smaller array with 37 cells and 0.15 m inter-element spacing, an observation sphere radius of 30.0 m was chosen for all simulations below.

When the observation point lies clearly in the far-field region of the array, it is noted that:

- As mentioned earlier, it would appear that the compensation scheme used in computing the *Leakg* values is not very effective when the case under study departs too much from the reference case which is a scatterer of shape and surface area corresponding to an octagonal array of 37 cells laid as per a square grid with 0.15 m inter-element spacing.

- Increasing the size of the octagonal array by increasing the number of elements increases $|LL^r|$ but it does not change significantly the ratio $|LL/RR|$ as does a change in the inter-element spacing. This suggests that 37 cells are sufficient to quantify accurately the CPSS operation of a design under study.

- Varying the incidence from normal to corner incidence increases the *Blckg* value and tends to decrease the *Leakg* value, as though the surface became denser, which situation might be expected from heuristic[4] considerations.

- The axial ratios are seen to degrade noticeably under corner incidence. Furthermore, the inter-element spacing that was found optimal with respect to

[4]Heuristic arguments, however, can be fallacious and should not be construed as proofs on their own merit. For example, the formation of grating lobes is favored by off-normal incidence even though the array appears visually increasingly more solid as the incidence angle departs from being normal, and even though the formation of grating lobes is discouraged by denser, i.e. more solid-like, arrays.

maximizing $|LL^r|$ at normal incidence, i.e. 0.25 m, is no longer optimal at corner incidence. Moreover, the performance degradation incurred by off-normal incidence is more severe for the the inter-element spacing optimal at normal incidence than that for the inter-element spacing not optimal at normal incidence.

This situation arises because, for the 0.25 m inter-element spacing, there is formation of grating lobes which causes a redistribution of the energy from the main lobe to the grating lobes. The grating lobe formation becomes even more troublesome as the incidence departs from normal, except for the case of the inter-element spacing being less than or equal to a half-wavelength in which case the entire visible region is then free of grating lobes [105, p. 44].

- The axial ratios ar^r and ar^t are smallest, i.e. best, at the expected frequency of 1.00 GHz and the expected cell thickness of $\lambda/4$, although the smallest values of $Blckg$ and $Leakg$ as well as the largest value of $|LL^r/RR^r|$ are not found at that frequency nor at that cell thickness value.

- The $Blckg$ and the ar^t values vary much more than the $Leakg$ and ar^r values on a percentage basis, respectively. This situation is indicative of the weakness of idealizing the principle of operation as assuming that the structure is transparent under RHCP illumination. Defining the operating range on the basis of $ar^t \leq 2$, one obtains:

  - 0.88 $GHz < f <$ 1.035 GHz, hence the performance is asymmetrical with respect to the nominal value of $f = 1.0$ GHz;
  - $0.234\lambda <$ cell thickness $< 0.260\lambda$, hence the performance is asymmetrical with respect to the nominal value of 0.250λ.
  - $\theta^i <<< 5°$; hence the performance degrades very quickly as the incidence departs from being normal.

- The performance has a complicated behavior with respect to θ^i and ϕ^i. The maximum $|LL^r|$ values occur for the diagonal directions, i.e. $\phi^i = 45^o$ and 225^o, whereas the minimum values occur for the anti-diagonal directions, i.e. $\phi^i = 135^o$ and 315^o. The ar^r and ar^t values are also better for the diagonal directions than for the anti-diagonal directions. The case of $\theta^i = 45^o$ with $\phi^i = 135^o$ stands out particularly as presenting a very poor performance.

  The diagonal and anti-diagonal directions correspond precisely to those for which the imbalance of the current induced on the wire was observed to be minimum and maximum, respectively. Thus, a current imbalance appears to degrade the performance of the Pierrot CPSS. This observation is consistent with the fact that the currents induced on the transverse sections depend on the tangential E field component of the incident wave. Thus, the effective length of each transverse wire varies by different amounts as the incidence angle is varied, this situation resulting in the imbalance of induced currents.

- The best choice of inter-element spacing on the basis of maximizing $|LL^r/RR^r|$ appears to be 0.25 m but there is formation of grating lobes which situation is undesirable. For the inter-element spacing between 0.12 m and 0.19 m, it is seen that the *Blckg* increases and the *Leakg* decreases as though the surface appears denser as the inter-element spacing decreases, which situation might be expected from heuristic considerations. For the inter-element spacing larger than 0.19 m, the *Leakg* value is seen to decrease but this situation might be an artifact resulting from the compensation scheme used in computing the *Leakg* value, when the case under study departs too much from the reference case.

- The *Blckg* level decreases up to a certain point as the gangbuster array becomes denser! However, in comparing the gangbuster arraying arrangement with the usual arraying arrangement on a square grid with $\lambda/2$ inter-element spacing, it

is seen that the latter displays yet better values of *Blckg* and *Leakg* although it displays also smaller $|LL^r|$ values for comparable ar^r and ar^t values. For this reason, gangbuster arrangements will not be considered any further. The effect of varying the wire radius from 0.002 m down to 0.001 m affects mostly only the *Blckg* values. As expected from heuristic considerations, the *Blckg* values are seen to decrease as the wire radius is decreased.

- Surprisingly, the results are not all the same for $\theta^i = 0^o$ as ϕ^i varies. This situation is brought about by the fact that the phase values for the near-field components as given by NEC-2 vary also with ϕ^i. For instance, the results for $\phi^i = \{0^o, 135^o\}$ are presented in Table 4.6. It is seen that the phase difference between the corresponding components of the two cases is precisely the phase difference between the two ϕ^i values, i.e. 135^o. Only the results for $\phi^i = 0^o$ will be considered as meaningful herein.

The GSM for the octagonal array made of 37 identical Pierrot LHCPSS cells with $\lambda/2$ inter-element spacing and illuminated at normal incidence was obtained as:

$$S(X,Y) = \begin{pmatrix} S_{11}^{XX} & S_{11}^{XY} & S_{12}^{XX} & S_{12}^{XY} \\ S_{11}^{YX} & S_{11}^{YY} & S_{12}^{YX} & S_{12}^{YY} \\ S_{21}^{XX} & S_{21}^{XY} & S_{22}^{XX} & S_{22}^{XY} \\ S_{21}^{YX} & S_{21}^{YY} & S_{22}^{YX} & S_{22}^{YY} \end{pmatrix} =$$

Table 4.6: Near-field results given by NEC-2 for two different ϕ^i values but the same $\theta^i = 0^o$.

ϕ^i	E_x		E_y		E_z	
$(^o)$	$\times 10^{-1}(V/m)$	$(^o)$	$\times 10^{-1}(V/m)$	$(^o)$	$\times 10^{-3}(V/m)$	$(^o)$
0	0.8530	+179.16	0.8553	-90.79	0.1705	-139.14
135	0.8530	-45.84	0.8553	+44.21	0.1705	-4.14

$$\begin{pmatrix} 1.2484\angle -160.32^o & 1.3333\angle -58.01^o & 1.8444\angle -39.58^o & 1.3333\angle -148.07^o \\ 1.3333\angle -58.01^o & 1.2484\angle +19.80^o & 1.3333\angle +32.05^o & 1.8444\angle -39.58^o \\ 1.8444\angle -39.58^o & 1.3333\angle +32.05^o & 1.2484\angle +19.80^o & 1.3333\angle -58.01^o \\ 1.3333\angle -148.07^o & 1.8444\angle -39.58^o & 1.3333\angle -58.01^o & 1.2484\angle -160.32^o \end{pmatrix}$$

where the incidence propagation vector was taken as pointing outwardly from the origin of the coordinate system. Each scattering coefficient is described by a pair whose first number pertains to the magnitude and second number pertains to the phase. Surprisingly, the magnitudes are larger than 1.0 V/m, the magnitude of the linearly polarized incident plane wave! As expected, the matrix is symmetrical with respect to the diagonal owing to the structure being reciprocal but surprisingly, the matrix is also symmetrical with respect to the anti-diagonal. Also as expected, the structure does not have the longitudinal reflection symmetry since one has:

$$\left.\begin{array}{l} +C_{21}^{EH} = -S_{21}^{XY} = +S_{21}^{YX} = -C_{21}^{HE} \Longrightarrow C_{21}^{EH} = -C_{21}^{HE} \\ -C_{12}^{EH} = -S_{12}^{XY} = +S_{12}^{YX} = +C_{12}^{HE} \Longrightarrow C_{12}^{EH} = -C_{12}^{HE} \end{array}\right\} \Longrightarrow C_{uv}^{pq} \neq C_{uv}^{qp}$$

Nothing can be said, however, with respect to the $2n$-fold rotational symmetry since, as was mentioned earlier, the GSM of a reciprocal structure for the case of normal incidence has $S_{vv}^{pq} = S_{vv}^{qp}$ owing to reciprocity alone, regardless of whether or not the structure is endowed with the property of $2n$-fold rotational symmetry, i.e. one has:

$$\left.\begin{array}{l} +C_{11}^{EH} = +S_{11}^{XY} = +S_{11}^{YX} = -C_{11}^{HE} \Longrightarrow C_{11}^{EH} = -C_{11}^{HE} \\ -C_{22}^{EH} = +S_{22}^{XY} = +S_{22}^{YX} = +C_{22}^{HE} \Longrightarrow C_{22}^{EH} = -C_{22}^{HE} \end{array}\right\} \Longrightarrow C_{vv}^{pq} = -C_{vv}^{qp}$$

even though the scatterer might not be endowed with the 2-fold rotational symmetry property. Thus, the GSM was also obtained for the case of a large departure from normal incidence, say $\theta^i = 150^o$. For two ports that are in a reciprocal relationship, say the port corresponding to $(\theta^i = 150^o, \phi^i = 250^o)$ and the port corresponding to $(\theta^i = 30^o, \phi^i = 70^o)$, the GSM was obtained as:

$$C(E,H) \;=\; \begin{pmatrix} C_{11}^{EE} & C_{11}^{EH} & C_{12}^{EE} & C_{12}^{EH} \\ C_{11}^{HE} & C_{11}^{HH} & C_{12}^{HE} & C_{12}^{HH} \\ C_{21}^{EE} & C_{21}^{EH} & C_{22}^{EE} & C_{22}^{EH} \\ C_{21}^{HE} & C_{21}^{HH} & C_{22}^{HE} & C_{22}^{HH} \end{pmatrix} =$$

$$\begin{pmatrix} 1.2801\angle+153.39^o & 1.2214\angle+69.68^o & 1.3977\angle-31.52^o & 0.9201\angle-150.03^o \\ 0.7198\angle-103.54^o & 1.3486\angle+173.63^o & 1.1974\angle+24.40^o & 1.9533\angle-44.86^o \\ 1.4486\angle-31.56^o & 1.2299\angle-154.61^o & 0.7228\angle+75.96^o & 1.6001\angle-17.48^o \\ 0.9703\angle+31.02^o & 2.0226\angle-45.57^o & 0.9312\angle+127.04^o & 1.0060\angle-46.18^o \end{pmatrix}$$

As expected, the matrix $C(E,H)$ is not symmetrical. Clearly now, one has $C_{uv}^{pq} \neq C_{uv}^{qp}$ and $C_{vv}^{pq} \neq -C_{vv}^{qp}$.

Table 4.7: Various statistics for the octagonal array with two different numbers of cells and two different values of inter-element spacing.

Cell size (m)	# cells	Array diameter D		$\frac{2D^2}{\lambda}$ (m)	Surface area	
		(m)	(λ)		(m^2)	(λ^2)
0.15	37	1.050	3.502	7.36	0.8325	9.263
"	156	2.100	7.004	29.42	3.5100	39.054
0.25	37	1.750	5.838	20.43	2.3125	25.730
"	156	3.500	11.676	81.72	9.7500	108.483

Table 4.8: Peak scattering values for octagonal arrays with two different numbers of Pierrot cells. The observation sphere radius is 4.2 m.

Incidence	Cell size (m)	# cells	Peak values				
			$\|LL\|$	$\|RR\|$	$\|RL\|$	$\|LR\|$	$\|LL/RR\|$
Normal	0.15	37	0.83346	0.09590	0.07375	0.01902	8.69
"	"	156	2.39340	0.30291	0.12937	0.03957	7.90
"	0.25	37	1.86955	0.04144	0.21083	0.02169	45.11
"	"	156	1.79772	0.04282	0.30260	0.04143	41.97
Corner	0.15	37	0.64821	0.14196	0.13666	0.11377	4.57
"	"	156	2.22237	0.49867	0.40157	0.38967	4.46
"	0.25	37	0.38118	0.14319	0.35027	0.11564	2.66
"	"	156	0.54794	0.26291	0.55700	0.18879	2.08

Table 4.9: Reflection beam values for octagonal arrays with two different numbers of Pierrot cells. The observation sphere radius is 4.2 m.

Incidence	Cell size (m)	# cells	Reflection beam values					
			$\|LL\|$	$\|RR\|$	$\|RL\|$	$\|LR\|$	ar	$Blckg$
Normal	0.15	37	0.83346	0.09547	0.00758	0.00046	1.0184	20.8518
"	"	156	2.39340	0.30290	0.02760	0.00351	1.0233	11.8085
"	0.25	37	1.86955	0.04143	0.01800	0.00065	1.0194	0.5090
"	"	156	0.96654	0.02374	0.05856	0.00127	1.1290	0.0094
Corner	0.15	37	0.62005	0.14196	0.06376	0.11377	1.2292	75.7100
"	"	156	2.12620	0.49867	0.20654	0.38967	1.2152	51.5390
"	0.25	37	0.34601	0.10401	0.03975	0.08643	1.2596	5.4220
"	"	156	0.18308	0.09864	0.04271	0.06394	1.6086	0.2305
The values for $Blckg$ have been multiplied by 10^3								

Table 4.10: Transmission beam values for octagonal arrays with two different numbers of Pierrot cells. The observation sphere radius is 4.2 m.

Incidence	Cell size (m)	# cells	Transmission beam values					
			$\|LL\|$	$\|RR\|$	$\|RL\|$	$\|LR\|$	ar	$Leakg$
Normal	0.15	37	0.83346	0.09548	0.00745	0.00117	1.0248	0.066391
"	"	156	2.39340	0.30291	0.02760	0.00329	1.0219	1.35099
"	0.25	37	1.86955	0.04144	0.01811	0.00137	1.0684	1.69395
"	"	156	0.96647	0.02379	0.05849	0.00228	1.2121	1.95490
Corner	0.15	37	0.64821	0.14106	0.11169	0.06176	2.5576	0.036702
"	"	156	2.22237	0.49717	0.38583	0.20831	2.4424	0.444798
"	0.25	37	0.38118	0.10431	0.07731	0.05776	3.4813	0.731020
"	"	156	0.22588	0.09583	0.04273	0.03921	2.3847	1.04065

Table 4.11: Peak scattering values for octagonal arrays with two different numbers of Pierrot cells. The observation sphere radius is 30.0 m.

Incidence	Cell size (m)	# cells	Peak values				
			$\|LL\|$	$\|RR\|$	$\|RL\|$	$\|LR\|$	$\|LL/RR\|$
Normal	0.15	37	0.12080	0.01359	0.01073	0.00263	8.89
"	"	156	0.49236	0.05848	0.01978	0.00548	8.42
"	0.25	37	0.29126	0.00609	0.02459	0.00326	47.83
"	"	156	1.30652	0.02587	0.03631	0.00593	50.50
Corner	0.15	37	0.09344	0.02020	0.02106	0.01632	4.63
"	"	156	0.40040	0.08777	0.06674	0.06978	4.56
"	0.25	37	0.05941	0.02251	0.05462	0.01793	2.64
"	"	156	0.24244	0.08736	0.22073	0.06836	2.78

Table 4.12: Reflection beam values for octagonal arrays with two different numbers of Pierrot cells. The observation sphere radius is 30.0 m.

Incidence	Cell size (m)	# cells	Reflection beam values					
			$\|LL\|$	$\|RR\|$	$\|RL\|$	$\|LR\|$	ar	$Blckg$
Normal	0.15	37	0.12080	0.01359	0.00017	0.00005	1.0028	21.5619
"	"	156	0.49236	0.05848	0.00065	0.00019	1.0026	22.4574
"	0.25	37	0.29126	0.00609	0.00038	0.00015	1.0026	0.5621
"	"	156	1.30652	0.02587	0.00150	0.00065	1.0023	0.5700
Corner	0.15	37	0.08948	0.02020	0.00920	0.01632	1.2291	78.7005
"	"	156	0.38352	0.08777	0.03947	0.06978	1.2294	82.5518
"	0.25	37	0.05383	0.01679	0.00700	0.01359	1.2989	7.0607
"	"	156	0.21658	0.06500	0.02544	0.05349	1.2662	6.0297
The values for $Blckg$ have been multiplied by 10^3								

Table 4.13: Transmission beam values for octagonal arrays with two different numbers of Pierrot cells. The observation sphere radius is 30.0 m.

Incidence	Cell size (m)	# cells	Transmission beam values					
			$\|LL\|$	$\|RR\|$	$\|RL\|$	$\|LR\|$	ar	$Leakg$
Normal	0.15	37	0.12080	0.01359	0.00016	0.00008	1.0119	0.371557
"	"	156	0.49229	0.05848	0.00058	0.00033	1.0113	0.202090
"	0.25	37	0.29126	0.00609	0.00037	0.00016	1.0534	0.291437
"	"	156	1.30652	0.02587	0.00150	0.00072	1.0571	0.699943
Corner	0.15	37	0.09344	0.02006	0.01557	0.00879	2.5590	0.121092
"	"	156	0.40040	0.08714	0.06652	0.03690	2.4688	0.074540
"	0.25	37	0.05941	0.01674	0.01143	0.00877	3.2002	0.682443
"	"	156	0.24244	0.06492	0.04360	0.03417	3.2224	0.674640

Table 4.14: Peak scattering values for octagonal arrays with two different numbers of Pierrot cells. The observation sphere radius is 84.0 m.

Incidence	Cell size (m)	# cells	Peak values				
			$\|LL\|$	$\|RR\|$	$\|RL\|$	$\|LR\|$	$\|LL/RR\|$
Normal	0.15	37	0.04320	0.00485	0.00384	0.00094	8.91
"	"	156	0.17713	0.02096	0.00708	0.00194	8.45
"	0.25	37	0.10380	0.00216	0.00849	0.00117	48.06
"	"	156	0.48642	0.00941	0.01316	0.00219	51.69
Corner	0.15	37	0.03343	0.00722	0.00758	0.00583	4.63
"	"	156	0.14392	0.03145	0.02458	0.02506	4.58
"	0.25	37	0.02128	0.00807	0.01957	0.00642	2.64
"	"	156	0.09021	0.03236	0.08138	0.02516	2.79

Table 4.15: Reflection beam values for octagonal arrays with two different numbers of Pierrot cells. The observation sphere radius is 84.0 m.

Incidence	Cell size (m)	# cells	Reflection beam values					
			$\|LL\|$	$\|RR\|$	$\|RL\|$	$\|LR\|$	ar	$Blckg$
Normal	0.15	37	0.04320	0.00485	0.00003	0.00002	1.0014	21.5558
"	"	156	0.17713	0.02096	0.00012	0.00009	1.0013	22.6110
"	0.25	37	0.10380	0.00216	0.00007	0.00005	1.0014	0.5533
"	"	156	0.48642	0.00941	0.00030	0.00025	1.0012	0.5912
Corner	0.15	37	0.03202	0.00722	0.00328	0.00583	1.2287	78.7798
"	"	156	0.13788	0.03145	0.01416	0.02506	1.2289	83.2473
"	0.25	37	0.01929	0.00603	0.00252	0.00487	1.3009	7.1271
"	"	156	0.08070	0.02410	0.00952	0.01980	1.2674	6.4906
The values for $Blckg$ have been multiplied by 10^3								

Table 4.16: Transmission beam values for octagonal arrays with two different numbers of Pierrot cells. The observation sphere radius is 84.0 m.

Incidence	Cell size (m)	# cells	Transmission beam values					
			$\|LL\|$	$\|RR\|$	$\|RL\|$	$\|LR\|$	ar	$Leakg$
Normal	0.15	37	0.04320	0.00485	0.00003	0.00003	1.0105	0.473680
"	"	156	0.17713	0.02096	0.00012	0.00011	1.0103	0.411657
"	0.25	37	0.10380	0.00216	0.00007	0.00005	1.0518	0.199406
"	"	156	0.48642	0.00941	0.00030	0.00026	1.0565	0.168013
Corner	0.15	37	0.03343	0.00717	0.00556	0.00314	2.5589	0.155656
"	"	156	0.14392	0.03123	0.02381	0.01323	2.4699	0.144932
"	0.25	37	0.02128	0.00601	0.00407	0.00313	3.1763	0.696687
"	"	156	0.09021	0.02407	0.01610	0.01257	3.1863	0.680433

Table 4.17: Assessment of the indicator ar^r for various cases of an octagonal array made of Pierrot LHCPSS cells for different values of observation sphere radius, incidence angle and inter-element spacing. The results for the 30.0 m observation sphere radius are taken as the reference.

Incidence	Cell size (m)	# cells	Observation sphere radius (m)			Error (%)	
			84.0	30.0	4.20	84.0	4.20
Normal	0.15	37	1.0014	1.0028	1.0184	-0.140	+1.556
"	"	156	1.0013	1.0026	1.0233	-0.130	+2.065
"	0.25	37	1.0014	1.0026	1.0194	-0.120	+1.676
"	"	156	1.0012	1.0023	1.1290	-0.110	+12.641
Corner	0.15	37	1.2287	1.2291	1.2292	-0.033	+0.008
"	"	156	1.2289	1.2294	1.2152	-0.041	-1.155
"	0.25	37	1.3009	1.2989	1.2596	+0.154	-3.026
"	"	156	1.2674	1.2662	1.6086	+0.095	+27.042

Table 4.18: Assessment of the indicator ar^t for various cases of an octagonal array made of Pierrot LHCPSS cells for different values of observation sphere radius, incidence angle and inter-element spacing. The results for the 30.0 m observation sphere radius are taken as the reference.

Incidence	Cell size (m)	# cells	Observation sphere radius (m)			Error (%)	
			84.0	30.0	4.20	84.0	4.20
Normal	0.15	37	1.0105	1.0119	1.0248	-0.138	+1.275
"	"	156	1.0103	1.0113	1.0219	-0.099	+1.048
"	0.25	37	1.0518	1.0534	1.0684	-0.152	+1.424
"	"	156	1.0565	1.0571	1.2121	-0.057	+14.663
Corner	0.15	37	2.5589	2.5590	2.5576	-0.004	-0.055
"	"	156	2.4699	2.4688	2.4424	+0.045	-1.110
"	0.25	37	3.1763	3.2002	3.4813	-0.747	+8.784
"	"	156	3.1863	3.2224	2.3847	-1.120	-25.996

Table 4.19: Assessment of the indicator *Blckg* for various cases of an octagonal array made of Pierrot LHCPSS cells for different values of observation sphere radius, incidence angle and inter-element spacing. The results for the 30.0 m observation sphere radius are taken as the reference.

Incidence	Cell size (m)	# cells	Observation sphere radius (m)			Error (%)	
			84.0	30.0	4.20	84.0	4.20
Normal	0.15	37	21.5558	21.5619	20.8518	-0.03	-3.29
"	"	156	22.6110	22.4574	11.8085	+0.68	-47.42
"	0.25	37	0.5533	0.5621	0.5090	-1.57	-9.45
"	"	156	0.5912	0.5700	0.0094	+3.72	-98.35
Corner	0.15	37	78.7798	78.7005	75.7100	+0.10	-3.80
"	"	156	83.2473	82.5518	51.5390	+0.84	-37.57
"	0.25	37	7.1271	7.0607	5.4220	+0.94	-23.21
"	"	156	6.4906	6.0297	0.2305	+7.64	-96.18
The values for *Blckg* have been multiplied by 10^3							

Table 4.20: Assessment of the indicator *Leakg* for various cases of an octagonal array made of Pierrot LHCPSS cells for different values of observation sphere radius, incidence angle and inter-element spacing. The results for the 30.0 m observation sphere radius are taken as the reference.

Incidence	Cell size (m)	# cells	Observation sphere radius (m)			Error (%)	
			84.0	30.0	4.20	84.0	4.20
Normal	0.15	37	0.473680	0.371557	0.0663914	+27.5	-82.1
"	"	156	0.411657	0.202090	1.35099	+103.7	+568.5
"	0.25	37	0.199406	0.291437	1.69395	-31.6	+481.2
"	"	156	0.168013	0.699943	1.95490	-76.0	+179.3
Corner	0.15	37	0.155656	0.121092	0.0367022	+28.5	-69.7
"	"	156	0.144932	0.0745403	0.444798	+94.4	+496.7
"	0.25	37	0.696687	0.682443	0.731020	+2.1	+7.1
"	"	156	0.680433	0.674640	1.04065	+0.9	+54.3

Table 4.21: $|LL^p|$ values of the octagonal array of 37 Pierrot cells for various incidences. The inter-element spacing is 0.15 m and the observation sphere radius is 30.0 m.

θ^i | ϕ^i	0^o	15^o	45^o	90^o	135^o	180^o	225^o	270^o	315^o
0^o	0.1208				0.1208				
5^o	0.1206	0.1205	0.1200	0.1198	0.1195	0.1191	0.1191	0.1202	0.1209
10^o	0.1184								
15^o	0.1153	0.1181	0.1199	0.1142					
20^o	0.1107								
30^o	0.0950			0.0978					
45^o	0.0675	0.0748	0.0934	0.0758	0.0541	0.0730	0.0863	0.0720	0.0548
60^o	0.0382			0.0466					
75^o	0.0262			0.0285					

Table 4.22: $|RR^p|$ values of the octagonal array of 37 Pierrot cells for various incidences. The inter-element spacing is 0.15 m and the observation sphere radius is 30.0 m.

θ^i | ϕ^i	0^o	15^o	45^o	90^o	135^o	180^o	225^o	270^o	315^o
0^o	0.0136				0.0136				
5^o	0.0159	0.0154	0.0141	0.0137	0.0134	0.0137	0.0141	0.0158	0.0165
10^o	0.0178								
15^o	0.0197	0.0185	0.0151	0.0133					
20^o	0.0216								
30^o	0.0262			0.0144					
45^o	0.0361	0.0286	0.0202	0.0180	0.0112	0.0242	0.0204	0.0356	0.0490
60^o	0.0344			0.0187					
75^o	0.0273			0.0186					

Table 4.23: $|LL^p/RR^p|$ values of the octagonal array of 37 Pierrot cells for various incidences. The inter-element spacing is 0.15 m and the observation sphere radius is 30.0 m.

θ^i | ϕ^i	0^o	15^o	45^o	90^o	135^o	180^o	225^o	270^o	315^o
0^o	8.89				8.89				
5^o	7.60	7.82	8.50	8.77	8.92	8.70	8.44	7.59	7.32
10^o	6.64								
15^o	5.85	6.37	7.92	8.58					
20^o	5.11								
30^o	3.62			6.80					
45^o	1.87	2.61	4.63	4.22	4.83	3.02	4.23	2.00	1.12
60^o	1.11			2.50					
75^o	0.96			1.54					

Table 4.24: $|LL^r|$ reflection beam values of the octagonal array of 37 Pierrot cells for various incidences. The inter-element spacing is 0.15 m and the observation sphere radius is 30.0 m.

θ^i | ϕ^i	0^o	15^o	45^o	90^o	135^o	180^o	225^o	270^o	315^o
0^o	0.1208				0.1208				
5^o	0.1195	0.1197	0.1200	0.1198	0.1195	0.1191	0.1191	0.1193	0.1195
10^o	0.1163								
15^o	0.1122	0.1158	0.1197	0.1142					
20^o	0.1071								
30^o	0.0911			0.0978					
45^o	0.0635	0.0718	0.0895	0.0737	0.0527	0.0627	0.0825	0.0720	0.0524
60^o	0.0342			0.0397					
75^o	0.0245			0.0234					

Table 4.25: $|LL^t|$ transmission beam values of the octagonal array of 37 Pierrot cells for various incidences. The inter-element spacing is 0.15 m and the observation sphere radius is 30.0 m.

θ^i | ϕ^i	0^o	15^o	45^o	90^o	135^o	180^o	225^o	270^o	315^o
0^o	0.1208				0.1208				
5^o	0.1206	0.1205	0.1200	0.1187	0.1181	0.1183	0.1191	0.1202	0.1209
10^o	0.1184								
15^o	0.1153	0.1181	0.1199	0.1113					
20^o	0.1107								
30^o	0.0950			0.0949					
45^o	0.0658	0.0740	0.0934	0.0742	0.0519	0.0730	0.0863	0.0645	0.0534
60^o	0.0345			0.0416					
75^o	0.0224			0.0254					

Table 4.26: $|RR^r|$ reflection beam values of the octagonal array of 37 Pierrot cells for various incidences. The inter-element spacing is 0.15 m and the observation sphere radius is 30.0 m.

θ^i | ϕ^i	0^o	15^o	45^o	90^o	135^o	180^o	225^o	270^o	315^o
0^o	0.0136				0.0136				
5^o	0.0136	0.0137	0.0137	0.0135	0.0134	0.0136	0.0138	0.0135	0.0134
10^o	0.0136								
15^o	0.0139	0.0144	0.0148	0.0132					
20^o	0.0146								
30^o	0.0173			0.0144					
45^o	0.0246	0.0233	0.0202	0.0180	0.0103	0.0242	0.0204	0.0176	0.0101
60^o	0.0256			0.0185					
75^o	0.0235			0.0180					

Table 4.27: $|RR^t|$ transmission beam values of the octagonal array of 37 Pierrot cells for various incidences. The inter-element spacing is 0.15 m and the observation sphere radius is 30.0 m.

θ^i | ϕ^i	0^o	15^o	45^o	90^o	135^o	180^o	225^o	270^o	315^o
0^o	0.0136				0.0136				
5^o	0.0158	0.0152	0.0137	0.0114	0.0104	0.0114	0.0138	0.0158	0.0165
10^o	0.0177								
15^o	0.0196	0.0184	0.0148	0.0078					
20^o	0.0216								
30^o	0.0262			0.0075					
45^o	0.0361	0.0286	0.0201	0.0115	0.0112	0.0113	0.0203	0.0356	0.0490
60^o	0.0344			0.0133					
75^o	0.0270			0.0153					

Table 4.28: $|RL^r|$ reflection beam values of the octagonal array of 37 Pierrot cells for various incidences. The inter-element spacing is 0.15 m and the observation sphere radius is 30.0 m.

θ^i | ϕ^i	0^o	15^o	45^o	90^o	135^o	180^o	225^o	270^o	315^o
0^o	0.0002				0.0002				
5^o	0.0069	0.0055	0.0020	0.0056	0.0093	0.0074	0.0018	0.0051	0.0081
10^o	0.0129								
15^o	0.0180	0.0154	0.0053	0.0176					
20^o	0.0225								
30^o	0.0282			0.0342					
45^o	0.0290	0.0299	0.0092	0.0420	0.0576	0.0492	0.0157	0.0244	0.0104
60^o	0.0168			0.0299					
75^o	0.0087			0.0195					

Table 4.29: $|RL^t|$ transmission beam values of the octagonal array of 37 Pierrot cells for various incidences. The inter-element spacing is 0.15 m and the observation sphere radius is 30.0 m.

θ^i | ϕ^i	0^o	15^o	45^o	90^o	135^o	180^o	225^o	270^o	315^o
0^o	0.0002				0.0002				
5^o	0.0076	0.0058	0.0015	0.0048	0.0080	0.0068	0.0015	0.0054	0.0094
10^o	0.0156								
15^o	0.0239	0.0186	0.0050	0.0118					
20^o	0.0321								
30^o	0.0450			0.0172					
45^o	0.0490	0.0414	0.0156	0.0193	0.0108	0.0307	0.0089	0.0374	0.0593
60^o	0.0282			0.0155					
75^o	0.0144			0.0137					

Table 4.30: $|LR^r|$ reflection beam values of the octagonal array of 37 Pierrot cells for various incidences. The inter-element spacing is 0.15 m and the observation sphere radius is 30.0 m.

θ^i | ϕ^i	0^o	15^o	45^o	90^o	135^o	180^o	225^o	270^o	315^o
0^o	0.0001				0.0001				
5^o	0.0074	0.0057	0.0019	0.0051	0.0081	0.0069	0.0019	0.0056	0.0093
10^o	0.0151								
15^o	0.0230	0.0179	0.0060	0.0133					
20^o	0.0307								
30^o	0.0433			0.0211					
45^o	0.0499	0.0416	0.0163	0.0244	0.0108	0.0288	0.0095	0.0409	0.0567
60^o	0.0323			0.0190					
75^o	0.0203			0.0169					

Table 4.31: $|LR^t|$ transmission beam values of the octagonal array of 37 Pierrot cells for various incidences. The inter-element spacing is 0.15 m and the observation sphere radius is 30.0 m.

θ^i | ϕ^i	0^o	15^o	45^o	90^o	135^o	180^o	225^o	270^o	315^o
0^o	0.0001				0.0001				
5^o	0.0054	0.0032	0.0015	0.0069	0.0081	0.0048	0.0015	0.0075	0.0093
10^o	0.0114								
15^o	0.0176	0.0109	0.0040	0.0176					
20^o	0.0239								
30^o	0.0339			0.0274					
45^o	0.0380	0.0260	0.0088	0.0309	0.0112	0.0182	0.0156	0.0487	0.0585
60^o	0.0229			0.0237					
75^o	0.0166			0.0193					

Table 4.32: ar^r reflection beam values of the octagonal array of 37 Pierrot cells for various incidences. The inter-element spacing is 0.15 m and the observation sphere radius is 30.0 m.

θ^i | ϕ^i	0^o	15^o	45^o	90^o	135^o	180^o	225^o	270^o	315^o
0^o	1.0028				1.003				
5^o	1.1222	1.097	1.034	1.099	1.169	1.132	1.031	1.089	1.145
10^o	1.2487								
15^o	1.3826	1.306	1.093	1.365					
20^o	1.5306								
30^o	1.8986			2.075					
45^o	2.6822	2.426	1.229	3.645	22.360	8.292	1.468	2.025	1.494
60^o	2.9331			7.127					
75^o	2.1069			11.154					

Table 4.33: ar^t transmission beam values of the octagonal array of 37 Pierrot cells for various incidences. The inter-element spacing is 0.15 m and the observation sphere radius is 30.0 m.

θ^i | ϕ^i	0^o	15^o	45^o	90^o	135^o	180^o	225^o	270^o	315^o
0^o	1.0119				1.012				
5^o	2.0497	1.539	1.244	4.017	7.917	2.462	1.240	2.823	3.609
10^o	4.8469								
15^o	18.7454	3.934	1.730	2.590					
20^o	20.0143								
30^o	7.8367			1.749					
45^o	39.9581	20.430	2.559	2.190	> 1000	4.231	7.670	6.427	11.298
60^o	4.9944			3.541					
75^o	4.2049			8.602					

Table 4.34: Blockage beam values of the octagonal array of 37 Pierrot cells for various incidences. The inter-element spacing is 0.15 m and the observation sphere radius is 30.0 m.

θ^i | ϕ^i	0^o	15^o	45^o	90^o	135^o	180^o	225^o	270^o	315^o
0^o	21.56				21.56				
5^o	27.97	25.66	22.45	24.39	28.68	27.12	22.48	25.03	30.99
10^o	48.47								
15^o	84.27	61.64	29.92	40.81					
20^o	135.06								
30^o	253.90			76.16					
45^o	361.80	264.89	78.70	107.38	25.92	164.72	59.03	231.38	386.63
60^o	197.67			81.97					
75^o	112.53			71.10					
The values for *Blckg* have been multiplied by 10^3									

Table 4.35: Leakage beam values of the octagonal array of 37 Pierrot cells for various incidences. The inter-element spacing is 0.15 m and the observation sphere radius is 30.0 m.

θ^i | ϕ^i	0^o	15^o	45^o	90^o	135^o	180^o	225^o	270^o	315^o
0^o	0.3716								
5^o	0.4033	0.3909	0.3773	0.4015	0.4234	0.4025	0.3753	0.3987	0.4246
10^o									
15^o	0.4659	0.4274	0.3590	0.4282					
20^o									
30^o	0.4777			0.3015					
45^o	0.4214	0.2805	0.1211	0.1595	0.3747	0.2308	0.1053	0.3133	0.7431
60^o	0.2667			0.1239					
75^o	0.0450			0.0299					

Table 4.36: Peak scattering values of the octagonal array of 37 Pierrot cells with various cell thickness values. The inter-element spacing is 0.15 m, the incidence is normal and the observation sphere radius is 30.0 m.

Cell thickness		Peak values				
(m)	(λ)	$\|LL\|$	$\|RR\|$	$\|RL\|$	$\|LR\|$	$\|LL/RR\|$
0.060	0.200	0.09653	0.02170	0.02122	0.01712	4.45
0.065	0.217	0.10528	0.01873	0.01714	0.01247	5.62
0.070	0.233	0.11355	0.01603	0.01391	0.00735	7.08
0.071	0.234	0.11511	0.01552	0.01330	0.00626	7.42
0.075	0.250	0.12080	0.01359	0.01073	0.00263	8.89
0.076	0.254	0.12200	0.01320	0.01008	0.00335	9.24
0.078	0.260	0.12397	0.01239	0.01033	0.00532	10.01
0.079	0.264	0.12473	0.01197	0.01117	0.00650	10.42
0.080	0.267	0.12534	0.01157	0.01222	0.00768	10.83
0.085	0.284	0.12599	0.00960	0.01802	0.01351	13.12
0.090	0.300	0.13247	0.00767	0.02476	0.02117	17.27

Table 4.37: Reflection beam values of the octagonal array of 37 Pierrot cells with various cell thickness values. The inter-element spacing is 0.15 m, the incidence is normal and the observation sphere radius is 30.0 m.

Cell thickness		Reflection beam values					
(m)	(λ)	$\|LL\|$	$\|RR\|$	$\|RL\|$	$\|LR\|$	ar	$Blckg$
0.060	0.200	0.09653	0.02170	0.01375	0.01378	1.3222	77.0989
0.065	0.217	0.10528	0.01873	0.01024	0.01027	1.2155	53.2351
0.070	0.233	0.11355	0.01603	0.00561	0.00564	1.1039	33.7136
0.071	0.234	0.11511	0.01552	0.00456	0.00458	1.0824	30.5679
0.075	0.250	0.12080	0.01359	0.00017	0.00005	1.0028	21.5619
0.076	0.254	0.12200	0.01313	0.00133	0.00130	1.0221	20.3189
0.078	0.260	0.12397	0.01221	0.00390	0.00388	1.0650	19.1700
0.079	0.264	0.12473	0.01177	0.00523	0.00521	1.0875	19.3200
0.080	0.267	0.12535	0.01132	0.00657	0.00655	1.1106	19.9486
0.085	0.284	0.12599	0.00910	0.01328	0.01328	1.2356	30.2440
0.090	0.300	0.13245	0.00709	0.02118	0.02117	1.3807	58.1728
The values for $Blckg$ have been multiplied by 10^3							

Table 4.38: Transmission beam values of the octagonal array of 37 Pierrot cells with various cell thickness values. The inter-element spacing is 0.15 m, the incidence is normal and the observation sphere radius is 30.0 m.

Cell thickness		Transmission beam values					
(m)	(λ)	$\|LL\|$	$\|RR\|$	$\|RL\|$	$\|LR\|$	ar	$Leakg$
0.060	0.200	0.09599	0.01911	0.01716	0.01712	18.2308	0.98307
0.065	0.217	0.10510	0.01763	0.01203	0.01200	5.2669	0.78138
0.070	0.233	0.11353	0.01578	0.00629	0.00624	2.3102	0.57322
0.071	0.234	0.11509	0.01536	0.00506	0.00502	1.9718	0.53203
0.075	0.250	0.12080	0.01359	0.00016	0.00008	1.0119	0.37156
0.076	0.254	0.12199	0.01312	0.00137	0.00140	1.2391	0.33384
0.078	0.260	0.12396	0.01217	0.00404	0.00408	2.0100	0.26327
0.079	0.264	0.12472	0.01169	0.00539	0.00543	2.7366	0.23152
0.080	0.267	0.12534	0.01121	0.00675	0.00678	4.0660	0.20258
0.085	0.284	0.12597	0.00895	0.01338	0.01343	4.9980	0.10843
0.090	0.300	0.13247	0.00767	0.02097	0.02101	2.1500	0.05830

Table 4.39: Peak scattering values of the octagonal array of 37 Pierrot cells for various frequency values. The inter-element spacing is 0.15 m, the incidence is normal and the observation sphere radius is 30.0 m.

Frequency (GHz)	Peak values				
	$\|LL\|$	$\|RR\|$	$\|RL\|$	$\|LR\|$	$\|LL/RR\|$
0.800	0.03910	0.02885	0.01141	0.01204	1.36
0.850	0.05093	0.02442	0.01065	0.01019	2.09
0.880	0.06031	0.02211	0.01058	0.00904	2.73
0.900	0.06756	0.02062	0.01056	0.00818	3.28
0.950	0.09210	0.01706	0.01055	0.00557	5.40
0.960	0.09788	0.01636	0.01057	0.00495	5.98
0.970	0.10369	0.01567	0.01060	0.00438	6.62
0.980	0.10947	0.01498	0.01065	0.00379	7.31
0.990	0.11514	0.01429	0.01069	0.00318	8.06
1.000	0.12080	0.01359	0.01073	0.00263	8.89
1.010	0.12532	0.01296	0.01063	0.00311	9.67
1.020	0.12875	0.01232	0.01072	0.00359	10.45
1.030	0.13098	0.01167	0.01128	0.00437	11.22
1.035	0.13261	0.01136	0.01130	0.00481	11.67
1.040	0.14213	0.01103	0.01114	0.00552	12.89
1.050	0.14098	0.01039	0.01229	0.00644	13.57
1.100	0.13375	0.00691	0.01654	0.01086	19.36
1.150	0.11541	0.00365	0.01809	0.01394	31.62
1.200	0.09675	0.00659	0.01877	0.01571	14.68

Table 4.40: Reflection beam values of the octagonal array of 37 Pierrot cells for various frequency values. The inter-element spacing is 0.15 m, the incidence is normal and the observation sphere radius is 30.0 m.

Frequency	Reflection beam values					
(GHz)	$\|LL\|$	$\|RR\|$	$\|RL\|$	$\|LR\|$	ar	$Blckg$
0.800	0.03910	0.02885	0.00390	0.00397	1.2216	154.643
0.850	0.05093	0.02442	0.00429	0.00434	1.1842	99.3751
0.880	0.06031	0.02211	0.00442	0.00447	1.1583	76.6616
0.900	0.06756	0.02062	0.00433	0.00438	1.1371	64.0159
0.950	0.09210	0.01706	0.00325	0.00327	1.0730	39.0342
0.960	0.09788	0.01636	0.00279	0.00281	1.0586	34.9149
0.970	0.10369	0.01567	0.00224	0.00226	1.0442	31.0817
0.980	0.10946	0.01498	0.00158	0.00160	1.0293	27.5878
0.990	0.11514	0.01429	0.00082	0.00083	1.0143	24.3838
1.000	0.12080	0.01359	0.00017	0.00005	1.0028	21.5619
1.010	0.12532	0.01290	0.00105	0.00102	1.0169	19.1721
1.020	0.12875	0.01221	0.00208	0.00206	1.0328	17.2072
1.030	0.13098	0.01150	0.00316	0.00313	1.0495	15.6364
1.035	0.13261	0.01115	0.00372	0.00370	1.0578	15.0344
1.040	0.14213	0.01078	0.00456	0.00453	1.0662	14.7672
1.050	0.14098	0.01003	0.00569	0.00567	1.0842	14.0615
1.100	0.13371	0.00585	0.01086	0.01086	1.1767	14.6679
1.150	0.11536	0.00092	0.01393	0.01394	1.2747	17.2301
1.200	0.09675	0.00539	0.01505	0.01506	1.3684	20.7413
The values for $Blckg$ have been multiplied by 10^3						

Table 4.41: Transmission beam values of the octagonal array of 37 Pierrot cells for various frequency values. The inter-element spacing is 0.15 m, the incidence is normal and the observation sphere radius is 30.0 m.

Frequency	Transmission beam values					
(GHz)	$\|LL\|$	$\|RR\|$	$\|RL\|$	$\|LR\|$	ar	$Leakg$
0.800	0.03804	0.02737	0.00992	0.00989	2.1317	1.90766
0.850	0.05044	0.02336	0.00830	0.00827	2.0961	1.72516
0.880	0.06004	0.02133	0.00728	0.00724	2.0281	1.56298
0.900	0.06739	0.02005	0.00650	0.00646	1.9501	1.43486
0.950	0.09207	0.01691	0.00400	0.00397	1.6130	1.00862
0.960	0.09786	0.01626	0.00334	0.00330	1.5093	0.88919
0.970	0.10368	0.01562	0.00260	0.00257	1.3938	0.76255
0.980	0.10947	0.01495	0.00180	0.00176	1.2663	0.63310
0.990	0.11513	0.01428	0.00093	0.00088	1.1306	0.50245
1.000	0.12080	0.01359	0.00016	0.00008	1.0119	0.37156
1.010	0.12532	0.01290	0.00107	0.00109	1.1851	0.25116
1.020	0.12875	0.01221	0.00211	0.00214	1.4254	0.15492
1.030	0.13098	0.01150	0.00317	0.00321	1.7729	0.09055
1.035	0.13261	0.01114	0.00372	0.00376	2.0182	0.07650
1.040	0.14213	0.01079	0.00455	0.00458	2.4747	0.04873
1.050	0.14097	0.01010	0.00557	0.00559	3.4856	0.00498
1.100	0.13375	0.00673	0.01034	0.01036	4.6966	0.33778
1.150	0.11541	0.00355	0.01351	0.01351	1.7119	0.91374
1.200	0.09665	0.00292	0.01572	0.01571	1.4558	1.34202

Table 4.42: Peak scattering values of the octagonal array of 37 Pierrot cells with different values of inter-element spacing. The incidence is normal and the observation sphere radius is 30.0 m.

Cell size		Peak values				
(m)	(λ)	$\|LL\|$	$\|RR\|$	$\|RL\|$	$\|LR\|$	$\|LL/RR\|$
gang*	0.125	0.13161	0.02338	0.01280	0.00361	5.63
gang*	0.163	0.13033	0.02134	0.01271	0.00329	6.11
gang	0.163	0.12797	0.02651	0.01293	0.00382	4.83
gang*	0.250	0.12304	0.03026	0.01084	0.00497	4.07
gang	0.250	0.12582	0.04473	0.01179	0.00672	2.81
0.120	0.400	0.08546	0.01839	0.01207	0.00407	4.65
0.130	0.434	0.09767	0.01671	0.01021	0.00329	5.85
0.140	0.467	0.10986	0.01507	0.01021	0.00291	7.29
0.150	0.500	0.12080	0.01359	0.01073	0.00263	8.89
0.160	0.534	0.13050	0.01246	0.01077	0.00227	10.47
0.170	0.567	0.14821	0.01156	0.01229	0.00194	12.82
0.180	0.600	0.15790	0.01076	0.01096	0.00193	14.68
0.190	0.634	0.17246	0.01004	0.01111	0.00187	17.18
0.200	0.667	0.19078	0.00941	0.01112	0.00224	20.27
0.210	0.700	0.21369	0.00882	0.01259	0.00262	24.23
0.220	0.734	0.23829	0.00816	0.01414	0.00239	29.20
0.230	0.767	0.26425	0.00747	0.01409	0.00224	35.38
0.240	0.801	0.29112	0.00682	0.01703	0.00286	42.69
0.250	0.834	0.29126	0.00609	0.02459	0.00326	47.83
0.260	0.867	0.24006	0.00509	0.04068	0.00489	47.16
0.270	0.901	0.17656	0.00871	0.04889	0.00866	20.27

gang pertains to the gangbuster arrangement with 0.002 m wire radius
gang* pertains to the gangbuster arrangement with 0.001 m wire radius

Table 4.43: Reflection beam values of the octagonal array of 37 Pierrot cells with different values of inter-element spacing. The incidence is normal and the observation sphere radius is 30.0 m.

Cell size		Reflection beam values					
(m)	(λ)	$\|LL\|$	$\|RR\|$	$\|RL\|$	$\|LR\|$	ar	$Blckg$
gang*	0.125	0.13161	0.02338	0.00017	0.00012	1.0025	63.8213
gang*	0.163	0.13033	0.02134	0.00017	0.00013	1.0026	53.1544
gang	0.163	0.12797	0.02650	0.00018	0.00013	1.0029	81.9775
gang*	0.250	0.12304	0.03026	0.00017	0.00009	1.0028	106.900
gang	0.250	0.12582	0.04473	0.00019	0.00009	1.0029	233.532
0.120	0.400	0.08546	0.01790	0.00013	0.00003	1.0032	91.3385
0.130	0.434	0.09766	0.01643	0.00014	0.00004	1.0029	55.8184
0.140	0.467	0.10986	0.01495	0.00016	0.00004	1.0029	34.3678
0.150	0.500	0.12080	0.01359	0.00017	0.00005	1.0028	21.5619
0.160	0.534	0.13050	0.01246	0.00018	0.00005	1.0027	14.0067
0.170	0.567	0.14821	0.01156	0.00016	0.00006	1.0021	9.4559
0.180	0.600	0.15790	0.01076	0.00022	0.00007	1.0028	6.5168
0.190	0.634	0.17246	0.01004	0.00023	0.00008	1.0026	4.5687
0.200	0.667	0.19078	0.00941	0.00029	0.00009	1.0031	3.2713
0.210	0.700	0.21369	0.00882	0.00030	0.00010	1.0028	2.3628
0.220	0.734	0.23822	0.00816	0.00036	0.00011	1.0031	1.6789
0.230	0.767	0.26425	0.00747	0.00037	0.00013	1.0028	1.1792
0.240	0.801	0.29105	0.00682	0.00044	0.00014	1.0030	0.8297
0.250	0.834	0.29126	0.00609	0.00038	0.00015	1.0026	0.5621
0.260	0.867	0.24006	0.00509	0.00036	0.00012	1.0030	0.3356
0.270	0.901	0.17656	0.00411	0.00022	0.00009	1.0025	0.1875

gang pertains to the gangbuster arrangement with 0.002 m wire radius
gang* pertains to the gangbuster arrangement with 0.001 m wire radius
The values for $Blckg$ have been multiplied by 10^3

Table 4.44: Transmission beam values of the octagonal array of 37 Pierrot cells with different values of inter-element spacing. The incidence is normal and the observation sphere radius is 30.0 m.

Cell size		Transmission beam values					
(m)	(λ)	$\|LL\|$	$\|RR\|$	$\|RL\|$	$\|LR\|$	ar	$Leakg$
gang*	0.125	0.13161	0.02338	0.00015	0.00002	1.0017	0.04477
gang*	0.163	0.13033	0.02134	0.00015	0.00002	1.0017	0.02128
gang	0.163	0.12797	0.02651	0.00015	0.00001	1.0009	0.01641
gang*	0.250	0.12304	0.03026	0.00014	0.00005	1.0036	0.45031
gang	0.250	0.12582	0.04473	0.00014	0.00006	1.0025	0.42790
0.120	0.400	0.08456	0.01790	0.00011	0.00006	1.0071	0.09876
0.130	0.434	0.09767	0.01643	0.00012	0.00007	1.0088	0.22257
0.140	0.467	0.10986	0.01495	0.00014	0.00007	1.0098	0.30227
0.150	0.500	0.12080	0.01359	0.00016	0.00008	1.0119	0.37156
0.160	0.534	0.13050	0.01246	0.00017	0.00008	1.0136	0.44209
0.170	0.567	0.14821	0.01156	0.00016	0.00009	1.0162	0.48556
0.180	0.600	0.15790	0.01076	0.00022	0.00010	1.0181	0.47380
0.190	0.634	0.17246	0.01004	0.00023	0.00010	1.0207	0.47919
0.200	0.667	0.19078	0.00941	0.00029	0.00011	1.0242	0.44467
0.210	0.700	0.21369	0.00882	0.00030	0.00012	1.0284	0.36401
0.220	0.734	0.23829	0.00816	0.00029	0.00013	1.0337	0.24013
0.230	0.767	0.26425	0.00747	0.00037	0.00015	1.0405	0.12199
0.240	0.801	0.29112	0.00682	0.00038	0.00016	1.0484	0.05981
0.250	0.834	0.29126	0.00609	0.00037	0.00016	1.0534	0.29144
0.260	0.867	0.24006	0.00509	0.00036	0.00013	1.0521	0.83805
0.270	0.901	0.17656	0.00411	0.00022	0.00009	1.0469	1.25385
gang pertains to the gangbuster arrangement with 0.002 m wire radius gang* pertains to the gangbuster arrangement with 0.001 m wire radius							

4.3 Comparison between the Pierrot and the Tilston designs

Figures 4.31, 4.32 and 4.33 show various octagonal arrays based on the Tilston cell. Tables 4.45 to 4.47 show the scattered electric field levels for arrays with various cell designs. In these tables, the results pertaining to the short-circuited and open-circuited turnstiles and to the Tilston turnstile were obtained with the length of the turnstile dipoles being $\approx 0.45\lambda$ instead of 0.50λ. This choice was made on the basis that a numerical analysis in which was varied the length of the dipoles of a single cell demonstrated a better response for the $\approx 0.45\lambda$ dipole. The data entered in the tables under the designation "Tilston-CW" or "Tilston-CCW" pertain to the Tilston turnstile dipoles bent 90^o clockwise (CW) or counter-clockwise (CCW), respectively, in the transverse plane at the mid length point of each dipole arm. This idea originates from a paper [19] in which it is reported that the scattering from short-circuited half-wavelength dipole turnstiles is improved by bending the dipoles at the mid length point. The best performance was reported to take place for a 89^o bend. The data entered in the tables under the designation "Tilston-X" pertains to the array shown in Figure 4.33.

It was confirmed that, as per reference [19], a surface made of short-circuited dipole turnstiles with $\lambda/2$ front-to-back thickness acted as a solid reflector, i.e. the polarization sense of the reflected CP wave was opposite to that of the incident CP wave. When the front-to-back thickness was reduced to $\lambda/4$, the surface acted as an artificially soft or hard surface, i.e. the polarization sense of the reflected CP wave was the same as that of the incident CP wave. Interestingly, it was found that bending the dipoles at the mid length point did not make the surface more sensitive to the polarization handedness suggested by the direction of the bend (i.e. CW or CCW). In fact, such a lack of sensitivity to the polarization handedness was also observed for the spiral antenna [2]. However, when the concept of bending the dipoles was

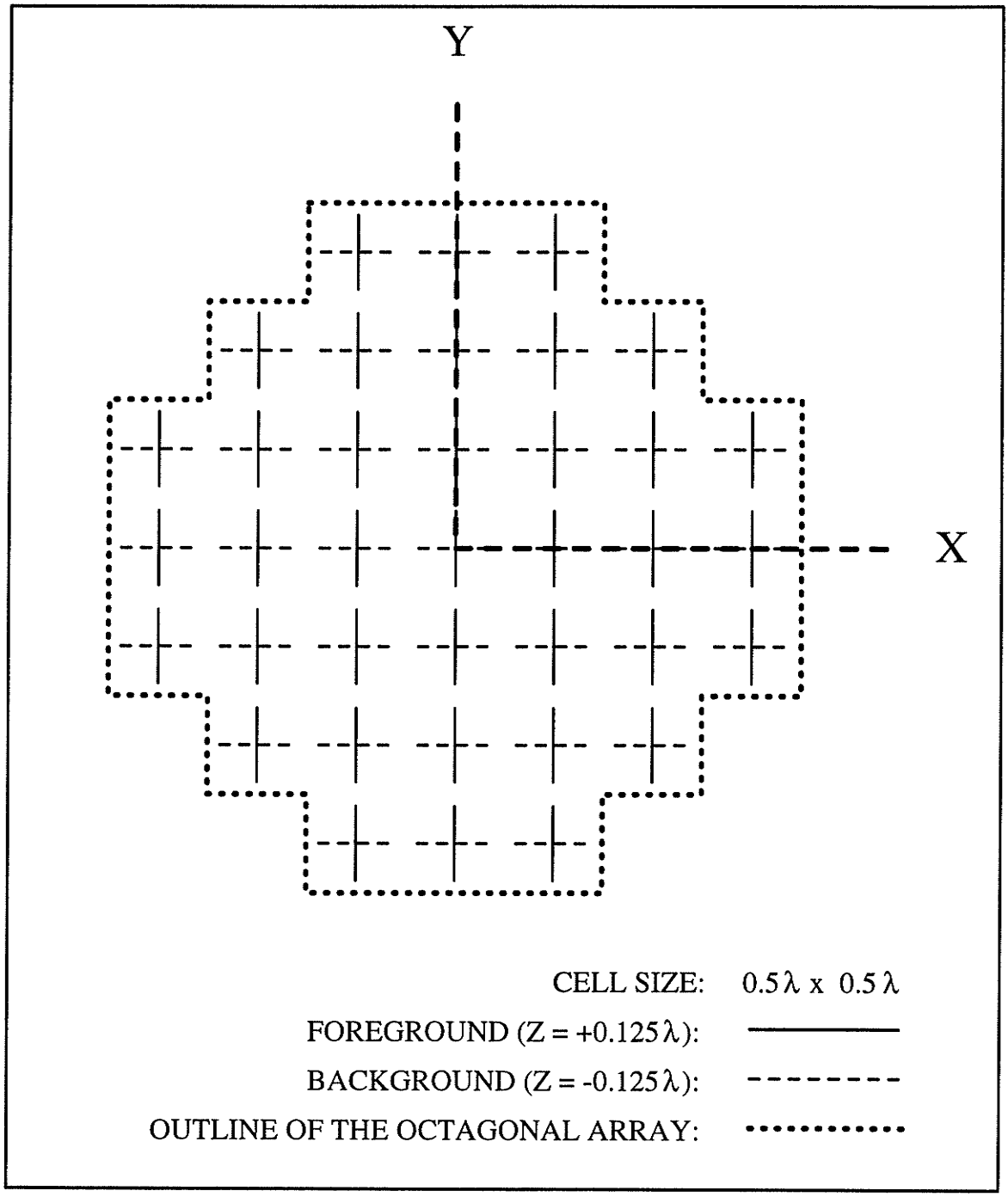

Figure 4.31: Configuration and orientation of the octagonal array made of 37 identical Tilston LHCPSS cells for operation at 1 GHz.

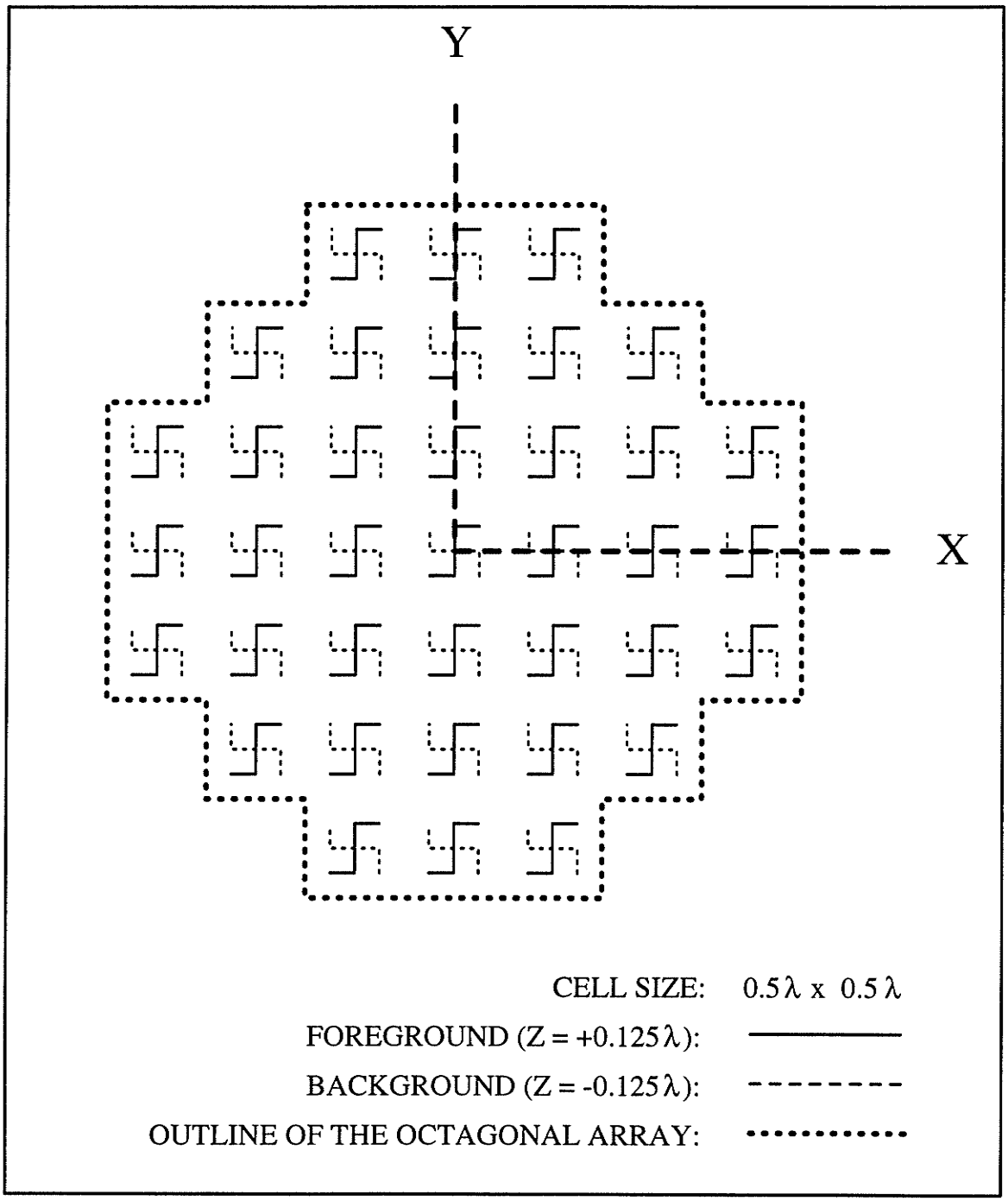

Figure 4.32: Configuration and orientation of the octagonal array made of 37 identical Tilston-CW LHCPSS cells for operation at 1 GHz. The CCW version follows naturally and is not shown.

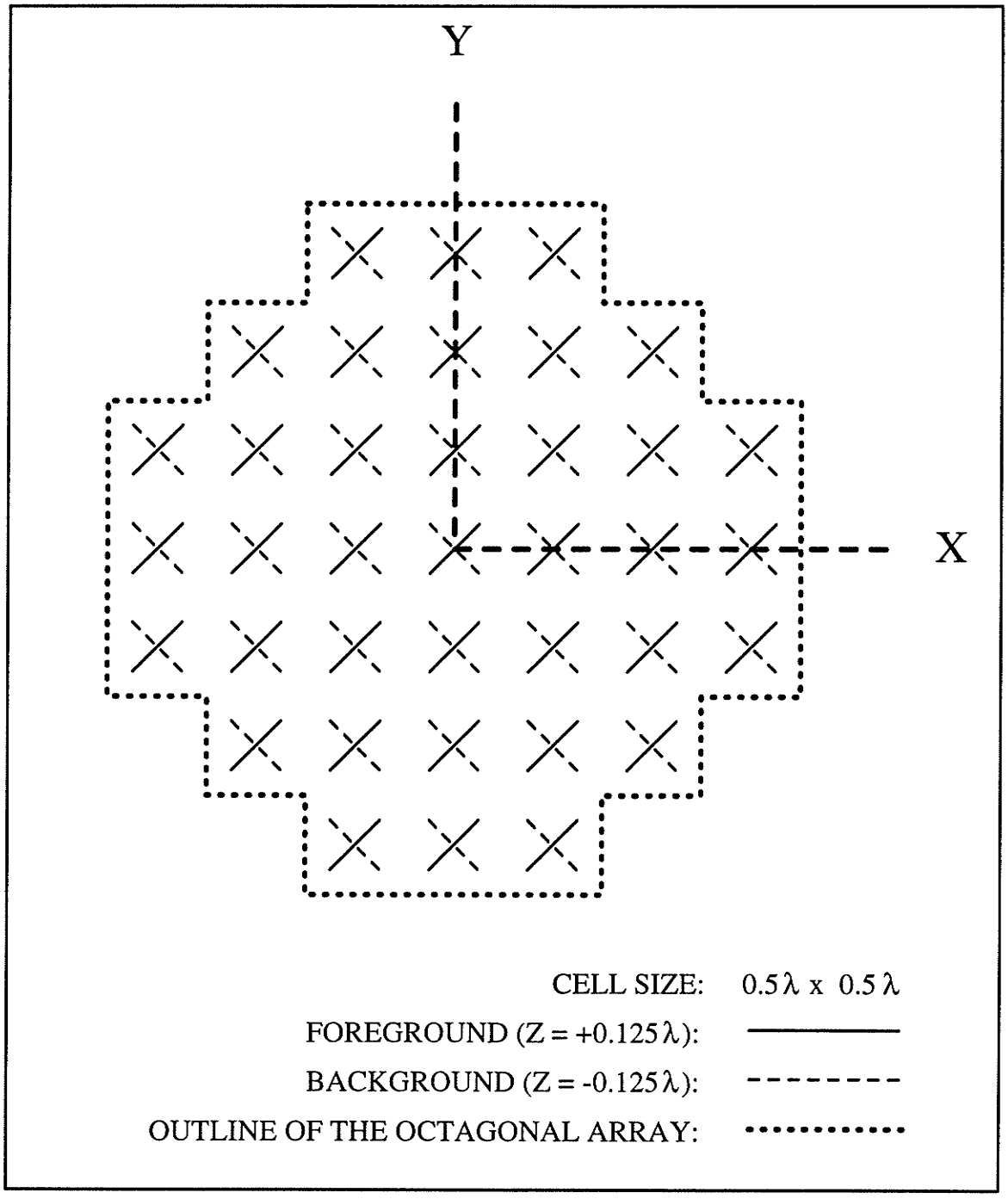

Figure 4.33: Configuration and orientation of the octagonal array made of 37 identical Tilston-X LHCPSS cells for operation at 1 GHz.

applied to the crank CPSS, it was found that the bends degraded the performance of the crank.

From the results in the tables, it is noted that:

- The short-circuited turnstile has $Blckg = 1.756$ which value is much larger than that for any other cell type, as expected, although it is yet not quite the maximum value which is ≈ 2.165 as obtained for the solid reflector. The open-circuited turnstile has $Leakg = 2.147$ which value is larger than that for any other cell type, as expected, although it is yet far from the maximum value which is equal to $|LL_o^t|^2 \left(\frac{r_o}{A_o}\right)^2 = 15.897$. The open-circuited turnstile does not quite have $Blckg = 0$ as would be expected if it were completely transparent, although its value is among the smallest values. Surprisingly, however, the Tilston-CW and the Tilston-CCW designs have smaller $Blckg$ values at normal incidence. The short-circuited turnstile does not quite have $Leakg = 0$ as would be expected if it were completely opaque, although its value is among the smallest values. Surprisingly, however, the Tilston design has slightly smaller $Leakg$ values.

- The results for the open-circuited and for the short-circuited turnstile antennas are CP insensitive as long as both the observation and the excitation directions lie in symmetry planes, as expected.

- The Tilston design does indeed behave similarly to a short-circuited turnstile for LHCP incidence, and to an open-circuited turnstile for RHCP incidence, as expected. Although the Tilston design is not quite as transparent as the open-circuited turnstile under RHCP illumination, however, it is more reflective than the short-circuited turnstile under LHCP illumination.

- The cell types designated as the Tilston-CW, the Tilston-CCW and the Tilston-X cell types offer no overall improvement over the regular Tilston design. Consequently, they will not be considered any further.

- The Tilston design outperforms the Pierrot design for all indicators at both normal and corner incidences, except for ar^t at corner incidence. It must be said, however, that ar^t for the Pierrot design varies widely over ϕ^i so that this exception is not meaningful. For instance, at $\theta^i = 45^o$ and $\phi^i = 135^o$, the Pierrot design has $ar^t > 1000$. Judging by the *Blckg* and *Leakg* values for the short-circuited and the open-circuited turnstiles so as to gauge how significantly better the performance of the Tilston cell compares with the performance of the Pierrot cell, one sees that the difference in performance is slight for normal incidence but is more important for corner incidence.

A numerical analysis consisting in varying the characteristic impedance of the transmission line of the Tilston design revealed that the results hardly vary over a very wide range of characteristic impedance values (from 1 to 1000 Ω). This is as expected since the input impedance of a half-wavelength transmission line is the same as the load connected at the other end of this transmission line for any value of characteristic impedance. According to the analysis by Tilston and to the more detailed analysis by Hurd in reference [8], the frequency behavior, however, would depend on the value of the characteristic impedance. All results shown herein pertain to a value of 50 Ω.

The results of the numerical analysis consisting in modifying gradually the position of the dipoles so as to create an increasingly more asymmetrical Tilston cell are shown in Tables 4.48 to 4.50. The asymmetry is created by offsetting the Tilston dipoles by an equal amount in the $\hat{x}$ and the $\hat{y}$ directions. As the segment lengths varied with offsetting the dipoles while keeping the feeding point on the longitudinal axis, the segmentation was changed from 3 segments per arm to 6 segments for the longer

arm and 2 segments for the shorter arm for the two cases of 0.040 m and 0.050 m asymmetry.

Since the requirement for the 2-fold rotational symmetry originates from the need for the reflection coefficients to obey the relationship $C_{vv}^{pq} = -C_{vv}^{qp}$ with $p \neq q$, and since all reciprocal structures obey this relationship in the neighborhood of normal incidence, the process of breaking increasingly more severely the 2-fold rotational symmetry of the Tilston cell is not expected to affect very much the results at normal incidence, provided that the asymmetry does not affect also the other relationship needed for a CPSS, i.e. $C_{uv}^{pq} = -C_{uv}^{qp}$ with $p \neq q$ and $u \neq v$. The results of the simulations show that only the *Blckg* value is affected significantly at normal incidence. It takes an asymmetry level of 0.015 $m \approx 0.05\lambda$ to bring the *Blckg* value for the Tilston cell up to the *Blckg* value for the Pierrot cell. Such a small level of asymmetry confirms that the 2-fold rotational symmetry requirement is not critical at normal incidence since a radically asymmetrical design like the Pierrot cell behaves as well as a slightly asymmetrical design like the above asymmetrical Tilston cell. One notes, however, an exponential rate of increase in the *Blckg* value with increasing the level of asymmetry so that there is a limit to how much asymmetry can be tolerated.

The results of Tables 4.62 to 4.65 show a definite superiority of the Tilston design over the Pierrot design at off-normal incidence angles. The range over which $ar^t < 2.0$ is about $\theta^i < 15^o$ for the Tilston design compared to $\theta^i <<< 5^o$ for the Pierrot design. Since the relationship $C_{vv}^{pq} = -C_{vv}^{pq}$ is necessary, although not sufficient, for the ideal CPSS, it is reasonable to hope that at off-normal incidence, the 2-fold rotational symmetry might be responsible for the better performance of the Tilston design over the performance of the Pierrot design. In an attempt to assess to what extent, if any, the 2-fold rotational symmetry was indeed responsible for this superiority, the 0.015 m asymmetrically configured Tilston cell, which has about the same *Blckg* value as does the Pierrot cell, was investigated with respect to the case of $\phi^i = 135^o$, which case

presented by far the worst ar^t values for the Pierrot design. The results are shown in Tables 4.66 to 4.68. Since the degradation in ar^t is rather moderate and very far from being as bad as that for the Pierrot design, one must conclude that the poor performance of the Pierrot design with respect to θ^i does not lie solely with its lack of the 2-fold rotational symmetry. This author surmises that the poor performance of the Pierrot design is also attributable to the presence of the longitudinal wire since the profile of this wire becomes increasingly larger as the angle θ^i increases from 0^o.

The longitudinal wire does not exist in the Tilston cell when modelling the transmission line by a non-radiating network with NEC-2. In practice, however, the actual wires of the transmission line, whether in bifilar or coaxial form, would present a longitudinal section which would create to some extent a problem similar to that incurred with the Pierrot design. In order for the two wires to behave as an ideal transmission line, the currents of one wire must be exactly equal and opposite to that of the other wire. If the transmission line is implemented in bifilar form, the two wires must be in very close proximity to one another so that, for all practical intent, the radiation from one wire be cancelled out by the radiation from the other wire at all points in the volume surrounding the two wires. If the transmission line is implemented in coaxial form, a balun must be used in order to avoid the current imbalance that would result from only the outside wire being exposed to the external fields. Either form of transmission line would incur a great increase in manufacturing complexity over that for the Pierrot design.

Tables 4.51 to 4.77 present the results obtained from varying the incidence angle, the cell thickness, the frequency and the cell size. As with the Pierrot design, the axial ratios ar^r and ar^t are seen to be smallest, i.e. best, at the expected frequency of 1.00 GHz and the expected cell thickness of $\lambda/4$, but contrary to the Pierrot design, the smallest values of $Blckg$ and $Leakg$ as well as the largest value of $|LL^r/RR^r|$ are also found at that cell thickness value. This observation suggests that the Tilston

design is optimized with respect to the cell thickness. Also contrary to the case of the Pierrot design, the axial ratio ar^t is no longer the limiting parameter at the upper edge of the frequency bandwidth. The limiting parameter is now either $|LL^r/RR^r|$ or *Blckg*.

As with the Pierrot design, the *Blckg* and the ar^t values vary much more than the *Leakg* and ar^r values on a percentage basis, respectively. This situation is again indicative of the weakness of idealizing the principle of operation by assuming that the structure is transparent under RHCP illumination. Defining the operating range on the basis of $ar^t \leq 2$, one obtains:

- $0.98\ GHz < f$ which is worse than the value of $0.88\ GHz$ for the Pierrot design.
- $0.240\lambda <$ cell thickness $< 0.260\lambda$, hence the performance is symmetrical with respect to the nominal value of 0.250λ, with the lower limit being now worse than the value of 0.234λ obtained for the Pierrot design.

The performance has a more complicated behavior with respect to θ^i and ϕ^i than that for the Pierrot design, although as expected, this behavior is symmetrical with respect to ϕ^i. For instance, the maximum $|LL^r|$ values for $\theta^i = 45^o$ occur for the diagonal directions, i.e. $\phi^i = 45^o$ and 225^o, whereas the minimum values occur for the anti-diagonal directions, i.e. $\phi^i = 135^o$ and 315^o, but the situation is reversed for $\theta^i = 5^o$. The ar^r, but not the ar^t, values are consistently better for the diagonal directions than for the anti-diagonal directions.

The best choice of inter-element spacing on the basis of maximizing $|LL^r/RR^r|$ appears to be $0.24\ m$ but there is formation of grating lobes which situation is undesirable. For the inter-element spacing between $0.14\ m$ and $0.18\ m$, it is seen that the *Blckg* increases and the *Leakg* decreases as though the surface appears denser as the inter-element spacing decreases, a situation which is expected from heuristic considerations. For the inter-element spacing larger than $0.18\ m$, the *Leakg* value is seen

to decrease but this situation might be an artifact resulting from the compensation scheme used in computing the *Leakg* value, when the case under study departs too much from the reference case.

The GSM for the octagonal array made of 37 identical Tilston LHCPSS with $\lambda/2$ inter-element spacing and illuminated at normal incidence was obtained as $S(X,Y) =$

$$\begin{pmatrix} 1.3534\angle -155.00^o & 1.2499\angle -74.62^o & 1.9945\angle -37.93^o & 1.2499\angle -164.68^o \\ 1.2499\angle -74.62^o & 1.3534\angle +25.12^o & 1.2499\angle +15.44^o & 1.9945\angle -37.93^o \\ 1.9945\angle -37.93^o & 1.2499\angle +15.44^o & 1.3534\angle +25.12^o & 1.2499\angle -74.62^o \\ 1.2499\angle -164.68^o & 1.9945\angle -37.93^o & 1.2499\angle -74.62^o & 1.3534\angle -155.00^o \end{pmatrix}$$

where the incidence propagation vector was taken as pointing outwardly from the origin of the coordinate system. Again, each scattering coefficient is described by a pair whose first number pertains to the magnitude and second number pertains to the phase. Surprisingly, the magnitudes are larger than 1.0 V/m, the magnitude of the linearly polarized incident plane wave! As expected, the matrix is symmetrical with respect to the diagonal owing to the structure being reciprocal but surprisingly, the matrix is also symmetrical with respect to the anti-diagonal. Also as expected, the structure does not have the longitudinal reflection symmetry but nothing can be said about the $2n$-fold rotational symmetry, by the same arguments as those invoked when dealing with the GSM for the Pierrot design. Thus, the GSM was also obtained for the case of a large departure from normal incidence, say $\theta^i = 150^o$. For two ports that are in a reciprocal relationship, say the port corresponding to $(\theta^i = 150^o, \phi^i = 250^o)$ and the port corresponding to $(\theta^i = 30^o, \phi^i = 70^o)$, the GSM was obtained as $C(E,H) =$

$$\begin{pmatrix} 1.0156\angle +149.60^o & 1.2447\angle +64.82^o & 1.7593\angle -36.71^o & 1.1070\angle -179.75^o \\ 1.2438\angle -115.21^o & 1.1295\angle +171.37^o & 1.1365\angle +23.06^o & 1.8793\angle -39.14^o \\ 1.7589\angle -36.72^o & 1.1374\angle -156.94^o & 1.1884\angle +67.22^o & 1.0533\angle -33.37^o \\ 1.1062\angle +0.25^o & 1.8799\angle -39.12^o & 1.0525\angle +146.68^o & 1.3309\angle +42.55^o \end{pmatrix}$$

As expected, the matrix $C(E,H)$ is not symmetrical, but contrary to the case of the Pierrot design, the results still show $C_{vv}^{pq} = -C_{vv}^{qp}$ in spite of the incidence being

markedly off-normal. It is noted also that although the two relationships $C_{vv}^{pq} = -C_{vv}^{qp}$ and $C_{uv}^{pq} = -C_{uv}^{qp}$ needed for the ideal CPSS are satisfied by the Tilston design at this markedly off-normal incidence, the performance is not yet ideal because these two relationships are necessary but not sufficient, as seen from the GSM for the ideal LHCPSS.

It is concluded that the performance of neither the Pierrot nor the Tilston CPSS is ideal even at normal incidence. The Pierrot design is quite sensitive to variations in both incidence angles θ^i and ϕ^i, the best performance being achieved at normal incidence. The Tilston design is more tolerant with respect to variations of the incidence angle but less tolerant with respect to variations in frequency or cell thickness.

Table 4.45: Peak scattering values for octagonal arrays of 37 cells with various cell designs and 0.15 m inter-element spacing. The observation sphere radius is 30.0 m.

Incidence	Cell design	Peak values				
		$\|LL\|$	$\|RR\|$	$\|RL\|$	$\|LR\|$	$\|LL/RR\|$
Normal	Pierrot	0.12080	0.01359	0.01073	0.00263	8.89
"	S-C turnstile	0.12268	0.12268	0.00636	0.00636	1.00
"	O-C turnstile	0.00941	0.00941	0.00043	0.00043	1.00
"	Tilston	0.12205	0.01144	0.00503	0.00059	10.67
"	Tilston-CW	0.06192	0.00689	0.00465	0.00147	8.99
"	Tilston-CCW	0.06199	0.00689	0.00463	0.00139	9.00
"	Tilston-X	0.10016	0.01069	0.00402	0.00056	9.37
"	Reflector	0.00000	0.00000	0.13620	0.13620	0.00
Corner	Pierrot	0.09344	0.02020	0.02106	0.01632	4.63
"	S-C turnstile	0.10160	0.06850	0.03463	0.03383	1.48
"	O-C turnstile	0.00698	0.00676	0.00301	0.00328	1.03
"	Tilston	0.09233	0.00827	0.01145	0.00743	11.16
"	Tilston-CW	0.04992	0.00617	0.01070	0.00869	8.09
"	Tilston-CCW	0.04995	0.00615	0.01200	0.00988	8.12
"	Tilston-X	0.07251	0.01302	0.02492	0.02231	5.57
"	Reflector	0.00411	0.00411	0.09664	0.09664	1.00
Note: S-C: Short-Circuited, O-C: Open-Circuited.						

Table 4.46: Reflection beam values for octagonal arrays of 37 cells with various cell designs and 0.15 m inter-element spacing. The observation sphere radius is 30.0 m.

Incidence	Cell design	Reflection beam values					
		$\|LL\|$	$\|RR\|$	$\|RL\|$	$\|LR\|$	ar	$Blckg$
Normal	Pierrot	0.12080	0.01359	0.00017	0.00005	1.0028	21.5619
"	S-C turnstile	0.12268	0.12268	0.00020	0.00020	1.0033	1756.65
"	O-C turnstile	0.00941	0.00941	0.00001	0.00001	1.0031	10.3257
"	Tilston	0.12205	0.01144	0.00016	0.00008	1.0027	15.2664
"	Tilston-CW	0.05798	0.00440	0.00139	0.00147	1.0492	2.5089
"	Tilston-CCW	0.05800	0.00442	0.00139	0.00139	1.0493	2.5010
"	Tilston-X	0.10016	0.01069	0.00012	0.00007	1.0025	13.3447
"	Reflector	0.00000	0.00000	0.13620	0.13620	1.0000	2165.15
Corner	Pierrot	0.08948	0.02020	0.00920	0.01632	1.2291	78.7005
"	S-C turnstile	0.08270	0.06779	0.03211	0.03210	2.2696	656.605
"	O-C turnstile	0.00494	0.00671	0.00301	0.00301	4.1187	6.3068
"	Tilston	0.09171	0.00807	0.00746	0.00743	1.1771	14.0361
"	Tilston-CW	0.04683	0.00340	0.00884	0.00869	1.4656	10.1564
"	Tilston-CCW	0.04642	0.00175	0.01015	0.00988	1.5594	11.7521
"	Tilston-X	0.07251	0.01302	0.02145	0.02146	1.8401	73.5237
"	Reflector	0.00411	0.00411	0.09664	0.09664	1.0888	1091.94
Note: S-C: Short-Circuited, O-C: Open-Circuited. $Blckg$ values are $\times 10^3$							

Table 4.47: Transmission beam values for octagonal arrays of 37 cells with various cell designs and 0.15 m inter-element spacing. The observation sphere radius is 30.0 m.

Incidence	Cell design	Transmission beam values					
		$\|LL\|$	$\|RR\|$	$\|RL\|$	$\|LR\|$	ar	$Leakg$
Normal	Pierrot	0.12080	0.01359	0.00016	0.00008	1.0119	0.37156
"	S-C turnstile	0.12268	0.12268	0.00016	0.00016	1.0025	0.31955
"	O-C turnstile	0.00941	0.00941	0.00001	0.00001	1.0024	2.14669
"	Tilston	0.12205	0.01144	0.00017	0.00005	1.0085	0.23269
"	Tilston-CW	0.06192	0.00689	0.00138	0.00133	1.4785	1.67110
"	Tilston-CCW	0.06199	0.00689	0.00124	0.00136	1.4923	1.71922
"	Tilston-X	0.10015	0.01069	0.00014	0.00004	1.0073	0.75117
"	Reflector	0.13620	0.13620	0.00000	0.00000	1.0000	0.00000
Corner	Pierrot	0.09344	0.02006	0.01557	0.00879	2.5590	0.12109
"	S-C turnstile	0.10160	0.06850	0.02123	0.02125	1.8992	0.09055
"	O-C turnstile	0.00698	0.00676	0.00224	0.00224	1.9906	1.08958
"	Tilston	0.09233	0.00827	0.00599	0.00601	6.3407	0.04170
"	Tilston-CW	0.04992	0.00617	0.00767	0.00859	6.0887	0.80846
"	Tilston-CCW	0.04995	0.00615	0.00876	0.00741	10.7893	0.83823
"	Tilston-X	0.07235	0.01157	0.02219	0.02231	3.1540	0.25552
"	Reflector	0.09664	0.09664	0.00411	0.00411	1.0888	0.00197
Note: S-C: Short-Circuited, O-C: Open-Circuited.							

Table 4.48: Peak scattering values for increasingly more asymmetrical Tilston cell designs. The number of cells is 37, the inter-element spacing is 0.15 m, the incidence is normal and the observation sphere radius is 30.0 m.

Offset		Peak values				
(m)	(λ)	$\|LL\|$	$\|RR\|$	$\|RL\|$	$\|LR\|$	$\|LL/RR\|$
0.000	0.000	0.12205	0.01144	0.00503	0.00059	10.67
0.005	0.017	0.12207	0.01168	0.00506	0.00063	10.45
0.010	0.033	0.12217	0.01239	0.00513	0.00069	9.86
0.015	0.050	0.12228	0.01363	0.00549	0.00085	8.97
0.020	0.067	0.12241	0.01542	0.00586	0.00115	7.94
0.025	0.083	0.12249	0.01785	0.00629	0.00153	6.86
0.030	0.100	0.12249	0.02105	0.00683	0.00203	5.82
0.040	0.133	0.12321	0.03208	0.00840	0.00354	3.84
0.050	0.167	0.12239	0.04833	0.01006	0.00563	2.53

Table 4.49: Reflection beam values for increasingly more asymmetrical Tilston cell designs. The number of cells is 37, the inter-element spacing is 0.15 m, the incidence is normal and the observation sphere radius is 30.0 m.

Offset		Reflection beam values					
(m)	(λ)	$\|LL\|$	$\|RR\|$	$\|RL\|$	$\|LR\|$	ar	$Blckg$
0.000	0.000	0.12205	0.01144	0.00016	0.00008	1.0027	15.266
0.005	0.017	0.12207	0.01167	0.00016	0.00008	1.0027	15.909
0.010	0.033	0.12217	0.01239	0.00016	0.00008	1.0027	17.931
0.015	0.050	0.12228	0.01363	0.00016	0.00008	1.0026	21.672
0.020	0.067	0.12241	0.01542	0.00016	0.00009	1.0026	27.759
0.025	0.083	0.12249	0.01785	0.00016	0.00009	1.0026	37.206
0.030	0.100	0.12249	0.02105	0.00016	0.00009	1.0025	51.719
0.040	0.133	0.12321	0.03208	0.00016	0.00010	1.0025	120.123
0.050	0.167	0.12239	0.04833	0.00015	0.00013	1.0025	272.624
The values for $Blckg$ have been multiplied by 10^3							

Table 4.50: Transmission beam values for increasingly more asymmetrical Tilston cell designs. The number of cells is 37, the inter-element spacing is 0.15 m, the incidence is normal and the observation sphere radius is 30.0 m.

Offset		Transmission beam values					
(m)	(λ)	$\|LL\|$	$\|RR\|$	$\|RL\|$	$\|LR\|$	ar	$Leakg$
0.000	0.000	0.12205	0.01144	0.00017	0.00005	1.0085	0.23269
0.005	0.017	0.12207	0.01168	0.00017	0.00005	1.0083	0.23321
0.010	0.033	0.12217	0.01239	0.00017	0.00005	1.0077	0.23461
0.015	0.050	0.12228	0.01363	0.00017	0.00005	1.0068	0.23720
0.020	0.067	0.12241	0.01542	0.00017	0.00004	1.0054	0.24104
0.025	0.083	0.12249	0.01785	0.00017	0.00004	1.0048	0.24589
0.030	0.100	0.12249	0.02105	0.00017	0.00004	1.0040	0.25114
0.040	0.133	0.12321	0.03207	0.00018	0.00003	1.0017	0.22530
0.050	0.167	0.12239	0.04833	0.00018	0.00002	1.0009	0.22271

Table 4.51: $|LL^p|$ values of the octagonal array of 37 Tilston cells for various incidences. The inter-element spacing is 0.15 m and the observation sphere radius is 30.0 m.

θ^i | ϕ^i	0^o	15^o	45^o	90^o	135^o	180^o	225^o	270^o	315^o
0^o	0.1221								
5^o	0.1227	0.1223	0.1218	0.1227	0.1234	0.1227	0.1218	0.1227	0.1234
15^o	0.1190		0.1211	0.1190					
30^o	0.1014		0.1114	0.1015					
45^o	0.0761	0.0803	0.0923	0.0767	0.0677	0.0761	0.0923	0.0767	0.0677
60^o	0.0430		0.0753	0.0441					
75^o	0.0236		0.0477	0.0242					

Table 4.52: $|RR^p|$ values of the octagonal array of 37 Tilston cells for various incidences. The inter-element spacing is 0.15 m and the observation sphere radius is 30.0 m.

θ^i | ϕ^i	0^o	15^o	45^o	90^o	135^o	180^o	225^o	270^o	315^o
0^o	0.0114								
5^o	0.0114	0.0114	0.0114	0.0114	0.0114	0.0114	0.0114	0.0114	0.0114
15^o	0.0111		0.0110	0.0112					
30^o	0.0106		0.0099	0.0117					
45^o	0.0123	0.0096	0.0083	0.0153	0.0157	0.0123	0.0083	0.0153	0.0157
60^o	0.0139		0.0070	0.0166					
75^o	0.0163		0.0064	0.0169					

Table 4.53: $|LL^p/RR^p|$ values of the octagonal array of 37 Tilston cells for various incidences. The inter-element spacing is 0.15 m and the observation sphere radius is 30.0 m.

θ^i | ϕ^i	0^o	15^o	45^o	90^o	135^o	180^o	225^o	270^o	315^o
0^o	10.67								
5^o	10.77	10.73	10.70	10.77	10.83	10.77	10.70	10.77	10.83
15^o	10.74		11.00	10.67					
30^o	9.55		11.31	8.65					
45^o	6.19	8.39	11.16	5.02	4.32	6.19	11.16	5.02	4.32
60^o	3.09		10.82	2.66					
75^o	1.44		7.51	1.43					

Table 4.54: $|LL^r|$ reflection beam values of the octagonal array of 37 Tilston cells for various incidences. The inter-element spacing is 0.15 m and the observation sphere radius is 30.0 m.

θ^i | ϕ^i	0^o	15^o	45^o	90^o	135^o	180^o	225^o	270^o	315^o
0^o	0.1221								
5^o	0.1227	0.1223	0.1218	0.1227	0.1234	0.1227	0.1218	0.1227	0.1234
15^o	0.1190		0.1211	0.1190					
30^o	0.1011		0.1112	0.1015					
45^o	0.0744	0.0789	0.0917	0.0758	0.0677	0.0744	0.0917	0.0758	0.0677
60^o	0.0376		0.0753	0.0395					
75^o	0.0215		0.0356	0.0216					

Table 4.55: $|LL^t|$ transmission beam values of the octagonal array of 37 Tilston cells for various incidences. The inter-element spacing is 0.15 m and the observation sphere radius is 30.0 m.

θ^i | ϕ^i	0^o	15^o	45^o	90^o	135^o	180^o	225^o	270^o	315^o
0^o	0.1221								
5^o	0.1227	0.1223	0.1218	0.1227	0.1234	0.1227	0.1218	0.1227	0.1234
15^o	0.1190		0.1211	0.1190					
30^o	0.1014		0.1114	0.1014					
45^o	0.0753	0.0802	0.0923	0.0753	0.0677	0.0753	0.0923	0.0753	0.0677
60^o	0.0385		0.0748	0.0385					
75^o	0.0213		0.0370	0.0213					

Table 4.56: $|RR^r|$ reflection beam values of the octagonal array of 37 Tilston cells for various incidences. The inter-element spacing is 0.15 m and the observation sphere radius is 30.0 m.

θ^i | ϕ^i	0^o	15^o	45^o	90^o	135^o	180^o	225^o	270^o	315^o
0^o	0.0114								
5^o	0.0114	0.0114	0.0114	0.0114	0.0114	0.0114	0.0114	0.0114	0.0114
15^o	0.0108		0.0110	0.0112					
30^o	0.0073		0.0098	0.0117					
45^o	0.0031	0.0031	0.0081	0.0153	0.0090	0.0031	0.0081	0.0153	0.0090
60^o	0.0111		0.0070	0.0166					
75^o	0.0155		0.0061	0.0168					

Table 4.57: $|RR^t|$ transmission beam values of the octagonal array of 37 Tilston cells for various incidences. The inter-element spacing is 0.15 m and the observation sphere radius is 30.0 m.

θ^i | ϕ^i	0^o	15^o	45^o	90^o	135^o	180^o	225^o	270^o	315^o
0^o	0.0114								
5^o	0.0114	0.0114	0.0114	0.0114	0.0114	0.0114	0.0114	0.0114	0.0114
15^o	0.0111		0.0110	0.0111					
30^o	0.0106		0.0099	0.0106					
45^o	0.0122	0.0096	0.0083	0.0122	0.0154	0.0122	0.0083	0.0122	0.0154
60^o	0.0139		0.0069	0.0139					
75^o	0.0159		0.0062	0.0159					

Table 4.58: $|RL^r|$ reflection beam values of the octagonal array of 37 Tilston cells for various incidences. The inter-element spacing is 0.15 m and the observation sphere radius is 30.0 m.

θ^i | ϕ^i	0^o	15^o	45^o	90^o	135^o	180^o	225^o	270^o	315^o
0^o	0.0002								
5^o	0.0007	0.0006	0.0002	0.0003	0.0006	0.0007	0.0002	0.0003	0.0006
15^o	0.0051		0.0014	0.0041					
30^o	0.0173		0.0046	0.0144					
45^o	0.0282	0.0245	0.0075	0.0239	0.0266	0.0282	0.0075	0.0239	0.0266
60^o	0.0246		0.0080	0.0214					
75^o	0.0188		0.0073	0.0181					

Table 4.59: $|RL^t|$ transmission beam values of the octagonal array of 37 Tilston cells for various incidences. The inter-element spacing is 0.15 m and the observation sphere radius is 30.0 m.

θ^i | ϕ^i	0^o	15^o	45^o	90^o	135^o	180^o	225^o	270^o	315^o
0^o	0.0002								
5^o	0.0003	0.0002	0.0001	0.0006	0.0006	0.0003	0.0001	0.0006	0.0006
15^o	0.0043		0.0010	0.0046					
30^o	0.0153		0.0036	0.0155					
45^o	0.0257	0.0222	0.0060	0.0256	0.0261	0.0257	0.0060	0.0256	0.0261
60^o	0.0232		0.0086	0.0231					
75^o	0.0190		0.0064	0.0185					

Table 4.60: $|LR^r|$ reflection beam values of the octagonal array of 37 Tilston cells for various incidences. The inter-element spacing is 0.15 m and the observation sphere radius is 30.0 m.

θ^i | ϕ^i	0^o	15^o	45^o	90^o	135^o	180^o	225^o	270^o	315^o
0^o	0.0001								
5^o	0.0005	0.0004	0.0001	0.0004	0.0005	0.0006	0.0001	0.0004	0.0005
15^o	0.0050		0.0013	0.0041					
30^o	0.0172		0.0046	0.0145					
45^o	0.0281	0.0244	0.0074	0.0240	0.0266	0.0281	0.0074	0.0240	0.0266
60^o	0.0246		0.0080	0.0214					
75^o	0.0188		0.0073	0.0181					

Table 4.61: $|LR^t|$ transmission beam values of the octagonal array of 37 Tilston cells for various incidences. The inter-element spacing is 0.15 m and the observation sphere radius is 30.0 m.

θ^i | ϕ^i	0^o	15^o	45^o	90^o	135^o	180^o	225^o	270^o	315^o
0^o	0.0001								
5^o	0.0005	0.0004	0.0001	0.0005	0.0006	0.0005	0.0001	0.0005	0.0006
15^o	0.0045		0.0010	0.0044					
30^o	0.0154		0.0036	0.0154					
45^o	0.0255	0.0205	0.0060	0.0257	0.0262	0.0255	0.0060	0.0257	0.0262
60^o	0.0231		0.0087	0.0232					
75^o	0.0185		0.0064	0.0190					

Table 4.62: ar^r reflection beam values of the octagonal array of 37 Tilston cells for various incidences. The inter-element spacing is 0.15 m and the observation sphere radius is 30.0 m.

θ^i | ϕ^i	0^o	15^o	45^o	90^o	135^o	180^o	225^o	270^o	315^o
0^o	1.0027								
5^o	1.0110	1.010	1.004	1.005	1.009	1.011	1.004	1.005	1.009
15^o	1.0898		1.024	1.071					
30^o	1.4127		1.087	1.331					
45^o	2.2196	1.898	1.177	1.923	2.298	2.220	1.177	1.923	2.298
60^o	4.7992		1.238	3.363					
75^o	14.7149		1.514	11.312					

Table 4.63: ar^t transmission beam values of the octagonal array of 37 Tilston cells for various incidences. The inter-element spacing is 0.15 m and the observation sphere radius is 30.0 m.

θ^i | ϕ^i	0^o	15^o	45^o	90^o	135^o	180^o	225^o	270^o	315^o
0^o	1.0085								
5^o	1.0918	1.066	1.014	1.083	1.101	1.092	1.014	1.083	1.101
15^o	2.3568		1.200	2.318					
30^o	5.4569		2.153	5.495					
45^o	2.8168	2.738	6.341	2.807	3.864	2.817	6.341	2.807	3.864
60^o	4.0191		8.605	3.999					
75^o	13.1262		77.045	11.221					

Table 4.64: Blockage beam values of the octagonal array of 37 Tilston cells for various incidences. The inter-element spacing is 0.15 m and the observation sphere radius is 30.0 m.

θ^i | ϕ^i	0^o	15^o	45^o	90^o	135^o	180^o	225^o	270^o	315^o
0^o	15.27								
5^o	15.18	15.16	15.14	15.17	15.20	15.18	15.14	15.17	15.20
15^o	16.65		14.33	16.54					
30^o	40.68		13.57	40.49					
45^o	93.52	70.53	14.04	94.13	92.23	93.52	14.04	94.13	92.23
60^o	84.72		13.14	85.35					
75^o	69.24		10.54	71.35					
The values for *Blckg* have been multiplied by 10^3									

Table 4.65: Leakage beam values of the octagonal array of 37 Tilston cells for various incidences. The inter-element spacing is 0.15 m and the observation sphere radius is 30.0 m.

θ^i | ϕ^i	0^o	15^o	45^o	90^o	135^o	180^o	225^o	270^o	315^o
0^o	0.2327								
5^o	0.2498	0.2534	0.2566	0.2498	0.2415	0.2498	0.2566	0.2498	0.2415
15^o	0.2581		0.2128	0.2585					
30^o	0.2165		0.0940	0.2169					
45^o	0.1687	0.1041	0.0417	0.1683	0.3586	0.1687	0.0417	0.1683	0.3586
60^o	0.1816		0.0449	0.1814					
75^o	0.0583		0.0156	0.0562					

Table 4.66: Peak scattering values of the octagonal array of 37 Tilston cells with 0.015 m asymmetry. The inter-element spacing is 0.15 m and the observation sphere radius is 30.0 m.

Incidence		Peak values				
$\theta^i(^o)$	$\phi^i(^o)$	$\|LL\|$	$\|RR\|$	$\|RL\|$	$\|LR\|$	$\|LL/RR\|$
5.0	135.0	0.12367	0.01361	0.00729	0.00155	9.09
45.0	135.0	0.06864	0.01279	0.03676	0.01893	5.37

Table 4.67: Reflection beam values of the octagonal array of 37 Tilston cells with 0.015 m asymmetry. The inter-element spacing is 0.15 m and the observation sphere radius is 30.0 m.

Incidence		Reflection beam values					
$\theta^i(^o)$	$\phi^i(^o)$	$\|LL\|$	$\|RR\|$	$\|RL\|$	$\|LR\|$	ar	$Blckg$
5.0	135.0	0.12367	0.01361	0.00226	0.00121	1.0372	21.7809
45.0	135.0	0.06761	0.00863	0.03449	0.01893	3.0830	50.4959
The values for $Blckg$ have been multiplied by 10^3							

Table 4.68: Transmission beam values of the octagonal array of 37 Tilston cells with 0.015 m asymmetry. The inter-element spacing is 0.15 m and the observation sphere radius is 30.0 m.

Incidence		Transmission beam values					
$\theta^i(^o)$	$\phi^i(^o)$	$\|LL\|$	$\|RR\|$	$\|RL\|$	$\|LR\|$	ar	$Leakg$
5.0	135.0	0.12367	0.01360	0.00120	0.00118	1.1899	0.25088
45.0	135.0	0.06864	0.01279	0.01860	0.01855	5.4471	0.32154

Table 4.69: Peak scattering values of the octagonal array of 37 Tilston cells with various cell thickness values. The inter-element spacing is 0.15 m, the incidence is normal and the observation sphere radius is 30.0 m.

Cell thickness		Peak values				
(m)	(λ)	$\|LL\|$	$\|RR\|$	$\|RL\|$	$\|LR\|$	$\|LL/RR\|$
0.060	0.200	0.11943	0.01273	0.01969	0.01965	9.38
0.065	0.217	0.12094	0.01195	0.01321	0.01319	10.12
0.070	0.233	0.12182	0.01156	0.00661	0.00659	10.54
0.071	0.237	0.12191	0.01152	0.00529	0.00526	10.58
0.072	0.240	0.12199	0.01148	0.00501	0.00392	10.63
0.075	0.250	0.12205	0.01144	0.00503	0.00059	10.67
0.078	0.260	0.12188	0.01148	0.00504	0.00408	10.62
0.079	0.264	0.12178	0.01151	0.00538	0.00541	10.58
0.080	0.267	0.12165	0.01155	0.00670	0.00674	10.53
0.085	0.284	0.12061	0.01193	0.01328	0.01331	10.11
0.090	0.300	0.11894	0.01270	0.01970	0.01974	9.37

Table 4.70: Reflection beam values of the octagonal array of 37 Tilston cells with various cell thickness values. The inter-element spacing is 0.15 m, the incidence is normal and the observation sphere radius is 30.0 m.

Cell thickness		Reflection beam values					
(m)	(λ)	$\|LL\|$	$\|RR\|$	$\|RL\|$	$\|LR\|$	ar	$Blckg$
0.060	0.200	0.11919	0.01022	0.01969	0.01965	1.3957	57.2897
0.065	0.217	0.12083	0.01080	0.01321	0.01319	1.2456	33.9335
0.070	0.233	0.12179	0.01126	0.00661	0.00659	1.1148	19.8695
0.071	0.237	0.12190	0.01132	0.00529	0.00526	1.0907	18.1941
0.072	0.240	0.12198	0.01137	0.00396	0.00392	1.0671	16.8811
0.075	0.250	0.12205	0.01144	0.00016	0.00008	1.0027	15.2664
0.078	0.260	0.12188	0.01138	0.00406	0.00408	1.0689	17.0667
0.079	0.264	0.12177	0.01133	0.00538	0.00541	1.0924	18.3974
0.080	0.267	0.12162	0.01127	0.00670	0.00674	1.1167	20.1215
0.085	0.284	0.12049	0.01082	0.01328	0.01331	1.2477	34.3404
0.090	0.300	0.11869	0.01026	0.01970	0.01974	1.3980	57.7579
The values for $Blckg$ have been multiplied by 10^3							

Table 4.71: Transmission beam values of the octagonal array of 37 Tilston cells with various cell thickness values. The inter-element spacing is 0.15 m, the incidence is normal and the observation sphere radius is 30.0 m.

Cell thickness		Transmission beam values					
(m)	(λ)	$\|LL\|$	$\|RR\|$	$\|RL\|$	$\|LR\|$	ar	$Leakg$
0.060	0.200	0.11943	0.01273	0.01815	0.01817	5.6845	0.27886
0.065	0.217	0.12094	0.01195	0.01218	0.01220	95.7027	0.25312
0.070	0.233	0.12182	0.01156	0.00609	0.00611	3.2421	0.23781
0.071	0.237	0.12191	0.01152	0.00486	0.00488	2.4708	0.23590
0.072	0.240	0.12199	0.01148	0.00362	0.00365	1.9314	0.23449
0.075	0.250	0.12205	0.01144	0.00017	0.00005	1.0085	0.23269
0.078	0.260	0.12188	0.01148	0.00377	0.00374	1.9673	0.23477
0.079	0.264	0.12178	0.01151	0.00499	0.00497	2.5208	0.23640
0.080	0.267	0.12165	0.01155	0.00621	0.00620	3.3146	0.23823
0.085	0.284	0.12061	0.01193	0.01228	0.01226	73.0082	0.25436
0.090	0.300	0.11894	0.01270	0.01821	0.01819	5.6329	0.28050

Table 4.72: Peak scattering values of the octagonal array of 37 Tilston cells for various frequency values. The inter-element spacing is 0.15 m, the incidence is normal and the observation sphere radius is 30.0 m.

Frequency	Peak values				
(GHz)	$\|LL\|$	$\|RR\|$	$\|RL\|$	$\|LR\|$	$\|LL/RR\|$
0.95	0.09843	0.00408	0.00460	0.00391	24.13
0.96	0.10354	0.00090	0.00486	0.00322	115.04
0.97	0.10882	0.00228	0.00509	0.00254	47.73
0.98	0.11421	0.00532	0.00530	0.00177	21.47
0.99	0.11879	0.00836	0.00531	0.00089	14.21
1.00	0.12205	0.01144	0.00503	0.00059	10.67
1.01	0.12472	0.01457	0.00654	0.00112	8.56
1.02	0.13684	0.01781	0.00644	0.00235	7.68
1.03	0.13542	0.02115	0.00644	0.00346	6.40
1.04	0.13602	0.02464	0.00616	0.00461	5.52
1.05	0.13648	0.02828	0.00598	0.00575	4.83
1.10	0.12895	0.05022	0.01127	0.01115	2.57
1.15	0.11171	0.08186	0.01744	0.01728	1.37

Table 4.73: Reflection beam values of the octagonal array of 37 Tilston cells for various frequency values. The inter-element spacing is 0.15 m, the incidence is normal and the observation sphere radius is 30.0 m.

Frequency (GHz)	Reflection beam values					
	$\|LL\|$	$\|RR\|$	$\|RL\|$	$\|LR\|$	ar	$Blckg$
0.95	0.09843	0.00408	0.00373	0.00373	1.0788	3.955
0.96	0.10354	0.00090	0.00319	0.00319	1.0636	1.390
0.97	0.10882	0.00221	0.00255	0.00254	1.0480	1.406
0.98	0.11420	0.00529	0.00180	0.00177	1.0320	3.779
0.99	0.11879	0.00835	0.00092	0.00089	1.0157	8.394
1.00	0.12205	0.01144	0.00016	0.00008	1.0027	15.266
1.01	0.12471	0.01457	0.00109	0.00112	1.0176	24.432
1.02	0.13684	0.01778	0.00231	0.00235	1.0343	36.093
1.03	0.13541	0.02111	0.00341	0.00346	1.0516	50.356
1.04	0.13601	0.02459	0.00455	0.00461	1.0692	67.516
1.05	0.13646	0.02823	0.00568	0.00575	1.0868	87.879
1.10	0.12895	0.05022	0.01064	0.01077	1.1798.	301.870
1.15	0.11171	0.08186	0.01537	0.01556	1.3191.	612.710
The values for $Blckg$ have been multiplied by 10^3						

Table 4.74: Transmission beam values of the octagonal array of 37 Tilston cells for various frequency values. The inter-element spacing is 0.15 m, the incidence is normal and the observation sphere radius is 30.0 m.

Frequency (GHz)	Transmission beam values					
	$\|LL\|$	$\|RR\|$	$\|RL\|$	$\|LR\|$	ar	$Leakg$
0.95	0.09843	0.00389	0.00393	0.00391	466.014	0.82285
0.96	0.10354	0.00078	0.00323	0.00322	1.642	0.70196
0.97	0.10882	0.00228	0.00249	0.00248	23.942	0.58132
0.98	0.11421	0.00532	0.00171	0.00170	1.941	0.45707
0.99	0.11879	0.00836	0.00085	0.00085	1.228	0.33378
1.00	0.12205	0.01144	0.00017	0.00005	1.009	0.23269
1.01	0.12472	0.01457	0.00103	0.00098	1.145	0.17301
1.02	0.13684	0.01781	0.00216	0.00212	1.271	0.07167
1.03	0.13542	0.02115	0.00319	0.00315	1.349	0.01913
1.04	0.13602	0.02464	0.00428	0.00423	1.415	0.00744
1.05	0.13648	0.02828	0.00542	0.00535	1.467	0.02261
1.10	0.12891	0.05009	0.01127	0.01115	1.573	0.42027
1.15	0.11146	0.08145	0.01744	0.01728	1.539	0.95984

Table 4.75: Peak scattering values of the octagonal array of 37 Tilston cells with different values of inter-element spacing. The incidence is normal and the observation sphere radius is 30.0 m.

Cell size		Peak values				
(m)	(λ)	$\|LL\|$	$\|RR\|$	$\|RL\|$	$\|LR\|$	$\|LL/RR\|$
0.14	0.467	0.11565	0.01210	0.00488	0.00090	9.56
0.15	0.500	0.12205	0.01144	0.00503	0.00059	10.67
0.16	0.534	0.13541	0.01126	0.00763	0.00047	12.03
0.17	0.567	0.14432	0.01120	0.00764	0.00055	12.89
0.18	0.500	0.15761	0.01119	0.00695	0.00056	14.09
0.19	0.634	0.17388	0.01121	0.00671	0.00052	15.51
0.20	0.667	0.19460	0.01125	0.00745	0.00080	17.30
0.21	0.700	0.21934	0.01130	0.00841	0.00094	19.41
0.22	0.734	0.24508	0.01135	0.00890	0.00087	21.59
0.23	0.767	0.27033	0.01143	0.01382	0.00078	23.65
0.24	0.801	0.28942	0.01151	0.01627	0.00099	25.14
0.25	0.834	0.27245	0.01161	0.02280	0.00110	23.47
0.26	0.867	0.21807	0.01173	0.03713	0.00166	18.59

Table 4.76: Reflection beam values of the octagonal array of 37 Tilston cells with different values of inter-element spacing. The incidence is normal and the observation sphere radius is 30.0 m.

Cell size		Reflection beam values					
(m)	(λ)	$\|LL\|$	$\|RR\|$	$\|RL\|$	$\|LR\|$	ar	$Blckg$
0.14	0.467	0.11565	0.01210	0.00015	0.00008	1.0027	22.5088
0.15	0.500	0.12205	0.01144	0.00016	0.00008	1.0027	15.2664
0.16	0.534	0.13541	0.01126	0.00018	0.00009	1.0027	11.4241
0.17	0.567	0.14432	0.01120	0.00023	0.00009	1.0031	8.8810
0.18	0.500	0.15761	0.01119	0.00023	0.00010	1.0029	7.0535
0.19	0.634	0.17388	0.01121	0.00023	0.00011	1.0026	5.7012
0.20	0.667	0.19460	0.01125	0.00030	0.00012	1.0030	4.6748
0.21	0.700	0.21934	0.01130	0.00030	0.00013	1.0027	3.8771
0.22	0.734	0.24508	0.01135	0.00030	0.00014	1.0025	3.2512
0.23	0.767	0.27033	0.01143	0.00037	0.00016	1.0028	2.7571
0.24	0.801	0.28942	0.01151	0.00037	0.00017	1.0025	2.3614
0.25	0.834	0.27238	0.01161	0.00030	0.00016	1.0022	2.0392
0.26	0.867	0.21807	0.01173	0.00029	0.00012	1.0027	1.7795
The values for $Blckg$ have been multiplied by 10^3							

Table 4.77: Transmission beam values of the octagonal array of 37 Tilston cells with different values of inter-element spacing. The incidence is normal and the observation sphere radius is 30.0 m.

Cell size		Transmission beam values					
(m)	(λ)	$\|LL\|$	$\|RR\|$	$\|RL\|$	$\|LR\|$	ar	$Leakg$
0.14	0.467	0.11565	0.01210	0.00017	0.00004	1.0074	0.04710
0.15	0.500	0.12205	0.01144	0.00017	0.00005	1.0085	0.23269
0.16	0.534	0.13541	0.01126	0.00018	0.00006	1.0102	0.33027
0.17	0.567	0.14432	0.01120	0.00022	0.00006	1.0108	0.40276
0.18	0.500	0.15761	0.01119	0.00022	0.00007	1.0122	0.42920
0.19	0.634	0.17388	0.01121	0.00023	0.00008	1.0137	0.41973
0.20	0.667	0.19460	0.01125	0.00029	0.00009	1.0157	0.36609
0.21	0.700	0.21934	0.01130	0.00030	0.00010	1.0179	0.26242
0.22	0.734	0.24501	0.01135	0.00037	0.00011	1.0202	0.14044
0.23	0.767	0.27033	0.01143	0.00037	0.00013	1.0225	0.05784
0.24	0.801	0.28942	0.01151	0.00037	0.00014	1.0243	0.12388
0.25	0.834	0.27245	0.01161	0.00037	0.00013	1.0227	0.53782
0.26	0.867	0.21807	0.01173	0.00029	0.00011	1.0181	1.07106

4.4 The cascade polarizer design

In order to obtain with NEC-2 the boundary value solution for a specific realization of the cascade polarizer design, each CP polarizer was realized with two parallel wire grids whose inter-wire spacing within each grid was nearly a quarter-wavelength, as reported by Bossuet and Gautier in their two patents [5, 6]. Such a realization was favored over the meander line CP polarizer in order to ensure that the complete LHCPSS structure could be simulated within the maximum number of segments for NEC-2. The LHCPSS required 2952 segments and the computation time was between 6 and 7 hours on a SPARC-10 desktop computer equipped with about 120 MBytes in RAM.

The principle of operation of the CP polarizer made of two parallel wire grids illuminated by a normally incident plane wave polarized at $+45^o$ to the wires, is as follows: The LP electric field component perpendicular to the wires is practically unaffected by the presence of the wires while the LP electric field component parallel to the wires is transmitted with some positive phase shift and with some magnitude attenuation. The attenuation is countered by using two identical grids spaced $\lambda/4$ along the longitudinal direction in order to implement the quarter-wavelength transformer. At the resonance frequency corresponding to the wavenumber λ, the reflection is reduced ideally to zero and thus, the transmission loss becomes also zero. From the analysis by Skwirzynski and Thackray cited in reference [87], the required $+45^o$ transmission phase shift for the LP electric field component parallel to the wires through each one of the two wire grids could be achieved with a wire radius $a = 0.005\lambda$ and an inter-wire spacing $s = 0.24\lambda$. The cumulative phase shift for the LP electric field component parallel to the wires through the two grids would then amount to $+90^o$ while that for the LP electric field perpendicular to the wires would still be zero, thus resulting in the output wave being circularly polarized.

The mutual coupling between the two parallel grids, however, causes some departure from the above specifications. For instance, a numerical analysis by variation of the parameters showed that the minimum reflection level obtained from the two parallel grids at normal incidence was $\approx 23\%$ instead of zero, and that the corresponding separation between the two grids was $d \approx 0.375\lambda = 0.1125\ m$ instead of $0.250\lambda = 0.1500\ m$. It must be pointed out also that, rigorously speaking, the quarter-wavelength transformer theory is not truly adequate for modelling the multiple grids. Here, each grid acts as a discontinuity along the same transmission line whereas, in the multi-step transformer theory, each discontinuity is created by a mismatch between the characteristic impedances of two different transmission lines. Consequently, in the multi-step transformer theory, the expression

$$\Gamma = \Gamma_1 + \frac{T_{12}T_{21}\Gamma_3 e^{-j2\theta}}{1 - \Gamma_2\Gamma_3 e^{-j2\theta}}$$

given by Collin in reference [20, p. 225] becomes:

$$\Gamma = \frac{\Gamma_1 + \Gamma_3 e^{-j2\theta}}{1 + \Gamma_1\Gamma_3 e^{-j2\theta}}$$

because the following simplifications hold: $\Gamma_2 = -\Gamma_1$, $T_{12} = 1 + \Gamma_2$ and $T_{21} = 1 + \Gamma_1$. Hence, the composite reflection coefficient Γ becomes zero when $\Gamma_1 = \Gamma_3$ and $\theta = 90^o$. However, in analyzing the series connection of the grids by the composite GSM technique, similar simplifications do not hold. Using MAPLE to find the inter-grid spacing required to obtain a zero value for both co-polarization and cross-polarization reflection coefficients at normal incidence yielded no possible solution, which situation agrees with the earlier observation that the minimum reflection level that could be obtained by varying the inter-grid spacing was not zero but 23%.

It must be pointed out that the NEC-2 simulations with the incident wave being normally incident and polarized at 45^o with respect to the wires shows no significant CP polarization being produced for a wide range of wire radius and for different values of inter-wire spacing. Yet, the analysis by Skwirzynski and Tachray is not in doubt

since the experimental results presented in reference [88] have shown a discrepancy smaller than 2 dB between the predicted and the measured values of transmission loss. The lack of CP polarization stems simply from the fact that NEC-2 provides not the total field but the scattered field. Hence, the CP polarization cannot be seen from the NEC-2 simulation results for the two wire grid CP polarizer because the LP electric field component perpendicular to the wires does not contribute to the scattered field.

Figure 4.34 depicts the generic configuration of the cascade polarizer LHCPSS design, with e_f and e_s designating respectively the fast and the slow axes of the retardation plates, with e_a designating the easy axis of the LP polarizer plate, and with $\phi_L = \phi_g \pm 90^o = \phi_R$. The orientation of the fast and the slow axes for the LHCP polarizer corresponds to the case e) of Figure 3.1. The orientation of the fast and the slow axes for the RHCP polarizer is that for the LHCP polarizer rotated by $\pm 90^o$ in the plane of the polarizer.

The NEC-2 simulations were conducted for the design depicted in Figure 4.34 for the shape and the size corresponding to an octagonal array of 37 cells with $\lambda/2$ inter-element spacing. Figure 4.35 shows one of the two octagonal plates of the LHCP polarizer, with an inter-wire spacing $s = 0.24\lambda$ and a wire radius $a = 0.0015\ m$. Figure 4.36 shows the octagonal LP polarizer plate with an inter-wire spacing $s = 0.025/\sqrt{2}\ m$ and a wire radius $a = 0.00281\ m$ as per the "same-surface-area" rule of thumb. Figure 4.37 shows one of the two octagonal plates of the RHCP polarizer, with an inter-wire spacing $s = 0.24\lambda$ and a wire radius $a = 0.0015\ m$.

The finite size of the scatterer brings about some concerns. The first concern pertains to the fact that since the octagonal LP polarizer plate includes very many wires of different lengths, some wires may happen to be of just the right length for geometrical resonance. The strong mutual coupling between closely spaced parallel wires, however, mitigates the problem by smoothing out the strong response from

any single wire over many adjacent wires, in effect trying to force all the wires to act as a single entity. Another concern deals with the difference between the charge accumulation at the edges of the solid reflector plate and that at the edges of the LP polarizer plate (i.e. the charge accumulation at the two ends of each wire in the LP polarizer plate). Such a difference might affect the field results in a way for which the use of a calibration factor based on the field results for a solid reflector plate of identical shape and size might not account. Similarly, there is also the concern about the difference between the thickness of the solid reflector plate and that of the overall CPSS structure. This difference would certainly affect the field results in a way for which the use of a calibration factor would not account. Thus admittedly, the use of calibration factors for computing the indicators *Leakg* and *Blckg* is more heuristic than rigorous.

Figures 4.38 to 4.41 present the results for the LP wire grid being at $+45^o$ and Figures 4.42 to 4.45 present the results for the LP wire grid being at -45^o. Clearly, the first case corresponds to an imperfect LHCPSS whereas the second case corresponds to an imperfect RHCPSS. Except for minute differences, the plots for these two cases are identical upon exchanging the LHCP and RHCP labels. This change from LHCPSS to RHCPSS by merely rotating the LP grid by $\pm 90^o$ in the plane of the grid was predicted in Chapter 3.

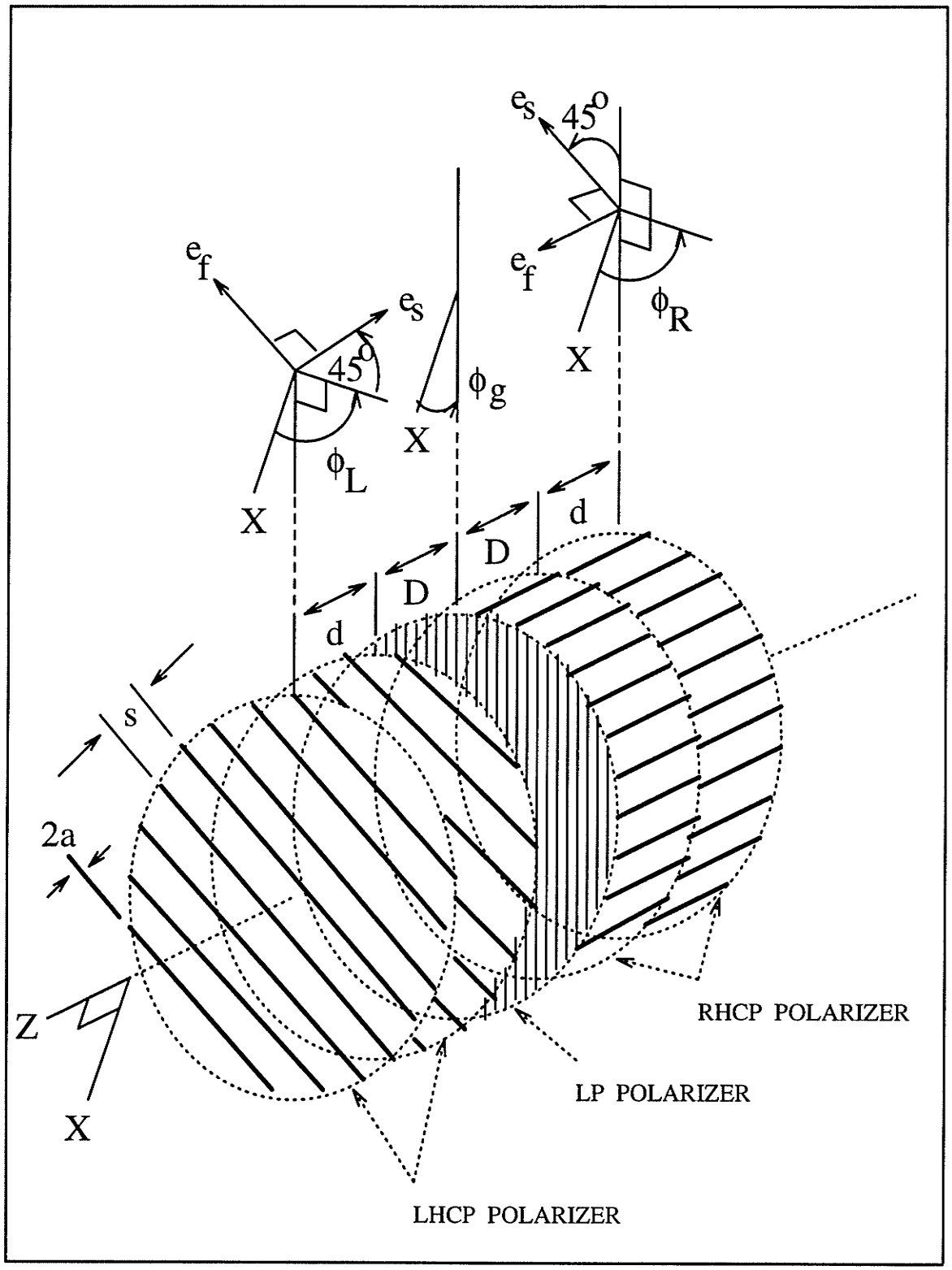

Figure 4.34: Generic configuration of the cascade polarizer LHCPSS design.

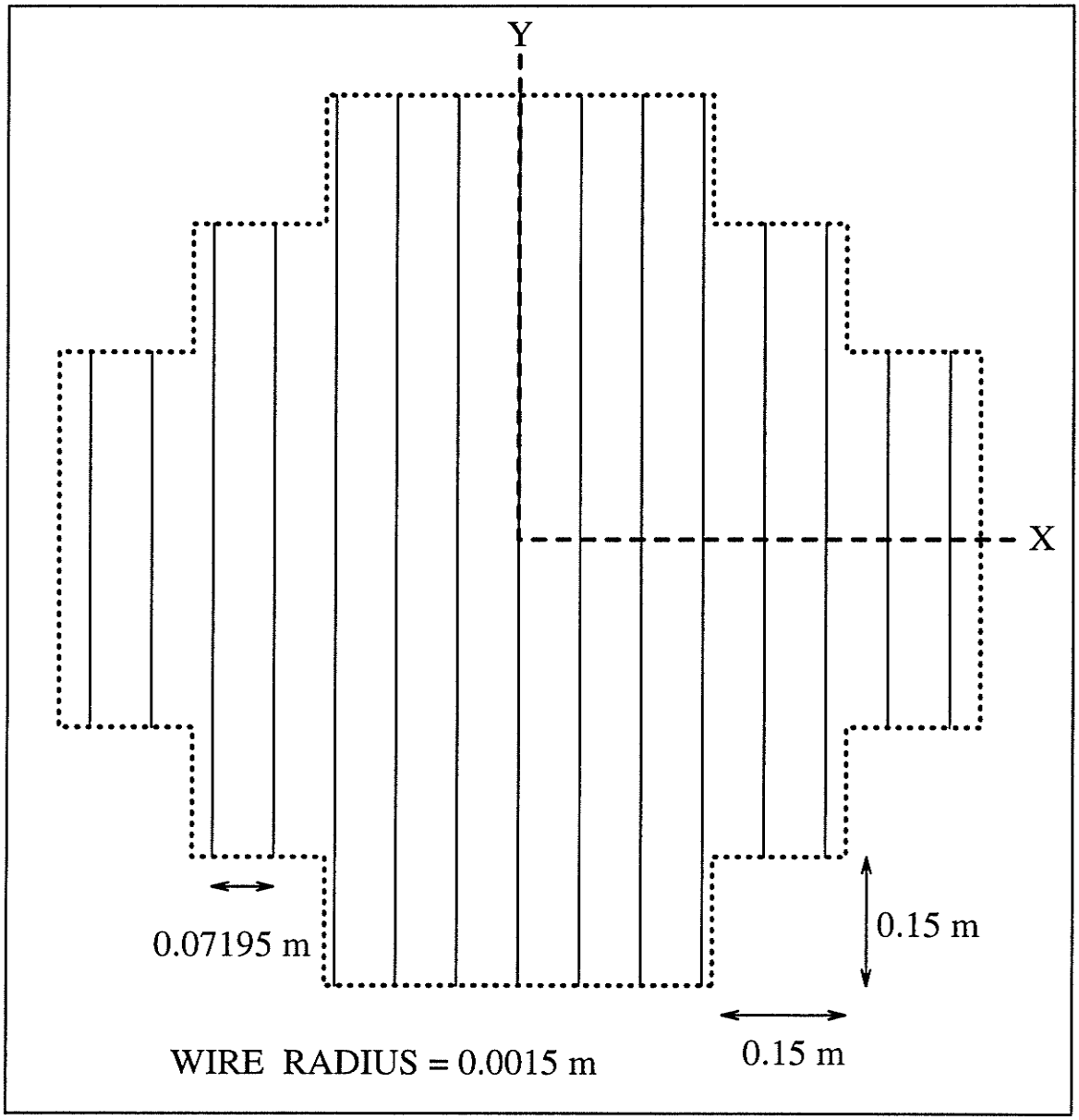

Figure 4.35: One of the two octagonal plates of the LHCP polarizer made of circular PEC wires with inter-wire spacing $s = 0.24\lambda$ within the grid and with wire radius $a = 0.005\lambda$.

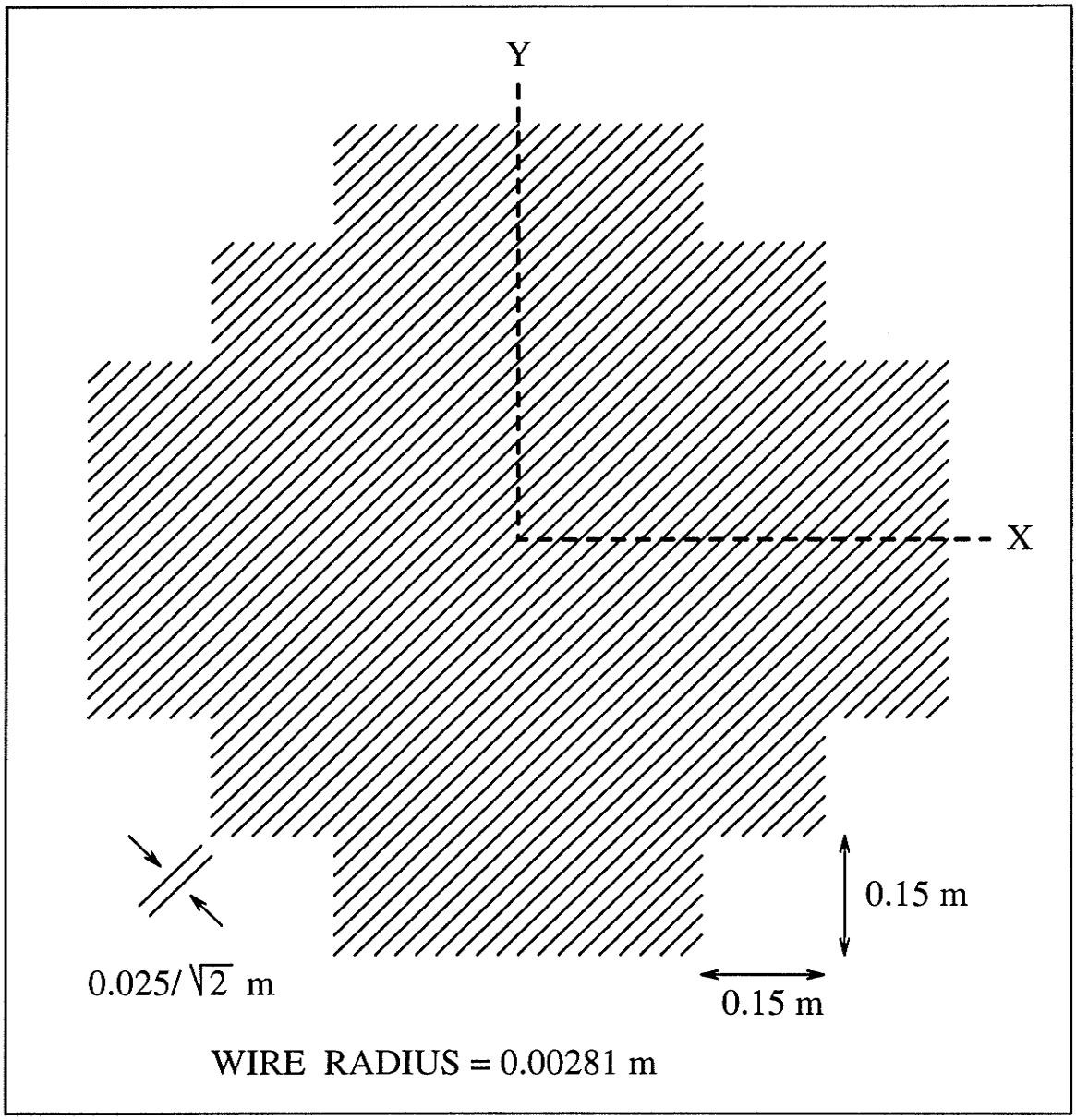

Figure 4.36: Octagonal LP polarizer plate made of circular PEC wires as per the "same-surface-area" rule of thumb for the cascade polarizer LHCPSS. This figure shows the case of 6 wires inclined at $+45^o$ per each 0.15 m side of the unit cell.

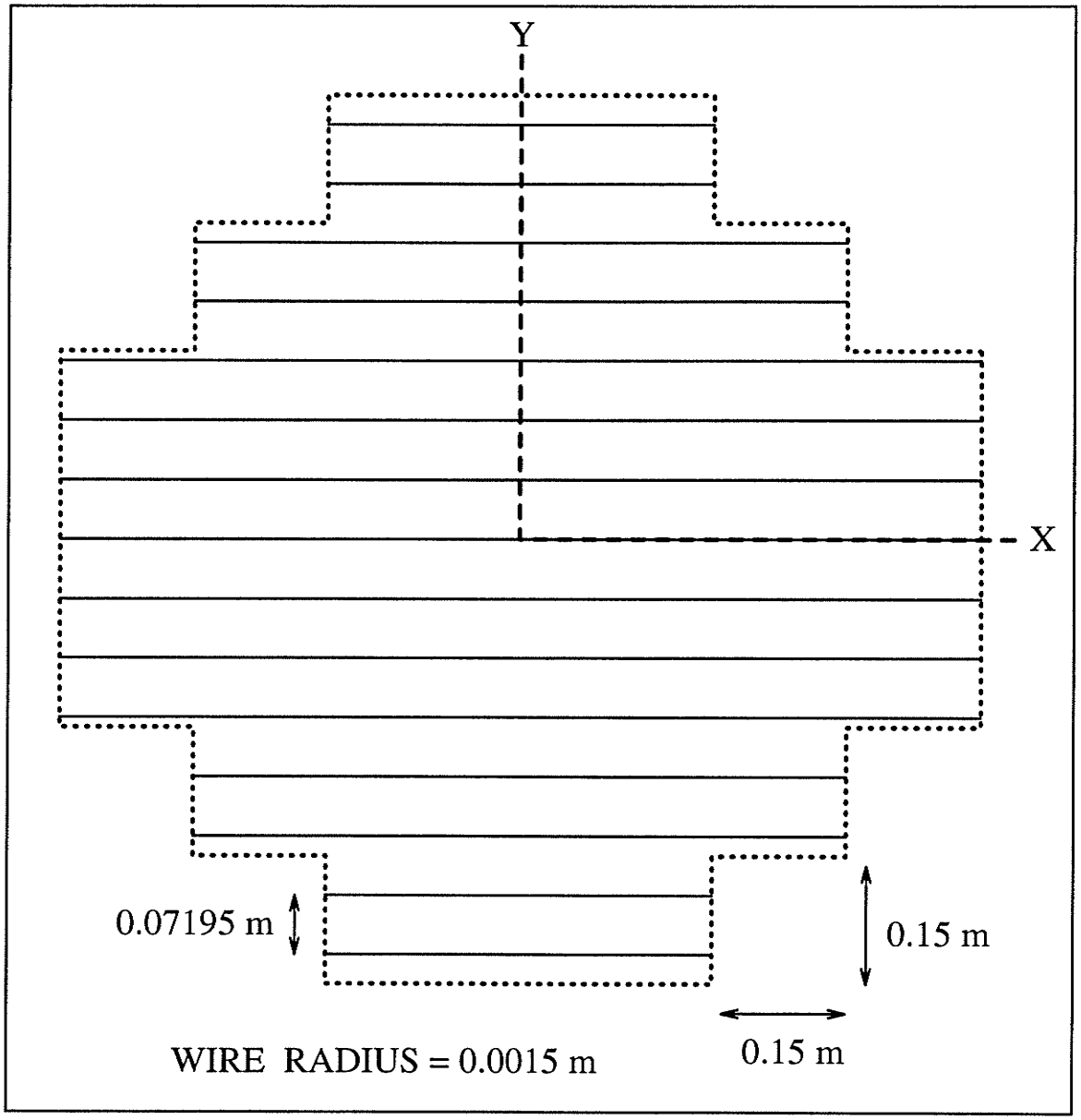

Figure 4.37: One of the two octagonal plates of the RHCP polarizer made of circular PEC wires with inter-wire spacing $s = 0.24\lambda$ within the grid and with wire radius $a = 0.005\lambda$.

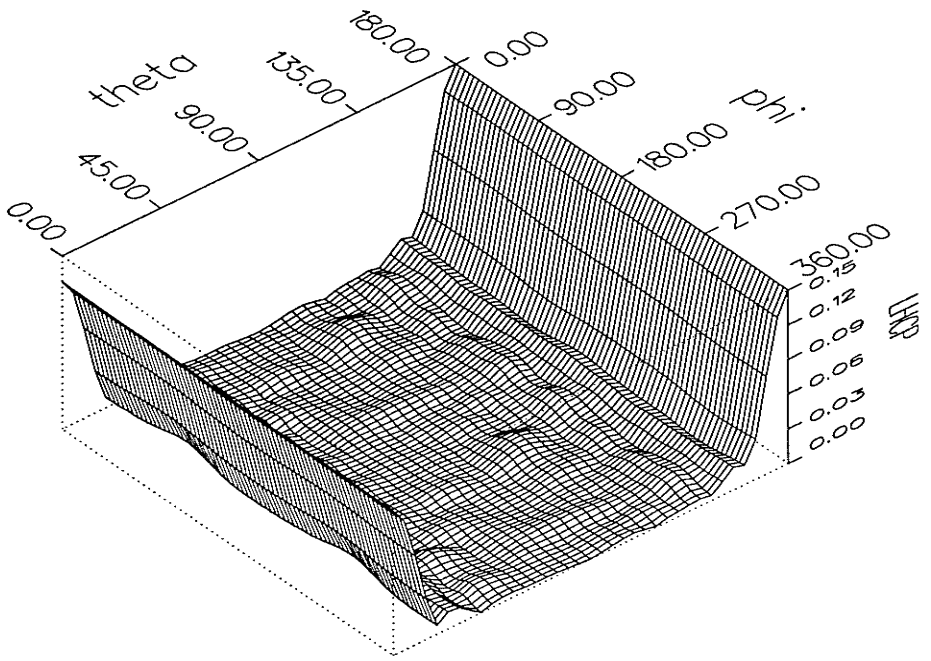

Figure 4.38: $|LL|$ of the cascade polarizer LHCPSS with $s = 0.07195\ m$, $d = 0.1125\ m$, $D = 0.1500\ m$, $a = 0.0015\ m$, $\theta^i = 0^o$, $\phi^i = 0^o$, $r = 30.0\ m$.

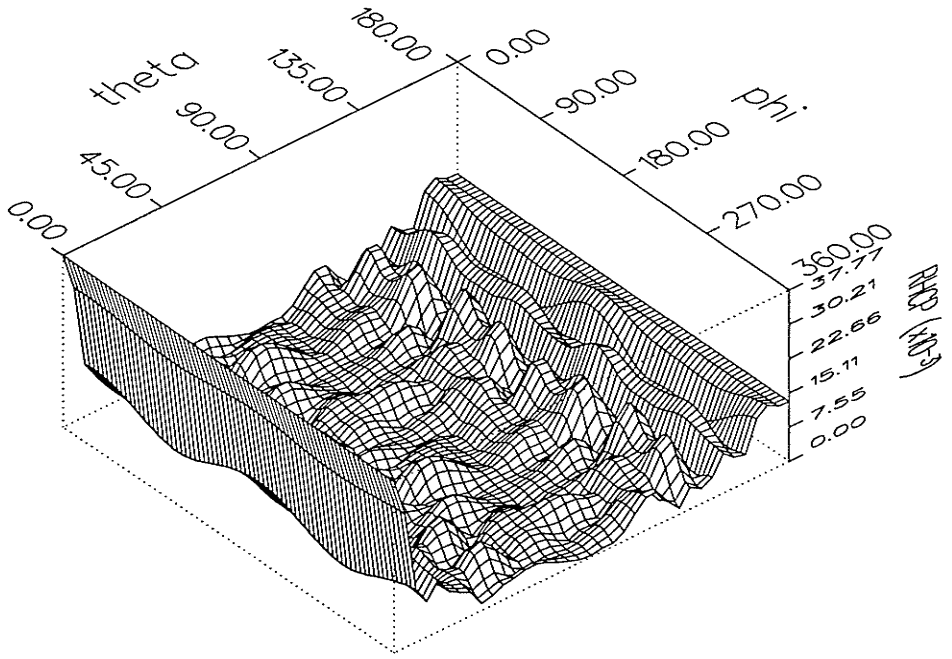

Figure 4.39: $|RL|$ of the cascade polarizer LHCPSS with $s = 0.07195\ m$, $d = 0.1125\ m$, $D = 0.1500\ m$, $a = 0.0015\ m$, $\theta^i = 0^o$, $\phi^i = 0^o$, $r = 30.0\ m$.

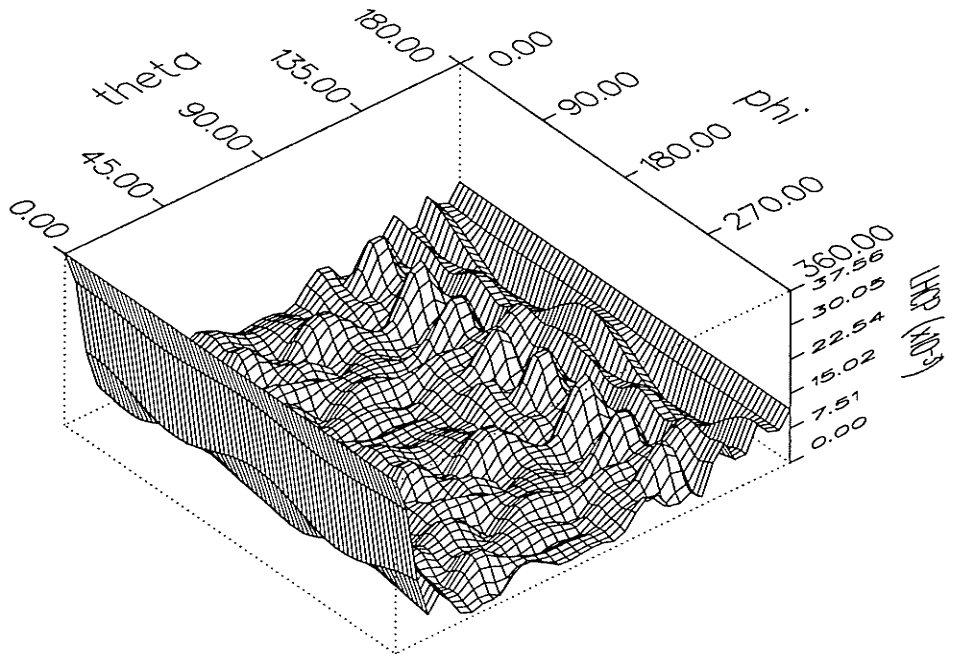

Figure 4.40: $|LR|$ of the cascade polarizer LHCPSS with $s = 0.07195\ m$, $d = 0.1125\ m$, $D = 0.1500\ m$, $a = 0.0015\ m$, $\theta^i = 0^o$, $\phi^i = 0^o$, $r = 30.0\ m$.

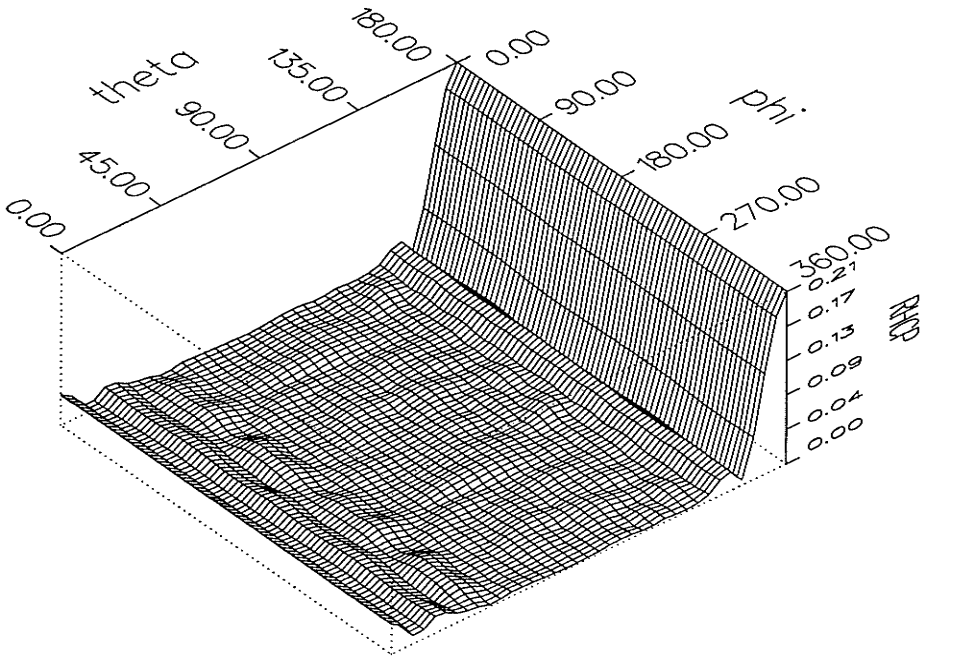

Figure 4.41: $|RR|$ of the cascade polarizer LHCPSS with $s = 0.07195\ m$, $d = 0.1125\ m$, $D = 0.1500\ m$, $a = 0.0015\ m$, $\theta^i = 0^o$, $\phi^i = 0^o$, $r = 30.0\ m$.

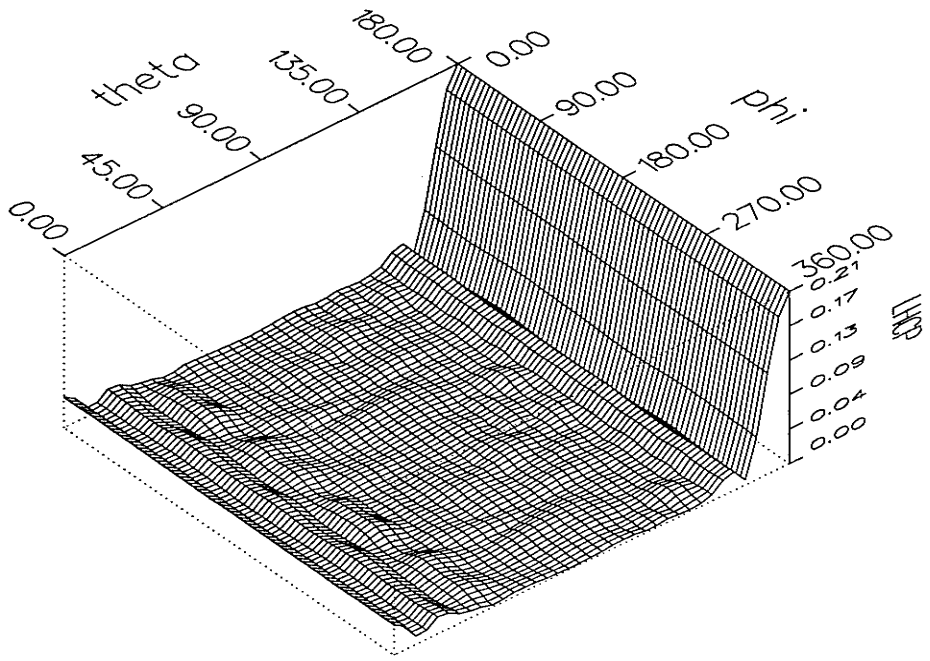

Figure 4.42: $|LL|$ of the cascade polarizer RHCPSS with $s = 0.07195\ m$, $d = 0.1125\ m$, $D = 0.1500\ m$, $a = 0.0015\ m$, $\theta^i = 0^o$, $\phi^i = 0^o$, $r = 30.0\ m$.

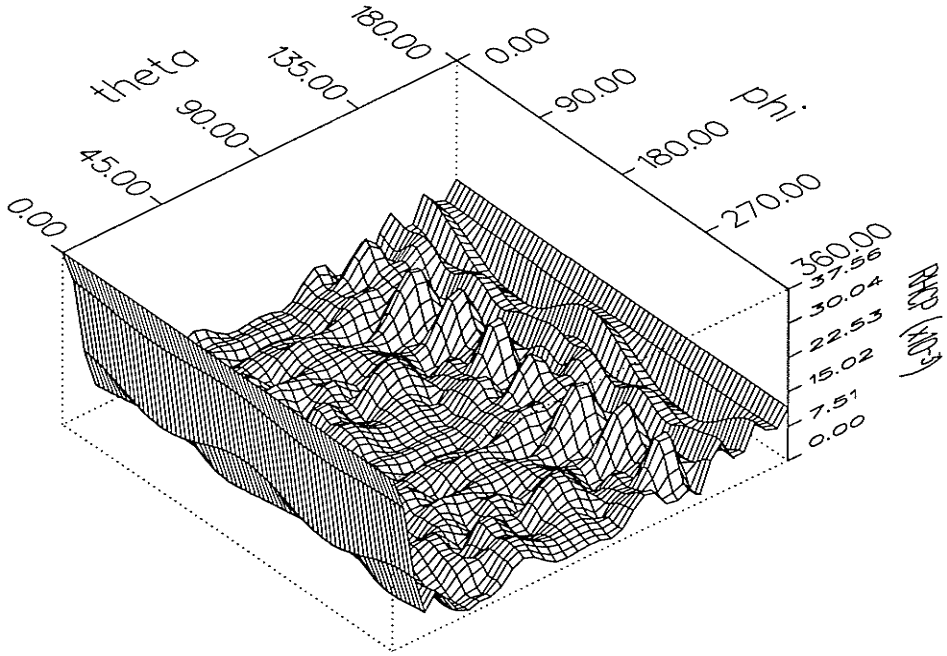

Figure 4.43: $|RL|$ of the cascade polarizer RHCPSS with $s = 0.07195\ m$, $d = 0.1125\ m$, $D = 0.1500\ m$, $a = 0.0015\ m$, $\theta^i = 0^o$, $\phi^i = 0^o$, $r = 30.0\ m$.

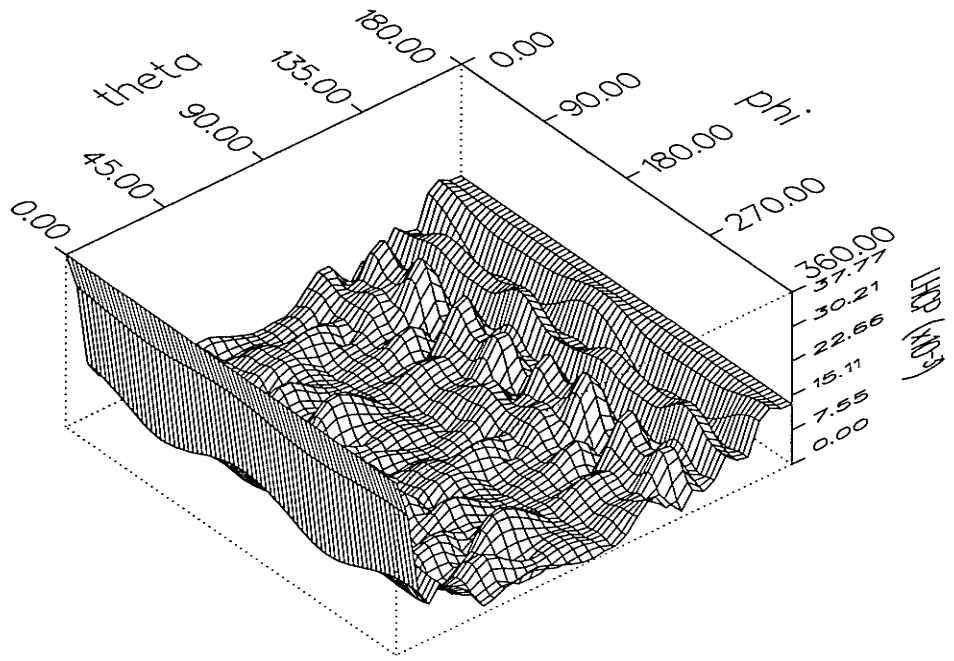

Figure 4.44: $|LR|$ of the cascade polarizer RHCPSS with $s = 0.07195\ m$, $d = 0.1125\ m$, $D = 0.1500\ m$, $a = 0.0015\ m$, $\theta^i = 0^o$, $\phi^i = 0^o$, $r = 30.0\ m$.

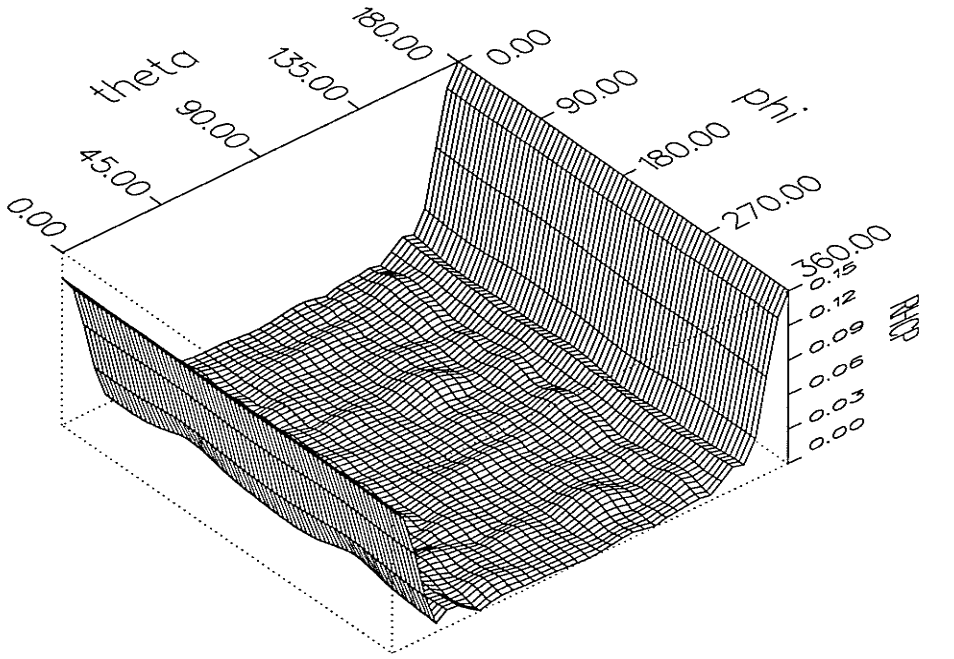

Figure 4.45: $|RR|$ of the cascade polarizer RHCPSS with $s = 0.07195\ m$, $d = 0.1125\ m$, $D = 0.1500\ m$, $a = 0.0015\ m$, $\theta^i = 0^o$, $\phi^i = 0^o$, $r = 30.0\ m$.

Tables 4.78 to 4.86 present the results obtained from varying the wire radius a, the inter-wire spacing s, the inter-grid spacing d for the CP polarizer grids, the spacing D between the CP polarizers and the LP polarizer, the wire radius and the inter-wire spacing for the LP polarizer. When varying the inter-wire spacing for the LP polarizer, the wire radius was chosen as per the "same-surface-area" rule of thumb, i.e. $a = 0.00281\ m$ for the $0.025/\sqrt{2} = 0.01768\ m$ inter-wire spacing and $a = 0.00338\ m$ for the $0.030/\sqrt{2} = 0.02121\ m$ inter-wire spacing. A major difference between the operation of the cascade polarizer design and that of the Pierrot or the Tilston designs is that upon RHCP illumination, the cascade polarizer structure appears translucent not by means of the structure not scattering the incoming wave but rather by means of a series of polarization transformation of the incoming wave. Consequently, the result for $|RR^t|$ is no longer nearly zero for the cascade polarizer design as it was for the Pierrot or the Tilston designs, and the indicator $|LL^p/RR^p|$ is no longer meaningful here. Another significant difference between the results for the cascade polarizer design and those for the Pierrot or the Tilston designs is that the values of the indicator $Blckg$ are seen to be much larger here than those for the Pierrot or the Tilston designs.

There is not a single optimum configuration for which all indicators are optimum simultaneously. Thus, the choice of the optimum configuration depends necessarily on the requirements for the specific application at hand. The configuration corresponding to $\{s = 0.07500\ m,\ a = 0.0008\ m,\ d = 0.1050\ m,\ D = 0.14\ m\}$ appears to be a good compromise and is taken hereafter as the baseline configuration.

The results show that the performance is very sensitive to a variation of the inter-grid spacing d or a variation of the frequency. This is not surprising, given the sharp notch response of the quarter-wavelength transformer (see reference [20, Figure 5.18, p. 223]). The effect of varying the other parameters is less important. Contrary to the Pierrot and the Tilston designs, the parameter limiting the range of operation is

not ar^t but ar^r and/or $Blckg$.

One notes that many values for $|LL^r|$ in Table 4.79, the largest recorded value being 0.13828 V/m, are slightly above the value $|RL^r| = 0.13620$ V/m for the solid PEC reflector plate. This situation suggests the somewhat startling conclusion that the cascade polarizer LHCPSS would be more opaque upon LHCP incidence than is the solid reflector. Such a situation might not be physically impossible since the reflector plate of a diameter of a few wavelengths supports both positive and negative currents whose contributions to the scattered field superimpose constructively or destructively depending on the observation point. If the cascade polarizer structure supports currents of mostly one polarity as a result of a judicious choice of the periodicity of the structure, it might become possible that the contribution to the scattered field become stronger than that of the solid reflector for some observation points. As to the many values for $|RR^t|$ in Table 4.80 that are well above the same 0.13620 V/m value, this situation does not necessarily mean that the cascade polarizer LHCPSS is either more or less transparent upon RHCP incidence than is the solid reflector since the incident wave must be vectorially added to the scattered wave in order to obtain the total wave in the transmission region.

The GSM for the octagonal cascade polarizer LHCPSS illuminated at normal incidence is obtained as $S(X,Y) =$

$$\begin{pmatrix} 2.0217\angle -85.57^o & 1.0504\angle -4.29^o & 3.1942\angle -102.65^o & 1.2429\angle -82.93^o \\ 1.0507\angle -4.27^o & 1.6653\angle 92.65^o & 0.9397\angle 74.14^o & 3.1937\angle -102.64^o \\ 3.1937\angle -102.64^o & 0.9397\angle 74.14^o & 1.6653\angle 92.65^o & 1.0507\angle -4.27^o \\ 1.2429\angle -82.93^o & 3.1941\angle -102.65^o & 1.0504\angle -4.29^o & 2.0217\angle -85.57^o \end{pmatrix}$$

where the incidence propagation vector is taken as pointing outwardly from the origin of the coordinate system. Again, each scattering coefficient is described by a pair whose first number pertains to the magnitude and second number pertains to the phase. Surprisingly, the magnitudes are larger than 1.0 V/m, the magnitude of the linearly polarized incident plane wave! As expected, the matrix is symmetrical with

respect to the diagonal owing to the structure being reciprocal but surprisingly, the matrix is also symmetrical with respect to the anti-diagonal. Also as expected, the structure does not have the longitudinal reflection symmetry but nothing can be said about the $2n$-fold rotational symmetry, by the same arguments as those invoked when dealing with the GSM for the Pierrot design.

The results at off-normal incidence are not provided as they would not be deemed accurate because the structure is so thick compared to its transverse dimensions that a significant portion of the edge of the structure would not be properly excited owing to the fact that some off-normal incident ray propagating in straight line and incident upon the edge of the structure would not pass through all the plates. This difficulty also arises with the Pierrot and the Tilston designs but to a much smaller extent since the thickness in the case of these two designs is only $0.075\ m = 0.25\lambda$ whereas the thickness in the case of the cascade polarizer design is $0.490\ m \approx 1.60\lambda$.

Table 4.78: Peak scattering values for the octagonal cascade polarizer LHCPSS. The incidence is normal and $r = 30.0\ m$.

variable		Peak values				
name	value	$\|LL\|$	$\|RR\|$	$\|RL\|$	$\|LR\|$	$\|LL/RR\|$
$s\ (m)$	0.07195	0.14761	0.21290	0.03777	0.03756	0.693
"	0.07500	0.15066	0.21318	0.03629	0.03622	0.707
$a = 0.0015\ m$, $d = 0.1125\ m$ and $D = 0.1500\ m$						
$s\ (m)$	0.07195	0.14511	0.19028	0.03436	0.03439	0.763
"	0.07500	0.14873	0.18897	0.03450	0.03459	0.787
$a = 0.0010\ m$, $d = 0.1125\ m$ and $D = 0.1500\ m$						
$d\ (m)$	0.0825	0.14155	0.21210	0.03106	0.02896	0.667
"	0.1025	0.14843	0.21088	0.01895	0.01666	0.704
"	0.1050	0.14886	0.20701	0.01741	0.01731	0.719
"	0.1075	0.14901	0.20194	0.02225	0.02223	0.738
"	0.1100	0.14897	0.19580	0.02799	0.02805	0.760
"	0.1125	0.14873	0.18897	0.03450	0.03459	0.787
"	0.1150	0.14839	0.18165	0.04156	0.04157	0.817
"	0.1425	0.15172	0.12870	0.13511	0.13489	1.179
$s = 0.07500\ m$, $a = 0.0010\ m$ and $D = 0.1500\ m$						
$a\ (m)$	0.0005	0.14791	0.17399	0.01994	0.02134	0.850
"	0.0007	0.14813	0.18914	0.01820	0.01812	0.783
"	0.0008	0.14837	0.19566	0.01758	0.01679	0.758
"	0.0009	0.14858	0.20166	0.01698	0.01665	0.737
"	0.0010	0.14886	0.20701	0.01741	0.01731	0.719
"	0.0015	0.15004	0.22515	0.02654	0.02612	0.666
$s = 0.07500\ m$, $d = 0.1050\ m$ and $D = 0.1500\ m$						
$D\ (m)$	0.1300	0.15320	0.19544	0.01787	0.01844	0.784
"	0.1400	0.15077	0.19530	0.01706	0.01707	0.772
"	0.1500	0.14837	0.19566	0.01758	0.01679	0.758
"	0.1600	0.14633	0.19572	0.02789	0.02786	0.748
"	0.1700	0.14571	0.19425	0.03569	0.03558	0.750
$s = 0.07500\ m$, $a = 0.0008\ m$ and $d = 0.1050\ m$						
$a\ (m)$	0.0007	0.15073	0.18914	0.01720	0.01760	0.797
"	0.0008	0.15077	0.19530	0.01706	0.01707	0.772
"	0.0009	0.15085	0.20096	0.01693	0.01660	0.751
"	0.0010	0.15091	0.20598	0.01680	0.01616	0.733
$s = 0.07500\ m$, $d = 0.1050\ m$ and $D = 0.1400\ m$						
$d\ (m)$	0.1025	0.15016	0.19933	0.01706	0.01753	0.753
"	0.1050	0.15077	0.19530	0.01706	0.01707	0.772
"	0.1075	0.15121	0.19035	0.01706	0.01675	0.794
$s = 0.07500\ m$, $a = 0.0008\ m$ and $D = 0.1400\ m$						

Table 4.79: Reflection beam values for the octagonal cascade polarizer LHCPSS. The incidence is normal and $r = 30.0\ m$.

variable		Reflection beam values					
name	value	$\|LL\|$	$\|RR\|$	$\|RL\|$	$\|LR\|$	ar	$Blckg$
$s\ (m)$	0.07195	0.12522	0.03755	0.03777	0.03756	1.8637	329.186
"	0.07500	0.13002	0.03596	0.03629	0.03622	1.7743	304.056
$a = 0.0015\ m$, $d = 0.1125\ m$ and $D = 0.1500\ m$							
$s\ (m)$	0.07195	0.12464	0.03827	0.03436	0.03439	1.7614	308.980
"	0.07500	0.12823	0.04058	0.03450	0.03459	1.7362	331.875
$a = 0.0010\ m$, $d = 0.1125\ m$ and $D = 0.1500\ m$							
$d\ (m)$	0.0825	0.13483	0.09045	0.01561	0.01609	1.2618	985.110
"	0.1025	0.13431	0.04001	0.01351	0.01330	1.2236	207.495
"	0.1050	0.13349	0.03553	0.01741	0.01731	1.3000	182.255
"	0.1075	0.13226	0.03438	0.02225	0.02223	1.4045	195.607
"	0.1100	0.13052	0.03653	0.02799	0.02805	1.5460	247.544
"	0.1125	0.12823	0.04058	0.03450	0.03459	1.7362	331.875
"	0.1150	0.12537	0.04488	0.04156	0.04157	1.9916	436.837
"	0.1425	0.04471	0.02963	0.13511	0.13489	1.9891	2226.19
$s = 0.07500\ m$, $a = 0.0010\ m$ and $D = 0.1500\ m$							
$a\ (m)$	0.0005	0.12915	0.03502	0.01983	0.02000	1.3627	189.773
"	0.0007	0.13156	0.03303	0.01695	0.01710	1.2957	161.455
"	0.0008	0.13240	0.03299	0.01649	0.01657	1.2846	159.038
"	0.0009	0.13301	0.03379	0.01665	0.01665	1.2862	165.632
"	0.0010	0.13349	0.03553	0.01741	0.01731	1.3000	182.255
"	0.0015	0.13353	0.05476	0.02654	0.02612	1.4961	429.545
$s = 0.07500\ m$, $d = 0.1050\ m$ and $D = 0.1500\ m$							
$D\ (m)$	0.1300	0.13719	0.03963	0.01447	0.01476	1.2359	208.760
"	0.1400	0.13789	0.03910	0.00719	0.00754	1.1100	185.089
"	0.1500	0.13240	0.03299	0.01649	0.01657	1.2846	159.038
"	0.1600	0.12261	0.02193	0.02789	0.02786	1.5889	146.699
"	0.1700	0.10969	0.00671	0.03569	0.03558	1.9646	152.977
$s = 0.07500\ m$, $a = 0.0008\ m$ and $d = 0.1050\ m$							
$a\ (m)$	0.0007	0.13731	0.03930	0.00862	0.00899	1.1340	189.682
"	0.0008	0.13789	0.03910	0.00719	0.00754	1.1100	185.089
"	0.0009	0.13824	0.04004	0.00616	0.00645	1.0932	191.933
"	0.0010	0.13828	0.04211	0.00554	0.00578	1.0835	210.822
$s = 0.07500\ m$, $d = 0.1050\ m$ and $D = 0.1400\ m$							
$d\ (m)$	0.1025	0.13759	0.03896	0.00780	0.00817	1.1201	184.915
"	0.1050	0.13789	0.03910	0.00719	0.00754	1.1100	185.089
"	0.1075	0.13790	0.04305	0.00942	0.00968	1.1466	227.264
$s = 0.07500\ m$, $a = 0.0008\ m$ and $D = 0.1400\ m$							
The values for $Blckg$ have been multiplied by 10^3							

Table 4.80: Transmission beam values for the octagonal cascade polarizer LHCPSS. The incidence is normal and $r = 30.0\ m$.

variable		Transmission beam values					
name	value	$\|LL\|$	$\|RR\|$	$\|RL\|$	$\|LR\|$	ar	$Leakg$
$s\ (m)$	0.07195	0.14761	0.21290	0.01321	0.01159	1.1151	0.171327
"	0.07500	0.15066	0.21318	0.00934	0.00751	1.0730	0.183635
$a = 0.0015\ m$, $d = 0.1125\ m$ and $D = 0.1500\ m$							
$s\ (m)$	0.07195	0.14511	0.19028	0.00762	0.00531	1.0574	0.140728
"	0.07500	0.14873	0.18897	0.00871	0.00666	1.0731	0.163365
$a = 0.0010\ m$, $d = 0.1125\ m$ and $D = 0.1500\ m$							
$d\ (m)$	0.0825	0.14155	0.21210	0.03106	0.02896	1.3163	0.219042
"	0.1025	0.14843	0.21088	0.01895	0.01666	1.1716	0.177798
"	0.1050	0.14886	0.20701	0.01604	0.01369	1.1417	0.172498
"	0.1075	0.14901	0.20194	0.01296	0.01057	1.1105	0.167671
"	0.1100	0.14897	0.19580	0.01024	0.00790	1.0841	0.164570
"	0.1125	0.14873	0.18897	0.00871	0.00666	1.0731	0.163365
"	0.1150	0.14839	0.18165	0.00946	0.00819	1.0945	0.164649
"	0.1425	0.15172	0.12870	0.03754	0.03650	1.7917	0.409137
$s = 0.07500\ m$, $a = 0.0010\ m$ and $D = 0.1500\ m$							
$a\ (m)$	0.0005	0.14791	0.17399	0.01994	0.01796	1.2301	0.186114
"	0.0007	0.14813	0.18914	0.01682	0.01464	1.1678	0.172110
"	0.0008	0.14837	0.19566	0.01612	0.01379	1.1517	0.170456
"	0.0009	0.14858	0.20166	0.01586	0.01353	1.1438	0.170431
"	0.0010	0.14886	0.20701	0.01604	0.01369	1.1417	0.172498
"	0.0015	0.15004	0.22515	0.02007	0.01787	1.1724	0.195710
$s = 0.07500\ m$, $d = 0.1050\ m$ and $D = 0.1500\ m$							
$D\ (m)$	0.1300	0.15320	0.19544	0.00998	0.00807	1.0861	0.180364
"	0.1400	0.15077	0.19530	0.01312	0.01094	1.1187	0.174242
"	0.1500	0.14837	0.19566	0.01612	0.01379	1.1517	0.170456
"	0.1600	0.14633	0.19572	0.01810	0.01569	1.1744	0.159274
"	0.1700	0.14571	0.19425	0.01849	0.01602	1.1798	0.144706
$s = 0.07500\ m$, $a = 0.0008\ m$ and $d = 0.1050\ m$							
$a\ (m)$	0.0007	0.15073	0.18914	0.01426	0.01215	1.1373	0.175046
"	0.0008	0.15077	0.19530	0.01312	0.01094	1.1187	0.174242
"	0.0009	0.15085	0.20096	0.01228	0.01004	1.1052	0.175988
"	0.0010	0.15091	0.20598	0.01165	0.00947	1.0964	0.179418
$s = 0.07500\ m$, $d = 0.1050\ m$ and $D = 0.1400\ m$							
$d\ (m)$	0.1025	0.15016	0.19933	0.01508	0.01298	1.1394	0.178971
"	0.1050	0.15077	0.19530	0.01312	0.01094	1.1187	0.174242
"	0.1075	0.15121	0.19035	0.01100	0.00886	1.0977	0.170191
$s = 0.07500\ m$, $a = 0.0008\ m$ and $D = 0.1400\ m$							

Table 4.81: Peak scattering values of the octagonal cascade polarizer LHCPSS for various wire thickness values of the LP polarizer plate. The observation sphere radius is $r = 30.0\ m$ and the incidence is normal.

Thickness	Peak values				
(m)	$\|LL\|$	$\|RR\|$	$\|RL\|$	$\|LR\|$	$\|LL/RR\|$
0.00100	0.16016	0.19566	0.01669	0.01702	0.819
0.00200	0.15403	0.19544	0.01683	0.01709	0.788
0.00281	0.15077	0.19530	0.01706	0.01707	0.772
0.00400	0.14691	0.19516	0.01736	0.01707	0.753
0.00500	0.14440	0.19523	0.01710	0.01708	0.740

Table 4.82: Reflection beam values of the octagonal cascade polarizer LHCPSS for various wire thickness values of the LP polarizer plate. The observation sphere radius is $r = 30.0\ m$ and the incidence is normal.

Thickness	Reflection beam values					
(m)	$\|LL\|$	$\|RR\|$	$\|RL\|$	$\|LR\|$	ar	$Blckg$
0.00100	0.13630	0.03923	0.00820	0.00850	1.1280	188.053
0.00200	0.13759	0.03913	0.00753	0.00788	1.1157	185.958
0.00281	0.13789	0.03910	0.00719	0.00754	1.1100	185.089
0.00400	0.13811	0.03904	0.00682	0.00716	1.1039	183.842
0.00500	0.13824	0.03892	0.00683	0.00717	1.1040	182.813
The values for $Blckg$ have been multiplied by 10^3						

Table 4.83: Transmission beam values of the octagonal cascade polarizer LHCPSS for various wire thickness values of the LP polarizer plate. The observation sphere radius is $r = 30.0\ m$ and the incidence is normal.

Thickness	Transmission beam values					
(m)	$\|LL\|$	$\|RR\|$	$\|RL\|$	$\|LR\|$	ar	$Leakg$
0.00100	0.16016	0.19566	0.01392	0.01168	1.1270	0.226967
0.00200	0.15403	0.19544	0.01337	0.01121	1.1216	0.187854
0.00281	0.15077	0.19530	0.01312	0.01094	1.1187	0.174242
0.00400	0.14691	0.19516	0.01284	0.01069	1.1159	0.163339
0.00500	0.14440	0.19523	0.01289	0.01078	1.1169	0.159199

Table 4.84: Peak scattering values of the octagonal cascade polarizer LHCPSS for two different values of the inter-wire spacing of the LP polarizer plate. The observation sphere radius is $r = 30.0\ m$ and the incidence is normal.

Spacing (m)	Peak values				
	$\|LL\|$	$\|RR\|$	$\|RL\|$	$\|LR\|$	$\|LL/RR\|$
0.01768	0.15077	0.19530	0.01706	0.01707	0.772
0.02121	0.14477	0.19461	0.01537	0.01762	0.744

Table 4.85: Reflection beam values of the octagonal cascade polarizer LHCPSS for two different values of the inter-wire spacing of the LP polarizer plate. The observation sphere radius is $r = 30.0\ m$ and the incidence is normal.

Spacing (m)	Reflection beam values					
	$\|LL\|$	$\|RR\|$	$\|RL\|$	$\|LR\|$	ar	$Blckg$
0.01768	0.13789	0.03910	0.00719	0.00754	1.1100	185.089
0.02121	0.13426	0.03791	0.00568	0.00586	1.0883	171.753
The values for $Blckg$ have been multiplied by 10^3						

Table 4.86: Transmission beam values of the octagonal cascade polarizer LHCPSS for two different values of the inter-wire spacing of the LP polarizer plate. The observation sphere radius is $r = 30.0\ m$ and the incidence is normal.

Spacing (m)	Transmission beam values					
	$\|LL\|$	$\|RR\|$	$\|RL\|$	$\|LR\|$	ar	$Leakg$
0.01768	0.15077	0.19530	0.01312	0.01094	1.1187	0.174242
0.02121	0.14477	0.19461	0.01348	0.01134	1.1237	0.193455

Table 4.87: Peak scattering values of the octagonal cascade polarizer LHCPSS for various frequency values. The observation sphere radius is $r = 30.0\ m$ and the incidence is normal.

Frequency	Peak values				
(GHz)	$\|LL\|$	$\|RR\|$	$\|RL\|$	$\|LR\|$	$\|LL/RR\|$
0.900	0.10008	0.13307	0.03474	0.03517	0.752
0.950	0.13672	0.16667	0.03294	0.03349	0.820
0.960	0.15379	0.18097	0.02828	0.02795	0.850
0.970	0.16339	0.19199	0.02645	0.02621	0.851
0.980	0.16853	0.20235	0.02184	0.02501	0.833
0.990	0.16085	0.20038	0.01934	0.02103	0.803
1.000	0.15077	0.19530	0.01706	0.01707	0.772
1.010	0.15094	0.19120	0.01787	0.01508	0.789
1.020	0.15299	0.18582	0.01647	0.01463	0.823
1.030	0.14149	0.17879	0.01587	0.01534	0.791
1.040	0.14126	0.17307	0.01802	0.01651	0.816
1.050	0.14408	0.16807	0.01871	0.01886	0.857
1.100	0.14375	0.14021	0.04304	0.04301	1.025

Table 4.88: Reflection beam values of the octagonal cascade polarizer LHCPSS for various frequency values. The observation sphere radius is $r = 30.0\ m$ and the incidence is normal.

Frequency	Reflection beam values					
(GHz)	$\|LL\|$	$\|RR\|$	$\|RL\|$	$\|LR\|$	ar	$Blckg$
0.900	0.08885	0.04241	0.03474	0.03517	2.2838	437.413
0.950	0.08064	0.00492	0.03294	0.03349	2.3814	148.185
0.960	0.07924	0.02042	0.02738	0.02795	2.0561	151.751
0.970	0.09291	0.03317	0.02124	0.02165	1.5926	194.611
0.980	0.11811	0.04760	0.01446	0.01453	1.2789	300.965
0.990	0.12894	0.04449	0.00643	0.00672	1.1049	241.106
1.000	0.13789	0.03910	0.00719	0.00754	1.1100	185.089
1.010	0.13731	0.03550	0.00937	0.00969	1.1465	154.913
1.020	0.13102	0.03227	0.01112	0.01143	1.1855	131.474
1.030	0.12843	0.02948	0.00956	0.00982	1.1609	106.256
1.040	0.13357	0.02953	0.01423	0.01442	1.2386	116.517
1.050	0.13055	0.03124	0.01871	0.01886	1.3346	140.948
1.100	0.11411	0.02589	0.04304	0.04301	2.2115	243.051
The values for $Blckg$ have been multiplied by 10^3						

Table 4.89: Transmission beam values of the octagonal cascade polarizer LHCPSS for various frequency values. The observation sphere radius is $r = 30.0\ m$ and the incidence is normal.

Frequency	Transmission beam values					
(GHz)	$\|LL\|$	$\|RR\|$	$\|RL\|$	$\|LR\|$	ar	$Leakg$
0.900	0.10008	0.13307	0.01427	0.01359	1.2275	0.093994
0.950	0.13672	0.16667	0.03058	0.02945	1.4292	0.170313
0.960	0.15379	0.18097	0.02828	0.02745	1.3576	0.194218
0.970	0.16339	0.19199	0.02289	0.02201	1.2590	0.194984
0.980	0.16853	0.20235	0.01535	0.01410	1.1498	0.238015
0.990	0.16085	0.20038	0.00811	0.00598	1.0615	0.239320
1.000	0.15077	0.19530	0.01312	0.01094	1.1187	0.174242
1.010	0.15094	0.19120	0.01417	0.01205	1.1345	0.178104
1.020	0.15299	0.18582	0.01371	0.01167	1.1341	0.222137
1.030	0.14149	0.17879	0.01360	0.01176	1.1408	0.212319
1.040	0.14126	0.17307	0.01802	0.01631	1.2081	0.168641
1.050	0.14408	0.16807	0.01858	0.01707	1.2261	0.179245
1.100	0.14375	0.14021	0.03406	0.03308	1.6176	0.282352

Chapter Five

Conclusion

5.1 Summary

This document has reported the research work dealing with the relatively unknown topic of CPSS. It was shown that Cornbleet's conjecture which states that an *ideal* CPSS is an impossible polarizer was found to be false since an *ideal* CPSS of the cascade polarizer design analyzed with the composite GSM approach yielded the GSM of the *ideal* CPSS predicted by the GSM-based technique developed herein. This GSM-based technique yields the GSM of a device from the knowledge of its prescribed operation. One significant merit of this GSM-based technique consists in identifying some geometrical constraints of the planar structure by observing the relationships between various scattering coefficients of the GSM corresponding to this structure. These relationships were identified for various properties, namely the reciprocity of electromagnetism, the 2-fold rotational symmetry and the longitudinal reflection symmetry. It was found that the CPSS requires in practice to have the 2-fold rotational symmetry, except in the neighborhood of the normal incidence where reciprocity suffices, and requires not to have the longitudinal reflection symmetry.

This research work included also an investigation into the subtleties of the GSM and its generalization to the case of off-normal incidence. Thus, it was found that eight rather than four voltage travelling waves become typically required for describing the

operation of the planar structure at off-normal incidence.

A literature survey revealed three existing CPSS designs whose principles of operation were, however, somewhat idealized. Simulations with the NEC-2 software yielded boundary value solutions for a finite size octagonal CPSS of each one of the three designs, and various indicators were developed to gauge the performance of these three designs. Thus, it was found that the Tilston design offered the best performance, specially at off-normal incidence, but presented also the greatest complications of manufacturing. These simulations suggested also that designs obeying the 2-fold rotational symmetry required for the ideal CPSS tended indeed to present better performance. The best performance, however, remained nevertheless disappointing, this range being limited to $\theta^i \approx 15^o$ even in the best case. Hence, more work is needed to find a design that performs well over a wider range of incidence angles.

5.2 Original Contributions

The original contributions made in the course of this work are as follows:

- Presented a detailed description of the concepts and subtleties of the GSM, including an expansion to arbitrary incidence angles and the relationship between the matrices $S(X,Y)$ and $S(E,H)$ at normal incidence;

- Developed an analysis/synthesis tool based on the GSM for studying a general structure from the prescribed operation of the structure and from fundamental principles, rather than from the specific boundary conditions of the structure;

- Presented a formalism that homogenizes the treatment of all propagation vectors, including the incident one (see Appendix A), and developed the resulting formulation for various fundamental principles: reciprocity principle of electromagnetism, rotational symmetry, transverse and longitudinal reflection symmetries. Many results obtained by Whites and Mittra in reference [30] were thus reproduced herein from a simpler approach. New results were also obtained.

- Pointed out the connection between the relationships between various cross-polarization scattering coefficients and the above fundamental principles, namely:

$$\left\{ \begin{array}{r} \text{Snell's law of reflection} \\ \text{reciprocity} \\ \text{2-fold rotational symmetry} \end{array} \right\} \iff C_{vv}^{pq} = \epsilon_H C_{vv}^{qp}$$

  except in the neighborhood of the normal incidence where reciprocity suffices.

$$\left\{ \begin{array}{r} \text{Snell's law of refraction with } \theta^t = \theta^i \\ \text{reciprocity} \\ \text{2-fold rotational symmetry} \\ \text{reflection symmetry about the } z = 0 \text{ plane} \end{array} \right\} \implies C_{uv}^{pq} = C_{uv}^{qp} \quad \text{for } u \neq v$$

- Identified the voltage GSM for various structures: the ideal solid PEC reflector, the free space slab, the dielectric slab, the artificially hard or soft surfaces, the ideal CPSS, the ideal LP, LHCP and RHCP polarizers.

- Presented the concept of the CPSS and presented a review of the prior art in the area of the CPSS;
- Refuted Cornbleet's assertion that the ideal CPSS represents an impossible polarizer;
- Proved that ideal LP and CP polarizers are possible only at normal incidence angle, regardless of their specific physical realizations;
- Identified that the ideal CPSS must have the $2n$-fold rotational symmetry except in a limited neighborhood of the normal incidence where reciprocity suffices, but cannot possibly have the longitudinal reflection symmetry;
- Identified performance levels for three different LHCPSS designs from the boundary value solution provided by NEC-2; the results suggest that better performances are indeed obtained with designs that obey the geometrical constraints of the ideal CPSS;
- Developed various indicators to assess the performance of an infinite size scattering surface from the results of a finite size scattering surface of the same nature but with just a few wavelengths in size;
- Established the correspondence between Jones' polarization matrix and the GSM;
- Made corrections to various papers as seen fit.

5.3 Directions for Further Research

It is stressed that although the cascade polarizer CPSS can provide an ideal performance (neglecting all losses) only at normal incidence, as a result of the LP and CP polarizers being themselves ideal only at normal incidence, the voltage scattering matrix of the ideal CPSS developed from general principles in Chapter 2 does not suggest that the ideal CPSS need be restricted to normal incidence. However, the knowledge of a specific geometry achieving the ideal CPSS performance for arbitrary incidence angles has remained elusive in the course of this work. Future work might attempt to identify just such a specific geometry with ideal CPSS performance under arbitrary incidence angles. One possible approach might consist in varying the angle between the transverse orientations of the dipoles of the Tilston CPSS, as suggested by Hurd's analysis in reference [8].

It is stressed that, although the analysis used herein was limited to the dominant mode only, the GSM-based technique as developed herein can accommodate multiple modes, evanescent as well as propagating. It might be useful to study the performance under the conditions that the adjacent layers are close enough for the evanescent modes to contribute in a significant manner to the coupling between layers. This situation affords the possibility that the operation of a particular structure might be so modified as to allow the structure to achieve an ideal CPSS performance under some off-normal incidence conditions. This possibility, however, appears admittedly remote.

Other directions for future research consist in investigating the performance of the CPSS:

- with curved rather than flat surfaces;
- with a point source rather than an incident plane wave;
- with a triangular rather than a square grid for the array;

- with incorporating the effect of the dielectric substrate.

The CPSS is a relatively new structure whose realms of applications need to be developed as well. The applications of filtering and diplexing come readily to mind. Pierrot had patented the idea of fabricating the subreflector of the Cassegrain antenna as a CPSS for the purpose of minimizing the blockage created by the subreflector. Tilston mentioned the application of focal plane scanning mirror antennas for circular polarization. Many applications based on linear polarization selection can probably be converted over to circular polarization selection. Many new applications probably await the inception of their CPSS as well!

Appendix A

Notational Convention

The familiar representation of the incidence propagation vector $\vec{k^i}$ as an incoming vector is sometimes a source of confusion in interpreting the results of the scattered field, specially so when the scattered field is circularly polarized. Figure A.1 shows the familiar (on the left) and the present (on the right) representations of the incidence propagation vector.

According to Snell's law of reflection and refraction (for convenience, $\theta^t = \theta^i$ was assumed), one has for the familiar representation:

$$\begin{array}{llll} \theta^i = \theta' & \theta^r = \theta' & \theta^t = \pi - \theta' & 0^o \leq \forall\theta \leq 180^o \\ \phi^i = \phi' & \phi^r = \pi + \phi' & \phi^t = \pi + \phi' & 0^o \leq \forall\phi \leq 360^o \end{array}$$

and for any positive or negative values of x, y, and z, one writes, with the $e^{+j\omega t}$ time convention, the incident, reflected and transmitted plane waves as:

$$\begin{aligned} \vec{E}^i &= E_o e^{+jk(sin(\theta')cos(\phi')x + sin(\theta')sin(\phi')y + cos(\theta')z)}\,\hat{E}^i \\ \vec{E}^r &= RE_o e^{+jk(sin(\theta')cos(\phi')x + sin(\theta')sin(\phi')y - cos(\theta')z)}\,\hat{E}^r \\ \vec{E}^t &= TE_o e^{+jk(sin(\theta')cos(\phi')x + sin(\theta')sin(\phi')y + cos(\theta')z)}\,\hat{E}^t \end{aligned}$$

The scattered wave ($\vec{E}^r$ for $z \geq 0$ and $\vec{E}^t$ for $z \leq 0$) can thus be written in the same form:

$$\vec{E}^s = SE_o e^{+jk(sin(\theta')cos(\phi')x + sin(\theta')sin(\phi')y - cos(\theta')|z|)}\,\hat{E}^s$$

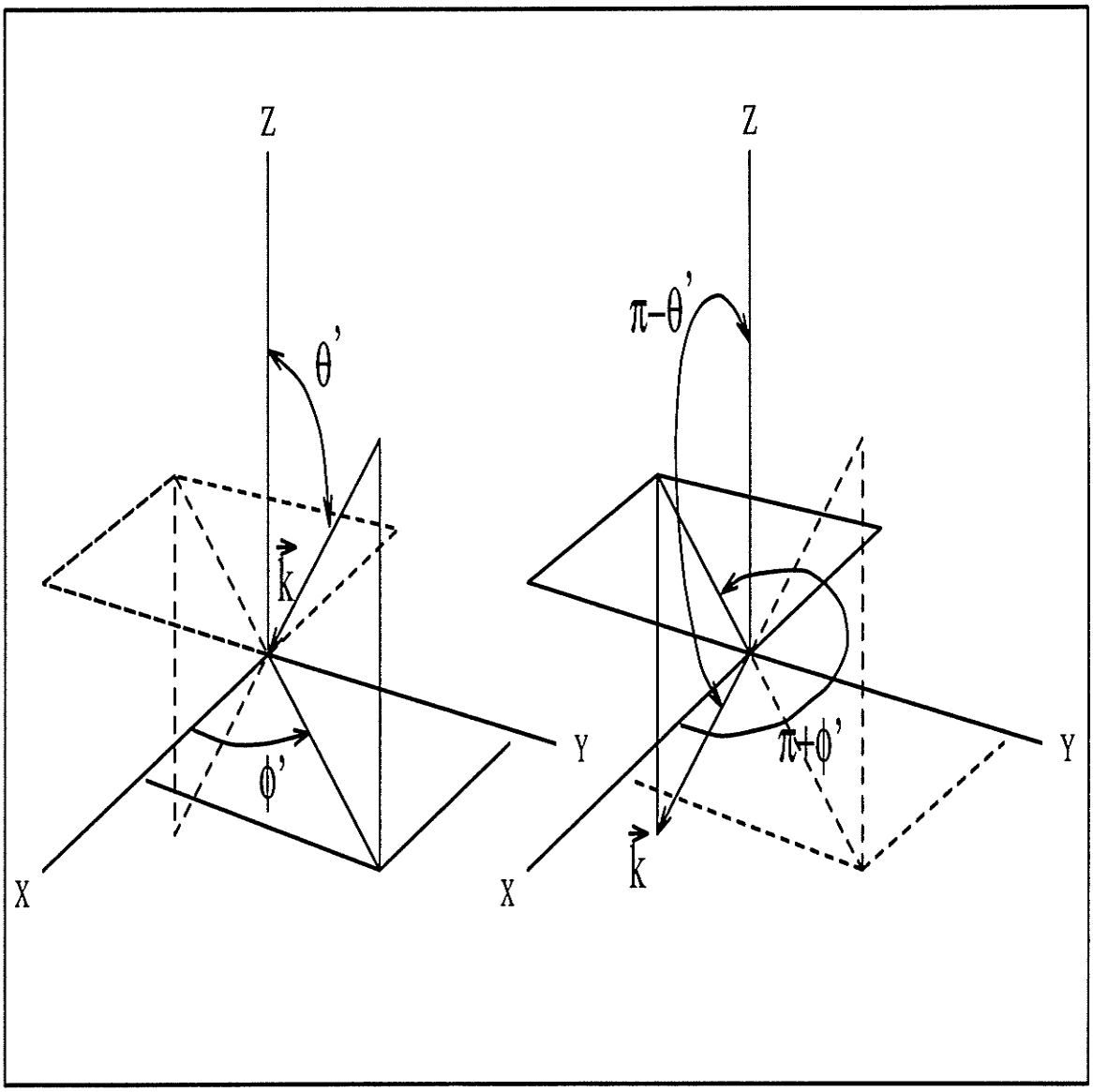

Figure A.1: The familiar (on the left) and the present (on the right) representations of the incident propagation vector $\vec{k}^i$.

However, with the present representation, the angles now become:

$$\theta^i = \pi - \theta' \qquad \theta^r = \theta' \qquad \theta^t = \pi - \theta' \qquad 0^o \leq \forall\theta \leq 180^o$$
$$\phi^i = \pi + \phi' \qquad \phi^r = \pi + \phi' \qquad \phi^t = \pi + \phi' \qquad 0^o \leq \forall\phi \leq 360^o$$

and for any positive or negative values of x, y, and z, one writes, with the $e^{+j\omega t}$ time convention, the incident, reflected and transmitted plane waves as:

$$\vec{E}^i = E_o e^{-jk(\underbrace{sin(\theta^i)}_{sin\theta'}\underbrace{cos(\phi^i)}_{-cos\phi'}x+\underbrace{sin(\theta^i)}_{sin\theta'}\underbrace{sin(\phi^i)}_{-sin\phi'}y+\underbrace{cos(\theta^i)}_{-cos\theta'}z)}\hat{E}^i$$

$$\vec{E}^r = RE_o e^{-jk(\underbrace{sin(\theta^r)}_{sin\theta'}\underbrace{cos(\phi^r)}_{-cos\phi'}x+\underbrace{sin(\theta^r)}_{sin\theta'}\underbrace{sin(\phi^r)}_{-sin\phi'}y+\underbrace{cos(\theta^r)}_{cos\theta'}z)}\hat{E}^r$$

$$\vec{E}^t = TE_o e^{-jk(\underbrace{sin(\theta^t)}_{sin\theta'}\underbrace{cos(\phi^t)}_{-cos\phi'}x+\underbrace{sin(\theta^t)}_{sin\theta'}\underbrace{sin(\phi^t)}_{-sin\phi'}y+\underbrace{cos(\theta^t)}_{-cos\theta'}z)}\hat{E}^t$$

which expressions are, of course, equivalent to those for the familiar representation, as evidenced by substituting the expressions for the angles.

The advantage of the present representation is that all waves, including the incident wave, have the same generic form $e^{-j\vec{k}\cdot\vec{r}}$ with the sign of $\vec{k}$ being taken into account implicitly by the angles θ and ϕ. This homogeneous terminology avoids a lot of confusion when dealing with the handedness of a circularly polarized wave. As an added bonus, all propagation vectors $\vec{k^i}$, $\vec{k^r}$, and $\vec{k^t}$, also end up having the same ϕ.

In writing the expressions for $\hat{E}^i$, $\hat{E}^r$ and $\hat{E}^t$ in spherical coordinates, one uses the unit vectors corresponding to the propagation vectors, e.g.:

$$\hat{E}^i = cos(\varsigma)\hat{\theta}^i + sin(\varsigma)\hat{\phi}^i$$

where $\hat{\theta}^i$ and $\hat{\phi}^i$ are the spherical coordinate unit vectors for $\vec{k^i}$. In forming the ratio of voltage travelling waves to obtain the voltage scattering coefficients, one must be wary of the fact that the unit vectors for the spherical coordinate system vary with

the position whereas those for the Cartesian coordinate system do not. For instance, in the limit that the incidence angle approaches the normal, $\hat{\theta}^i \rightarrow \hat{x}^i$ but $\hat{\theta}^r \rightarrow -\hat{x}^r$ since $\hat{x}^i \equiv \hat{x}^r$. Since with this convention $\vec{k^i}$, $\vec{k^r}$ and $\vec{k^t}$ have the same $\hat{\phi}$ but not necessarily the same $\hat{\theta}$, the scattering coefficients in the spherical coordinates are not necessarily identical to their counterparts in the Cartesian coordinates even for the case of normal incidence (see Chapter 2).

Appendix B

TM and TE modes

This chapter presents the development of TM^u and TE^u modes from the approach of the vector potential formalism [94] rather than from the approach of the modal formalism [89, 90, 91] [92, pp. 235-238]. Although both approaches produce the same expressions for the modes, they differ in concept: in the modal formalism, the transverse field components are considered to be the independent parameters whereas in the vector potential formalism, the longitudinal field components are taken to be the independent parameters.

The time convention $e^{+j\omega t}$ is taken throughout this document. The vector potential formulation is:

$$\vec{H^A} = +\frac{\nabla \times \vec{A}}{\mu} \quad \text{and} \quad \vec{E^F} = -\frac{\nabla \times \vec{F}}{\varepsilon}$$

$$\begin{aligned} \vec{E} &= \vec{E^A} + \vec{E^F} &&= -j\omega\vec{A} - \tfrac{j}{\omega\mu\varepsilon}\nabla(\nabla \cdot \vec{A}) - \tfrac{1}{\varepsilon}\nabla \times \vec{F} \\ \vec{H} &= \vec{H^A} + \vec{H^F} &&= -j\omega\vec{F} - \tfrac{j}{\omega\mu\varepsilon}\nabla(\nabla \cdot \vec{F}) + \tfrac{1}{\mu}\nabla \times \vec{A} \end{aligned}$$

For $u \equiv z$, one has:

$$\begin{aligned}
&\vec{A} = A\hat{z} && \vec{F} = F\hat{z} \\
&\nabla^2 A + \omega^2\mu\varepsilon A = 0 && \nabla^2 F + \omega^2\mu\varepsilon F = 0 \\
&E_x^A = -\tfrac{j}{\omega\mu\varepsilon}\tfrac{\partial^2 A}{\partial x \partial z} && E_x^F = -\tfrac{1}{\varepsilon}\tfrac{\partial F}{\partial y} \\
&E_y^A = -\tfrac{j}{\omega\mu\varepsilon}\tfrac{\partial^2 A}{\partial y \partial z} && E_y^F = +\tfrac{1}{\varepsilon}\tfrac{\partial F}{\partial x} \\
&E_z^A = -\tfrac{j}{\omega\mu\varepsilon}\left(\tfrac{\partial^2 A}{\partial z^2} + \omega^2\mu\varepsilon A\right) && E_z^F = 0 \Rightarrow TE^z \\
&H_x^A = +\tfrac{1}{\mu}\tfrac{\partial A}{\partial y} && H_x^F = -\tfrac{j}{\omega\mu\varepsilon}\tfrac{\partial^2 F}{\partial x \partial z} \\
&H_y^A = -\tfrac{1}{\mu}\tfrac{\partial A}{\partial x} && H_y^F = -\tfrac{j}{\omega\mu\varepsilon}\tfrac{\partial^2 F}{\partial y \partial z} \\
&H_z^A = 0 \Rightarrow TM^z && H_z^F = -\tfrac{j}{\omega\mu\varepsilon}\left(\tfrac{\partial^2 F}{\partial z^2} + \omega^2\mu\varepsilon F\right)
\end{aligned}$$

Since one has:

$$\begin{cases} E_z^F = 0 & \Longrightarrow \quad E_z^A = E_z \\ H_z^A = 0 & \Longrightarrow \quad H_z^F = H_z \end{cases}$$

the uncoupling of the TM^z and TE^z modes always results if the electromagnetic (EM) field can be decomposed into TM^z and TE^z modes, and more generally, TM^u (or LSM^u) and TE^u (or LSE^u) modes. Such a decomposition, however, is possible only if for $U\hat{u} = \{\vec{A}, \vec{F}\}$ one has [93, 94]:

$$\hat{u} = \begin{cases} \{\hat{x}, \hat{y}, \hat{z}, \hat{r}, \hat{a}\} & \text{if } U \text{ depends on all three coordinates of the system} \\ \{\hat{\rho}, \hat{\phi}\} & \text{if } U \text{ is independent of the } \phi \text{ coordinate} \end{cases}$$

where $\hat{a}$ is a an arbitrary constant unit vector.

Now, assuming the functional dependence of A and F to be of the forms:

$$A = f(x,y)e^{-jk_z z} \quad \text{and} \quad F = g(x,y)e^{-jk_z z}$$

and assuming k_z to be constant with respect to x and y, i.e. $\frac{\partial}{\partial z} = -jk_z$, then one obtains:

$$\vec{E_z^A} = -\frac{j}{\omega\mu\varepsilon}\left((-jk_z)^2 + \omega^2\mu\varepsilon\right)A \Longrightarrow A = \frac{j\omega\mu\varepsilon}{k_o^2 - k_z^2}E_z^A$$

where $k_o^2 = \omega^2 \mu\varepsilon$, and thus:

$$\begin{aligned}
E_x^A &= \frac{k_z}{j(k_o^2-k_z^2)} \frac{\partial E_z^A}{\partial x} \\
E_y^A &= \frac{k_z}{j(k_o^2-k_z^2)} \frac{\partial E_z^A}{\partial y} \\
H_x^A &= \frac{-\omega\varepsilon}{j(k_o^2-k_z^2)} \frac{\partial E_z^A}{\partial y} \\
H_y^A &= \frac{+\omega\varepsilon}{j(k_o^2-k_z^2)} \frac{\partial E_z^A}{\partial x} \\
Z_W^A &= \frac{E_x^A}{H_y^A} = -\frac{E_y^A}{H_x^A} = \frac{k_z}{\omega\varepsilon}
\end{aligned}$$

By duality ($E \to H, H \to -E, \varepsilon \to \mu, \mu \to \varepsilon$), one obtains:

$$F = \frac{j\omega\mu\varepsilon}{k_o^2 - k_z^2} H_z^F$$

$$\begin{aligned}
H_x^F &= \frac{k_z}{j(k_o^2-k_z^2)} \frac{\partial H_z^F}{\partial x} \\
H_y^F &= \frac{k_z}{j(k_o^2-k_z^2)} \frac{\partial H_z^F}{\partial y} \\
E_x^F &= \frac{+\omega\mu}{j(k_o^2-k_z^2)} \frac{\partial H_z^F}{\partial y} \\
E_y^F &= \frac{-\omega\mu}{j(k_o^2-k_z^2)} \frac{\partial H_z^F}{\partial x} \\
Z_W^F &= \frac{E_x^F}{H_y^F} = -\frac{E_y^F}{H_x^F} = \frac{\omega\mu}{k_z}
\end{aligned}$$

Therefore, providing that $k_o \neq k_z$, one can write all the actual transverse field components directly in terms of the actual longitudinal field components as following:

$$\begin{aligned}
E_x &= \frac{1}{j(k_o^2-k_z^2)} \left(k_z \frac{\partial E_z}{\partial x} + \omega\mu \frac{\partial H_z}{\partial y} \right) \\
E_y &= \frac{1}{j(k_o^2-k_z^2)} \left(k_z \frac{\partial E_z}{\partial y} - \omega\mu \frac{\partial H_z}{\partial x} \right) \\
H_x &= \frac{1}{j(k_o^2-k_z^2)} \left(-\omega\varepsilon \frac{\partial E_z}{\partial y} + k_z \frac{\partial H_z}{\partial x} \right) \\
H_y &= \frac{1}{j(k_o^2-k_z^2)} \left(+\omega\varepsilon \frac{\partial E_z}{\partial x} + k_z \frac{\partial H_z}{\partial y} \right)
\end{aligned}$$

Since E_z and H_z belong necessarily to the same EM field structure, they travel in unison in the same direction and at the same phase velocity. And since $E_z \equiv E_z^A$ and $H_z \equiv H_z^F$, both TM^z and TE^z have the same eigenvalue $k_c^2 = k_o^2 - k_z^2$. Therefore, in a Cartesian coordinate system, the TM^z and TE^z modes are necessarily degenerate, i.e. to the same eigenvalue correspond two eigenmodes. The development presented

above shows also that the knowledge of only two field components, namely here E_z and H_z, is sufficient to obtain the knowledge of the whole EM field structure.

The E-type and the H-type modes correspond to E and H modes taken with respect to a transverse direction rather than with respect to the longitudinal direction. These type-modes stand in contrast to the ordinary E and H modes in that, at off-normal incidence, a free-standing lossless metallic grid causes a coupling between the ordinary E and H modes but does not cause a coupling between the E-type and the H-type modes, whereas a dielectric interface between two homogeneous media does not cause a coupling between the ordinary E and H modes but does cause a coupling between the E-type and the H-type modes (see reference [43, p. 220]). For normal incidence, the E-type and the H-type modes reduce to the ordinary H and E modes, respectively (see reference [43, p. 216]). Hence, one can expect that, for the grid, the coupling between the ordinary E and H modes increases from zero at normal incidence to some maximum as the incidence is increasingly off-normal, and conversely for the dielectric interface, one can expect the coupling between the E-type and H-type modes to increase from zero at normal incidence to some maximum as the incidence is increasingly off-normal. This author notes in passing that an important minus sign is missing from the expression for h''_{xi} on p. 220 of reference [43] and on p. 12 of reference [44]. Otherwise, the duality between the expressions for the E-type and the H-type modes would be violated. Other papers [42, 80, 39] dealing with these type-modes show correctly the presence of this minus sign.

The following development deals with obtaining a result needed in Chapter 2. Assuming the functional dependence of A and F to be of the forms:

$$A = A_o e^{-j\vec{k}\cdot\vec{r}} \quad \text{and} \quad F = F_o e^{-j\vec{k}\cdot\vec{r}}$$

and assuming k_x, k_y and k_z to be constant with respect to x, y and z, i.e.:

$$\frac{\partial}{\partial x} = -jk_x \quad \text{and} \quad \frac{\partial}{\partial y} = -jk_y \quad \text{and} \quad \frac{\partial}{\partial z} = -jk_z$$

then one obtains:

$$\begin{aligned} E_x^A &= -\tfrac{k_x k_z}{(k_o^2 - k_z^2)} E_z^A \\ E_y^A &= -\tfrac{k_y k_z}{(k_o^2 - k_z^2)} E_z^A \\ E_x^F &= -\omega\mu \tfrac{k_y}{(k_o^2 - k_z^2)} H_z^F \\ E_y^F &= +\omega\mu \tfrac{k_x}{(k_o^2 - k_z^2)} H_z^F \end{aligned}$$

from which one obtains:

$$\frac{E_t^A}{E_o^A} = \left[\frac{(E_x^A)^2 + (E_y^A)^2}{(E_x^A)^2 + (E_y^A)^2 + (E_z^A)^2}\right]^{1/2} = \frac{|k_z|}{k_o}$$

$$\frac{E_t^F}{E_o^F} = \left[\frac{(E_x^F)^2 + (E_y^F)^2}{(E_x^F)^2 + (E_y^F)^2}\right]^{1/2} \equiv 1$$

Hence, one obtains the desired result as:

$$\frac{E_t^A}{E_o^A} = |cos(\theta)| \quad \text{and} \quad \frac{E_t^F}{E_o^F} \equiv 1$$

Appendix C

Wave Impedance for Arbitrary Incidence

This appendix presents the wave impedance concept by forming the ratio E_t/H_t where the subscript t refers either to the components tangential to a planar surface onto which a plane wave impinges at arbitrary angle with arbitrary polarization, or more generally, to the components transverse to a prescribed direction which does not necessarily coincide with the direction of propagation of the plane wave. Figure C.1 depicts the situation and the representation in Appendix A is used. Since ϕ is the vector common to both the inclined and the horizontal planes, $+\hat{\phi}$ is selected as the reference axis from which to describe the polarization by the angle ς as:

$$\vec{E} = E_o \left(sin(\varsigma)\hat{\theta} + cos(\varsigma)\hat{\phi} \right)$$

$$\begin{aligned} \vec{H} &= \frac{E_o}{\eta} \left(sin(\varsigma - 90^o)\hat{\theta} + cos(\varsigma - 90^o)\hat{\phi} \right) \\ &= \frac{E_o}{\eta} \left(-cos(\varsigma)\hat{\theta} + sin(\varsigma)\hat{\phi} \right) \end{aligned}$$

As the tangential (with respect to a plane $z = cte$) component of an arbitrary vector $\vec{A}$ is given by:

$$\vec{A}_t = \hat{z} \times (\vec{A} \times \hat{z})$$

One obtains:

$$\begin{aligned} \vec{E}_t &= \hat{z} \times (\vec{E} \times \hat{z}) \\ &= \hat{z} \times \left(E_o \left[sin(\varsigma)\hat{\theta} + cos(\varsigma)\hat{\phi} \right] \times \hat{z} \right) \\ &= E_o \left(sin(\varsigma) \left[\hat{z} \times (\hat{\theta} \times \hat{z}) \right] + cos(\varsigma) \left[\hat{z} \times (\hat{\phi} \times \hat{z}) \right] \right) \\ &= E_o \left(sin(\varsigma) \left[\hat{z} \times (-cos(\theta)\hat{\phi}) \right] + cos(\varsigma) \left[\hat{z} \times \hat{\rho} \right] \right) \\ &= E_o \left(sin(\varsigma)cos(\theta)\hat{\rho} + cos(\varsigma)\hat{\phi} \right) \end{aligned}$$

Similarly,

$$\begin{aligned}\vec{H}_t &= \hat{z} \times (\vec{H} \times \hat{z}) \\ &= \hat{z} \times \left(\tfrac{E_o}{\eta}\left[sin(\varsigma - 90^o)\hat{\theta} + cos(\varsigma - 90^o)\hat{\phi}\right] \times \hat{z}\right) \\ &= \tfrac{E_o}{\eta}\left(sin(\varsigma - 90^o)cos(\theta)\hat{\rho} + cos(\varsigma - 90^o)\hat{\phi}\right) \\ &= \tfrac{E_o}{\eta}\left(-cos(\varsigma)cos(\theta)\hat{\rho} + sin(\varsigma)\hat{\phi}\right)\end{aligned}$$

Therefore, the wave impedance is obtained as:

$$\begin{aligned}Z_W = \frac{E_t}{H_t} &= \frac{\sqrt{E_\rho^2 + E_\phi^2}}{\sqrt{H_\rho^2 + H_\phi^2}} \\ &= \eta\sqrt{\frac{sin^2(\varsigma)cos^2(\theta) + cos^2(\varsigma)}{cos^2(\varsigma)cos^2(\theta) + sin^2(\varsigma)}}\end{aligned}$$

Since the TM^z mode corresponds to $\varsigma = 90^o$ and the TE^z mode corresponds to $\varsigma = 0^o$, the wave impedance reduces to:

$$Z_W = \begin{cases} \eta\ cos(\theta) & \text{for } \varsigma = 90^o \quad \Rightarrow TM^z \text{ or } E^z \text{ mode} \\ \eta/cos(\theta) & \text{for } \varsigma = 0^o \quad \Rightarrow TE^z \text{ or } H^z \text{ mode} \end{cases}$$

The angle ξ is obtained as:

$$\xi_E = Arctan\left(\frac{E_\rho}{E_\phi}\right) = Arctan\left(cos(\theta)tan(\varsigma)\right)$$

Similarly:

$$\xi_H = Arctan\left(\frac{H_\rho}{H_\phi}\right) = Arctan\left(cos(\theta)tan(\varsigma - 90^o)\right) = Arctan\left(\frac{cos(\theta)}{tan(\varsigma)}\right)$$

Thus, it is seen that although $\vec{E}_o^i$ and $\vec{H}_o^i$ are orthogonal to one another, their corresponding transverse components are not so, unless $\vec{E}_o^i = \{E_o\hat{\theta} \text{ or } E_o\hat{\phi}\}$. For instance:

$$\left\{\begin{array}{l}\theta = 30^o \\ \phi = 70^o\end{array}\right\} \Longrightarrow \left\{\begin{array}{lcl}\xi_E & = & 67.20^o \\ \xi_E - 90^o & = & -22.80^o \\ \xi_H & = & -17.50^o\end{array}\right\} \Longrightarrow \xi_H \neq \xi_E - 90^o$$

The angles ς and ξ are defined in the range $\{-180^o, +180^o\}$. The angle ς is counted positive when winding CCW about the $\hat{k}$ axis while looking into the $+\hat{k}$ direction. The angle ξ is counted positive when winding CCW about the $\hat{z}$ axis while looking into the $+\hat{z}$ direction. Since however, the angle ξ is defined with respect to the unit

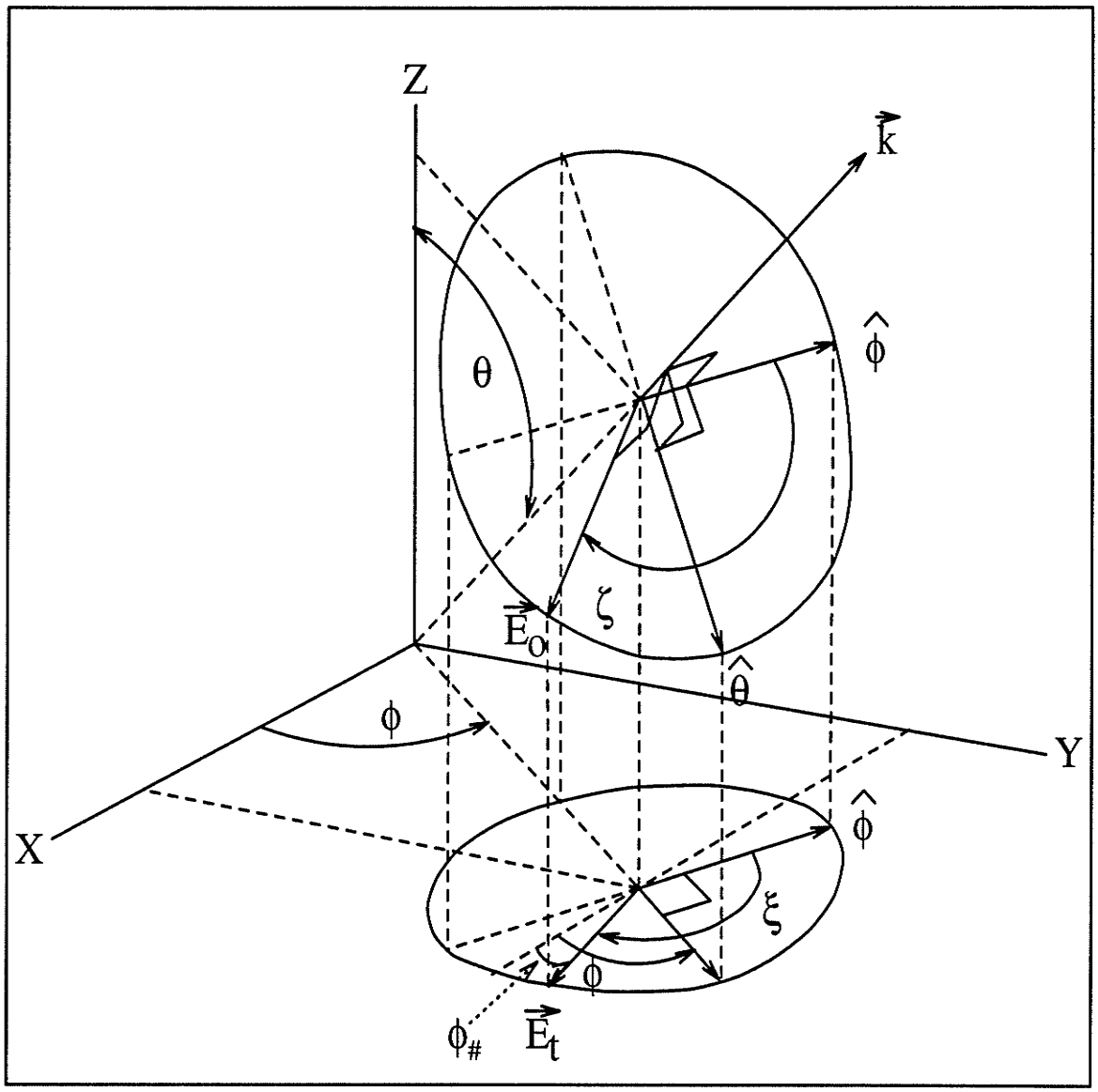

Figure C.1: Depiction of a plane wave incident at an arbitrary angle with an arbitrary polarization.

vector $+\hat{\phi}$, the angle ξ varies with the angle ϕ. The direction $\phi = \phi_{\#}$ that corresponds to the angle ξ is obtained as (see Figure C.1):

$$\phi_{\#} = \phi + 90^{o} - \xi$$

where the 90^{o} accounts for the fact that the direction indicated by the unit vector $\hat{\phi}$ is 90^{o} ahead of the direction indicated by the corresponding angle $\phi = cte$, and the minus sign accounts for the fact that the angles $\phi_{\#}$ and ξ are counted positive in opposite directions. For instance, if the direction corresponding to $\phi_{\#}$ represents the direction of the wires of a grid, then one obtains:

$$\phi_{\#} \equiv \phi_{g} \Longrightarrow \xi = \phi + 90^{o} - \phi_{g}$$

One notes also that since the value of E_{ρ} depends here on $cos(\theta)$, the angle ς must change sign as the $\theta = 90^{o}$ plane is crossed for ξ to remain the same (see Figure C.2).

More generally [95, pp. 49-51], if one has:

$$\vec{E} = E_{o}\left(sin(\varsigma)e^{j\delta_{\theta}}\hat{\theta} + cos(\varsigma)e^{j\delta_{\phi}}\hat{\phi}\right)$$

the resulting polarization is an ellipse with tilt angle ψ and axial ratio ar obtained as:

$$\psi = \frac{1}{2}\left(\pi - Arctan\left(\frac{2\ p\ cos(\delta)}{1-p^{2}}\right)\right)$$

$$ar = \sqrt{\frac{(1+p^{2}) + \sqrt{1+p^{4}+2p^{2}cos(2\delta)}}{(1+p^{2}) - \sqrt{1+p^{4}+2p^{2}cos(2\delta)}}}$$

where ψ is the angle between the major axis and the $+\hat{\phi}$ axis, and is counted positive by the same convention as that for ς, the axial ratio ar is defined as the ratio of the major axis over the minor axis, thus $ar \geq 0$, and the polarization ratio P is defined as:

$$P = \frac{E_{\phi}}{E_{\theta}} = pe^{j\delta} \text{ where } \begin{cases} p = [cotan(\varsigma)]^{\pm 1} \\ \delta = \delta_{\phi} - \delta_{\theta} \end{cases}$$

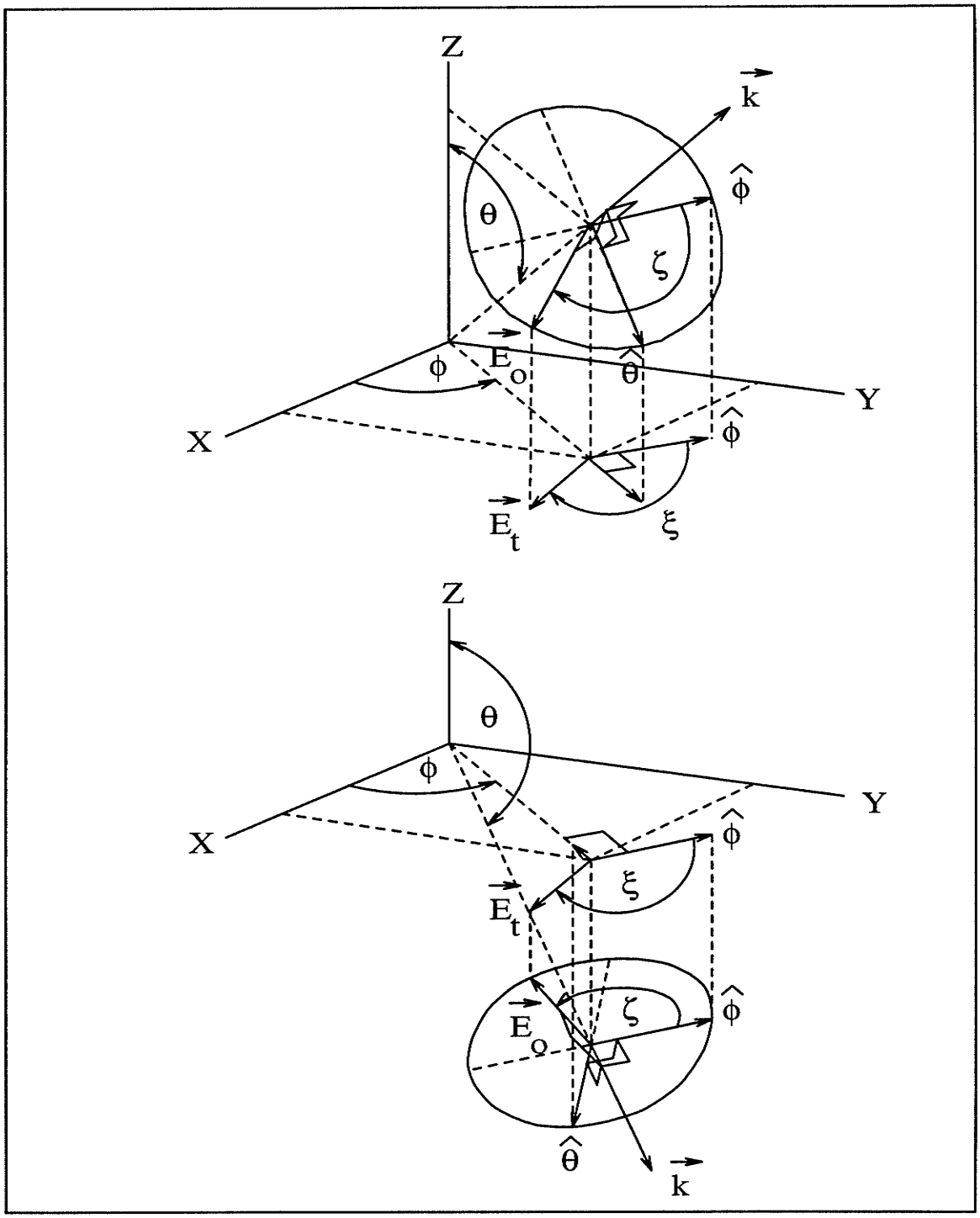

Figure C.2: Two cases for which ξ is the same for two different values of θ.

with the exponent in the expression for p chosen such that $ar \geq 0$. Thus, one has:

$$\begin{cases} \delta = \{0^o, \pm 180^o\} & \Longrightarrow \quad ar = \infty & \Longrightarrow \text{ LP} \\ \delta = \{\pm 90^o\} & \Longrightarrow \quad ar = \frac{1}{p} \geq 0 & \Longrightarrow \begin{cases} \delta < 0 & \Longrightarrow \text{ RHCP} \\ \delta > 0 & \Longrightarrow \text{ LHCP} \end{cases} \end{cases}$$

where the handedness of the CP wave is defined with respect to the $+\hat{k}$, i.e. $+\hat{r}$, direction. It must be pointed out that this definition of the polarization sense for an elliptically polarized wave propagating in the $+\hat{r}$ direction is the one commonly used in Engineering and is opposite to the one commonly used in Physics [47, pp. 398-401], [1, pp. 293-296], [48, p. 681].

Appendix D

Various Results for the Polarization Efficiency

This appendix is meant to fix the ideas on the significance of the polarization efficiency f by working out its value for different cases. The situation is depicted in Figure D.1 where it is to be noted that only the x coordinate axis for the Rx antenna is in the same direction as the x' coordinate axis for the Tx antenna. With this arrangement, the polarization ellipse of either the Rx or the Tx antennas is defined as if the antenna were transmitting and the relative angle between the two major axes of the two polarization ellipses is $\Psi = \psi_R + \psi_T$. The parameter ϵ is the polarization sense defined with respect to the z and z' directions for the Rx and Tx antennas respectively, as +1 if RHCP and -1 if LHCP, with the polarization ellipse of an antenna defined as if the antenna were transmitting. For a purely linearly polarized antenna, ϵ can be taken as either +1 or -1. In what follows, the subindices R and T stand for the Rx and Tx antennas, respectively.

- Both the Rx and the Tx antennas are elliptically polarized, this is the general case and the polarization efficiency f is given as (see [1, p. 305],[104][1]):

$$f = \frac{(1 + ar_R^2)(1 + ar_T^2) + 4\ \epsilon_R\ ar_R\ \epsilon_T\ ar_T + (1 - ar_R^2)(1 - ar_T^2)cos2\Psi}{2(1 + ar_R^2)(1 + ar_T^2)}$$

[1]The expression for f in reference [104] is marred by misprints. The expression in reference [1] is correct even though the definition of the axial ratio ar is taken therein as the inverse of the definition taken herein.

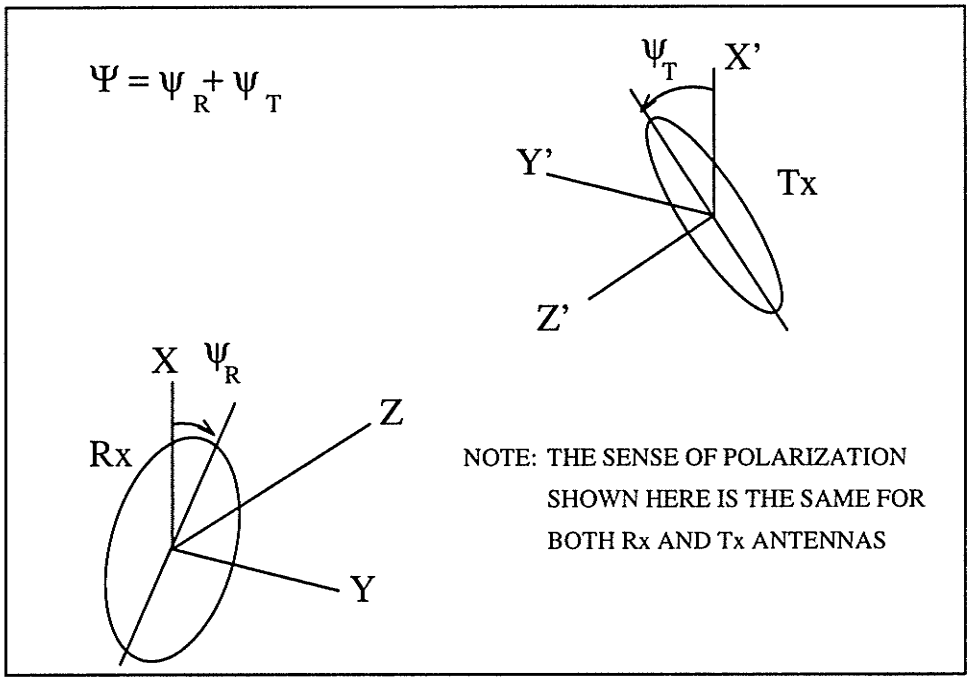

Figure D.1: Coordinate definition for the two arbitrarily elliptically polarized antennas.

It is seen that if $ar_R \neq 1$ and $ar_T \neq 1$, then $f \neq 0$ even if the polarization senses of the two antennas are opposite.

- Both the Rx and the Tx antennas are linearly polarized, hence one has:

$$ar_R = ar_T = \infty \Longrightarrow f = (cos\Psi)^2$$

- Both the Rx and the Tx antennas are circularly polarized, hence one has:

$$ar_R = ar_T = 1 \Longrightarrow f = \begin{cases} 1 \text{ ..... if } \epsilon_R = \epsilon_T \\ 0 \text{ .... if } \epsilon_R = -\epsilon_T \end{cases}$$

- One antenna, say Tx, is circularly polarized and the other antenna, thus Rx, is linearly polarized. Hence one has:

$$\left.\begin{array}{l} ar_T = 1 \\ ar_R = \infty \end{array}\right\} \Longrightarrow f = 0.5 \text{ ..... regardless of } \Psi \text{ and } \epsilon_R$$

- One antenna, say Tx, is circularly polarized and the other antenna, thus Rx, is elliptically polarized. Hence one has:

$$ar_T = 1 \Longrightarrow f = \frac{(1+\epsilon_T\ \epsilon_R\ ar_R)^2}{2\ (1+ar_R^2)} \text{..... regardless of } \Psi$$

- One antenna, say Tx, is linearly polarized and the other antenna, thus Rx, is elliptically polarized. Hence one has:

$$ar_T = \infty \Longrightarrow f = 0.5\ \left(1 - \frac{1-ar_R^2}{1+ar_R^2}\ cos2\Psi\right) \text{ ..... regardless of } \epsilon_R$$

This case produces the dumb-bell shape of the polarization pattern.

- Both antennas are elliptically polarized and Ψ is varied over 360^o, thus one has:

$$\text{when } \Psi = 0^o \text{ or } 180^o,\ f = f_{max} = \frac{(1+\epsilon_R\ ar_R\ \epsilon_T\ ar_T)^2}{(1+ar_R^2)\ (1+ar_T^2)}$$

$$\text{when } \Psi = 90^o \text{ or } -90^o,\ f = f_{min} = \frac{(ar_R+\epsilon_R\ \epsilon_T\ ar_T)^2}{(1+ar_R^2)\ (1+ar_T^2)}$$

The composite axial ratio ar_{RT} becomes:

$$ar_{RT} = \pm\sqrt{\frac{f_{max}}{f_{min}}} = \pm\left(\frac{1+\epsilon_R\ ar_R\ \epsilon_T\ ar_T}{ar_R+\epsilon_R\ \epsilon_T\ ar_T}\right)$$

where the sign is chosen such that $ar_{RT} \geq 1$.

It is seen from the expression for f_{max} that, in order to have $f = 1$, one requires simultaneously:

1. $ar_R = ar_T$
2. $\Psi = 0^o$ or 180^o
3. $\epsilon_R = \epsilon_T$

This case corresponds to the elliptically co-polarized component.

Similarly, it is seen from the expression for f_{min} that in order to have $f = 0$, one requires simultaneously:

1. $ar_R = ar_T$
2. $\Psi = \pm 90^o$
3. $\epsilon_R = -\epsilon_T$

This case corresponds to the elliptically cross-polarized component.

Appendix E

Validation of the GSM-based Technique

In this appendix, structures with known operations are analyzed in order to demonstrate and to validate the GSM-based technique. These structures are the solid Perfect Electrically Conducting (PEC) planar reflector, the free space slab, the artificially soft or hard surfaces, the ideal LP, LHCP and RHCP polarizers. In Chapter 2, the GSM-based technique was used to obtain the GSM for the ideal CPSS and the non-ideal CPSS.

E.0.1 Solid PEC Planar Reflector

The operation consisting in reflecting an incident CP plane wave into a CP plane wave whose handedness is opposite to that of the incident wave, is phrased as:

$$\begin{cases} \text{If } (E_o^i)_v^H = \pm j(E_o^i)_v^E \text{ for } (E_o^i)_u^l = 0, u \neq v, l = \{E, H\} \\ \text{then} \begin{cases} (E_o^s)_v^H = \mp j(E_o^s)_v^E \quad v = \{1,2,3,4\} \\ (E_o^s)_u^H = (E_o^s)_u^E = 0 \quad u\text{-ness} \neq v\text{-ness} \end{cases} \end{cases}$$

Say, $v = 1$. One obtains:

$$\begin{cases} (E_o^s)_1^E &= C_{11}^{EE}(E_o^i)_1^E + C_{11}^{EH}(E_o^i)_1^H \\ (E_o^s)_1^H &= C_{11}^{HE}(E_o^i)_1^E + C_{11}^{HH}(E_o^i)_1^H \end{cases}$$

$$(E_o^i)_1^H = \pm j(E_o^i)_1^E \Longrightarrow \begin{cases} (E_o^s)_1^E = \left(C_{11}^{EE} \pm jC_{11}^{EH}\right)(E_o^i)_1^E \\ (E_o^s)_1^H = \left(C_{11}^{HE} \pm jC_{11}^{HH}\right)(E_o^i)_1^E \end{cases}$$

$$\begin{aligned} (E_o^s)_1^H = \mp j(E_o^s)_1^E &\Longrightarrow \left(C_{11}^{HE} \pm jC_{11}^{HH}\right) = \mp j\left(C_{11}^{EE} \pm jC_{11}^{EH}\right) \\ &\Longrightarrow \left(C_{11}^{HE} - C_{11}^{EH}\right) = \mp j\left(C_{11}^{EE} + C_{11}^{HH}\right) \end{aligned}$$

$$\begin{cases} (E_o^s)_2^E &= C_{21}^{EE}(E_o^i)_1^E + C_{21}^{EH}(E_o^i)_1^H \\ (E_o^s)_2^H &= C_{21}^{HE}(E_o^i)_1^E + C_{21}^{HH}(E_o^i)_1^H \end{cases}$$

$$(E_o^i)_1^H = \pm j(E_o^i)_1^E \Longrightarrow \begin{cases} (E_o^s)_2^E = \left(C_{21}^{EE} \pm jC_{21}^{EH}\right)(E_o^i)_1^E \\ (E_o^s)_2^H = \left(C_{21}^{HE} \pm jC_{21}^{HH}\right)(E_o^i)_1^E \end{cases}$$

$$\begin{cases} (E_o^s)_2^E = 0 \Longrightarrow C_{21}^{EE} = \mp jC_{21}^{EH} \\ (E_o^s)_2^H = 0 \Longrightarrow C_{21}^{HE} = \mp jC_{21}^{HH} \end{cases}$$

From the combination of reciprocity, 2-fold rotational symmetry and Snell's law of reflection, with $u = v = 1, p = E, q = H$, one obtains:

$$C_{11}^{EH} = -C_{11}^{HE}$$

Consequently:

$$\underbrace{\left(C_{11}^{HE} - C_{11}^{EH}\right)}_{-2C_{11}^{EH}} = \mp j\left(C_{11}^{EE} + C_{11}^{HH}\right) \Longrightarrow C_{11}^{HH} = -C_{11}^{EE} \mp j2C_{11}^{EH}$$

From above, one knows:

$$C_{21}^{EE}(\theta^s, \phi^s|\theta^i, \phi^i) = \mp j C_{21}^{EH}(\theta^s, \phi^s|\theta^i, \phi^i)$$

From reciprocity and reflection symmetry about the $z = 0$ plane with $u = 2, v = 1, p = E, q = H$, one has:

$$C_{21}^{EH}(\theta^s, \phi^s|\theta^i, \phi^i) = C_{21}^{HE}(\theta^i, \pi + \phi^i|\theta^s, \pi + \phi^s)$$

From above, one also knows:

$$C_{21}^{HE}(\theta^i, \pi + \phi^i|\theta^s, \pi + \phi^s) = \mp j C_{21}^{HH}(\theta^i, \pi + \phi^i|\theta^s, \pi + \phi^s)$$

From reciprocity and reflection symmetry about the $z = 0$ plane with $u = 2, v = 1, p = q = H$, one has:

$$C_{21}^{HH}(\theta^i, \pi + \phi^i|\theta^s, \pi + \phi^s) = C_{21}^{HH}(\theta^s, 2\pi + \phi^s|\theta^i, 2\pi + \phi^i)$$

From the 2π periodicity of the angle ϕ one obtains:

$$C_{21}^{HH}(\theta^s, 2\pi + \phi^s|\theta^i, 2\pi + \phi^i) = C_{21}^{HH}(\theta^s, \phi^s|\theta^i, \phi^i)$$

Consequently, pulling everything together, one obtains:

$$C_{21}^{EE}(\theta^s, \phi^s|\theta^i, \phi^i) = -C_{21}^{HH}(\theta^s, \phi^s|\theta^i, \phi^i)$$

Therefore:

$$C_{21}^{EE} = -C_{21}^{HH}$$

Hence:

$$\left\{ \begin{array}{lcl} C_{21}^{EH} & = & \pm j C_{21}^{EE} \\ C_{21}^{EE} & = & -C_{21}^{HH} \\ C_{21}^{HH} & = & \pm j C_{21}^{HE} \end{array} \right\} \Longrightarrow C_{21}^{EH} = C_{21}^{HE}$$

As seen previously, this result is consistent with the structure obeying the combination of reciprocity, 2-fold rotational symmetry, longitudinal reflection symmetry and Snell's law of refraction with $\theta^t = \theta^i$.

Now, from the unitary property of the matrix, one has:

$$C_{11}^{EE}(C_{11}^{EH})^* + C_{11}^{HE}(C_{11}^{HH})^* + C_{21}^{EE}(C_{21}^{EH})^* + C_{21}^{HE}(C_{21}^{HH})^* = 0$$

Substituting in this expression the various equivalences obtained above, one finds:

$$\underbrace{C_{11}^{EE}(C_{11}^{EH})^* + C_{11}^{EH}(C_{11}^{EE})^*}_{2Real\left[C_{11}^{EE}(C_{11}^{EH})^*\right]} \mp j\left(2\left|C_{11}^{EH}\right|^2 + \left|C_{21}^{EE}\right|^2 + \left|C_{21}^{HH}\right|^2\right) = 0$$

$$\left\{\left|C_{11}^{EH}\right| = \left|C_{21}^{EE}\right| = \left|C_{21}^{HH}\right| = 0\right\} \Longrightarrow \begin{cases} C_{11}^{HH} = -C_{11}^{EE} \\ C_{11}^{HE} = 0 \\ C_{21}^{EH} = C_{21}^{HE} = 0 \end{cases}$$

Also from the unitary property of the matrix, one has:

$$\left|C_{11}^{EE}\right|^2 + \left|C_{11}^{HE}\right|^2 + \left|C_{21}^{EE}\right|^2 + \left|C_{21}^{HE}\right|^2 = 1$$

Again, substituting in this expression the various equivalences obtained above, one finds:

$$\left|C_{11}^{EE}\right| = 1 \Longrightarrow \left|C_{11}^{HH}\right| = 1$$

In summary, one has:

$$C_{11}^{EH} = C_{11}^{HE} = C_{21}^{EE} = C_{21}^{EH} = C_{21}^{HE} = C_{21}^{HH} = 0$$

$$C_{11}^{EE} = -C_{11}^{HH} \text{ with } \left|C_{11}^{EE}\right| = \left|C_{11}^{HH}\right| = 1$$

One notes that since:

$$C_{11}^{EH} = C_{11}^{HE} = C_{21}^{EH} = C_{21}^{HE} = 0$$

then in particular:

$$C_{uv}^{pq}(\theta^s, \phi^s = \chi + m\pi | \theta^i, \phi^i = \chi + m\pi) = 0 \text{ for } p \neq q \text{ and } m = 0, \pm 1, \pm 2, \ldots.$$

which is a statement of the principle of reflection symmetry about the plane $y = tan(\chi)x$.

One notes that the phases of the scattering coefficients C_{11}^{EE} and C_{11}^{HH} are yet undetermined. This means that a purely reactive anisotropic surface like a metallic capacitive mesh or grid, or an array of dipole turnstiles with $\lambda/2$ front-to-back thickness [19] are structures befitting the desired operation. This situation is consistent with the fact that only the 2-fold rotational symmetry rather than the ∞-fold rotational symmetry was invoked in the above development. In order to identify specifically the structure as a solid reflector, i.e. a surface for which the tangential electric field scattered is the opposite of the tangential electric field incident for all ϕ angles, one needs also to specify:

$$(E_o^s)_v^H = -(E_o^i)_v^H \Longrightarrow C_{11}^{HH} = -1 \Longrightarrow C_{11}^{EE} = 1$$

The same analysis can be repeated for the other cases of v. Finally, one obtains the voltage scattering matrix of the solid PEC planar reflector as:

$$C(E,H) = \begin{pmatrix} 1 & 0 & 0 & 0 \\ 0 & -1 & 0 & 0 \\ 0 & 0 & 1 & 0 \\ 0 & 0 & 0 & -1 \end{pmatrix}$$

and thus, it is seen readily from equation (2.1) that $S(E,H) = C(E,H)$. It is also seen readily from equation (2.3) that $S(X,Y) = -I$ as expected from the reversal of all x and y components of the electric field. It may seem somewhat strange that the development invokes reflection symmetry about the $z = 0$ plane when the surface is a solid PEC reflector, as the two regions are completely isolated from one another. However, since the longitudinal reflection symmetry was invoked only for C_{21}^{pq} and since it was found afterwards that $C_{21}^{pq} = 0$, then the use of the longitudinal reflection symmetry was, in effect, of no consequence and there is no inconsistency incurred by invoking it.

E.0.2 Free Space Slab

The operation consisting in a slab being perfectly transparent to an incident CP wave, is phrased as:

$$\begin{cases} \text{If } (E_o^i)_v^H = \pm j(E_o^i)_v^E \text{ for } (E_o^i)_u^l = 0, u \neq v, l = \{E, H\} \\ \text{then} \begin{cases} (E_o^s)_v^H = (E_o^s)_v^E = 0 \quad v = \{1,2,3,4\} \\ (E_o^s)_u^H = \pm j(E_o^s)_u^E \quad u\text{-ness} \neq v\text{-ness} \end{cases} \end{cases}$$

Say, $v = 1$. One obtains:

$$\begin{cases} (E_o^s)_2^E &= C_{21}^{EE}(E_o^i)_1^E + C_{21}^{EH}(E_o^i)_1^H \\ (E_o^s)_2^H &= C_{21}^{HE}(E_o^i)_1^E + C_{21}^{HH}(E_o^i)_1^H \end{cases}$$

$$(E_o^i)_1^H = \pm j(E_o^i)_1^E \Longrightarrow \begin{cases} (E_o^s)_2^E = \left(C_{21}^{EE} \pm jC_{21}^{EH}\right)(E_o^i)_1^E \\ (E_o^s)_2^H = \left(C_{21}^{HE} \pm jC_{21}^{HH}\right)(E_o^i)_1^E \end{cases}$$

$$\begin{aligned} (E_o^s)_2^H = \pm j(E_o^s)_2^E &\Longrightarrow \left(C_{21}^{HE} \pm jC_{21}^{HH}\right) = \pm j\left(C_{21}^{EE} \pm jC_{21}^{EH}\right) \\ &\Longrightarrow \left(C_{21}^{HE} + C_{21}^{EH}\right) = \pm j\left(C_{21}^{EE} - C_{21}^{HH}\right) \end{aligned}$$

$$\begin{cases} (E_o^s)_1^E &= C_{11}^{EE}(E_o^i)_1^E + C_{11}^{EH}(E_o^i)_1^H \\ (E_o^s)_1^H &= C_{11}^{HE}(E_o^i)_1^E + C_{11}^{HH}(E_o^i)_1^H \end{cases}$$

$$(E_o^i)_1^H = \pm j(E_o^i)_1^E \Longrightarrow \begin{cases} (E_o^s)_1^E = \left(C_{11}^{EE} \pm jC_{11}^{EH}\right)(E_o^i)_1^E \\ (E_o^s)_1^H = \left(C_{11}^{HE} \pm jC_{11}^{HH}\right)(E_o^i)_1^E \end{cases}$$

$$\begin{cases} (E_o^s)_1^E = 0 \Longrightarrow C_{11}^{EE} = \mp jC_{11}^{EH} \\ (E_o^s)_1^H = 0 \Longrightarrow C_{11}^{HE} = \mp jC_{11}^{HH} \end{cases}$$

From the combination of reciprocity, reflection symmetry about the $z = 0$ plane, 2-fold rotational symmetry and Snell's law of refraction with $\theta^t = \theta^i$, and with $u = 2, v = 1, p = E, q = H$, one obtains:

$$C_{21}^{EH} = C_{21}^{HE}$$

Consequently:

$$\underbrace{\left(C_{21}^{HE} + C_{21}^{EH}\right)}_{2C_{21}^{EH}} = \pm j\left(C_{21}^{EE} - C_{21}^{HH}\right) \Longrightarrow C_{21}^{HH} = C_{21}^{EE} \pm j2C_{21}^{EH}$$

From above, one knows:

$$C_{11}^{EE}(\theta^s,\phi^s|\theta^i,\phi^i) = \mp jC_{11}^{EH}(\theta^s,\phi^s|\theta^i,\phi^i)$$

From reciprocity with $u = v = 1, p = E, q = H$, one has:

$$C_{11}^{EH}(\theta^s,\phi^s|\theta^i,\phi^i) = -C_{11}^{HE}(\pi-\theta^i,\pi+\phi^i|\pi-\theta^s,\pi+\phi^s)$$

From above, one also knows:

$$C_{11}^{HE}(\pi-\theta^i,\pi+\phi^i|\pi-\theta^s,\pi+\phi^s) = \mp jC_{11}^{HH}(\pi-\theta^i,\pi+\phi^i|\pi-\theta^s,\pi+\phi^s)$$

From reciprocity with $u = v = 1, p = q = H$, one has:

$$C_{11}^{HH}(\pi-\theta^i,\pi+\phi^i|\pi-\theta^s,\pi+\phi^s) = +C_{11}^{HH}(\theta^s,\phi^s|\theta^i,\phi^i)$$

Consequently, pulling everything together, one obtains:

$$C_{11}^{EE}(\theta^s,\phi^s|\theta^i,\phi^i) = +C_{11}^{HH}(\theta^s,\phi^s|\theta^i,\phi^i)$$

Therefore:

$$C_{11}^{EE} = C_{11}^{HH}$$

Hence:

$$\left\{\begin{array}{lcl} C_{11}^{EH} & = & \pm jC_{11}^{EE} \\ C_{11}^{EE} & = & C_{11}^{HH} \\ C_{11}^{HH} & = & \pm jC_{11}^{HE} \end{array}\right\} \Longrightarrow C_{11}^{EH} = -C_{11}^{HE}$$

As seen previously, this result is consistent with the structure obeying the combination of reciprocity, 2-fold rotational symmetry and Snell'a law of reflection.

Now, from the unitary property of the matrix, one has:

$$C_{11}^{EE}(C_{11}^{EH})^* + C_{11}^{HE}(C_{11}^{HH})^* + C_{21}^{EE}(C_{21}^{EH})^* + C_{21}^{HE}(C_{21}^{HH})^* = 0$$

Substituting in this expression the various equivalences obtained above, one finds:

$$\mp j\underbrace{\left(\left|C_{11}^{EE}\right|^2 + \left|C_{11}^{HH}\right|^2 + 2\left|C_{21}^{EH}\right|^2\right)}_{2\left(\left|C_{11}^{EE}\right|^2+\left|C_{21}^{EH}\right|^2\right)} + \underbrace{C_{21}^{EE}(C_{21}^{EH})^* + C_{21}^{EH}(C_{21}^{EE})^*}_{2Real\left[C_{21}^{EE}(C_{21}^{EH})^*\right]} = 0$$

Hence:

$$\left|C_{11}^{EE}\right|^2 + \left|C_{21}^{EH}\right|^2 = 0 = Real\left[C_{21}^{EE}(C_{21}^{EH})^*\right] \Longrightarrow \left|C_{11}^{EE}\right| = \left|C_{21}^{EH}\right| = 0$$

Hence, one has:

$$C_{21}^{EH} = 0 \Longrightarrow \begin{cases} C_{11}^{EE} = 0 \Longrightarrow C_{11}^{HH} = C_{11}^{EH} = C_{11}^{HE} = 0 \\ C_{21}^{HH} = C_{21}^{EE} \end{cases}$$

Also from the unitary property of the matrix, one has:

$$\left|C_{11}^{EE}\right|^2 + \left|C_{11}^{HE}\right|^2 + \left|C_{21}^{EE}\right|^2 + \left|C_{21}^{HE}\right|^2 = 1$$

Again, substituting in this expression the various equivalences obtained above, one finds:

$$\left|C_{21}^{EE}\right| = 1$$

In summary, one has:

$$C_{11}^{EH} = C_{11}^{HE} = C_{11}^{EE} = C_{11}^{HH} = C_{21}^{EH} = C_{21}^{HE} = 0$$

$$C_{21}^{EE} = C_{21}^{HH} \text{ with } \left|C_{21}^{EE}\right| = \left|C_{21}^{HH}\right| = 1$$

One notes that since:

$$C_{11}^{EH} = C_{11}^{HE} = C_{21}^{EH} = C_{21}^{HE} = 0$$

then in particular:

$$C_{uv}^{pq}(\theta^s, \phi^s = \chi + m\pi | \theta^i, \phi^i = \chi + m\pi) = 0 \text{ for } p \neq q \text{ and } m = 0, \pm 1, \pm 2, \ldots.$$

which is a statement of the principle of reflection symmetry about the plane $y = tan(\chi)x$.

One notes that the phases of the scattering coefficients C_{21}^{EE} and C_{21}^{HH} are yet undetermined. This means that a purely reactive anisotropic surface like a metallic inductive mesh or grid is still not ruled out, as it is befitting the desired operation. This situation is consistent with the fact that only the 2-fold rotational symmetry

rather than the ∞-fold rotational symmetry was invoked in the above development. This situation is also consistent with the fact that the slab thickness was not prescribed, and thus, the phase shift incurred by the propagation delay through the slab remains necessarily undetermined. In order to identify specifically the structure as a free space slab of thickness d, one needs also to specify:

$$(E_o^s)_u^p = e^{-jk_z d}(E_o^i)_v^p \quad \text{for} \quad u \neq v \Longrightarrow C_{21}^{EE} = e^{-jk_z d} \Longrightarrow C_{21}^{HH} = e^{-jk_z d}$$

The same analysis can be repeated for the other cases of v. Finally, one obtains the voltage scattering matrix of the free space slab of thickness d as:

$$C(E,H) = e^{-jk_z d} \begin{pmatrix} 0 & 0 & 1 & 0 \\ 0 & 0 & 0 & 1 \\ 1 & 0 & 0 & 0 \\ 0 & 1 & 0 & 0 \end{pmatrix}$$

It is seen readily from equation (2.1) that $C(E,H) = S(E,H)$.

E.0.3 Artificially Soft or Hard Planar Surfaces

The operation consisting in reflecting an incident CP plane wave into a CP plane wave whose handedness is the same as that of the incident wave, is phrased as:

$$\begin{cases} \text{If } (E_o^i)_v^H = \pm j(E_o^i)_v^E \text{ for } (E_o^i)_u^l = 0, u \neq v, l = \{E, H\} \\ \text{then} \begin{cases} (E_o^s)_v^H = \pm j(E_o^s)_v^E & v = \{1,2,3,4\} \\ (E_o^s)_u^H = (E_o^s)_u^E = 0 & u\text{-ness} \neq v\text{-ness} \end{cases} \end{cases}$$

Say, $v = 1$. One obtains:

$$\begin{cases} (E_o^s)_1^E &= C_{11}^{EE}(E_o^i)_1^E + C_{11}^{EH}(E_o^i)_1^H \\ (E_o^s)_1^H &= C_{11}^{HE}(E_o^i)_1^E + C_{11}^{HH}(E_o^i)_1^H \end{cases}$$

$$(E_o^i)_1^H = \pm j(E_o^i)_1^E \Longrightarrow \begin{cases} (E_o^s)_1^E = \left(C_{11}^{EE} \pm jC_{11}^{EH}\right)(E_o^i)_1^E \\ (E_o^s)_1^H = \left(C_{11}^{HE} \pm jC_{11}^{HH}\right)(E_o^i)_1^E \end{cases}$$

$$\begin{aligned} (E_o^s)_1^H = \pm j(E_o^s)_1^E &\Longrightarrow \left(C_{11}^{HE} \pm jC_{11}^{HH}\right) = \pm j\left(C_{11}^{EE} \pm jC_{11}^{EH}\right) \\ &\Longrightarrow \left(C_{11}^{HE} + C_{11}^{EH}\right) = \pm j\left(C_{11}^{EE} - C_{11}^{HH}\right) \end{aligned}$$

$$\begin{cases} (E_o^s)_2^E &= C_{21}^{EE}(E_o^i)_1^E + C_{21}^{EH}(E_o^i)_1^H \\ (E_o^s)_2^H &= C_{21}^{HE}(E_o^i)_1^E + C_{21}^{HH}(E_o^i)_1^H \end{cases}$$

$$(E_o^i)_1^H = \pm j(E_o^i)_1^E \Longrightarrow \begin{cases} (E_o^s)_2^E = \left(C_{21}^{EE} \pm jC_{21}^{EH}\right)(E_o^i)_1^E \\ (E_o^s)_2^H = \left(C_{21}^{HE} \pm jC_{21}^{HH}\right)(E_o^i)_1^E \end{cases}$$

$$\begin{cases} (E_o^s)_2^E = 0 \Longrightarrow C_{21}^{EE} = \mp jC_{21}^{EH} \\ (E_o^s)_2^H = 0 \Longrightarrow C_{21}^{HE} = \mp jC_{21}^{HH} \end{cases}$$

From the combination of reciprocity, 2-fold rotational symmetry and Snell's law of reflection, with $u = v = 1, p = E, q = H$, one obtains:

$$C_{11}^{EH} = -C_{11}^{HE}$$

Consequently:

$$\underbrace{\left(C_{11}^{HE} + C_{11}^{EH}\right)}_{0} = \pm j\left(C_{11}^{EE} - C_{11}^{HH}\right) \Longrightarrow C_{11}^{HH} = C_{11}^{EE}$$

From above, one knows:

$$C_{21}^{EE}(\theta^s, \phi^s|\theta^i, \phi^i) = \mp j C_{21}^{EH}(\theta^s, \phi^s|\theta^i, \phi^i)$$

From reciprocity and reflection symmetry about the $z = 0$ plane with $u = 2, v = 1, p = E, q = H$, one has:

$$C_{21}^{EH}(\theta^s, \phi^s|\theta^i, \phi^i) = C_{21}^{HE}(\theta^i, \pi + \phi^i|\theta^s, \pi + \phi^s)$$

From above, one also knows:

$$C_{21}^{HE}(\theta^i, \pi + \phi^i|\theta^s, \pi + \phi^s) = \mp j C_{21}^{HH}(\theta^i, \pi + \phi^i|\theta^s, \pi + \phi^s)$$

From reciprocity and reflection symmetry about the $z = 0$ plane with $u = 2, v = 1, p = q = H$, one has:

$$C_{21}^{HH}(\theta^i, \pi + \phi^i|\theta^s, \pi + \phi^s) = C_{21}^{HH}(\theta^s, 2\pi + \phi^s|\theta^i, 2\pi + \phi^i)$$

From the 2π periodicity of the angle ϕ one obtains:

$$C_{21}^{HH}(\theta^s, 2\pi + \phi^s|\theta^i, 2\pi + \phi^i) = C_{21}^{HH}(\theta^s, \phi^s|\theta^i, \phi^i)$$

Consequently, pulling everything together, one obtains:

$$C_{21}^{EE}(\theta^s, \phi^s|\theta^i, \phi^i) = -C_{21}^{HH}(\theta^s, \phi^s|\theta^i, \phi^i)$$

Therefore:

$$C_{21}^{EE} = -C_{21}^{HH}$$

Hence:

$$\left\{ \begin{array}{rcl} C_{21}^{EH} & = & \pm j C_{21}^{EE} \\ C_{21}^{EE} & = & -C_{21}^{HH} \\ C_{21}^{HH} & = & \pm j C_{21}^{HE} \end{array} \right\} \Longrightarrow C_{21}^{EH} = C_{21}^{HE}$$

As seen previously, this result is consistent with the structure obeying the combination of reciprocity, 2-fold rotational symmetry, longitudinal reflection symmetry and Snell's law of refraction with $\theta^t = \theta^i$.

Now, from the unitary property of the matrix, one has:

$$C_{11}^{EE}(C_{11}^{EH})^* + C_{11}^{HE}(C_{11}^{HH})^* + C_{21}^{EE}(C_{21}^{EH})^* + C_{21}^{HE}(C_{21}^{HH})^* = 0$$

Substituting in this expression the various equivalences obtained above, one finds:

$$\underbrace{C_{11}^{EE}(C_{11}^{EH})^* - C_{11}^{EH}(C_{11}^{EE})^*}_{j2\ Imag\left[C_{11}^{EE}(C_{11}^{EH})^*\right]} \mp j \underbrace{\left(\left|C_{21}^{EH}\right|^2 + \left|C_{21}^{HH}\right|^2\right)}_{2\left|C_{21}^{EE}\right|^2} = 0$$

$$\Longrightarrow Imag\left[C_{11}^{EE}(C_{11}^{EH})^*\right] = \pm\left|C_{21}^{EE}\right|^2$$

At this point, many different designs are possible: one being a corrugated metallic plane or a strip grating above a grounded substrate [45, 46], another one being an array of dipole turnstiles with $\lambda/4$ front-to-back thickness [19]. Taking the first design for expediency, the structure incorporates an infinite ground plane and thus, one has $C_{uv}^{pq} = 0$ for $u \neq v$. Hence, there obtains:

$$C_{21}^{EE} = 0 \Longrightarrow \{C_{11}^{EE} = C_{11}^{HH} = 0 \text{ or } C_{11}^{EH} = C_{11}^{HE} = 0\}$$

This author takes the second possibility since the first one seems unreasonable.

Also from the unitary property of the matrix, one has:

$$\left|C_{11}^{EE}\right|^2 + \left|C_{11}^{HE}\right|^2 + \left|C_{21}^{EE}\right|^2 + \left|C_{21}^{HE}\right|^2 = 1$$

Substituting in this expression the various equivalences obtained above, one finds:

$$\left|C_{11}^{EE}\right| = 1$$

In summary, one has:

$$C_{11}^{EH} = C_{11}^{HE} = C_{21}^{EE} = C_{21}^{EH} = C_{21}^{HE} = C_{21}^{HH} = 0$$

$$C_{11}^{EE} = C_{11}^{HH} \text{ with } \left|C_{11}^{EE}\right| = \left|C_{11}^{HH}\right| = 1$$

One notes that since:

$$C_{11}^{EH} = C_{11}^{HE} = C_{21}^{EH} = C_{21}^{HE} = 0$$

then in particular:

$$C_{uv}^{pq}(\theta^s, \phi^s = \chi + m\pi | \theta^i, \phi^i = \chi + m\pi) = 0 \text{ for } p \neq q \text{ and } m = 0, \pm 1, \pm 2, \ldots.$$

which states the principle of reflection symmetry about the plane $y = tan(\chi)x$.

One notes that the phases of the scattering coefficients C_{vv}^{pp} are yet undetermined. This means that a purely reactive anisotropic surface like a corrugated metallic plane or a strip grating above a grounded substrate [45, 46] is possible.

The same analysis can be repeated for the other cases of v where, here, the operation of a solid PEC reflector was assumed, owing to the presence of the infinite ground plane backing the structure. Finally, one obtains the voltage scattering matrix of the artificially soft or hard surface as:

$$C(E,H) = \begin{pmatrix} A & 0 & 0 & 0 \\ 0 & A & 0 & 0 \\ 0 & 0 & 1 & 0 \\ 0 & 0 & 0 & -1 \end{pmatrix} \text{ where } A = e^{j\alpha} \text{ and } \alpha \text{ is real valued.}$$

It is seen readily from equation (2.1) that $C(E,H) = S(E,H)$. Again, it may seem somewhat strange that the development invokes reflection symmetry about the $z = 0$ plane when the surface incorporates an infinite ground plane, as the two regions are completely isolated from one another. However again, the longitudinal reflection symmetry was invoked only for C_{21}^{pq} and since one found afterwards that $C_{21}^{pq} = 0$, then the use of the longitudinal reflection symmetry was, in effect, of no consequence and there is no inconsistency incurred by invoking it.

E.0.4 Recall

From Appendix C, it is known that an arbitrarily polarized uniform plane wave characterized as:

$$\vec{E}_o = E_o \left(sin(\varsigma)\hat{\theta} + cos(\varsigma)\hat{\phi} \right)$$

projects onto a plane such that one has:

$$tan(\xi) = cos(\theta)tan(\varsigma)$$

where ξ and ς are respectively the angle between $\hat{\phi}$ and $\vec{E}_t$, and the angle between $\hat{\phi}$ and $\vec{E}_o$ (See Figure C.1). One obtains:

$$\left\{ \begin{array}{rcl} (E_o)_v^E & = & E_o sin(\varsigma) \\ (E_o)_v^H & = & E_o cos(\varsigma) \end{array} \right\} \Longrightarrow \frac{(E_o)_v^E}{(E_o)_v^H} = tan(\varsigma) = \frac{tan(\xi)}{cos(\theta)}$$

When it is needed to refer to a fixed direction corresponding to the angle $\phi = \phi_g$ in the projection plane, e.g. the direction of the wires of a grid, one uses:

$$\xi = \phi + 90^o - \phi_g$$

Since the notation of Appendix 1 leads to $\phi^i = \phi^r = \phi^t$, thus $\xi^i = \xi^r = \xi^t$. In other words, there is no need to specify the nature of the wave as far as ξ is concerned. From Appendix C, one recalls also that although two directions are orthogonal in the projection plane, e.g. $\phi = \phi_g$ and $\phi = \phi_g \pm 90^o$, their corresponding vectors in the plane whose normal lies in the direction of the propagation vector are not orthogonal in general.

E.0.5 Ideal Linear Polarizer

The operation consisting in the LP polarizer reflecting an incident LP plane wave when $\vec{E}_t$ is parallel to the direction of the wires of the grid given by $\phi = \phi_g$, and in being transparent when $\vec{E}_t$ is perpendicular to that same direction, is depicted in Figure E.1 and is phrased as:

$$\begin{cases} \text{If } \frac{(E_o^i)_v^E}{(E_o^i)_v^H} = tan\left(\varsigma_{\|}^i + n\pi\right) = \frac{tan(\xi_{\|})}{cos(\theta^i)} \text{ for } (E_o^i)_u^l = 0, u \neq v, l = \{E, H\} \\ \text{then} \begin{cases} \frac{(E_o^s)_v^E}{(E_o^s)_v^H} = tan\left(\varsigma_{\|}^s + n\pi\right) = \frac{tan(\xi_{\|})}{cos(\theta^s)} & v = \{1,2,3,4\} \\ \left(E_o^s\right)_u^H = \left(E_o^s\right)_u^E = 0 & u\text{-ness} \neq v\text{-ness} \end{cases} \\ \text{If } \frac{(E_o^i)_v^E}{(E_o^i)_v^H} = tan\left(\varsigma_{\perp}^i + n\pi\right) = \frac{tan(\xi_{\perp})}{cos(\theta^i)} \text{ for } (E_o^i)_u^l = 0, u \neq v, l = \{E, H\} \\ \text{then} \begin{cases} \left(E_o^s\right)_v^H = \left(E_o^s\right)_v^E = 0 & v = \{1,2,3,4\} \\ \frac{(E_o^s)_u^E}{(E_o^s)_u^H} = tan\left(\varsigma_{\perp}^s + n\pi\right) = \frac{tan(\xi_{\perp})}{cos(\theta^s)} & u\text{-ness} \neq v\text{-ness} \end{cases} \end{cases}$$

$$\text{where } \xi_{\|} = \phi^i + 90^o - \phi_g \quad \text{and} \quad \xi_{\perp} = \xi_{\|} \pm 90^o$$

Say, $v = 1$. One obtains:

$$\begin{cases} (E_o^s)_1^E &= C_{11}^{EE}(E_o^i)_1^E + C_{11}^{EH}(E_o^i)_1^H \\ (E_o^s)_1^H &= C_{11}^{HE}(E_o^i)_1^E + C_{11}^{HH}(E_o^i)_1^H \end{cases}$$

$$(E_o^i)_1^H = \frac{cos(\theta^i)}{tan(\xi_{\|})}(E_o^i)_1^E \Longrightarrow \begin{cases} (E_o^s)_1^E = \left(C_{11}^{EE} + \frac{cos(\theta^i)}{tan(\xi_{\|})}C_{11}^{EH}\right)(E_o^i)_1^E \\ (E_o^s)_1^H = \left(C_{11}^{HE} + \frac{cos(\theta^i)}{tan(\xi_{\|})}C_{11}^{HH}\right)(E_o^i)_1^E \end{cases}$$

$$(E_o^s)_1^H = \frac{cos(\theta^s)}{tan(\xi_{\|})}(E_o^s)_1^E \implies \left(C_{11}^{HE} + \frac{cos(\theta^i)}{tan(\xi_{\|})}C_{11}^{HH}\right) = \frac{cos(\theta^s)}{tan(\xi_{\|})}\left(C_{11}^{EE} + \frac{cos(\theta^i)}{tan(\xi_{\|})}C_{11}^{EH}\right)$$

$$\theta^s = \pi - \theta^i \Longrightarrow C_{11}^{HE} = -\left(\frac{cos(\theta^i)}{tan(\xi_{\|})}\right)^2 C_{11}^{EH} - \left(\frac{cos(\theta^i)}{tan(\xi_{\|})}\right)\left(C_{11}^{EE} + C_{11}^{HH}\right) \qquad \text{(E.1)}$$

$$\begin{cases} (E_o^s)_2^E &= C_{21}^{EE}(E_o^i)_1^E + C_{21}^{EH}(E_o^i)_1^H \\ (E_o^s)_2^H &= C_{21}^{HE}(E_o^i)_1^E + C_{21}^{HH}(E_o^i)_1^H \end{cases}$$

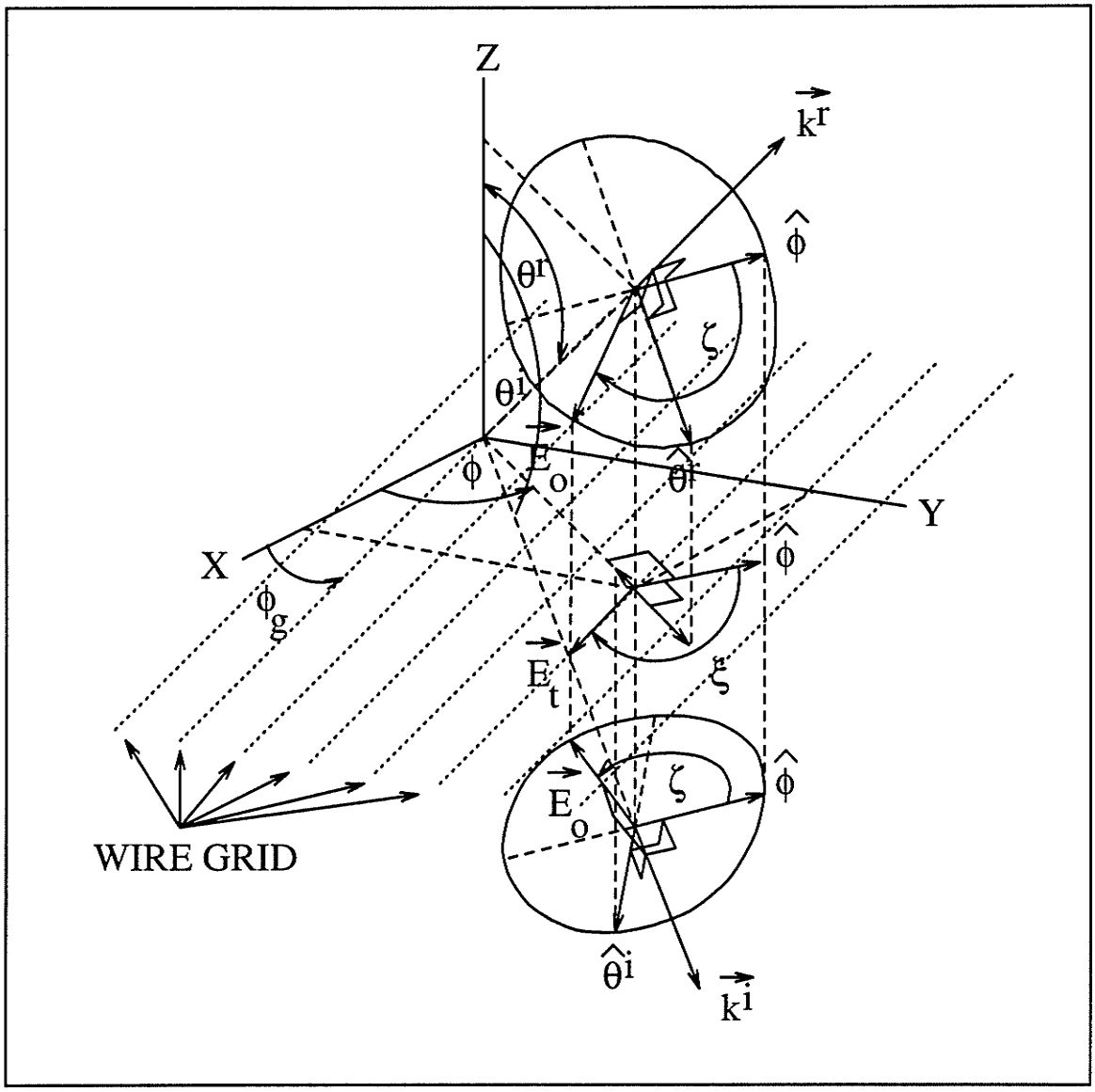

Figure E.1: Depiction of the operation of an ideal wire grid LP polarizer.

$$(E_o^i)_1^H = \frac{cos(\theta^i)}{tan(\xi_{\|})}(E_o^i)_1^E \Longrightarrow \begin{cases} (E_o^s)_2^E = \left(C_{21}^{EE} + \frac{cos(\theta^i)}{tan(\xi_{\|})}C_{21}^{EH}\right)(E_o^i)_1^E \\ (E_o^s)_2^H = \left(C_{21}^{HE} + \frac{cos(\theta^i)}{tan(\xi_{\|})}C_{21}^{HH}\right)(E_o^i)_1^E \end{cases}$$

$$(E_o^s)_2^E = 0 \Longrightarrow C_{21}^{EH} = -\frac{tan(\xi_{\|})}{cos(\theta^i)}C_{21}^{EE} \tag{E.2}$$

$$(E_o^s)_2^H = 0 \Longrightarrow C_{21}^{HH} = -\frac{tan(\xi_{\|})}{cos(\theta^i)}C_{21}^{HE} \tag{E.3}$$

Similarly, one has:

$$\begin{cases} (E_o^s)_1^E &= C_{11}^{EE}(E_o^i)_1^E + C_{11}^{EH}(E_o^i)_1^H \\ (E_o^s)_1^H &= C_{11}^{HE}(E_o^i)_1^E + C_{11}^{HH}(E_o^i)_1^H \end{cases}$$

$$(E_o^i)_1^H = \frac{cos(\theta^i)}{tan(\xi_{\perp})}(E_o^i)_1^E \Longrightarrow \begin{cases} (E_o^s)_1^E = \left(C_{11}^{EE} + \frac{cos(\theta^i)}{tan(\xi_{\perp})}C_{11}^{EH}\right)(E_o^i)_1^E \\ (E_o^s)_1^H = \left(C_{11}^{HE} + \frac{cos(\theta^i)}{tan(\xi_{\perp})}C_{11}^{HH}\right)(E_o^i)_1^E \end{cases}$$

$$(E_o^s)_1^E = 0 \Longrightarrow C_{11}^{EH} = -\frac{tan(\xi_{\perp})}{cos(\theta^i)}C_{11}^{EE} \tag{E.4}$$

$$(E_o^s)_1^H = 0 \Longrightarrow C_{11}^{HH} = -\frac{tan(\xi_{\perp})}{cos(\theta^i)}C_{11}^{HE} \tag{E.5}$$

$$\begin{cases} (E_o^s)_2^E &= C_{21}^{EE}(E_o^i)_1^E + C_{21}^{EH}(E_o^i)_1^H \\ (E_o^s)_2^H &= C_{21}^{HE}(E_o^i)_1^E + C_{21}^{HH}(E_o^i)_1^H \end{cases}$$

$$(E_o^i)_1^H = \frac{cos(\theta^i)}{tan(\xi_{\perp})}(E_o^i)_1^E \Longrightarrow \begin{cases} (E_o^s)_2^E = \left(C_{21}^{EE} + \frac{cos(\theta^i)}{tan(\xi_{\perp})}C_{21}^{EH}\right)(E_o^i)_1^E \\ (E_o^s)_2^H = \left(C_{21}^{HE} + \frac{cos(\theta^i)}{tan(\xi_{\perp})}C_{21}^{HH}\right)(E_o^i)_1^E \end{cases}$$

$$(E_o^s)_2^H = \frac{cos(\theta^s)}{tan(\xi_{\perp})}(E_o^s)_2^E \implies \left(C_{21}^{HE} + \frac{cos(\theta^i)}{tan(\xi_{\perp})}C_{21}^{HH}\right) = \frac{cos(\theta^s)}{tan(\xi_{\perp})}\left(C_{21}^{EE} + \frac{cos(\theta^i)}{tan(\xi_{\perp})}C_{21}^{EH}\right)$$

$$\theta^s = \theta^i \Longrightarrow C_{21}^{HE} = \left(\frac{cos(\theta^i)}{tan(\xi_{\perp})}\right)^2 C_{21}^{EH} + \left(\frac{cos(\theta^i)}{tan(\xi_{\perp})}\right)\left(C_{21}^{EE} - C_{21}^{HH}\right) \tag{E.6}$$

Substituting equations (E.4) and (E.5) into equation (E.1), one finds:

$$C_{11}^{HE} = -\frac{cos(\theta^i)}{tan(\xi_{\|})}C_{11}^{EE} = -\frac{cos(\theta^i)}{tan(\xi_{\perp})}C_{11}^{HH} \Longrightarrow C_{11}^{HH} = \frac{tan(\xi_{\perp})}{tan(\xi_{\|})}C_{11}^{EE} \tag{E.7}$$

Substituting equations (E.2) and (E.3) into equation (E.6), one finds:

$$C_{21}^{HE} = \frac{cos(\theta^i)}{tan(\xi_\perp)} C_{21}^{EE} = -\frac{cos(\theta^i)}{tan(\xi_{||})} C_{21}^{HH} \Longrightarrow C_{21}^{HH} = -\frac{tan(\xi_{||})}{tan(\xi_\perp)} C_{21}^{EE} \tag{E.8}$$

Now, from the unitary property of the matrix, one has:

$$C_{11}^{EE}(C_{11}^{EH})^* + C_{11}^{HE}(C_{11}^{HH})^* + C_{21}^{EE}(C_{21}^{EH})^* + C_{21}^{HE}(C_{21}^{HH})^* = 0$$

Substituting in this expression the various equivalences obtained above, one finds:

$$\left|C_{21}^{EE}\right| = \sqrt{-\left(\frac{tan(\xi_\perp)}{tan(\xi_{||})}\right)\left(\frac{1+\left(\frac{cos(\theta^i)}{tan(\xi_{||})}\right)^2}{1+\left(\frac{cos(\theta^i)}{tan(\xi_\perp)}\right)^2}\right)}\left|C_{11}^{EE}\right| \tag{E.9}$$

Also from the unitary property of the matrix, one has:

$$\left|C_{11}^{EE}\right|^2 + \left|C_{11}^{HE}\right|^2 + \left|C_{21}^{EE}\right|^2 + \left|C_{21}^{HE}\right|^2 = 1$$

Substituting in these expressions the various equivalences obtained above, one finds:

$$\left|C_{11}^{EE}\right| = \frac{1}{\sqrt{1+\left(\frac{cos(\theta^i)}{tan(\xi_{||})}\right)^2}} \frac{1}{\sqrt{1-\frac{tan(\xi_\perp)}{tan(\xi_{||})}}} \tag{E.10}$$

Also from the unitary property of the matrix, one has:

$$\left|C_{11}^{EH}\right|^2 + \left|C_{11}^{HH}\right|^2 + \left|C_{21}^{EH}\right|^2 + \left|C_{21}^{HH}\right|^2 = 1$$

Substituting in these expressions the various equivalences obtained above, one finds:

$$\left|C_{11}^{EE}\right| = \frac{1}{\sqrt{\left(\frac{tan(\xi_{||})}{cos(\theta^i)}\right)^2 + 1}} \frac{1}{\sqrt{\frac{tan(\xi_\perp)}{tan(\xi_{||})}\left(\frac{tan(\xi_\perp)}{tan(\xi_{||})} - 1\right)}} \tag{E.11}$$

From equations (E.10) and (E.11), one obtains:

$$cos^2(\theta^i) = -tan(\xi_{||})tan(\xi_\perp)$$

Now, one has:

$$\xi_\perp = \xi_{||} \pm 90^o \Longrightarrow tan(\xi_{||})tan(\xi_\perp) = -1 \Longrightarrow cos(\theta^i) = \pm 1$$

Therefore, one discovers that an ideal LP polarizer with the operation prescribed herein is possible only at normal incidence, regardless of the actual physical implementation! Although the physical LP polarizer realized with a wire grid cannot be ideal at off-normal incidence, the polarization of the transmitted wave is nevertheless always linear, as a result of the electric field component parallel to the wires being reflected by the grid.

Employing $cos^2(\theta^i) = 1$ in equation (E.10), one obtains:

$$\left|C_{11}^{EE}\right| = sin^2(\xi_{||}) = \frac{1}{2}(1 - cos(2\xi_{||}))$$

Employing $cos^2(\theta^i) = 1$ in equation (E.9), one obtains:

$$\left|C_{21}^{EE}\right| = cos^2(\xi_{||}) = \frac{1}{2}(1 + cos(2\xi_{||}))$$

From these last two expressions, one obtains the expressions for the remaining terms with $cos(\theta^i) = -1$ as:

$$\left\{\begin{array}{lcll} C_{11}^{EH} & = & -\frac{tan(\xi_\perp)}{cos(\theta^i)}C_{11}^{EE} & = -\frac{1}{2}sin(2\xi_{||})e^{j\alpha} \\ C_{11}^{HE} & = & -\frac{cos(\theta^i)}{tan(\xi_{||})}C_{11}^{EE} & = +\frac{1}{2}sin(2\xi_{||})e^{j\alpha} \\ C_{11}^{HH} & = & +\frac{tan(\xi_\perp)}{tan(\xi_{||})}C_{11}^{EE} & = -\frac{1}{2}(1 + cos(2\xi_{||}))e^{j\alpha} \\ C_{21}^{EH} & = & -\frac{tan(\xi_{||})}{cos(\theta^i)}C_{21}^{EE} & = +\frac{1}{2}sin(2\xi_{||})e^{j\beta} \\ C_{21}^{HE} & = & +\frac{cos(\theta^i)}{tan(\xi_\perp)}C_{21}^{EE} & = +\frac{1}{2}sin(2\xi_{||})e^{j\beta} \\ C_{21}^{HH} & = & -\frac{tan(\xi_{||})}{tan(\xi_\perp)}C_{21}^{EE} & = +\frac{1}{2}(1 - cos(2\xi_{||}))e^{j\beta} \end{array}\right.$$

where α and β are real valued. One observes that, as expected, all scattering coefficients remain unchanged upon replacing $\xi_{||}$ by $\xi_{||} + n\pi$ with $n = 0, \pm 1, \pm 2, \ldots$.

One does similarly for the other cases of $v = 2, 3, 4$, being mindful of the sign change brought about by $cos(\theta^i)$ when $v = \{2, 4\}$. One obtains the voltage scattering matrix for the LP polarizer as:

$$C(E,H) = \frac{1}{2}\begin{pmatrix} (1-P)e^{j\alpha} & -Qe^{j\alpha} & (1+P)e^{j\beta} & -Qe^{j\beta} \\ Qe^{j\alpha} & -(1+P)e^{j\alpha} & -Qe^{j\beta} & (1-P)e^{j\beta} \\ (1+P)e^{j\beta} & Qe^{j\beta} & (1-P)e^{j\alpha} & Qe^{j\alpha} \\ Qe^{j\beta} & (1-P)e^{j\beta} & -Qe^{j\alpha} & -(1+P)e^{j\alpha} \end{pmatrix}$$

$$\text{where: } \begin{cases} P = cos(2(\phi^i + 90^o - \phi_g)) \\ Q = sin(2(\phi^i + 90^o - \phi_g)) \end{cases}$$

It is noted again that the above results are valid only at normal incidence.

Since $C_{vv}^{pq} = -C_{vv}^{qp}$ with $p \neq q$, the structure has the 2-fold rotational symmetry. Since $C_{uv}^{pq}(\theta^s, \phi^s = (\phi_g + n90^o) + m180^o | \theta^i, \phi^i = (\phi_g + n90^o) + m180^o) = 0$ for $p \neq q$, $n = 0, \pm 1, \pm 2, \ldots$ and $m = 0, \pm 1, \pm 2, \ldots$, the structure has the reflection symmetry about the plane $y = tan(\phi_g + n90^o)x$. Since $C_{uv}^{pq} = C_{uv}^{qp}$ with $p \neq q$ and $u \neq v$, the structure may possibly have the longitudinal reflection symmetry. All these characteristics befit perfectly the well known wire grid LP polarizer.

E.0.6 Ideal Circular Polarizers

There are many ways to phrase the operation[1] of a CP polarizer according to Figure 3.1.

For $\theta^i > 90^o$, i.e. for v = odd-numbered, the operation of the ideal CP polarizer with the fast axis oriented as in Figure 3.1 can be described in two ways:

1. an incident LP plane wave oriented as shown in case a) with $\vec{E}_t^i$ parallel to a prescribed direction given by $\phi = \phi_L$ is transformed into a LHCP plane wave, whereas an incident LP plane wave oriented as shown in case c) with $\vec{E}_t^i$ perpendicular to that same prescribed direction is transformed into a RHCP plane wave.

2. an incident LHCP plane wave is transformed into a LP plane wave oriented as shown in case e) with $\vec{E}_t^t$ perpendicular to the prescribed direction given by $\phi = \phi_L$, and an incident RHCP plane wave is transformed into a LP plane wave oriented as shown in case g) with $\vec{E}_t^t$ parallel to that same prescribed direction.

Each way leads to a different set of GSM scattering coefficients C_{u1}^{pq}. By equating these two sets so that the CP polarizer be made to correspond to both ways simultaneously, one finds that all the cross-polarized coefficients reduce to zero.

[1]It must be pointed out that this operation is based on the wave propagating at normal incidence through a retardation plate. The operation for a retardation plate realized from a uniaxial anisotropic slab illuminated with a plane wave of arbitrary incidence and arbitrary polarization would be different. One would require to invoke the existence of two different rays, the ordinary and the extraordinary rays, with each ray corresponding to a different polarization and travelling at a different velocity and in a different direction in the uniaxial slab. Thus in general, the output wave would be elliptically polarized. The case of normal incidence represents a degenerate case because the two rays travel then in the same direction. In this case, the ray having its polarization in the direction of the fast axis travels at one velocity while the ray having its polarization in the direction of the slow axis travels at another velocity. The velocity difference between the two rays accounts for the operation of the retardation plate and the output wave is circularly polarized if the retardation plate has the appropriate thickness.

In contrast, the retardation provided by the phase shift incurred by propagation through a wire grid does not require to invoke the existence of two different rays. Nevertheless, the operation prescribed here for the ideal CP polarizer might still be physically impossible to realize because the operation is phrased from a phenomenological point of view rather than a physical point of view. Indeed, it will be found on the next pages that the above prescribed operation is possible only at normal incidence regardless of how this operation is physically realized.

Similarly, for $\theta^i < 90^o$, i.e. for v = even-numbered, the operation of the ideal CP polarizer with the fast axis oriented as in Figure 3.1 can be described in two ways which correspond, respectively, to the reciprocal operation of the two ways described just above:

1. an incident LHCP plane wave is transformed into a LP plane wave oriented as shown in case b) with $\vec{E}_t^t$ parallel to the prescribed direction given by $\phi = \phi_L$, and an incident RHCP plane wave is transformed into a LP plane wave oriented as shown in case d) with $\vec{E}_t^t$ perpendicular to that same prescribed direction.

2. an incident LP plane wave oriented as shown in case f) with $\vec{E}_t^i$ perpendicular to a prescribed direction given by $\phi = \phi_L$ is transformed into a LHCP plane wave, whereas an incident LP plane wave oriented as shown in case h) with $\vec{E}_t^i$ parallel to that same prescribed direction is transformed into a RHCP plane wave.

Again, each way leads to a different set of GSM scattering coefficients C_{u2}^{pq}. By equating these two sets so that the CP polarizer be made to correspond to both ways simultaneously, one finds that all the cross-polarized coefficients reduce to zero.

The following development deals with obtaining the GSM coefficients corresponding to the four ways described above. The order of presentation follows also that above. The operation of the ideal CP polarizer corresponding to the first way is phrased as:

$$
\begin{cases}
\text{If } \dfrac{(E_o^i)_v^E}{(E_o^i)_v^H} = tan\left(\varsigma_{\|} + n\pi\right) = \dfrac{tan(\xi_{\|})}{cos(\theta^i)} \text{ for } (E_o^i)_u^l = 0, u \neq v, l = \{E, H\} \\
\text{then} \begin{cases} \left(E_o^s\right)_v^H = \left(E_o^s\right)_v^E = 0 & v = \{1,3\} \\ \left(E_o^s\right)_u^H = +j\left(E_o^s\right)_u^E & u\text{-ness} \neq v\text{-ness} \end{cases} \\
\text{If } \dfrac{(E_o^i)_v^E}{(E_o^i)_v^H} = tan\left(\varsigma_{\perp} + n\pi\right) = \dfrac{tan(\xi_{\perp})}{cos(\theta^i)} \text{ for } (E_o^i)_u^l = 0, u \neq v, l = \{E, H\} \\
\text{then} \begin{cases} \left(E_o^s\right)_v^H = \left(E_o^s\right)_v^E = 0 & v = \{1,3\} \\ \left(E_o^s\right)_u^H = -j\left(E_o^s\right)_u^E & u\text{-ness} \neq v\text{-ness} \end{cases}
\end{cases}
$$

$$
\text{where } \xi_{\|} = \phi^i + 90^o - \phi_L \quad \text{and} \quad \xi_{\perp} = \xi_{\|} \pm 90^o
$$

For $v = 1$, one obtains:

$$
\begin{cases}
(E_o^s)_1^E &= C_{11}^{EE}(E_o^i)_1^E + C_{11}^{EH}(E_o^i)_1^H \\
(E_o^s)_1^H &= C_{11}^{HE}(E_o^i)_1^E + C_{11}^{HH}(E_o^i)_1^H
\end{cases}
$$

$$
(E_o^i)_1^H = \frac{cos(\theta^i)}{tan(\xi_{\|})}(E_o^i)_1^E \Longrightarrow \begin{cases} (E_o^s)_1^E = \left(C_{11}^{EE} + \frac{cos(\theta^i)}{tan(\xi_{\|})}C_{11}^{EH}\right)(E_o^i)_1^E \\ (E_o^s)_1^H = \left(C_{11}^{HE} + \frac{cos(\theta^i)}{tan(\xi_{\|})}C_{11}^{HH}\right)(E_o^i)_1^E \end{cases}
$$

$$
\begin{aligned}
(E_o^s)_1^E = 0 &\implies C_{11}^{EE} = -\tfrac{cos(\theta^i)}{tan(\xi_{\|})}C_{11}^{EH} \\
(E_o^s)_1^H = 0 &\implies C_{11}^{HE} = -\tfrac{cos(\theta^i)}{tan(\xi_{\|})}C_{11}^{HH}
\end{aligned}
$$

$$
\begin{cases}
(E_o^s)_2^E &= C_{21}^{EE}(E_o^i)_1^E + C_{21}^{EH}(E_o^i)_1^H \\
(E_o^s)_2^H &= C_{21}^{HE}(E_o^i)_1^E + C_{21}^{HH}(E_o^i)_1^H
\end{cases}
$$

$$
(E_o^i)_1^H = \frac{cos(\theta^i)}{tan(\xi_{\|})}(E_o^i)_1^E \Longrightarrow \begin{cases} (E_o^s)_2^E = \left(C_{21}^{EE} + \frac{cos(\theta^i)}{tan(\xi_{\|})}C_{21}^{EH}\right)(E_o^i)_1^E \\ (E_o^s)_2^H = \left(C_{21}^{HE} + \frac{cos(\theta^i)}{tan(\xi_{\|})}C_{21}^{HH}\right)(E_o^i)_1^E \end{cases}
$$

$$
(E_o^s)_2^H = +j(E_o^s)_2^E \implies \left(C_{21}^{HE} + \tfrac{cos(\theta^i)}{tan(\xi_{\|})}C_{21}^{HH}\right) = +j\left(C_{21}^{EE} + \tfrac{cos(\theta^i)}{tan(\xi_{\|})}C_{21}^{EH}\right)
$$

Similarly, one has:

$$
\begin{cases}
(E_o^s)_1^E &= C_{11}^{EE}(E_o^i)_1^E + C_{11}^{EH}(E_o^i)_1^H \\
(E_o^s)_1^H &= C_{11}^{HE}(E_o^i)_1^E + C_{11}^{HH}(E_o^i)_1^H
\end{cases}
$$

$$(E_o^i)_1^H = \frac{cos(\theta^i)}{tan(\xi_\perp)}(E_o^i)_1^E \Longrightarrow \begin{cases} (E_o^s)_1^E = \left(C_{11}^{EE} + \frac{cos(\theta^i)}{tan(\xi_\perp)} C_{11}^{EH}\right)(E_o^i)_1^E \\ (E_o^s)_1^H = \left(C_{11}^{HE} + \frac{cos(\theta^i)}{tan(\xi_\perp)} C_{11}^{HH}\right)(E_o^i)_1^E \end{cases}$$

$$\begin{aligned} (E_o^s)_1^E = 0 &\implies C_{11}^{EE} = -\frac{cos(\theta^i)}{tan(\xi_\perp)} C_{11}^{EH} \\ (E_o^s)_1^H = 0 &\implies C_{11}^{HE} = -\frac{cos(\theta^i)}{tan(\xi_\perp)} C_{11}^{HH} \end{aligned}$$

$$\begin{cases} (E_o^s)_2^E &= C_{21}^{EE}(E_o^i)_1^E + C_{21}^{EH}(E_o^i)_1^H \\ (E_o^s)_2^H &= C_{21}^{HE}(E_o^i)_1^E + C_{21}^{HH}(E_o^i)_1^H \end{cases}$$

$$(E_o^i)_1^H = \frac{cos(\theta^i)}{tan(\xi_\perp)}(E_o^i)_1^E \Longrightarrow \begin{cases} (E_o^s)_2^E = \left(C_{21}^{EE} + \frac{cos(\theta^i)}{tan(\xi_\perp)} C_{21}^{EH}\right)(E_o^i)_1^E \\ (E_o^s)_2^H = \left(C_{21}^{HE} + \frac{cos(\theta^i)}{tan(\xi_\perp)} C_{21}^{HH}\right)(E_o^i)_1^E \end{cases}$$

$$(E_o^s)_2^H = -j(E_o^s)_2^E \implies \left(C_{21}^{HE} + \frac{cos(\theta^i)}{tan(\xi_\perp)} C_{21}^{HH}\right) = -j\left(C_{21}^{EE} + \frac{cos(\theta^i)}{tan(\xi_\perp)} C_{21}^{EH}\right)$$

In summary, one has:

$$\begin{aligned} C_{11}^{EE} = -\frac{cos(\theta^i)}{tan(\xi_\parallel)} C_{11}^{EH} = -\frac{cos(\theta^i)}{tan(\xi_\perp)} C_{11}^{EH} \Longrightarrow C_{11}^{EH} = 0 \Longrightarrow C_{11}^{EE} = 0 \\ C_{11}^{HE} = -\frac{cos(\theta^i)}{tan(\xi_\parallel)} C_{11}^{HH} = -\frac{cos(\theta^i)}{tan(\xi_\perp)} C_{11}^{HH} \Longrightarrow C_{11}^{HH} = 0 \Longrightarrow C_{11}^{HE} = 0 \end{aligned}$$

$$(E_o^s)_2^H = +j(E_o^s)_2^E \Longrightarrow \left(C_{21}^{HE} + \frac{cos(\theta^i)}{tan(\xi_\parallel)} C_{21}^{HH}\right) = +j\left(C_{21}^{EE} + \frac{cos(\theta^i)}{tan(\xi_\parallel)} C_{21}^{EH}\right) \quad \text{(E.12)}$$

$$(E_o^s)_2^H = -j(E_o^s)_2^E \Longrightarrow \left(C_{21}^{HE} + \frac{cos(\theta^i)}{tan(\xi_\perp)} C_{21}^{HH}\right) = -j\left(C_{21}^{EE} + \frac{cos(\theta^i)}{tan(\xi_\perp)} C_{21}^{EH}\right) \quad \text{(E.13)}$$

Subtracting equation (E.13) from equation (E.12) produces:

$$cos(\theta^i)\left(\frac{1}{tan(\xi_\parallel)} - \frac{1}{tan(\xi_\perp)}\right) C_{21}^{HH} = j2C_{21}^{EE} + jcos(\theta^i)\left(\frac{1}{tan(\xi_\parallel)} + \frac{1}{tan(\xi_\perp)}\right) C_{21}^{EH} \quad \text{(E.14)}$$

From this last equation, one obtains:

$$C_{21}^{HH} = j\frac{2C_{21}^{EE} + cos(\theta^i)\left(\frac{1}{tan(\xi_\parallel)} + \frac{1}{tan(\xi_\perp)}\right) C_{21}^{EH}}{cos(\theta^i)\left(\frac{1}{tan(\xi_\parallel)} - \frac{1}{tan(\xi_\perp)}\right)} \quad \text{(E.15)}$$

Adding equation (E.13) to equation (E.12) produces:

$$2C_{21}^{HE} + cos(\theta^i)\left(\frac{1}{tan(\xi_\parallel)} + \frac{1}{tan(\xi_\perp)}\right) C_{21}^{HH} = jcos(\theta^i)\left(\frac{1}{tan(\xi_\parallel)} - \frac{1}{tan(\xi_\perp)}\right) C_{21}^{EH} \quad \text{(E.16)}$$

Performing:

$$\left(\frac{1}{tan(\xi_{||})}+\frac{1}{tan(\xi_{\perp})}\right)(\text{E.14})-\left(\frac{1}{tan(\xi_{||})}-\frac{1}{tan(\xi_{\perp})}\right)(\text{E.16})$$

produces:

$$-\left(\frac{1}{tan(\xi_{||})}-\frac{1}{tan(\xi_{\perp})}\right)C_{21}^{HE} = j\left(\frac{1}{tan(\xi_{||})}+\frac{1}{tan(\xi_{\perp})}\right)C_{21}^{EE}+\frac{j2cos(\theta^i)}{tan(\xi_{||})tan(\xi_{\perp})}C_{21}^{EH}$$

from which one obtains:

$$C_{21}^{HE}=-j\frac{\frac{2cos(\theta^i)}{tan(\xi_{||})tan(\xi_{\perp})}C_{21}^{EH}+\left(\frac{1}{tan(\xi_{||})}+\frac{1}{tan(\xi_{\perp})}\right)C_{21}^{EE}}{\left(\frac{1}{tan(\xi_{||})}-\frac{1}{tan(\xi_{\perp})}\right)} \qquad \text{(E.17)}$$

Now, from the unitary property of the matrix, one has:

$$C_{11}^{EE}(C_{11}^{EH})^*+C_{11}^{HE}(C_{11}^{HH})^*+C_{21}^{EE}(C_{21}^{EH})^*+C_{21}^{HE}(C_{21}^{HH})^*=0$$

Substituting in this expression the various equivalences obtained above, one finds:

$$\frac{4cos(\theta^i)}{tan(\xi_{||})tan(\xi_{\perp})}Real\left[C_{21}^{EE}(C_{21}^{EH})^*\right]= -\left(\frac{1}{tan(\xi_{||})}+\frac{1}{tan(\xi_{\perp})}\right)\left(\left|C_{21}^{EE}\right|^2+\frac{cos^2(\theta^i)}{tan(\xi_{||})tan(\xi_{\perp})}\left|C_{21}^{EH}\right|^2\right)$$

From this last equation and the various equivalences obtained above, one finds:

$$\begin{aligned}\left|C_{21}^{HE}\right|^2 &= -\frac{cos^2(\theta^i)}{tan(\xi_{||})tan(\xi_{\perp})}\left|C_{21}^{EH}\right|^2\\ \left|C_{21}^{HH}\right|^2 &= -\frac{tan(\xi_{||})tan(\xi_{\perp})}{cos^2(\theta^i)}\left|C_{21}^{EE}\right|^2\end{aligned}$$

Hence, one has:

$$-\frac{tan(\xi_{||})tan(\xi_{\perp})}{cos^2(\theta^i)}=\frac{\left|C_{21}^{HH}\right|^2}{\left|C_{21}^{EE}\right|^2}=\frac{\left|C_{21}^{EH}\right|^2}{\left|C_{21}^{HE}\right|^2} \qquad \text{(E.18)}$$

Also from the unitary property of the matrix, one has:

$$\begin{cases}\left|C_{11}^{EE}\right|^2+\left|C_{11}^{HE}\right|^2+\left|C_{21}^{EE}\right|^2+\left|C_{21}^{HE}\right|^2 &= 1\\ \left|C_{11}^{EH}\right|^2+\left|C_{11}^{HH}\right|^2+\left|C_{21}^{EH}\right|^2+\left|C_{21}^{HH}\right|^2 &= 1\end{cases}$$

Substituting in these expressions the various equivalences obtained above, and in particular equation (E.18), one finds:

$$\left|C_{21}^{EE}\right|^2 + \left|C_{21}^{EH}\right|^2 = 1 = \left|C_{21}^{EE}\right|^2 + \left|C_{21}^{HE}\right|^2$$

Hence, there obtains these important results:

$$\begin{cases} \left|C_{21}^{EH}\right| = \left|C_{21}^{HE}\right| \\ \left|C_{21}^{HH}\right| = \left|C_{21}^{EE}\right| \\ cos^2(\theta^i) = -tan(\xi_{||})tan(\xi_{\perp}) \end{cases}$$

Now, one has:

$$\xi_{\perp} = \xi_{||} \pm 90^o \Longrightarrow tan(\xi_{||})tan(\xi_{\perp}) = -1 \Longrightarrow cos^2(\theta^i) = 1$$

Therefore, one discovers that an ideal CP polarizer with the operation prescribed herein is possible only at normal incidence, regardless of the actual physical implementation! At this point, it is helpful to sketch the generic 2-port voltage scattering matrix for the CP polarizer according to:

$$\left\{ \begin{array}{l} \left|C_{21}^{EH}\right| = \left|C_{21}^{HE}\right| \\ \left|C_{21}^{HH}\right| = \left|C_{21}^{EE}\right| \\ \text{unitary property} \end{array} \right\}$$

One obtains:

$$C(E,H) = \begin{pmatrix} 0 & 0 & \dots & \dots \\ 0 & 0 & \dots & \dots \\ \sqrt{\mathcal{A}}e^{j\alpha_1} & \sqrt{1-\mathcal{A}}e^{j\alpha_2} & 0 & 0 \\ \sqrt{1-\mathcal{A}}e^{j\alpha_3} & -\sqrt{\mathcal{A}}e^{j(\alpha_2-\alpha_1+\alpha_3)} & 0 & 0 \end{pmatrix}$$

Substituting these generic expressions into the equations (E.15) and (E.17), one obtains after many algebraic manipulations:

$$\begin{cases} cos(\alpha_1 - \alpha_2) = \frac{(1-\mathcal{A})\left(tan(\xi_{\perp})-\tan(\xi_{||})\right)^2 - \mathcal{A}\left(tan(\xi_{\perp})+tan(\xi_{||})\right)^2 - 4(1-\mathcal{A})cos^2(\theta^i)}{4cos(\theta^i)\sqrt{\mathcal{A}(1-\mathcal{A})}\left(tan(\xi_{\perp})+tan(\xi_{||})\right)} \\ \frac{2\sqrt{\mathcal{A}}cos^2(\theta^i)}{tan(\xi_{||})tan(\xi_{\perp})}cos(2\alpha_2 - \alpha_1) + \frac{(2\mathcal{A}-1)cos(\theta^i)}{\sqrt{1-\mathcal{A}}}\left(\frac{1}{tan(\xi_{||})} + \frac{1}{tan(\xi_{\perp})}\right)cos(\alpha_2) - 2\sqrt{\mathcal{A}}cos(\alpha_1) = 0 \\ \frac{2\sqrt{\mathcal{A}}cos^2(\theta^i)}{tan(\xi_{||})tan(\xi_{\perp})}sin(2\alpha_2 - \alpha_1) + \frac{(2\mathcal{A}-1)cos(\theta^i)}{\sqrt{1-\mathcal{A}}}\left(\frac{1}{tan(\xi_{||})} + \frac{1}{tan(\xi_{\perp})}\right)sin(\alpha_2) - 2\sqrt{\mathcal{A}}sin(\alpha_1) = 0 \end{cases}$$

Substituting the third last equation into the last two equations and forming their ratio, one obtains:

$$\begin{aligned} tan(\alpha_1) = tan(\alpha_2) &\Longrightarrow \alpha_2 = \alpha_1 + m\pi \text{ where } m = 0, \pm 1, \pm 2, \ldots \\ &\Longrightarrow e^{j\alpha_2} = (-1)^m e^{j\alpha_1} \end{aligned}$$

Substituting $\alpha_2 = \alpha_1 + m\pi$ back into either one of the two aforementioned equations and squaring up that expression in order to eliminate the presence of the square root operator results in this quadratic expression in $\mathcal{A}$:

$$4\left(U^2 + V^2\right)\mathcal{A}^2 - 4\left(U^2 + V^2\right)\mathcal{A} + V^2 = 0$$

$$\text{where } \left\{ \begin{array}{l} U = tan(\xi_{||})tan(\xi_{\perp}) - cos^2(\theta^i) \\ V = cos(\theta^i)\left(tan(\xi_{||}) + tan(\xi_{\perp})\right) \end{array} \right.$$

The solution to this quadratic expression is:

$$\mathcal{A} = \frac{1}{2}\left(1 \pm \frac{U}{\sqrt{U^2 + V^2}}\right)$$

Furthermore:

$$\left\{ \begin{array}{l} cos^2(\theta^i) = -tan(\xi_{||})tan(\xi_{\perp}) \\ tan(\xi_{\perp}) = -1/tan(\xi_{||}) \end{array} \right\} \Longrightarrow \left\{ \begin{array}{rcl} \mathcal{A} & = & \frac{1}{2}\left(1 \mp sin(2\xi_{||})\right) \\ 1 - \mathcal{A} & = & \frac{1}{2}\left(1 \pm sin(2\xi_{||})\right) \end{array} \right.$$

Thus, the choice of the sign is not critical since:

$$\left\{ \begin{array}{rcccl} \mathcal{A} & = & \frac{1}{2}\left(1 - sin(2\xi_{||})\right) & = & 1 - \mathcal{A}' \\ 1 - \mathcal{A} & = & \frac{1}{2}\left(1 + sin(2\xi_{||})\right) & = & \mathcal{A}' \end{array} \right.$$

both choices $\mathcal{A}$ and $\mathcal{A}'$ being equally valid. For notational convenience, one takes hereafter:

$$\mathcal{A} = \frac{1}{2}\left(1 \pm sin(2\xi_{||})\right)$$

After some more algebraic manipulations, one obtains:

$$C_{21}^{HE} = \sqrt{1 - \mathcal{A}}e^{j\alpha_3} = je^{j\alpha_1}\left((-1)^m cos(\theta^i)sin(2\xi_{||})\sqrt{1 - \mathcal{A}} - cos(2\xi_{||})\sqrt{\mathcal{A}}\right)$$

$$\Longrightarrow \left\{ \begin{array}{rcl} \sqrt{1 - \mathcal{A}} & = & (-1)^m cos(\theta^i)sin(2\xi_{||})\sqrt{1 - \mathcal{A}} - cos(2\xi_{||})\sqrt{\mathcal{A}} \\ e^{j\alpha_3} & = & je^{j\alpha_1} \end{array} \right.$$

Thus, one has:

$$\left.\begin{array}{rcl}\sqrt{1-\mathcal{A}} & = & (-1)^m cos(\theta^i) sin(2\xi_{\|})\sqrt{1-\mathcal{A}} - cos(2\xi_{\|})\sqrt{\mathcal{A}} \\ \mathcal{A} & = & \frac{1}{2}\left(1 \pm sin(2\xi_{\|})\right)\end{array}\right\} \Longrightarrow (-1)^m cos(\theta^i) = \mp 1$$

Thus, it is seen that the value for $\mathcal{A}$ is independent of m or $cos(\theta^i)$. There obtains:

$$(-1)^m cos(\theta^i) = \mp 1 \Longrightarrow \left\{\begin{array}{l}(u = \mathrm{e},\, v = \mathrm{o}) \Longrightarrow cos(\theta^i) = -1 \Longrightarrow (-1)^m = \pm 1 \\ (u = \mathrm{o},\, v = \mathrm{e}) \Longrightarrow cos(\theta^i) = +1 \Longrightarrow (-1)^m = \mp 1\end{array}\right.$$

where e and o refer to even-numbered and odd-numbered waves, respectively. Substituting $e^{j\alpha_2}$ by $(-1)^m e^{j\alpha_1} = \pm e^{j\alpha_1}$ and $e^{j\alpha_3}$ by $je^{j\alpha_1}$, there obtains:

$$\left\{\begin{array}{rcl}C_{21}^{HE} & = & \sqrt{1-\mathcal{A}}e^{j\alpha_3} = je^{j\alpha_1}\sqrt{1-\mathcal{A}} \\ C_{21}^{HH} & = & -\sqrt{\mathcal{A}}e^{j(\alpha_2-\alpha_1+\alpha_3)} = \mp je^{j\alpha_1}\sqrt{\mathcal{A}}\end{array}\right.$$

Finally, one obtains the generic 2-port voltage scattering matrix for the CP polarizer as:

$$C(E,H) = \frac{e^{j\alpha}}{\sqrt{2}}\begin{pmatrix} 0 & 0 & \ldots & \ldots \\ 0 & 0 & \ldots & \ldots \\ Q^{\pm} & \mp Q^{\mp} & 0 & 0 \\ jQ^{\mp} & \mp jQ^{\pm} & 0 & 0 \end{pmatrix}$$

$$\text{where: } \left\{\begin{array}{l}Q^{\pm} = \sqrt{1 \pm sin(2\xi_{\|})} \\ Q^{\mp} = \sqrt{1 \mp sin(2\xi_{\|})} \\ \alpha \text{ is real valued}\end{array}\right.$$

The operation of the ideal CP polarizer corresponding to the second way is phrased as:

$$\left\{\begin{array}{l}\text{If } \left(E_o^i\right)_v^H = +j\left(E_o^i\right)_v^E \text{ for } (E_o^i)_u^l = 0, u \neq v, l = \{E,H\} \\ \quad \text{then } \left\{\begin{array}{ll}\left(E_o^s\right)_v^H = \left(E_o^s\right)_v^E = 0 & v = \{1,3\} \\ \frac{(E_o^s)_u^E}{(E_o^s)_u^H} = tan\left(\varsigma_{\perp} + n\pi\right) = \frac{tan(\xi_{\perp})}{cos(\theta^s)} & u\text{-ness} \neq v\text{-ness}\end{array}\right. \\ \text{If } \left(E_o^i\right)_v^H = -j\left(E_o^i\right)_v^E \text{ for } (E_o^i)_u^l = 0, u \neq v, l = \{E,H\} \\ \quad \text{then } \left\{\begin{array}{ll}\left(E_o^s\right)_v^H = \left(E_o^s\right)_v^E = 0 & v = \{1,3\} \\ \frac{(E_o^s)_u^E}{(E_o^s)_u^H} = tan\left(\varsigma_{\|} + n\pi\right) = \frac{tan(\xi_{\|})}{cos(\theta^s)} & u\text{-ness} \neq v\text{-ness}\end{array}\right.\end{array}\right.$$

$$\text{where } \xi_{\|} = \phi^i + 90^o - \phi_L \quad \text{and} \quad \xi_{\perp} = \xi_{\|} \pm 90^o$$

For $v = 1$, one obtains:

$$\begin{cases} (E_o^s)_1^E &= C_{11}^{EE}(E_o^i)_1^E + C_{11}^{EH}(E_o^i)_1^H \\ (E_o^s)_1^H &= C_{11}^{HE}(E_o^i)_1^E + C_{11}^{HH}(E_o^i)_1^H \end{cases}$$

$$(E_o^s)_1^H = +j(E_o^s)_1^E \Longrightarrow \begin{cases} (E_o^s)_1^E = \left(C_{11}^{EE} + jC_{11}^{EH}\right)(E_o^i)_1^E \\ (E_o^s)_1^H = \left(C_{11}^{HE} + jC_{11}^{HH}\right)(E_o^i)_1^E \end{cases}$$

$$\begin{aligned} (E_o^s)_1^E = 0 &\Longrightarrow C_{11}^{EE} = -jC_{11}^{EH} \\ (E_o^s)_1^H = 0 &\Longrightarrow C_{11}^{HE} = -jC_{11}^{HH} \end{aligned}$$

$$\begin{cases} (E_o^s)_2^E &= C_{21}^{EE}(E_o^i)_1^E + C_{21}^{EH}(E_o^i)_1^H \\ (E_o^s)_2^H &= C_{21}^{HE}(E_o^i)_1^E + C_{21}^{HH}(E_o^i)_1^H \end{cases}$$

$$(E_o^i)_1^H = +j(E_o^i)_1^E \Longrightarrow \begin{cases} (E_o^s)_2^E = \left(C_{21}^{EE} + jC_{21}^{EH}\right)(E_o^i)_1^E \\ (E_o^s)_2^H = \left(C_{21}^{HE} + jC_{21}^{HH}\right)(E_o^i)_1^E \end{cases}$$

$$(E_o^s)_2^H = \frac{cos(\theta^s)}{tan(\xi_{\perp})}(E_o^s)_2^E \Longrightarrow \left(C_{21}^{HE} + jC_{21}^{HH}\right) = \frac{cos(\theta^i)}{tan(\xi_{\perp})}\left(C_{21}^{EE} + jC_{21}^{EH}\right)$$

Similarly, one has:

$$\begin{cases} (E_o^s)_1^E &= C_{11}^{EE}(E_o^i)_1^E + C_{11}^{EH}(E_o^i)_1^H \\ (E_o^s)_1^H &= C_{11}^{HE}(E_o^i)_1^E + C_{11}^{HH}(E_o^i)_1^H \end{cases}$$

$$(E_o^s)_1^H = -j(E_o^s)_1^E \Longrightarrow \begin{cases} (E_o^s)_1^E = \left(C_{11}^{EE} - jC_{11}^{EH}\right)(E_o^i)_1^E \\ (E_o^s)_1^H = \left(C_{11}^{HE} - jC_{11}^{HH}\right)(E_o^i)_1^E \end{cases}$$

$$\begin{aligned} (E_o^s)_1^E = 0 &\Longrightarrow C_{11}^{EE} = +jC_{11}^{EH} \\ (E_o^s)_1^H = 0 &\Longrightarrow C_{11}^{HE} = +jC_{11}^{HH} \end{aligned}$$

$$\begin{cases} (E_o^s)_2^E &= C_{21}^{EE}(E_o^i)_1^E + C_{21}^{EH}(E_o^i)_1^H \\ (E_o^s)_2^H &= C_{21}^{HE}(E_o^i)_1^E + C_{21}^{HH}(E_o^i)_1^H \end{cases}$$

$$(E_o^i)_1^H = -j(E_o^i)_1^E \Longrightarrow \begin{cases} (E_o^s)_2^E = \left(C_{21}^{EE} - jC_{21}^{EH}\right)(E_o^i)_1^E \\ (E_o^s)_2^H = \left(C_{21}^{HE} - jC_{21}^{HH}\right)(E_o^i)_1^E \end{cases}$$

$$(E_o^s)_2^H = \frac{cos(\theta^s)}{tan(\xi_{||})}(E_o^s)_2^E \Longrightarrow \left(C_{21}^{HE} - jC_{21}^{HH}\right) = \frac{cos(\theta^i)}{tan(\xi_{||})}\left(C_{21}^{EE} - jC_{21}^{EH}\right)$$

In summary, one has:

$$C_{11}^{EE} = -jC_{11}^{EH} = +jC_{11}^{EH} \Longrightarrow C_{11}^{EH} = 0 \Longrightarrow C_{11}^{EE} = 0$$
$$C_{11}^{HE} = -jC_{11}^{HH} = +jC_{11}^{HH} \Longrightarrow C_{11}^{HH} = 0 \Longrightarrow C_{11}^{HE} = 0$$

$$(E_o^s)_2^H = \frac{cos(\theta^s)}{tan(\xi_{\perp})}(E_o^s)_2^E \Longrightarrow \left(C_{21}^{HE} + jC_{21}^{HH}\right) = \frac{cos(\theta^i)}{tan(\xi_{\perp})}\left(C_{21}^{EE} + jC_{21}^{EH}\right)$$

$$(E_o^s)_2^H = \frac{cos(\theta^s)}{tan(\xi_{||})}(E_o^s)_2^E \Longrightarrow \left(C_{21}^{HE} - jC_{21}^{HH}\right) = \frac{cos(\theta^i)}{tan(\xi_{||})}\left(C_{21}^{EE} - jC_{21}^{EH}\right)$$

Upon rearranging the terms, one obtains:

$$\left(-C_{21}^{HE} + \frac{cos(\theta^i)}{tan(\xi_{||})}C_{21}^{EE}\right) = +j\left(-C_{21}^{HH} + \frac{cos(\theta^i)}{tan(\xi_{||})}C_{21}^{EH}\right)$$

$$\left(-C_{21}^{HE} + \frac{cos(\theta^i)}{tan(\xi_{\perp})}C_{21}^{EE}\right) = -j\left(-C_{21}^{HH} + \frac{cos(\theta^i)}{tan(\xi_{\perp})}C_{21}^{EH}\right)$$

These equations have exactly the same form as the equations (E.12) and (E.13), respectively, if the following substitutions are made:

$$\left\{\begin{array}{rcl} C_{21}^{EE} & \leftarrow & -C_{21}^{HH} \\ C_{21}^{EH} & \leftarrow & +C_{21}^{EH} \\ C_{21}^{HE} & \leftarrow & -C_{21}^{HE} \\ C_{21}^{HH} & \leftarrow & +C_{21}^{EE} \end{array}\right\}$$

Thus, proceeding exactly the same way as before, one would find correspondingly that:

$$\begin{cases} \left|C_{21}^{EH}\right| = \left|C_{21}^{HE}\right| \\ \left|C_{21}^{HH}\right| = \left|C_{21}^{EE}\right| \\ cos^2(\theta^i) = 1 \end{cases}$$

Now if a sketch similar to that for the development of the first way was adopted here for the generic 2-port voltage scattering matrix, the same mathematical form

would not be maintained for the ensuing equations and some more mathematical development would be needed for the rest of the problem. However, the mathematical form does remain the same if the generic 2-port voltage scattering matrix is sketched differently, as follows:

$$C(E,H) = \begin{pmatrix} 0 & 0 & \dots & \dots \\ 0 & 0 & \dots & \dots \\ \sqrt{\mathcal{A}}e^{j(\alpha_2-\alpha_1+\alpha_3)} & \sqrt{1-\mathcal{A}}e^{j\alpha_2} & 0 & 0 \\ -\sqrt{1-\mathcal{A}}e^{j\alpha_3} & \sqrt{\mathcal{A}}e^{j\alpha_1} & 0 & 0 \end{pmatrix}$$

Again, proceeding exactly as before, one would obtain the generic 2-port voltage scattering matrix for the ideal CP polarizer as:

$$C(E,H) = \frac{e^{j\alpha}}{\sqrt{2}} \begin{pmatrix} 0 & 0 & \dots & \dots \\ 0 & 0 & \dots & \dots \\ \mp jQ^{\pm} & \mp Q^{\mp} & 0 & 0 \\ -jQ^{\mp} & -Q^{\pm} & 0 & 0 \end{pmatrix}$$

Now equating term by term the coefficients for the two GSM's corresponding to the first and the second ways, one obtains:

$$jQ^{\mp} = -jQ^{\mp} \Longrightarrow Q^{\mp} = 0 \Longrightarrow \xi_{\|} = \pm 45^{o}$$

the upper and the lower signs matching the upper and the lower signs in $Q^{\pm}$, respectively. Thus, one obtains:

$$\begin{cases} Q^{\mp} = 0 \\ Q^{\pm} = \sqrt{2} \end{cases}$$

and the GSM matrix by the first way becomes:

$$C(E,H) = \begin{pmatrix} 0 & 0 & \dots & \dots \\ 0 & 0 & \dots & \dots \\ e^{j\alpha_a} & 0 & 0 & 0 \\ 0 & \mp je^{j\alpha_a} & 0 & 0 \end{pmatrix}$$

and the GSM matrix by the second way becomes:

$$C(E,H) = \begin{pmatrix} 0 & 0 & \dots & \dots \\ 0 & 0 & \dots & \dots \\ \mp j e^{j\alpha_b} & 0 & 0 & 0 \\ 0 & -e^{j\alpha_b} & 0 & 0 \end{pmatrix}$$

Although both formulations are not identical, they are equivalent since it is the relationship between C_{21}^{EE} and C_{21}^{HH} that defines the operation of the LHCP polarizer, i.e. $C_{21}^{HH} = \mp j C_{21}^{EE}$. It becomes apparent here that the upper sign violates the initial hypothesis, thus, only the lower sign is admissible, thus $\xi_{\|} = -45^o$. Taking $e^{j\alpha_b} = j e^{j\alpha_a}$, the GSM matrix becomes:

$$C(E,H) = e^{j\alpha_a} \begin{pmatrix} 0 & 0 & \dots & \dots \\ 0 & 0 & \dots & \dots \\ 1 & 0 & 0 & 0 \\ 0 & j & 0 & 0 \end{pmatrix}$$

The operation of the ideal CP polarizer corresponding to the third way is phrased as:

$$\begin{cases} \text{If } \left(E_o^i\right)_v^H = +j\left(E_o^i\right)_v^E \text{ for } (E_o^i)_u^l = 0, u \neq v, l = \{E,H\} \\ \text{then} \begin{cases} \left(E_o^s\right)_v^H = \left(E_o^s\right)_v^E = 0 & v = \{2,4\} \\ \frac{(E_o^s)_u^E}{(E_o^s)_u^H} = tan\left(\varsigma_{\|} + n\,\pi\right) = \frac{tan(\xi_{\|})}{cos(\theta^s)} & u\text{-ness} \neq v\text{-ness} \end{cases} \\ \text{If } \left(E_o^i\right)_v^H = -j\left(E_o^i\right)_v^E \text{ for } (E_o^i)_u^l = 0, u \neq v, l = \{E,H\} \\ \text{then} \begin{cases} \left(E_o^s\right)_v^H = \left(E_o^s\right)_v^E = 0 & v = \{2,4\} \\ \frac{(E_o^s)_u^E}{(E_o^s)_u^H} = tan\left(\varsigma_{\perp} + n\,\pi\right) = \frac{tan(\xi_{\perp})}{cos(\theta^s)} & u\text{-ness} \neq v\text{-ness} \end{cases} \end{cases}$$

$$\text{where } \xi_{\|} = \phi^i + 90^o - \phi_L \quad \text{and} \quad \xi_{\perp} = \xi_{\|} \pm 90^o$$

For $v = 2$, one obtains:

$$\begin{cases} (E_o^s)_1^E &= C_{12}^{EE}(E_o^i)_2^E + C_{12}^{EH}(E_o^i)_2^H \\ (E_o^s)_1^H &= C_{12}^{HE}(E_o^i)_2^E + C_{12}^{HH}(E_o^i)_2^H \end{cases}$$

$$(E_o^s)_2^H = +j(E_o^s)_2^E \Longrightarrow \begin{cases} (E_o^s)_1^E = \left(C_{12}^{EE} + jC_{12}^{EH}\right)(E_o^i)_2^E \\ (E_o^s)_1^H = \left(C_{12}^{HE} + jC_{12}^{HH}\right)(E_o^i)_2^E \end{cases}$$

$$(E_o^s)_1^H = \frac{cos(\theta^s)}{tan(\xi_{||})}(E_o^s)_1^E \Longrightarrow \left(C_{12}^{HE} + jC_{12}^{HH}\right) = \frac{cos(\theta^i)}{tan(\xi_{||})}\left(C_{12}^{EE} + jC_{12}^{EH}\right)$$

$$\begin{cases} (E_o^s)_2^E &= C_{22}^{EE}(E_o^i)_2^E + C_{22}^{EH}(E_o^i)_2^H \\ (E_o^s)_2^H &= C_{22}^{HE}(E_o^i)_2^E + C_{22}^{HH}(E_o^i)_2^H \end{cases}$$

$$(E_o^i)_2^H = +j(E_o^i)_2^E \Longrightarrow \begin{cases} (E_o^s)_2^E = \left(C_{22}^{EE} + jC_{22}^{EH}\right)(E_o^i)_2^E \\ (E_o^s)_2^H = \left(C_{22}^{HE} + jC_{22}^{HH}\right)(E_o^i)_2^E \end{cases}$$

$$\begin{aligned} (E_o^s)_2^E = 0 &\Longrightarrow C_{22}^{EE} = -jC_{22}^{EH} \\ (E_o^s)_2^H = 0 &\Longrightarrow C_{22}^{HE} = -jC_{22}^{HH} \end{aligned}$$

Similarly, one has:

$$\begin{cases} (E_o^s)_1^E &= C_{12}^{EE}(E_o^i)_2^E + C_{12}^{EH}(E_o^i)_2^H \\ (E_o^s)_1^H &= C_{12}^{HE}(E_o^i)_2^E + C_{12}^{HH}(E_o^i)_2^H \end{cases}$$

$$(E_o^s)_2^H = -j(E_o^s)_2^E \Longrightarrow \begin{cases} (E_o^s)_1^E = \left(C_{12}^{EE} - jC_{12}^{EH}\right)(E_o^i)_2^E \\ (E_o^s)_1^H = \left(C_{12}^{HE} - jC_{12}^{HH}\right)(E_o^i)_2^E \end{cases}$$

$$(E_o^s)_1^H = \frac{cos(\theta^s)}{tan(\xi_{\perp})}(E_o^s)_1^E \Longrightarrow \left(C_{12}^{HE} - jC_{12}^{HH}\right) = \frac{cos(\theta^i)}{tan(\xi_{\perp})}\left(C_{12}^{EE} - jC_{12}^{EH}\right)$$

$$\begin{cases} (E_o^s)_2^E &= C_{22}^{EE}(E_o^i)_2^E + C_{22}^{EH}(E_o^i)_2^H \\ (E_o^s)_2^H &= C_{22}^{HE}(E_o^i)_2^E + C_{22}^{HH}(E_o^i)_2^H \end{cases}$$

$$(E_o^i)_2^H = -j(E_o^i)_2^E \Longrightarrow \begin{cases} (E_o^s)_2^E = \left(C_{22}^{EE} - jC_{22}^{EH}\right)(E_o^i)_2^E \\ (E_o^s)_2^H = \left(C_{22}^{HE} - jC_{22}^{HH}\right)(E_o^i)_2^E \end{cases}$$

$$\begin{aligned} (E_o^s)_2^E = 0 &\Longrightarrow C_{22}^{EE} = +jC_{22}^{EH} \\ (E_o^s)_2^H = 0 &\Longrightarrow C_{22}^{HE} = +jC_{22}^{HH} \end{aligned}$$

In summary, one has:

$$\begin{aligned} C_{22}^{EE} = -jC_{22}^{EH} = +jC_{22}^{EH} \Longrightarrow C_{22}^{EH} = 0 \Longrightarrow C_{22}^{EE} = 0 \\ C_{22}^{HE} = -jC_{22}^{HH} = +jC_{22}^{HH} \Longrightarrow C_{22}^{HH} = 0 \Longrightarrow C_{22}^{HE} = 0 \end{aligned}$$

$$(E_o^s)_1^H = \frac{cos(\theta^s)}{tan(\xi_{||})}(E_o^s)_1^E \Longrightarrow \left(C_{12}^{HE} + jC_{12}^{HH}\right) = \frac{cos(\theta^i)}{tan(\xi_{||})}\left(C_{12}^{EE} + jC_{12}^{EH}\right)$$

$$(E_o^s)_1^H = \frac{cos(\theta^s)}{tan(\xi_{\perp})}(E_o^s)_1^E \Longrightarrow \left(C_{12}^{HE} - jC_{12}^{HH}\right) = \frac{cos(\theta^i)}{tan(\xi_{\perp})}\left(C_{12}^{EE} - jC_{12}^{EH}\right)$$

Upon rearranging the terms, one obtains:

$$\left(-C_{12}^{HE} + \frac{cos(\theta^i)}{tan(\xi_{||})}C_{12}^{EE}\right) = +j\left(C_{12}^{HH} - \frac{cos(\theta^i)}{tan(\xi_{||})}C_{12}^{EH}\right)$$

$$\left(-C_{12}^{HE} + \frac{cos(\theta^i)}{tan(\xi_{\perp})}C_{12}^{EE}\right) = -j\left(C_{12}^{HH} - \frac{cos(\theta^i)}{tan(\xi_{\perp})}C_{12}^{EH}\right)$$

These equations have exactly the same form as the equations (E.12) and (E.13), respectively, if the following substitutions are made:

$$\left\{\begin{array}{lcl} C_{21}^{EE} & \leftarrow & +C_{12}^{HH} \\ C_{21}^{EH} & \leftarrow & -C_{12}^{EH} \\ C_{21}^{HE} & \leftarrow & -C_{12}^{HE} \\ C_{21}^{HH} & \leftarrow & +C_{12}^{EE} \end{array}\right\}$$

Thus, proceeding exactly the same way as before, one would find correspondingly that:

$$\left\{\begin{array}{l} \left|C_{12}^{EH}\right| = \left|C_{12}^{HE}\right| \\ \left|C_{12}^{HH}\right| = \left|C_{12}^{EE}\right| \\ cos^2(\theta^i) = 1 \end{array}\right.$$

The mathematical development remains the same as in that for the first way if the generic 2-port voltage scattering matrix is sketched differently, as follows:

$$C(E,H) = \left(\begin{array}{cccc} 0 & 0 & -\sqrt{\mathcal{A}}e^{j(\alpha_2-\alpha_1+\alpha_3)} & -\sqrt{1-\mathcal{A}}e^{j\alpha_2} \\ 0 & 0 & -\sqrt{1-\mathcal{A}}e^{j\alpha_3} & \sqrt{\mathcal{A}}e^{j\alpha_1} \\ \ldots & \ldots & 0 & 0 \\ \ldots & \ldots & 0 & 0 \end{array}\right)$$

Again, proceeding exactly as before and recalling that, here, one has:

$$cos(\theta^i) = +1 \Longrightarrow (-1)^m = \mp 1 \Longrightarrow e^{j\alpha_2} = (-1)^m e^{j\alpha_1} = \mp e^{j\alpha_1}$$

i.e. $e^{j\alpha_2}$ has the opposite sign to that it had in the development for the first way, one obtains the generic 2-port voltage scattering matrix for the ideal CP polarizer as:

$$C(E,H) = \frac{e^{j\alpha}}{\sqrt{2}} \begin{pmatrix} 0 & 0 & \pm jQ^{\pm} & \mp Q^{\mp} \\ 0 & 0 & -jQ^{\mp} & Q^{\pm} \\ \dots & \dots & 0 & 0 \\ \dots & \dots & 0 & 0 \end{pmatrix}$$

The operation of the ideal CP polarizer corresponding to the fourth way is phrased as:

$$\begin{cases} \text{If } \frac{(E_o^i)_v^E}{(E_o^i)_v^H} = tan\left(\varsigma_{\|} + n\,\pi\right) = \frac{tan(\xi_{\|})}{cos(\theta^i)} \text{ for } (E_o^i)_u^l = 0, u \neq v, l = \{E,H\} \\ \text{then} \begin{cases} (E_o^s)_v^H = (E_o^s)_v^E = 0 & v = \{2,4\} \\ (E_o^s)_u^H = -j(E_o^s)_u^E & u\text{-ness} \neq v\text{-ness} \end{cases} \\ \text{If } \frac{(E_o^i)_v^E}{(E_o^i)_v^H} = tan\left(\varsigma_{\perp} + n\,\pi\right) = \frac{tan(\xi_{\perp})}{cos(\theta^i)} \text{ for } (E_o^i)_u^l = 0, u \neq v, l = \{E,H\} \\ \text{then} \begin{cases} (E_o^s)_v^H = (E_o^s)_v^E = 0 & v = \{2,4\} \\ (E_o^s)_u^H = +j(E_o^s)_u^E & u\text{-ness} \neq v\text{-ness} \end{cases} \end{cases}$$

$$\text{where } \xi_{\|} = \phi^i + 90^o - \phi_L \quad \text{and} \quad \xi_{\perp} = \xi_{\|} \pm 90^o$$

For $v = 2$, one obtains:

$$\begin{cases} (E_o^s)_1^E &= C_{12}^{EE}(E_o^i)_2^E + C_{12}^{EH}(E_o^i)_2^H \\ (E_o^s)_1^H &= C_{12}^{HE}(E_o^i)_2^E + C_{12}^{HH}(E_o^i)_2^H \end{cases}$$

$$(E_o^i)_2^H = \frac{cos(\theta^i)}{tan(\xi_{\|})}(E_o^i)_2^E \Longrightarrow \begin{cases} (E_o^s)_1^E = \left(C_{12}^{EE} + \frac{cos(\theta^i)}{tan(\xi_{\|})}C_{12}^{EH}\right)(E_o^i)_2^E \\ (E_o^s)_1^H = \left(C_{12}^{HE} + \frac{cos(\theta^i)}{tan(\xi_{\|})}C_{12}^{HH}\right)(E_o^i)_2^E \end{cases}$$

$$(E_o^s)_1^H = -j(E_o^s)_1^E \implies \left(C_{12}^{HE} + \frac{cos(\theta^i)}{tan(\xi_{\|})}C_{12}^{HH}\right) = -j\left(C_{12}^{EE} + \frac{cos(\theta^i)}{tan(\xi_{\|})}C_{12}^{EH}\right)$$

$$\begin{cases} (E_o^s)_2^E &= C_{22}^{EE}(E_o^i)_2^E + C_{22}^{EH}(E_o^i)_2^H \\ (E_o^s)_2^H &= C_{22}^{HE}(E_o^i)_2^E + C_{22}^{HH}(E_o^i)_2^H \end{cases}$$

$$(E_o^i)_2^H = \frac{cos(\theta^i)}{tan(\xi_{\|})}(E_o^i)_2^E \Longrightarrow \left\{ \begin{array}{l} (E_o^s)_2^E = \left(C_{22}^{EE} + \frac{cos(\theta^i)}{tan(\xi_{\|})} C_{22}^{EH}\right)(E_o^i)_2^E \\ (E_o^s)_2^H = \left(C_{22}^{HE} + \frac{cos(\theta^i)}{tan(\xi_{\|})} C_{22}^{HH}\right)(E_o^i)_2^E \end{array} \right.$$

$$\begin{array}{rcl} (E_o^s)_2^E = 0 & \Longrightarrow & C_{22}^{EE} = -\frac{cos(\theta^i)}{tan(\xi_{\|})} C_{22}^{EH} \\ (E_o^s)_2^H = 0 & \Longrightarrow & C_{22}^{HE} = -\frac{cos(\theta^i)}{tan(\xi_{\|})} C_{22}^{HH} \end{array}$$

Similarly, one has:

$$\left\{ \begin{array}{rcl} (E_o^s)_1^E & = & C_{12}^{EE}(E_o^i)_2^E + C_{12}^{EH}(E_o^i)_2^H \\ (E_o^s)_1^H & = & C_{12}^{HE}(E_o^i)_2^E + C_{12}^{HH}(E_o^i)_2^H \end{array} \right.$$

$$(E_o^i)_2^H = \frac{cos(\theta^i)}{tan(\xi_{\perp})}(E_o^i)_2^E \Longrightarrow \left\{ \begin{array}{l} (E_o^s)_1^E = \left(C_{12}^{EE} + \frac{cos(\theta^i)}{tan(\xi_{\perp})} C_{12}^{EH}\right)(E_o^i)_2^E \\ (E_o^s)_1^H = \left(C_{12}^{HE} + \frac{cos(\theta^i)}{tan(\xi_{\perp})} C_{12}^{HH}\right)(E_o^i)_2^E \end{array} \right.$$

$$(E_o^s)_1^H = +j(E_o^s)_1^E \Longrightarrow \left(C_{12}^{HE} + \frac{cos(\theta^i)}{tan(\xi_{\perp})} C_{12}^{HH}\right) = +j\left(C_{12}^{EE} + \frac{cos(\theta^i)}{tan(\xi_{\perp})} C_{12}^{EH}\right)$$

$$\left\{ \begin{array}{rcl} (E_o^s)_2^E & = & C_{22}^{EE}(E_o^i)_2^E + C_{22}^{EH}(E_o^i)_2^H \\ (E_o^s)_2^H & = & C_{22}^{HE}(E_o^i)_2^E + C_{22}^{HH}(E_o^i)_2^H \end{array} \right.$$

$$(E_o^i)_2^H = \frac{cos(\theta^i)}{tan(\xi_{\perp})}(E_o^i)_2^E \Longrightarrow \left\{ \begin{array}{l} (E_o^s)_2^E = \left(C_{22}^{EE} + \frac{cos(\theta^i)}{tan(\xi_{\perp})} C_{22}^{EH}\right)(E_o^i)_2^E \\ (E_o^s)_2^H = \left(C_{22}^{HE} + \frac{cos(\theta^i)}{tan(\xi_{\perp})} C_{22}^{HH}\right)(E_o^i)_2^E \end{array} \right.$$

$$\begin{array}{rcl} (E_o^s)_2^E = 0 & \Longrightarrow & C_{22}^{EE} = -\frac{cos(\theta^i)}{tan(\xi_{\perp})} C_{22}^{EH} \\ (E_o^s)_2^H = 0 & \Longrightarrow & C_{22}^{HE} = -\frac{cos(\theta^i)}{tan(\xi_{\perp})} C_{22}^{HH} \end{array}$$

In summary, one has:

$$C_{22}^{EE} = -\frac{cos(\theta^i)}{tan(\xi_{\|})} C_{22}^{EH} = -\frac{cos(\theta^i)}{tan(\xi_{\perp})} C_{22}^{EH} \Longrightarrow C_{22}^{EH} = 0 \Longrightarrow C_{22}^{EE} = 0$$

$$C_{22}^{HE} = -\frac{cos(\theta^i)}{tan(\xi_{\|})} C_{22}^{HH} = -\frac{cos(\theta^i)}{tan(\xi_{\perp})} C_{22}^{HH} \Longrightarrow C_{22}^{HH} = 0 \Longrightarrow C_{22}^{HE} = 0$$

$$(E_o^s)_1^H = -j(E_o^s)_1^E \Longrightarrow \left(C_{12}^{HE} + \frac{cos(\theta^i)}{tan(\xi_{\|})} C_{12}^{HH}\right) = -j\left(C_{12}^{EE} + \frac{cos(\theta^i)}{tan(\xi_{\|})} C_{12}^{EH}\right)$$

$$(E_o^s)_1^H = +j(E_o^s)_1^E \Longrightarrow \left(C_{12}^{HE} + \frac{cos(\theta^i)}{tan(\xi_{\perp})} C_{12}^{HH}\right) = +j\left(C_{12}^{EE} + \frac{cos(\theta^i)}{tan(\xi_{\perp})} C_{12}^{EH}\right)$$

These equations have exactly the same form as the equations (E.12) and (E.13), respectively, if the following substitutions are made:

$$\left\{ \begin{array}{rcl} C_{21}^{EE} & \leftarrow & -C_{12}^{EE} \\ C_{21}^{EH} & \leftarrow & -C_{12}^{EH} \\ C_{21}^{HE} & \leftarrow & +C_{12}^{HE} \\ C_{21}^{HH} & \leftarrow & +C_{12}^{HH} \end{array} \right\}$$

Thus, proceeding exactly the same way as before, one would find correspondingly that:

$$\begin{cases} \left|C_{12}^{EH}\right| = \left|C_{12}^{HE}\right| \\ \left|C_{12}^{HH}\right| = \left|C_{12}^{EE}\right| \\ cos^2(\theta^i) = 1 \end{cases}$$

Again, the mathematical development remains the same if the generic 2-port voltage scattering matrix is sketched differently, as follows:

$$C(E,H) = \begin{pmatrix} 0 & 0 & -\sqrt{\mathcal{A}}e^{j\alpha_1} & -\sqrt{1-\mathcal{A}}e^{j\alpha_2} \\ 0 & 0 & \sqrt{1-\mathcal{A}}e^{j\alpha_3} & -\sqrt{\mathcal{A}}e^{j(\alpha_2-\alpha_1+\alpha_3)} \\ \dots & \dots & 0 & 0 \\ \dots & \dots & 0 & 0 \end{pmatrix}$$

Again, proceeding exactly as before and recalling that, here, one has:

$$cos(\theta^i) = +1 \Longrightarrow (-1)^m = \mp 1 \Longrightarrow e^{j\alpha_2} = (-1)^m e^{j\alpha_1} = \mp e^{j\alpha_1}$$

i.e. $e^{j\alpha_2}$ has the opposite sign to that it had in the development for the first way, one obtains the generic 2-port voltage scattering matrix for the ideal CP polarizer as:

$$C(E,H) = \frac{e^{j\alpha}}{\sqrt{2}} \begin{pmatrix} 0 & 0 & -Q^{\pm} & \mp Q^{\mp} \\ 0 & 0 & jQ^{\mp} & \pm jQ^{\pm} \\ \dots & \dots & 0 & 0 \\ \dots & \dots & 0 & 0 \end{pmatrix}$$

Now equating term by term the coefficients for the two GSM's corresponding to the third and the fourth ways, one obtains:

$$jQ^{\mp} = -jQ^{\mp} \Longrightarrow Q^{\mp} = 0 \Longrightarrow \xi_{\|} = \pm 45^{\circ}$$

the upper and the lower signs matching the upper and the lower signs in $Q^{\pm}$, respectively. Thus, one obtains:

$$\begin{cases} Q^{\mp} = 0 \\ Q^{\pm} = \sqrt{2} \end{cases}$$

and the GSM matrix by the third way becomes:

$$C(E,H) = \begin{pmatrix} 0 & 0 & \pm je^{j\alpha_c} & 0 \\ 0 & 0 & 0 & e^{j\alpha_c} \\ \dots & \dots & 0 & 0 \\ \dots & \dots & 0 & 0 \end{pmatrix}$$

and the GSM matrix by the fourth way becomes:

$$C(E,H) = \begin{pmatrix} 0 & 0 & -e^{j\alpha_d} & 0 \\ 0 & 0 & 0 & \pm je^{j\alpha_d} \\ \dots & \dots & 0 & 0 \\ \dots & \dots & 0 & 0 \end{pmatrix}$$

Although both formulations are not identical, they are equivalent since it is the relationship between C_{12}^{EE} and C_{12}^{HH} that defines the operation of the LHCP polarizer, i.e. $C_{12}^{HH} = \mp jC_{12}^{EE}$. It becomes apparent here that the upper sign violates the initial hypothesis, thus, only the lower sign is admissible, thus again $\xi_{\|} = -45^o$. Taking $e^{j\alpha_d} = je^{j\alpha_c}$, the GSM matrix becomes:

$$C(E,H) = e^{j\alpha_c} \begin{pmatrix} 0 & 0 & -j & 0 \\ 0 & 0 & 0 & 1 \\ \dots & \dots & 0 & 0 \\ \dots & \dots & 0 & 0 \end{pmatrix}$$

The complete formulation of the generic 2-port voltage scattering matrix for the ideal LHCP polarizer becomes:

$$C(E,H) = \begin{pmatrix} 0 & 0 & -je^{j\alpha_c} & 0 \\ 0 & 0 & 0 & e^{j\alpha_c} \\ e^{j\alpha_a} & 0 & 0 & 0 \\ 0 & je^{j\alpha_a} & 0 & 0 \end{pmatrix}$$

where α_a and α_c are real valued. It is noted again that the above results are valid only at normal incidence. Thus, the matrix would be symmetrical if $e^{j\alpha_c} = je^{j\alpha_a}$. That such is indeed the case can be argued from the fact that for the above matrix $C(E,H)$, the equation (2.3) implies that $C(E,H) = S(X,Y)$ at normal incidence.

Since $S(X,Y)$ is reciprocal, so must also be the above matrix $C(E,H)$. Therefore, one obtains:

$$C(E,H) = S(X,Y) = e^{j\alpha} \begin{pmatrix} 0 & 0 & 1 & 0 \\ 0 & 0 & 0 & j \\ 1 & 0 & 0 & 0 \\ 0 & j & 0 & 0 \end{pmatrix} \quad \text{where } \alpha \text{ is real valued.}$$

Since $C_{uv}^{pq} = 0$ with $p \neq q$ results from having $\xi_{||} = -45^o$, i.e. since $C_{uv}^{pq} = C_{uv}^{qp}$ as much as $C_{uv}^{pq} = -C_{uv}^{qp}$, nothing can be said as to whether or not the LHCP polarizer must be endowed with the 2-fold rotational or the longitudinal reflection symmetry.

The voltage scattering matrix for the RHCP polarizer is obtained simply by replacing all occurrences of j by $-j$ except in the exponent of the arbitrary phase term $e^{j\alpha}$. Such a result would also be obtained with the present development by replacing $\xi_{||}$ with $\xi_{\perp}$. One would then find $\xi_{\perp} = +45^o$ in order to conform to the initial hypothesis $C_{uv}^{HH} = -jC_{uv}^{EE}$ and thus, one would find $\xi_{||} = -45^o$ where $\xi_{||}$ is the direction of the input LP wave required to produce an output RHCP wave. This observation is in agreement with the observation made in Chapter 3 stating that an ideal RHCP polarizer is the same as an ideal LHCP polarizer rotated $\pm 90^o$ in the plane of the polarizer plate. Alternatively, one could make $\xi_{||}$ correspond to the direction of the input wave required to produce an output RHCP wave and repeat the initial development with j replaced by $-j$. One would again find $\xi_{||} = -45^o$ in order to conform to the initial hypothesis $C_{uv}^{HH} = -jC_{uv}^{EE}$.

Appendix F

MAPLE Results

This appendix presents a sample of the output results produced by the software MAPLE in computing the composite scattering matrix for the ideal cascade polarizer design of a CPSS and comparing it to the scattering matrix for the ideal CPSS.

The letter "I" within MAPLE stands for the imaginary number j. The angle (kzD) refers to the electrical length of the transmission line modelling the propagation medium of thickness D between any two consecutive layers. The angle (la) and (lb) refer to the two arbitrary angles in the GSM for the LP polarizer. The angle (ca) refers to the arbitrary angle in the GSM for each CP polarizer. The angles (sa) and (sb) refer to the two arbitrary angles in the GSM for the ideal LHCPSS or RHCPSS.

Comparison between the GSM for the ideal LHCPSS and the composite GSM for the ideal cascade polarizer LHCPSS reveals that both matrices are indeed identical upon taking (sa) = (la) + 2 (ca) - 2(kzD) and (sb) = (lb) + 2 (ca) - 2(kzD), and similarly for the case of the RHCPSS.

The results presented below pertain to the case with $\xi_{\|}^{LP} = +45^{o}$.

```
> evalm(SS11);
```

$$\begin{bmatrix} -\frac{1}{2}\,\frac{\%4^2\,\%2\,\%1}{\%3} & -\frac{1}{2}\,\frac{I\,\%4^2\,\%2\,\%1}{\%3} \\ -\frac{1}{2}\,\frac{I\,\%4^2\,\%2\,\%1}{\%3} & \frac{1}{2}\,\frac{\%4^2\,\%2\,\%1}{\%3} \end{bmatrix}$$

```
%1 := cos(kzD) - I sin(kzD)

%2 := cos(la) + I sin(la)

%3 := cos(kzD) + I sin(kzD)

%4 := cos(ca) + I sin(ca)
```

```
> evalm(SS22);
```

$$\begin{bmatrix} -\frac{1}{2}\,\frac{\%4^2\,\%2\,\%1}{\%3} & \frac{1}{2}\,\frac{I\,\%4^2\,\%2\,\%1}{\%3} \\ \frac{1}{2}\,\frac{I\,\%4^2\,\%2\,\%1}{\%3} & \frac{1}{2}\,\frac{\%4^2\,\%2\,\%1}{\%3} \end{bmatrix}$$

```
%1 := cos(kzD) - I sin(kzD)

%2 := cos(la) + I sin(la)

%3 := cos(kzD) + I sin(kzD)

%4 := cos(ca) + I sin(ca)
```

```
> evalm(SS21);
```

$$\begin{bmatrix} 1/2\,\frac{\%3^2\,\%1}{\%2^2} & -1/2\,\frac{I\,\%3^2\,\%1}{\%2^2} \\ 1/2\,\frac{I\,\%3^2\,\%1}{\%2^2} & 1/2\,\frac{\%3^2\,\%1}{\%2^2} \end{bmatrix}$$

$$\%1 := \cos(lb) + I\sin(lb)$$

$$\%2 := \cos(kzD) + I\sin(kzD)$$

$$\%3 := \cos(ca) + I\sin(ca)$$

```
> evalm(SS12);
```

$$\begin{bmatrix} 1/2\,\frac{\%3^2\,\%1}{\%2^2} & 1/2\,\frac{I\,\%3^2\,\%1}{\%2^2} \\ -1/2\,\frac{I\,\%3^2\,\%1}{\%2^2} & 1/2\,\frac{\%3^2\,\%1}{\%2^2} \end{bmatrix}$$

$$\%1 := \cos(lb) + I\sin(lb)$$

$$\%2 := \cos(kzD) + I\sin(kzD)$$

$$\%3 := \cos(ca) + I\sin(ca)$$

The results presented below pertain to the case with $\xi_{\|}^{LP} = -45^{o}$.

```
> evalm(SS11);
```

$$\begin{bmatrix} -\frac{1}{2}\,\frac{\%4^2\,\%2\,\%1}{\%3} & \frac{1}{2}\,\frac{I\,\%4^2\,\%2\,\%1}{\%3} \\ \frac{1}{2}\,\frac{I\,\%4^2\,\%2\,\%1}{\%3} & \frac{1}{2}\,\frac{\%4^2\,\%2\,\%1}{\%3} \end{bmatrix}$$

$$\%1 := \cos(kzD) - I\sin(kzD)$$

$$\%2 := \cos(la) + I\sin(la)$$

$$\%3 := \cos(kzD) + I\sin(kzD)$$

$$\%4 := \cos(ca) + I\sin(ca)$$

```
> evalm(SS22);
```

$$\begin{bmatrix} -\frac{1}{2}\,\frac{\%4^2\,\%2\,\%1}{\%3} & -\frac{1}{2}\,\frac{I\,\%4^2\,\%2\,\%1}{\%3} \\ -\frac{1}{2}\,\frac{I\,\%4^2\,\%2\,\%1}{\%3} & \frac{1}{2}\,\frac{\%4^2\,\%2\,\%1}{\%3} \end{bmatrix}$$

$$\%1 := \cos(kzD) - I\sin(kzD)$$

$$\%2 := \cos(la) + I\sin(la)$$

$$\%3 := \cos(kzD) + I\sin(kzD)$$

$$\%4 := \cos(ca) + I\sin(ca)$$

```
> evalm(SS21);
```

$$\begin{bmatrix} \frac{1/2\ \%3^2\ \%1}{\%2^2} & \frac{1/2\ I\ \%3^2\ \%1}{\%2^2} \\ \\ \frac{-1/2\ I\ \%3^2\ \%1}{\%2^2} & \frac{1/2\ \%3^2\ \%1}{\%2^2} \end{bmatrix}$$

$$\%1 := \cos(lb) + I \sin(lb)$$

$$\%2 := \cos(kzD) + I \sin(kzD)$$

$$\%3 := \cos(ca) + I \sin(ca)$$

```
> evalm(SS12);
```

$$\begin{bmatrix} \frac{1/2\ \%3^2\ \%1}{\%2^2} & \frac{-1/2\ I\ \%3^2\ \%1}{\%2^2} \\ \\ \frac{1/2\ I\ \%3^2\ \%1}{\%2^2} & \frac{1/2\ \%3^2\ \%1}{\%2^2} \end{bmatrix}$$

$$\%1 := \cos(lb) + I \sin(lb)$$

$$\%2 := \cos(kzD) + I \sin(kzD)$$

$$\%3 := \cos(ca) + I \sin(ca)$$

```
> evalm(LHCPSSideal);
```

$$\begin{bmatrix} -\%1 & -I\,\%1 & \%2 & I\,\%2 \\ -I\,\%1 & \%1 & -I\,\%2 & \%2 \\ \%2 & -I\,\%2 & -\%1 & I\,\%1 \\ I\,\%2 & \%2 & I\,\%1 & \%1 \end{bmatrix}$$

$$\%1 := \frac{1}{2}\cos(sa) + \frac{1}{2} I \sin(sa)$$

$$\%2 := \frac{1}{2}\cos(sb) + \frac{1}{2} I \sin(sb)$$

```
> evalm(RHCPSSideal);
```

$$\begin{bmatrix} -\%1 & I\,\%1 & \%2 & -I\,\%2 \\ I\,\%1 & \%1 & I\,\%2 & \%2 \\ \%2 & I\,\%2 & -\%1 & -I\,\%1 \\ -I\,\%2 & \%2 & -I\,\%1 & \%1 \end{bmatrix}$$

$$\%1 := \frac{1}{2}\cos(sa) + \frac{1}{2} I \sin(sa)$$

$$\%2 := \frac{1}{2}\cos(sb) + \frac{1}{2} I \sin(sb)$$

REFERENCES

[1] S. Cornbleet, Microwave Optics: the optics of microwave antenna design, Academic Press, 1976.

[2] J.E. Roy and L. Shafai, "Scattering Properties of Archimedean Spirals", *Proc. ANTEM'92*, Winnipeg, Canada, Aug. 1992, paper 540-545.

[3] R. G. Corzine and J. A. Mosko, Four-Arm Spiral Antennas, Artech House, 1990, ISBN 0-89006-348-6.

[4] R. Pierrot, "Éléments résonants en polarization circulaire et réflecteur semi-transparent composé de ces éléments", French Republic Patent# 89.609, No. 1.512.598, Dec. 30, 1966.

[5] P. Bossuet and F. Gautier, "Electromagnetic Wave Spatial Filter with Circular Polarization", USA Patent# 4,652,891, March 24, 1987.

[6] P. Bossuet and F. Gautier, "Electromagnetic Wave Spatial Filter with Circular Polarization and a Cassegrain Antenna Comprising Such a Filter", USA Patent# 4,728,961, March 1, 1988.

[7] W.V. Tilston, T. Tralman and S.M. Khanna, "A Polarization Selective Surface for Circular Polarization", *Proc. IEEE AP-Symposium*, 1988, Vol. II, pp. 762-765.

[8] W.V. Tilston, C. Cannon, Y. Sabourin and A. Hurd, A Polarization Selective

Surface for Circular Polarization, DREO Contract# 2SV84-00198, Til-tek, Final Report, March 30 ,1986.

[9] D.A. Tilston and J. Towne, Development of a 15 GHz Circular Polarization Selective Surface, DREO Contract# W7714-8-5651/01-SV, Final Report.

[10] Y.L. Chow, Analytical Study of the Circular Polarization Selective Surfaces - 7.75 and 15 GHz, DREO Contract# W7714-8-5652/01-SS, Final Report, March 1990.

[11] G.A. Morin, "A Simple Circular Polarization Selective Surface (CPSS)", *Proc. IEEE AP-Symposium*, 1990, pp. 100-101.

[12] J.E. Roy, G.A. Morin and L. Shafai, "Performance of a Simple Circular Polarization Selective Surface", *Proc. Canadian Conference on Electrical and Computer Engineering*, Sept. 1991, Vol. II, paper 38.4.1 .

[13] J.E. Roy, J. Shaker and L. Shafai, Theoretical Study of a Circularly Polarized Symmetric Cassegrain Antenna Using a CPSS Subreflector,
DREO Contract# W7714-8-9439/01-SS, Final Report, 1992.

[14] G.A. Morin, "Circular Polarization Selective Surfaces Made of Resonant Spirals", private communication.

[15] Wei-min Shi and Ming-gui Zhao, "Calculation of Circular Polarization Selective Structure", *Proc. ISAE'93*, pp. 345-348.

[16] B.A. Munk, R.G. Kouyoumjian and L. Peters JR., "Reflection Properties of Periodic Surfaces of Loaded Dipoles", *IEEE Trans. AP*, Vol. AP-19, No. 5, Sept. 1971, pp. 612-617.

[17] G.J. Burke and A.J. Poggio, Numerical Electromagnetic Code (NEC)

-Method of Moments, Naval Electronic Systems Command, Technical Document 116, Part I: Program Description-Theory, Part II: Program Description-Code, Part III: User's Manual, Revised on 2 Jan. 1980.

[18] R.L. Haupt and M. Cote, "Snell's Law Applied to Finite Surfaces", *IEEE Trans. AP*, Vol. AP-41, No. 2, Febr. 1994, pp. 227-230.

[19] H. Nakano, A. Yoshizawa, and J. Yamauchi, "Characteristics of a Crossed-Wire Scatterer Without a Junction Point for an Incident Wave of Circular Polarization", *IEEE Trans. AP*, AP-33, 1985, pp. 409-415.

[20] R.E. Collin, Foundation of Microwave Engineering, McGraw-Hill, 1966, pp. 170-179.

[21] J.L. Altman, Microwave Circuits, Van Nostrand, 1964, pp. 39.

[22] D.K. Cheng, Field and Wave Electromagnetics, Second Ed., Addison-Wesley Pub., 1989.

[23] R.C. Hall, R. Mittra and K.M. Mitzner, "Analysis of Multilayered Periodic Structures Using Generalized Scattering Matrix Theory", *IEEE Trans. AP*, Vol. 36, No. 4, April 1988, pp. 511-517.

[24] T. Cwik and R. Mittra, "The Cascade Connection of Planar Periodic Surfaces and Lossy Dielectric Layers to Form an Arbitrary Periodic Screen", *IEEE Trans. AP*, Vol. 35, No. 12, December 1987, pp. 1397-1405.

[25] T. Cwik and R. Mittra, "Correction to "The Cascade Connection of Planar Periodic Surfaces and Lossy Dielectric Layers to Form an Arbitrary Periodic Screen", *IEEE Trans. AP*, Vol. 36, No. 9, September 1988, pp. 1335.

[26] R. Mittra, C.H. Chan and T. Cwik, "Techniques for Analyzing Frequency Selective Surfaces - A Review", *Proc. IEEE*, Vol. 76, No. 12, December 1988,

pp. 1593-1615.

[27] T.R. Schimert, A.J. Brouns, C.H. Chan and R. Mittra, "Investigation of Millimeter-Wave Scattering from Frequency Selective Surfaces", *IEEE-MTT*, Vol. 39, No. 2, February 1991, pp. 315-322.

[28] S. Contu and R. Tascone, "Scattering From Passive Arrays In Plane Stratified Regions", *Electromagnetics*, No. 5, 1985, pp. 285-306.

[29] R.E. Jorgenson and R. Mittra, "Oblique Scattering from Lossy Strip Structures with One-Dimensional Periodicity", *IEEE Trans. AP*, Vol. 38, No. 2, February 1990, pp. 212-219.

[30] K.W. Whites and R. Mittra, "Scattered Field Properties of Symmetric Periodic Structures", *IEEE Trans. AP*, Vol. 42, No. 5, May 1994, pp. 722-727.

[31] G.M. Whitman and F. Schwering, "Reciprocity Identity for Periodic Surface Scattering", *IEEE Trans. AP*, Vol. 27, No. 2, March 1979, pp. 252-254.

[32] T. Cwik and R. Mittra, "Scattered from General Periodic Screens", *Electromagnetics*, No. 5, 1985, pp. 263-283.

[33] A. Mackay, "Proof of Polarization Independence and Nonexistence of Crosspolar Terms for Targets Presenting n-fold ($n > 2$) Rotational Symmetry with Special Reference to Frequency-Selective Surfaces", *Electronics Letters*, Vol. 25, No. 24, November 1989, pp. 1624-1625.

[34] G.E. Heath, "Bistatic Scattering Reflection Asymmetry, Polarization Reversal Asymmetry, and Polarization Reversal Reflection Symmetry", *IEEE Trans. AP*, Vol. 29, No. 3, May 1981, pp. 429-434.

[35] C.E. Baum and H.N. Kritikos, "Symmetry in Electromagnetics", Physics Notes, Note 2, December 1990, pp. 1-70.

[36] H. Mott, Antennas for Radar and Communications: A Polarimetric Approach, John Wiley & Sons, 1992, Chapter 6.

[37] N. Hill and S. Cornbleet, "Microwave Transmission Through a Series of Inclined Gratings", *Proc. IEE*, Vol. 120, No. 4, April 1973, pp. 407-412.

[38] N. Amitay and A.A.M. Saleh, "Broad-Band Wide-Angle Quasi-Optical Polarization Rotators", *IEEE Trans. AP*, Vol. 31, No. 1, January 1983, pp. 73-76.

[39] M.H. Chen, "Design Formulas for a Quasi-Optical Diplexer or Multiplexer", *IEEE Trans. MTT*, Vol. MTT-28, No. 4, April 1980, pp. 363-368.

[40] M. Ando, A. Kondo and K. Kagoshima, "Scattering of an arbitrary wave by a thin strip grating reflector", *IEE Proc.*, Vol. 133 Pt. H, No. 3, June 1986, pp. 203-208.

[41] M. Ando and K. Takei, "Reflection and Transmission Coefficients of a Thin Strip Grating for Antenna Application", *IEEE Trans. AP*, Vol. AP-135, No. 4, April 1987, pp. 367-371.

[42] B. Gimeno, J.L. Cruz, E.A. Navarro and V. Such, "A Polarizer Rotator System for Three-Dimensional Oblique Incidence", *IEEE Trans. AP*, Vol. 42, No. 7, July 1994, pp. 912-919.

[43] H.M. Altschuler and L.O. Goldstone, "On Network Representations of Certain Obstacles in Waveguide Regions", *IRE Trans. on Microw. and Techn.*, April 1959, pp. 213-221.

[44] H.M. Altschuler and L.O. Goldstone, A Class of Alternative Modal Representations for Uniform Waveguide Regions, Research Report R-557, PIB-485 for Air Force Cambridge Research Center, Contract AF-19(604)-2031, February 27, 1957.

[45] Per-Simon Kildal, "Artificially Soft and Hard Surfaces in Electromagnetics", *IEEE Trans. AP*, Vol. 38, No. 10, October 1990, pp. 1537-1544.

[46] J.A. Aas, "Plane-Wave Reflection Properties of Two Artificially Hard Surfaces", *IEEE Trans. AP*, Vol. 39, No. 5, May 1991, pp. 651-656.

[47] F.S. Crawford Jr., Berkeley Physics Course: Waves, Vol. 3, McGraw-Hill, 1968.

[48] R.C. Jones, "A New Calculus for the Treatment of Optical System. Part VII. Properties of the N-matrices", *J. Opt. Soc. Am.*, Vol. 38, No. 8, Aug. 1948, pp. 671-685.

[49] R.E. Collin and J. Brown, "The Design of Quarter-Wave Matching Layers for Dielectric Surfaces", Monograph No. 149 R, Sept. 1955, pp. 153-158.

[50] E.M.T. Jones, T. Morita and S.B. Cohn, "Measured Performance of Matched Dielectric Lenses", *IRE Trans. AP*, Vol 4, Jan. 1956, pp. 31-33.

[51] T. Morita and S.B. Cohn, "Microwave Lens Matching by Simulated Quarter-Wave Transformers", *IRE Trans. AP*, Vol 4, Jan. 1956, pp. 33-39.

[52] R.E. Collin, "Reflection and Transmission at a Slotted Dielectric Interface", *Can. J. Phys.*, Vol 34, 1956, pp. 308-411.

[53] R.E. Collin, "A Simple Anisotropic Dielectric Medium", *IRE Trans. MTT.*, April 1958, pp. 206-209.

[54] R.E. Collin, Correction to "A Simple Anisotropic Dielectric Medium", *IRE Trans. MTT.*, Oct. 1958, pp. 414.

[55] R.E. Collin, "Properties of Slotted Dielectric Interfaces", *IRE Trans. Ant. Prop.*, Jan. 1964, pp. 62-73.

[56] H.S. Kirschbaum and S. Chen, "A Method of Producing Broad-Band Circular Polarization Employing an Anisotropic Dielectric", *IRE Trans. MTT*, July 1957, pp. 199-203.

[57] M. Born and E. Wolf, Principles of Optics, Pergamon Press Inc., 1959, pp. 702-704.

[58] R. Petit, Electromagnetic Theory of Gratings, Springer-Verlag Berlin Heidelberg, 1980

[59] R. Magnusson and T.K. Gaylord, "Diffraction efficiencies of thin phase gratings with arbitrary grating shape", *J. Opt. Soc. Am.*, Vol. 68, No. 6, June 1968, pp. 806-809.

[60] M.G. Moharam and T.K. Gaylord, "Chain-matrix analysis of arbitrary-thickness dielectric reflection gratings", *J. Opt. Soc. Am.*, Vol. 72, No. 2, Feb. 1982, pp. 187-190.

[61] S.L. Chuang and J.A. Kong, "Wave scattering from a periodic dielectric surface for a general angle of incidence", *Radio Science*, Vol. 17, No. 3, May 1982, pp. 545-557.

[62] M.K. Moaveni, "Plane Wave Diffraction by Dielectric Gratings, Finite-Difference Formulation", *IEEE Trans. AP*, Vol 37, No. 8, Aug. 1989, pp. 1026-1031.

[63] L.R. Lewis and A. Hessel, "Propagation Characteristics of Periodic Arrays of Dielectric Slabs", *IRE Trans. MTT*, Vol MTT-19, No. 3, March 1971, pp. 276-286.

[64] D.G. Bodnar and H.L. Basset, "Analysis of an Anisotropic Dielectric Radome", *IRE Trans. AP*, Nov. 1975, pp. 841-846.

[65] R. Padman, "Reflection and Cross-Polarization Properties of Grooved Dielectric Panels", *IRE Trans. AP*, Vol AP-26, No. 5, Sept. 1978, pp. 741-743.

[66] S.R. Seshadri, "Reflection and Transmission Coefficients of a Periodic Dielectric Slab", *Proc. IEEE*, Vol 66, No. 6, June 1978, pp. 699-700.

[67] H.L. Bertoni, L-H.S. Cheo and T. Tamir, "Frequency-Selective Reflection and Transmission by a Periodic Dielectric Layer", *IEEE Trans. AP*, Vol 37, No. 1, Jan. 1989, pp. 78-83.

[68] R. Magnusson, S.S. Wang, T.D. Black and A. Sohn, "Resonance Properties of Dielectric Waveguide Gratings: Theory and Experiments at 4-18 GHz", *IEEE Trans. AP*, Vol 42, No. 4, Apr. 1994, pp. 567-569.

[69] W.T. Pinello, R. Lee and A.C. Cangellaris, "Finite Element Modeling of Electromagnetic Wave Interactions with Periodic Dielectric Structures", *IEEE Trans. MTT*, Vol. 42, No. 12, Dec. 1994, pp. 2294-2301.

[70] R.E. Collin, Field Theory of Guided Waves, McGraw-Hill, 1960, Chapter 12.

[71] R.E. Collin and F.J. Zucker, Antenna Theory, part II, McGraw-Hill, 1969, Chapter 18 by J. Brown.

[72] R.S. Elliott, Antenna Theory and Design, Prentice-Hall, 1981, pp. 538-545.

[73] D.S. Lerner, "A Wave Polarization Converter for Circular Polarization", *IEEE Trans. AP*, Jan. 1965, pp. 3-7.

[74] A.J. Lait, "Broadband Circular Polarisers", *The Marconi Review*, Second Quarter, 1969, pp. 159-184.

[75] L. Young, L.A. Robinson and C.A. Hacking, "Meander-Line Polarizer", *IEEE Trans. AP*, May 1973, pp. 376-378.

[76] K.A.J. Warren, "A Planar Antenna Circular Polarization Converter Utilizing Printed Circuit Technology", *The Marconi Review*, Third Quarter, 1980, pp. 177-184.

[77] P. Poey and P-L. Guigue, "Determination of the Current Distribution on an Infinite Periodic Structure of Thin-Metallic Wires", *IEEE Trans. AP*, Vol. AP-32, No. 1, Jan. 1984, pp. 93-95.

[78] P. Poey and P-L. Guigue, "Determination of the Current Distribution on a Bidimensional Infinite Periodic Structure of Thin Metallic Wires Using the Method of the Singular Integral Equation", *IEEE Trans. AP*, Vol. AP-35, No. 2, Febr. 1987, pp. 221-224.

[79] C. Terret, J.R. Levrel and K. Mahdjoubi, "Susceptance Computation of a Meander-Line Polarizer Layer", *IEEE Trans. AP*, Vol. AP-32, No. 9, Sept. 1984, pp. 1007-1011.

[80] Ruey-Shi Chu and Kuan-Min Lee, "Analytical Model of a Multilayered Meander-Line Polarizer Plate with Normal and Oblique Plane-Wave Incidence", *IEEE Trans. AP*, Vol. AP-35, No. 6, June 1987, pp. 652-661.

[81] Ruey-Shi Chu and Kuan-Min Lee, Correction to "Analytical Model of a Multilayered Meander-Line Polarizer Plate with Normal and Oblique Plane-Wave Incidence", *IEEE Trans. AP*, Vol. AP-36, No. 7, July 1988, pp. 1041.

[82] E. Orleansky, C. Samson and M. Havkin, "A Broadband Meanderline Twistreflector for the Inverse Cassegrain Antenna", *Microwave Journal*, Oct. 1987, pp. 185-192.

[83] E.A. Parker, A.N.A. El Sheikh and A.C. de C. Lima, "Convoluted frequency-selective array elements derived from linear and crossed dipoles", *IEE Proc.-H*, Vol. 140, No. 5, Oct. 1993, pp. 378-380.

[84] Te-Kao Wu, "Meander-Line Polarizer for Arbitrary Rotation of Linear Polarization", *IEEE Microw. and Guided Wave Letters*, Vol. 4, No. 6, June 1994, pp. 199-201.

[85] A.D. Shatrow, A.D. Chuprin and A.N. Sinov, "Constructing the Phase Converters Consisting of Arbitrary Number of Translucent Surfaces", *IEEE Trans. AP*, Vol. 43, No. 1, Jan. 1995, pp. 109-113.

[86] R.C. Johnson, Antenna Engineering Handbook, Third Ed., McGraw-Hill, 1993, pp. 23:25-23:28, 46:10-46:14.

[87] J.K. Skwirzynski and J.C. Thackray, "Transmission of Electromagnetic Waves Through Wire Gratings (theory)", *The Marconi Review*, Second Quarter, 1959, pp. 77-90.

[88] E.G.A. Goodall and J.A.C. Jackson, "Transmission of Electromagnetic Waves Through Wire Gratings (experimental)", *The Marconi Review*, Second Quarter, 1959, pp. 91-98.

[89] N. Marcuvitz and J. Schwinger, "On the Representation of the Electric and Magnetic Fields Produced by Currents and Discontinuities in Wave Guides. I*", *J. Applied Physics*, Vol. 22, No. 6, June 1951, pp. 806-819.

[90] N. Marcuvitz, Waveguide Handbook, McGraw-Hill, 1951, pp. 3-7.

[91] L.B. Felsen and N. Marcuvitz, Radiation and Scattering of Waves, Prentice-Hall, 1973, pp. 185-192.

[92] R.E. Collin and F.J. Zucker, Antenna Theory, part II, McGraw-Hill, 1969.

[93] D.C. Stinson, Intermediate Mathematics of Electromagnetics, Prentice-Hall, 1976, pp. 159, 255-257.

[94] R.F. Harrington, Time-Harmonic Electromagnetic Fields, McGraw-Hill, 1961, pp. 129-132.

[95] C.A. Balanis, Antenna Theory, Analysis and Design, John Wiley & Sons, 1982.

[96] Y. Zhang, K. Hirasawa and K. Fujimoto, "Opened Parasitic Elements Nearby a Driven Dipole", *IEEE Trans. AP*, Vol. AP-34, No. 5, May 1986, pp. 711-713.

[97] W.K. Khan and H. Kurss, "Minimum-Scattering Antennas", *IEEE Trans. AP*, Vol. AP-13, No. 9, Sept. 1965, pp. 671-675.

[98] W. Wasylkiwskyj and W.K. Khan, "Theory of Mutual Coupling Among Minimum-Scattering Antennas", *IEEE Trans. AP*, Vol. AP-18, No. 2, Febr. 1970, pp. 204-216.

[99] P.G. Rogers, "Application of the Minimum Scattering Antenna Theory to Mismatched Antennas", *IEEE Trans. AP*, Vol. AP-34, No. 10, Oct. 1986, pp. 1223-1228.

[100] D.M. Pozar, "Antenna Synthesis and Optimization Using Weighted Inagaki Modes", *IEEE Trans. AP*, Vol. AP-32, No. 2, Feb. 1986, pp. 159-165.

[101] D.M. Pozar, Corrections to "Antenna Synthesis and Optimization Using Weighted Inagaki Modes", *IEEE Trans. AP*, Vol. AP-35, No. 6, June 1987, p. 742.

[102] R.J. Garbacz and R.H. Turpin, "A Generalized Expansion for Radiated and Scattered fields", *IEEE Trans. AP*, Vol. AP-19, No. 5, May 1971, pp. 348-358.

[103] D. Liu, R.J. Garbacz and D.M. Pozar, "Antenna Synthesis and Optimization Using Generalized Characteristic Modes", *IEEE Trans. AP*, Vol. AP-38, No. 6, June 1990, pp. 862-868.

[104] M.L. Kales, "Part III - Elliptically Polarized Waves and Antennas", *Proc. IRE*, Vol. 39, pp. 544-549, May 1951.

[105] N. Amitay, V. Galindo and C.P. Wu, Theory and Analysis of Phased Array Antennas, Wiley-Interscience, 1972.

[106] R. Mittra, Y. Rahmat-Samii, D.V. Jamnejad and W.A. Davis, "A new look at the thin-plate scattering problem", *Radio Science*, Vol. 8, No. 10, Oct. 1973, pp. 869-875.

[107] C.W. Trueman and S.J. Kubina, "RCS of Fundamental Scatterers in the HF Band by Wire-Grid Modelling", *Canadian Conference on Electrical and Computer Engineering*, Ottawa, Sept. 3-6, 1990, pp. 54.3.1-54.3.4 .

[108] X.H. Yang, L. Shafai and A. Sebak, "A Comparison Study on Wire-Grid Model and Point Matching Technique with Subdomain Basis Functions", *Proc. ANTEM'92*, Winnipeg, Canada, Aug. 5-7, 1992, pp. 656-661.

[109] S.W. Schneider and B.A. Munk, "The Scattering Properties of "Super Dense" Arrays of Dipoles", *IEEE Trans. AP*, Vol. AP-42, No. 2, April 1994, pp. 463-472.